Scuola Normale Superiore

Anno Accademico 2020/2021

Tesi di perfezionamento in Nanoscienze

Dissipative quantum systems: theoretical foundations and applications

Candidato:

Donato Farina

Scuola Normale Superiore, Istituto Italiano di Tecnologia

Relatori:

Prof. **Vittorio Giovannetti**

Scuola Normale Superiore

Prof. **Marco Polini**

Università di Pisa

February 25, 2021

ABSTRACT

Motivated by the continuous advancements in the miniaturization of devices down to reveal the quantum nature of matter, in this thesis we investigate the way a quantum system is affected by the presence of a thermal environment and propose methodologies to exploit this kind of sensitivity for quantum technologies. Since treating exactly the dynamics of the full system-environment compound is generally problematic for the diverging number of degrees of freedom involved in the calculation, effective master equations for the reduced system density matrix were developed in literature during the last century. Among them, the Redfield approach is an equation obtained under weak-coupling (or Born) and Markovian assumptions. Despite offering effective descriptions in a plethora of situations, it was criticized for not preserving the positivity (and hence the complete positivity) of the system density matrix. The latter property is in general a fundamental feature for assigning a probabilistic interpretation to the theory. We hence begin by facing the problem of the non-positivity character of the Redfield equation, curing it of the strict amount that is necessary via coarse-grain averaging performed on the Redfield equation in the interaction picture. In the analysis a central role is played by the coarse grain timescale. Once set it equal to a critical threshold value, the resulting equation (*CP-Redfield*) enables conserving the predictive power of the Redfield approach and preserving positivity at the same time. About it, we report both practical estimation and self-consistent methods to evaluate the critical timescale. Our strategy also allows to continuously map the Redfield equation into the *secular* master equation (*diverging* coarse-grain time interval) by appropriately tuning the coarse grain time, the latter being the equation usually adopted in the literature for ensuring thermodynamic consistency by enforcing a rotating-wave approximation. Starting from a minimal example concerning the dipole coupling between a qubit and a bosonic bath, we then apply this methodology to dissipative multipartite systems, for which the *local vs global* debate is of current interest. The local master equation is instead the equation that is obtained by assigning to each subsystem its proper thermal dissipator, preserving the local character of the microscopic interactions, while the global approach is the Redfield equation in the secular limit. In this context, we studied an *asymmetric* en-

ergy transfer model constituted by harmonic oscillators which, being exactly solvable, provides the appropriate benchmark for testing the efficiency of the different master equations. Beyond finding useful the application of the CP-Redfield equation, we point out a sensible convex-mixture of the local and global solutions based on the timescale separation of the two strategies. The local approach is then applied in the context of quantum batteries, a field that was previously analyzed under closed (i.e. Hamiltonian) settings. We hence provide one of the first attempts of schematizing an open quantum battery, where, recalling in part the aforementioned *asymmetric* model, the charging process originates from external sources (coherent and/or noisy) and is mediated by a proper quantum charger. By studying different implementations, particular attention was devoted to find possible interplay between coherent and incoherent energy supply mechanisms in producing stored energy and ergotropy, the latter being defined in literature as the maximum extractable work. As a central result, increasing temperature is not always detrimental for the stored ergotropy. Going beyond the particular instance of bosonic bath, the sensitivity of a quantum system to its surrounding environment is finally exploited in the context of statistical tagging, where one aims to guess the quantum statistics (fermionic or bosonic) of a thermal bath of interest, introducing in this way a novel research line in the field of quantum metrology. We propose an indirect measurement protocol in which a quantum probe is let to interact with the unknown bath and relies on the consideration that, despite the final probe equilibrium configuration is not necessarily influenced by the bath nature, the latter generally leaves residual imprintings in the probe state before thermalization, i.e. out-of-equilibrium. Using figures of merit taken from quantum metrology such as the Holevo-Helstrom probability of error and the quantum Chernoff bound, we treated the cases of qubit and harmonic oscillator probes, finding that, generally, the presence of coherences in the input state of the probe is beneficial for the discrimination capability and noticing a bosonic advantage in reducing to zero the error probability.

Keywords: *Open quantum systems*, *Redfield equation*, *Open quantum batteries*, *Statistics tagging*, *Quantum metrology*.

TABLE OF CONTENTS

CHAPTER 1

Introduction

We start discussing the motivations which led to the writing of this thesis, giving an overview of the research environment in which we carried out the research, and providing a brief summary of the personal contributions in the field of open quantum systems, both at a fundamental level of the theory and regarding some applications that may be useful for current and future nano-technology advancements.

1.1 Preface

It is now established that, for describing phenomena at the nano-scale, classical physics fails miserably in the majority of cases, while the principles of quantum mechanics represent building blocks for modeling and, therefore, for making predictions. The fundamental laws of quantum mechanics have been set during the last century. The superposition principle and the tensor product structure of the Hilbert space are the elements which entail the novel resources of the theory: quantum coherence and entanglement. In our era it is the time of developing new technologies based on these new principles at a fundamental level, trying to exploit the new resources with the ideal perspective of getting some advantages with respect to the classical processes. In such a sense, we are in the middle of a second quantum revolution (Dowling and Milburn 2003). However, even in the cases where quantum coherence does not imply relevant technological advantages, in the nano-scale world we are often still constrained to take into account the new actual rules of the game. Put differently, one can state that, depending on the context, the new rules can lead to technological advantages or even disadvantages. However, since those rules do control the nano-scale phenomena, they certainly must be taken into account for an accurate modeling. Here some examples:

- One can think to build a thermal engine at the nano-scale or to model some small biological mechanism of interest, entering in the context of quantum thermodynamics (Vinjanampathy and Anders 2016);
- One can need to measure the temperature or any parameters of very small systems or subsystems, entering in the framework of quantum thermometry and, more generally, of quantum metrology (Giovannetti et al. 2006);

- One can aim to overcome the efficiency of the existing security protocols using quantum mechanics, entering in the field of quantum cryptography and quantum communication (Gisin and Thew 2007);
- Finally, probably the most attracting context where quantum mechanics is expected to provide a fundamental improvement is quantum computation. Exploiting quantum resources into the data processing, protocols which are of exponential overhead on classical computers become (in principle) of polynomial overhead on a quantum computer, one of the most famous examples being the Peter Shor's factoring algorithm (Shor 1994).

However, in most of the cases, protocols that are theoretically perfectly consistent with the quantum theory are very difficult to implement in a laboratory. This happens because a quantum system is never completely isolated, but, unavoidably, interacts with unwanted external degrees of freedom, that are generically referred as environment. Basic examples are vibrations or spurious light on the sample. The effect of this surroundings is generally detrimental, destroying those quantum resources that make the gap with classical protocols. Paradoxically, this happens just because the environment establishes quantum correlations with the system, inducing decoherence locally on the reduced state of the latter, formally obtained by tracing out the environmental degrees of freedom. Intuitively, this can be understood thinking at the case of a Bell's state, i.e. a maximally entangled state, whose parts are locally completely mixed, i.e. without any coherence. On the opposite side, an interesting aspect to mention is that the interaction with the environment can be engineered in some cases in order to generate quantum correlations into the system. This happens, for instance, in the non-equilibrium steady state of a two-qubit entanglement engine described by Khandelwal et al. (2020), where instead of work, entanglement is the resource generated from the incoherent interaction of the system with two thermal baths.

Such considerations lead to the necessity of having at disposal methods to appropriately model the effect of the environment on the system and, for doing so, of tagging key features of the environment itself. In the cases one knows precisely the details of the microscopic model underlying the experimental setup of interest, a first naive attempt is to consider the system-environment compound as a closed object, hence jointly evolving through a unitary map. This route is usually computationally unsuccessful: being the environment a macroscopic object, finding the exact dynamics of the whole compound can be very problematic. Fortunately, under some often reliable assumptions, the reduced dynamics of the system can be approximated through the so-called Gorini-Kossakowski-Lindblad-Sudarshan master equation (Gorini et al. 1976, Lindblad 1976), that for brevity we call Lindblad ME throughout the text. It appears as a correction to the quantum Liouville equation for the closed system dynamics: the new Liouvillian generator is composed of the original free system Hamiltonian term plus a term account-

ing for the environmental disturbance, with the main characteristics of the environment - temperature, statistics etc. - being encoded in the coefficients of this second term. The steps for deriving a Lindblad ME starting from the exact microscopic model of the system-environment compound are essentially three: the Born, Markov and Secular approximations (Breuer et al. 2002). Whether the Born approximation is based on the assumption of weak system-environment coupling and the Markovian approximation is generally justified by the narrowness of the bath correlation functions (leading to a time independent generator, hence implying the lack of any memory effects in the dynamics), the main role of the secular approximation is to guarantee the complete-positivity of the resulting transformation. Such property is necessary for a map (intended as an application from density matrices to density matrices) to be consistent with the Copenhagen interpretation of quantum mechanics and is generally lost as a consequence of the previous approximations. The equation that is obtained after the Born and Markov approximation, without the implementation of the secular approximation, is referred as Redfield equation (Redfield 1957). Despite being ill-defined for its non-positivity character, this equation often provides better results than the equation which results from the indiscriminate implementation of the secular approximation. As we shall see next, the superiority of the Redfield equation is manifested especially if one takes into account the whole evolution of the system density matrix, namely both the transient regime and the steady state.

1.2 Brief summary

Open quantum system dynamics

In Farina and Giovannetti (2019) we faced the problem of the non-positive character of the Redfield equation. We constructed a continuous mapping from the Redfield equation to the Secular Lindblad master equation, by modulating the free coarse-grain time interval related to a temporal coarse-grain averaging applied on the Redfield equation in interaction picture. More importantly, there exist a finite threshold value of such coarse-grain time-scale above which the "corrected" Redfield equation is ensured to be completely-positive. Now, to cure the non-positivity character one has two choices at disposal: taking very large coarse grain times obtaining the Secular Lindblad master equation (i.e., remaining in the standard microscopic derivation framework) or setting it to the finite threshold value still obtaining a well defined ME. The last approach, allows to preserve positivity still conserving the predictive power of the Redfield equation and turns out to be particularly useful when the system is multipartite.

The dissipative dynamics of a multipartite quantum system is currently under the so called *local vs global* debate. For a first understanding of the problem, one can consider the case of two interacting subsystems, each, in turn, microscopically coupled to a given

own thermal reservoir, still keeping in mind that the same problematic naturally applies to more complex structures. In this scenario, in order to describe the steady state of the system, one must choose either the local or the global master equation depending on the parameters of the model (González et al. 2017, Hofer et al. 2017). In the local master equation the dissipators act locally on the two subsystems, mimicking the original Hamiltonian interaction between subsystems and respective environments. On the contrary, in the global master equation, which is obtained through the secular approximation, the dissipators are built up through the eigenstates of the system Hamiltonian, including the internal coupling between the two subsystems. González et al. (2017) and Hofer et al. (2017) showed that, in order accurately approximate the out-of-equilibrium steady state of the system, for weak internal coupling the local master equation is the correct method, while in the opposite regime the right choice turns out to be the global master equation.

In Farina et al. (2020), we tried to go beyond the descriptive power of the global and local master equations, not restricting ourselves to an analysis of the steady state properties but including the transient evolution as well. We considered the following *asymmetric* thermal charging configuration: the system is composed of two interacting harmonic oscillators A and B, with only A interacting with a thermal bath - collection of other harmonic oscillators - and we studied the equilibration process of the system initially in the ground state with the bath finite temperature. By evaluating the exact dynamics of this minimal model and using it as benchmark, we showed that the completely-positive version of the Redfield equation - obtained through the tight coarse-grain average procedure of Farina and Giovannetti (2019), i.e., with the coarse-grain time interval being set at threshold value - and an appropriate time-dependent convex mixture of the local and global solutions give rise to the most accurate approximations of the whole exact system dynamics, i.e. both at short and at long time scales, outperforming the local and global approaches. Regarding the last method, intuitively it was expected the local master equation to accurately predict the transient properties of the dynamics, that involve coherent internal energy exchanges between the subsystems A and B, and the global master equation to yield the correct equilibrium steady state. In full accordance with thermodynamic expectations, the latter is the Gibbsian thermal state, whose Hamiltonian includes the internal interaction term. Based on this reasoning, we considered a time-dependent convex mixture of the local and global quantum channels - which is still a well defined quantum channel - such that the local and the global components matter at short and at long time-scales, respectively. We also found that the corrected version of the Redfield equation yields comparable accuracy, a result of the fact that the Redfield equation is the starting point - i.e. one approximation back - for both the local (Hofer et al. 2017) and global (Breuer et al. 2002) approximations. Regarding the topic of positivity, we showed that while the non-positive nature of the uncorrected Redfield

equation implies a breaking of the uncertainty relation, its positivity-corrected version is well behaving. Furthermore the latter, as well as the original equation, is able to capture some non-weak coupling corrections for the steady state of the system that are completely neglected when using the local, global and convex mixture approaches. Our general results hold true at any internal coupling strengths, even in those intermediate regimes where the choice between the local and global MEs is more subtle.

Applications to quantum nano-technology

Despite the *asymmetric* thermal charging model treated in Farina et al. (2020) was chosen primarily for its minimal character, possible implementations of the set up can be found in cavity (or in circuit) quantum electrodynamics. An example is the open Dicke model (Dicke 1954) for large enough number of two-level atoms inside the cavity (Emary and Brandes 2003) and assuming that the interaction of the cavity mode with the radiation field is more relevant than the direct coupling of the radiation field with the atoms. Alternatively, our bipartite system may directly describe coupled cavities in an array (Hartmann et al. 2008) in the instance of two cavities. About the kind of dynamics we chose, it may be of interest for ground state storage in quantum computation (Nielsen and Chuang 2010) or, conversely, for thermal charging tasks (Farina, Andolina, Mari, Polini and Giovannetti 2019, Hovhannisyan et al. 2020).
In fact, from the technological point of view, we can think at the asymmetric thermal charging scheme presented above as a first attempt to model the energy charging process of an open quantum battery by exploiting a thermal energy supply. For Alicki and Fannes (2013), a quantum battery is an object at the nano-scale able to be energetically charged, store the energy for a certain time period and finally provide it to a consumption center (see also a recent review on the topic by Campaioli et al. (2018)).

In Farina, Andolina, Mari, Polini and Giovannetti (2019) we analyzed the energy charging of a quantum battery in an open setting. In our scheme, the interaction between the battery element B and the external power source is mediated by an ancillary system - the quantum charger A - that acts as a controllable switch. By analyzing different implementations, we studied the effects of coherent energy pumping and thermalization, being particularly interested to possible interplay mechanisms between the two sources. The coherent source was schematized as a resonant driving field also applied to the subsystem A. As a quantifier of the stored energy fraction that can be extracted as work, we considered the ergotropy of B, which can be defined as the maximum extractable work from B via unitary operations (Allahverdyan et al. 2004). Whether by using a purely thermal charging protocol no work can be extracted from the battery (i.e. the ergotropy is zero), in a mixed protocol where both coherent and thermal sources are present, temperature plays a role in even increasing the ergotropy of B. As a key result

of the analysis, we found that, allowing the presence of effective non-linearities in the system - A and B are both two-level systems in the example provided in the paper - increasing temperature can decrease or, quite interestingly, increase the ergotropy of B. On the contrary, this does not happens when considering a linear system - two-harmonic oscillator model in the paper. There, extractable work only comes from the coherent source because an energetic separation between coherent and incoherent components is present. It is worth mentioning that the best condition for realizing a coherent charging by exploiting the out-of-equilibrium properties is provided by the hybrid model, where A is a quantum harmonic oscillator and B is a qubit. In this hybrid model, the large amount of energy hosted by the unbounded spectrum of the harmonic oscillator implies a speedup in the charging of the two-level system. This last result was consistent with a previous paper of our group: Andolina et al. (2018), where we analyzed the same combinations of qubit and harmonic oscillators for describing the charger-battery compound, but without additional external sources and dissipative mechanisms, with the initial energy being contained in the charger itself.

Regarding the nature of the environment we considered, in Farina, Andolina, Mari, Polini and Giovannetti (2019) we restricted the analysis to a thermal environment composed of non-interacting bosons, a common situation encountered in experiments of quantum optics and solid state physics. However, in principle, the environmental component could belong to different classes: for instance it could be characterized by fermionic statistics. In this respect, we found useful to develop techniques to recognize at least the statistical nature of a quantum environment, being a key ingredient in setting the thermalization decay rate. Specifically, we developed a protocol - called "Quantum bath statistics tagging" - to answer this necessity (Farina, Cavina and Giovannetti 2019), assuming equal temperature for the two bath hypotheses. In this scheme, the discrimination of the statistics of a thermal bath is achieved through indirect measurements performed on a quantum probe. The tagging capability relies on the fact that, when weakly coupled with the environment of interest, the transient evolution of the probe toward its final thermal configuration is strongly affected by the fermionic or bosonic nature of the bath excitations. Notice that in our setting no information can be encoded in the probe state at time zero - where the probe is in the initial preparation state - and at asymptotically large times - where the probe has reached its thermal state independently of the bath statistics. Hence, there must exist an intermediate time instant that is the most suitable for the statistics tagging. Using figures of merit taken from quantum metrology such as the Holevo-Helstrom probability of error and the quantum Chernoff bound, we discussed how to achieve the greatest precision in this statistics tagging procedure, analyzing different models of probes and different initial preparations and by optimizing over the time of exposure of the probe. We derived analytic expressions for such time-scale both for the case of qubit probe and for the case of quantum harmonic

oscillator probe. Regarding the corresponding minimal error probability, whether for the qubit case it is lower bounded by a finite value, we found that for the quantum harmonic oscillator probe it can be sent to zero by exploiting the possibility of considering arbitrary high energy in the initial preparation of the probe state. For showing that behavior, we restricted for simplicity the analysis to Gaussian states, finding a clear analytic result when the probe initial state has the same temperature as the thermal bath, but a certain initial displacement.
The analysis has been naturally extended to the case where the two thermal baths we want to distinguish have both different statistics and temperatures (Gianani et al. 2020). Notice that in the case of unequal temperatures finite discrimination capability is found also at large time scales since the two thermal states now differ. In this study, we restricted ourselves to the case of a qubit probe because that was suitable for experimental linear-optical simulations. As intuitively expected, the best discrimination capability can only be attained by enforcing the probe initial state to be pure. For input energy eigenstates, our inspection has revealed a transition between temperature regimes in which either equilibrium (large time-scales) or nonequilibrium states (short time-scales) are optimal. Such behavior has been illustrated both theoretically and in a linear-optical simulation. However, only the inclusion of input states with quantum coherence allows one to reach the highest possible discrimination capability and also implies that non-equilibrium measurement conditions are generally optimal, breaking in this way the aforementioned transition.

Final remarks

The thesis, despite containing different topics, generally puts emphasis on the importance of precisely treat and recognize the environment that implies disturbance on the quantum system of interest. In this direction novel methods have been developed both for bath tagging purposes and for precisely describing the effects of the environment on the system dynamics. Applications to open quantum batteries are also provided as an example where the theory can be applied for clear nano-technological scopes.

1.3 Structure of the thesis

A literature review, divided in three main research areas, is reported in Chapter 2, while the remaining chapters are dedicated to our research findings. Specifically, in Chapter 3, the formalism of the coarse-grained Redfield equation is introduced together with the related discussion on the complete-positivity of the channel (Farina and Giovannetti 2019). The theory finds its application when we present methods to go beyond the local and global approaches for multipartite system dissipation (Farina et al. 2020). In Chapter 4 the local master equation is used to describe an open quantum battery (Farina,

Andolina, Mari, Polini and Giovannetti 2019). Chapter 5 deals with the statistics and temperature discrimination problem of quantum baths (Farina, Cavina and Giovannetti 2019, Gianani et al. 2020). Finally, Chapter 6 contains a brief summary and the main conclusions of the thesis.

CHAPTER 2

Literature Review

In this Chapter we prepare the ground for the three macro research areas. Specifically,

- Sec. 2.1 introduces theoretical concepts - quantum channels, Born-Markov-secular microscopic derivation of Lindblad master equations - which are the starting point for Chapter 3, which is dedicated to our contributions to the foundations of the theory of open quantum systems;
- Sec. 2.2 reviews the literature of quantum batteries, useful for Chapter 4, treating the concept of ergotropy and introducing the formalism of single-mode gaussian states;
- and, finally, Sec. 2.3 gives an outline of the field of quantum metrology, linked to the bath tagging problems of Chapter 5, with a specific focus on quantum state discrimination by introducing the Helstrom error probability and the quantum Chernoff bound.

A reader interested only in a specific topic can here refer to the appropriate section and then go to the related research chapter.

2.1 Open quantum systems

In the rising field of quantum technology (Riedel et al. 2017), considering a quantum system isolated from its surroundings is a non-realistic idealization. In the majority of the implementations of quantum information algorithms (Nielsen and Chuang 2010) and quantum computation (Arute et al. 2019), the interaction with the environment is detrimental for quantum resources, becoming a crucial ingredient to monitor, with the scope of reducing its effects or with the aim of accounting for it by applying quantum error correction methods. Interestingly, in more rare cases the environment itself acts as a mediator for the production of quantum correlations into the system [see e.g. Benatti et al. (2003*a*)].

Unfortunately, our ability in accounting for environmental effects is severely limited by the difficulty of keeping track of the exact dynamics of the entire system-environment compound: a problem which is made computationally hard by the large number of degrees of freedom involved in the process. For this reason, effective models for the way the environment acts on the reduced system density matrix have been developed, leading to the master equation (ME) formalism (Lindblad 1976, Gorini et al. 1976). The lowest level of approximation contemplates the assumption of weak system-environment coupling (Born approximation) and time-divisibility for the system dynamics (Markov approximation). This leads to the Redfield equation (Redfield 1957, Breuer et al. 2002, Jeske and Cole 2013) which regrettably, while being able to capture some important features of the model (Lim et al. 2017, Purkayastha et al. 2016), does not ensure positive (and hence completely positive) evolution (Gaspard and Nagaoka 1999, Argentieri et al. 2014, Ishizaki and Fleming 2009, Benatti et al. 2003*b*, Wilkie 2001, Suárez et al. 1992, Dümcke and Spohn 1979, Benatti and Floreanini 2005). In quantum mechanics, the positivity of density matrices – i.e. the fact that all their eigenvalues are non-negative – is an essential property imposed by the probabilistic interpretation of the theory (Nielsen and Chuang 2010). Allowing for mathematical structures that do not comply with such requirement paves the way to a series of inconsistencies that include *negative probabilities* of measurements outcomes, violation of the uncertainty relation (an example will be given in Sec. 3.3), and, ultimately, the non-contractive character of the underlying dynamics. Ways to correct or to circumvent the pathology exhibited by the Redfield equation typically relay on the full (Breuer et al. 2002) or the partial (Schaller and Brandes 2008, Cresser and Facer 2017, Seah et al. 2018, Jeske et al. 2015, Rivas 2017, Farina and Giovannetti 2019) implementation of the secular approximation: a coarse-grain temporal average of the system dynamics which, performed in conjunction with the above mentioned Born and Markov approximations, leads to a more reliable differential equation for the system density matrix known as the Gorini-Kossakowski-Sudarshan-Lindblad (GKSL) master

equation (Lindblad 1976, Gorini et al. 1976).

2.1.1 Quantum channels

Working in the most general scenario, a physical super-operator (i.e. a proper quantum channel) must necessarily satisfy three structural properties: it has to be linear, trace preserving and completely positive (CPT). We clarify here what one means with these three requirements (Holevo 2012).
Let us call Φ a generic super-operator that maps linear operators defined on the Hilbert space $\mathscr{H}_{\mathrm{S}}$ of the system $\mathcal{S}$ into linear operators defined on the same Hilbert space:

$$\Phi : \rho \to \rho', \quad \text{with} \quad \rho,\ \rho' \text{ linear operators on } \mathscr{H}_{\mathrm{S}}. \tag{2.1}$$

Such super-operator has to be

Linear

$$\Phi(\alpha\rho_1 + \beta\rho_2) = \alpha\Phi(\rho_1) + \beta\Phi(\rho_2), \tag{2.2}$$
$$\forall\rho_1,\ \rho_2 \text{ linear operators on } \mathscr{H}_{\mathrm{S}},\ \forall\alpha,\ \beta \in \mathbb{C}.$$

Trace-preserving

$$\mathrm{Tr}[\Phi(\rho)] = \mathrm{Tr}[\rho], \quad \forall\rho \text{ linear operator on } \mathscr{H}_{\mathrm{S}}. \tag{2.3}$$

This property ensures that the evolved state is normalized as well as the input state.

Completely positive *Let us call $\mathcal{A}$ an ancillary system which is allowed to be in a joint state ρ_{SA} with the system $\mathcal{S}$. Being ρ_{SA} a state, it certainly holds that the matrix ρ_{SA} is positive semi-definite (we use for it the shorthand notation $\rho_{\mathrm{SA}} \geq 0$). A property that must be preserved when applying locally on $\mathcal{S}$ the transformation Φ, namely:*

$$(\Phi \otimes I)(\rho_{\mathrm{SA}}) \geq 0\ , \quad \forall\rho_{\mathrm{SA}}\ . \tag{2.4}$$

This requirement avoids having encoded in the system state "negative probabilities" for measurement outcomes, hence preserving the probabilistic interpretation of the theory.

As we shall see in the following, the last property can be violated by some kind of *ill-defined* master equations, as well as it happens for the less stringent **positivity** re-

quirement

$$\Phi(\rho_{\rm S}) \geq 0, \quad \forall \rho_{\rm S} \geq 0 \text{ linear operator on } \mathscr{H}_{\rm S}. \tag{2.5}$$

Notice that the last property is automatically guaranteed when complete positivity does hold. To see this, just take a factorized state $\rho_{\rm S} \otimes \rho_{\rm A}$ as $\rho_{\rm SA}$ in (2.4).

2.1.2 Microscopic derivation of the Lindblad master equation: general formalism

Passing to more concrete treatments, we now review the microscopic derivation of the Redfield equation and how one can arrive from it to a proper GKSL form via secular approximation. Following Breuer et al. (2002), we shall work in a general setting, limiting to a minimum all the assumptions on the system Hamiltonian and on its environment.

Let S be a quantum system interacting with an external environment E. Following conventional approach we assume the SE compound to be isolated and describe their joint evolution in terms of a total Hamiltonian $H_{\rm SE}$ composed of three (time-independent) terms:

$$H_{\rm SE} = H_{\rm S} + H_{\rm E} + H_1 \,, \tag{2.6}$$

with $H_{\rm S}$ and $H_{\rm E}$ being local contributions, and with H_1 being the coupling Hamiltonian which, in full generality, we express as

$$H_1 = \sum_{\alpha=1}^{M} A_\alpha \otimes B_\alpha \,, \tag{2.7}$$

where A_α and B_α are not-null self-adjoint operators acting on S and E, respectively, and where the parameter M enumerates the number of non trivial terms entering the decomposition. As input state we take a factorized density matrix of the form

$$\rho_{\rm SE}(0) = \rho_{\rm S}(0) \otimes \rho_{\rm E}(0) \,, \tag{2.8}$$

with the $\rho_{\rm E}(0)$ environment component fulfilling the following *stationary* conditions:

- invariance under the action of the local Hamiltonian, i.e. ,

$$\Big[\rho_{\rm E}(0), H_{\rm E}\Big]_- = 0 \,; \tag{2.9}$$

  where hereafter the symbols $[\cdots,\cdots]_\pm$ will be used to represent the commutator $(-)$ and the anti-commutator $(+)$, respectively;

- zero expectation value of the operators B_α entering the coupling Hamiltonian (2.7),

i.e. ,

$$\mathrm{Tr}_{\mathrm{E}}\{\rho_{\mathrm{E}}(0)B_\alpha\} = 0\,, \qquad \forall\alpha \in \{1,\cdots,M\}\,, \tag{2.10}$$

the symbol $\mathrm{Tr}_{\mathrm{E}}\{\cdots\}$ representing the partial trace with respect to the environment degrees of freedom.

As we shall see in the following, condition (2.10) is essential for dropping first order contributions in the system master equation: it should be stressed that however it is not as stringent as it may looks at first site, as it can always be enforced by properly redefining the free Hamiltonian of S.

We hence move in the interaction picture in which the free Hamiltonian of the universe $H_0 = H_{\mathrm{S}} + H_{\mathrm{E}}$ is integrated away, introducing the operators

$$\tilde{H}_1(t) := e^{iH_0t}H_1e^{-iH_0t}\,, \tag{2.11}$$

$$\tilde{\rho}_{\mathrm{SE}}(t) := e^{iH_0t}\rho_{\mathrm{SE}}(t)e^{-iH_0t}\,, \tag{2.12}$$

$$\tilde{\rho}_{\mathrm{S}}(t) := \mathrm{Tr}_{\mathrm{E}}\{\tilde{\rho}_{\mathrm{SE}}(t)\} = e^{iH_{\mathrm{S}}t}\rho_{\mathrm{S}}(t)e^{-iH_{\mathrm{S}}t}\,, \tag{2.13}$$

with $\rho_{\mathrm{SE}}(t)$ the density matrix of SE at time t and $\rho_S(t) := \mathrm{Tr}_{\mathrm{E}}\{\rho_{\mathrm{SE}}(t)\}$ its reduced form describing the corresponding state of S ($\hbar$ having been set equal to 1). Accordingly the dynamics of the joint system reads $\dot{\tilde{\rho}}_{\mathrm{SE}}(t) = -i[\tilde{H}_1(t), \tilde{\rho}_{\mathrm{SE}}(t)]_-$, which, upon formal integration, can be equivalently expressed as

$$\begin{aligned}\dot{\tilde{\rho}}_{\mathrm{SE}}(t) &= -i\Big[\tilde{H}_1(t), \rho_{\mathrm{SE}}(0)\Big]_- \\ &\quad - \int_0^t d\tau \Big[\tilde{H}_1(t), \Big[\tilde{H}_1(t-\tau), \tilde{\rho}_{\mathrm{SE}}(t-\tau)\Big]_-\Big]_-\,.\end{aligned} \tag{2.14}$$

Taking the partial trace with respect to E the left-hand-side of Eq. (2.14) reduces to the first derivative of $\tilde{\rho}_{\mathrm{S}}(t)$ while the first term on the right-hand-side disappears thanks to the cooperative effect of the stationary conditions (2.9) and (2.10).

2.1.2.1 Born and Markov approximations

The integral contribution in (2.14), on the contrary, still exhibits a non-trivial functional dependence on the joint state $\tilde{\rho}_{\mathrm{SE}}(t)$ which we treat by invoking the *Born* (or *weak-coupling*) *approximation*, requiring that the state of the environment is not affected by the presence of S, i.e. writing

$$\tilde{\rho}_{\mathrm{SE}}(t) \simeq \tilde{\rho}_{\mathrm{S}}(t) \otimes \tilde{\rho}_{\mathrm{E}}(0)\,. \tag{2.15}$$

Under this condition we hence arrive to the homogenous equation for S

$$\begin{aligned}\dot{\tilde{\rho}}_{\rm S}(t) &\simeq \int_0^t d\tau \sum_{\alpha,\beta=1}^{M} c_{\alpha\beta}(\tau)\Big(\tilde{A}_\beta(t-\tau)\tilde{\rho}_{\rm S}(t-\tau)\tilde{A}_\alpha(t) \\ &- \tilde{A}_\alpha(t)\tilde{A}_\beta(t-\tau)\tilde{\rho}_{\rm S}(t-\tau)\Big) + h.c.\,, \end{aligned} \tag{2.16}$$

with $\tilde{A}_\alpha(t) = e^{iH_{\rm S}t}A_\alpha e^{-iH_{\rm S}t}$ and where $c_{\alpha\beta}(\tau)$ are environment correlation functions defined as

$$c_{\alpha\beta}(\tau) := {\rm Tr}_{\rm E}\{\rho_{\rm E}(0)e^{iH_{\rm E}\tau}B_\alpha e^{-iH_{\rm E}\tau}B_\beta\}\,, \tag{2.17}$$

that, exploiting Eq. (2.9) and the fact that the B_αs are self-adjoint operators, can be shown to fulfil the condition

$$c^*_{\alpha\beta}(\tau) = c_{\beta\alpha}(-\tau)\ . \tag{2.18}$$

Next assumption concerns the memory properties of the environment. We call $\tau_{\rm E}$ the characteristic width of the environment correlation functions $c_{\alpha\beta}(\tau)$ and we assume that the time scales δt over which the system S significantly evolves in the interaction picture satisfy the condition $\delta t \gg \tau_{\rm E}$. This hypothesis justifies the *Markov approximation* which in Eq. (2.16) neglects *i)* the τ dependence of the state and *ii)* substitutes the upper extreme of integration with $+\infty$, leading to the Redfield equation (Redfield 1957, Breuer et al. 2002)

$$\begin{aligned}\dot{\tilde{\rho}}_{\rm S}(t) &\simeq \int_0^\infty d\tau \sum_{\alpha,\beta=1}^{M} c_{\alpha\beta}(\tau)\Big(\tilde{A}_\beta(t-\tau)\tilde{\rho}_{\rm S}(t)\tilde{A}_\alpha(t) - \tilde{A}_\alpha(t)\tilde{A}_\beta(t-\tau)\tilde{\rho}_{\rm S}(t)\Big) + h.c. \\ &= \sum_{ij}\Gamma_{ij}(t)\left(A_j^\dagger\tilde{\rho}_{\rm S}(t)A_i - A_iA_j^\dagger\tilde{\rho}_{\rm S}(t)\right) + h.c.\,, \end{aligned} \tag{2.19}$$

where the last identity has been obtained by decomposing the operators A_α in terms of the eigenvectors of the free system Hamiltonian. Specifically, we write

$$A_\alpha = \sum_\omega A_{\alpha\omega}\ , \tag{2.20}$$

with

$$A_{\alpha\omega} := \sum_{\epsilon_1\,,\,\epsilon_2:\epsilon_1-\epsilon_2=\omega} \pi_{\epsilon_1}A_\alpha\pi_{\epsilon_2} = \sum_\epsilon \pi_{\epsilon+\omega}A_\alpha\pi_\epsilon\,, \tag{2.21}$$

where π_ϵ is the projector associated with the eigenvalue ϵ of $H_{\rm S}$, i.e. $H_{\rm S} = \sum_\epsilon \epsilon\,\pi_\epsilon$. The new variable $\omega := \epsilon_1 - \epsilon_2$ spans a range of G different cases, counting all the energy

differences of $H_{\rm S}$ (including the zero energy gap value associated with the terms where $\epsilon_1 = \epsilon_2$) that are different in value. Introducing then the collective indices $i = (\alpha, \omega)$ and $j = (\beta, \omega')$ which run over a set of $N = GM$ different entries, and noticing that $A_{\beta-\omega'} = A^\dagger_{\beta\omega'}$, the right-hand side of the Redfield equation in the first line of (2.19) can hence be arranged as shown in its last line, with the $N \times N$ matrix $\Gamma_{ij}(t)$ given by

$$\Gamma_{ij}(t) = e^{i(\omega-\omega')t}\Omega_{\alpha\beta}(\omega') \ , \tag{2.22}$$

where, for each value of the energy gap ω, the coefficients

$$\Omega_{\alpha\beta}(\omega) \ := \ \int_0^\infty d\tau c_{\alpha\beta}(\tau)e^{i\omega\tau} \tag{2.23}$$

identify an $M \times M$ complex matrix $\Omega(\omega)$ that is going to play an important role in what follows.

2.1.2.2 Secular approximation

Equation (2.19) can be further simplified by neglecting the terms with unequal energy gaps, i.e., the contributions for which $\omega \neq \omega'$ (non-secular terms), that are all considered fast oscillating on the relevant timescales. This procedure is referred as secular approximation, formally justified only when the smallest difference between energy gaps is much larger than the characteristic rate of the system in interaction picture (Breuer et al. 2002). In formulas:

$$\min_{\omega,\omega':\omega\neq\omega'} |\omega - \omega'| \gg 1/\delta t \ . \tag{2.24}$$

Going back in Schrödinger picture, one obtains a *secular* master equation with constant generator terms

$$\dot\rho_{\rm S}(t) \simeq -i\left[H_{\rm S}^{(\infty)}, \rho_{\rm S}(t)\right]_- + \sum_{\alpha\beta\omega}\gamma_{\alpha\beta}(\omega)\Big(A^\dagger_{\beta\omega}\rho_{\rm S}(t)A_{\alpha\omega} - \frac{1}{2}\Big[A_{\alpha\omega}A^\dagger_{\beta\omega}, \rho_{\rm S}(t)\Big]_+\Big) \ , \tag{2.25}$$

where

$$H_{\rm S}^{(\infty)} \ := \ H_{\rm LS}^{(\infty)} + H_{\rm S} \ , \tag{2.26}$$

$$H_{\rm LS}^{(\infty)} \ := \ \sum_{\alpha\beta\omega}\eta_{\alpha\beta}(\omega)A_{\alpha\omega}A^\dagger_{\beta\omega} \ , \tag{2.27}$$

and

$$\gamma_{\alpha\beta}(\omega) := \Omega_{\alpha\beta}(\omega) + \Omega^*_{\beta\alpha}(\omega)\,, \tag{2.28}$$

$$\eta_{\alpha\beta}(\omega) := [\Omega_{\alpha\beta}(\omega) - \Omega^*_{\beta\alpha}(\omega)]/(2i) \tag{2.29}$$

are the dissipation and Lamb shift (hermitian) matrices, respectively. The last passage needed to put Eq. (2.25) in GKSL form is the diagonalization of the dissipation matrices $\gamma_{\alpha\beta}(\omega)$. We show now that all the eigenvalues of such matrix are non-negative, a condition that guarantees the complete positivity of the resulting transformation (Lindblad 1976, Alicki and Lendi 2007).

2.1.2.3 Positive semi-definiteness of the secular dissipation matrix

We discuss here the positivity of the matrix

$$\gamma_{\alpha\beta}(\omega) = \int_{-\infty}^{+\infty} c_{\alpha\beta}(\tau) e^{i\omega\tau} d\tau\,, \tag{2.30}$$

with $c_{\alpha\beta}(\tau)$ being the bath correlation functions given in Eq. (2.17). We should prove that

$$\sum_{\alpha\beta} u^*_\alpha(\omega)\gamma_{\alpha\beta}(\omega)u_\beta(\omega) \geq 0 \tag{2.31}$$

for any $\vec{u}(\omega) \in \mathbb{C}^M$. The above expression is actually the Fourier transform of a function $f(\tau)$:

$$\sum_{\alpha\beta} u^*_\alpha(\omega)\gamma_{\alpha\beta}(\omega)u_\beta(\omega) = \int_{-\infty}^{+\infty} e^{i\omega\tau} f(\tau) d\tau \tag{2.32}$$

with

$$f(\tau) := \langle \Theta^\dagger(\tau)\Theta(0)\rangle\,, \tag{2.33}$$

$$\Theta(\tau) := \sum_\alpha u_\alpha \tilde{B}_\alpha(\tau)\,, \tag{2.34}$$

with $\tilde{B}_\alpha(\tau)$ being the operators on the thermal bath (in interaction picture) appearing in Eqs. (2.7) and (2.17). From the function $f(\tau)$ it is possible to define an $n \times n$ matrix f_{lm} in the following way:

$$f_{lm} := f(\tau_l - \tau_m) = \langle \Theta^\dagger(\tau_l)\Theta(\tau_m)\rangle\,, \tag{2.35}$$

with $\tau_i \in \{\tau_1, \tau_2, ..., \tau_n\}$. Such matrix is positive semi-definite for any choices of the times τ_l and of the dimension n. This can be proven by using the fact that the trace of

the product of two positive semi-definite operators is non negative. In formulas:

$$\sum_{lm} v_l^* f_{lm} v_m = \langle \Delta^\dagger \Delta \rangle := \mathrm{Tr}_\mathrm{E}\{\rho_\mathrm{E} \Delta^\dagger \Delta\} \geq 0\,, \tag{2.36}$$

for any complex vectors $\vec{v}$, with

$$\Delta := \sum_m v_m \Theta(\tau_m)\,. \tag{2.37}$$

From the positivity of the matrix f_{lm} it follows that the Fourier transform of $f(\tau)$ is always non-negative (Bochner's theorem) and hence the positivity of the matrix $\gamma_{\alpha\beta}(\omega)$ is guaranteed (see Eq. (2.32)).
This can be understood by thinking integrals as summations. Indeed the Fourier transform in the right-hand side of Eq. (2.32) can be written in a form which is analogous to the left-hand side of Eq. (2.36) which we know to be a positive quantity:

$$\begin{aligned} &\int_{-\infty}^{+\infty} ds' e^{i\omega s'} f(s') \\ &\quad = \frac{1}{2T} \int_{-T}^{+T} dl \int_{-\infty}^{+\infty} ds\, u^*(s) f(s-l) u(l) \geq 0\,, \end{aligned} \tag{2.38}$$

with $u(\tau) := e^{-i\omega\tau}$ and for any T.

2.1.3 Dissipation of multipartite systems: *Local vs Global* debate

When the system is composed of two or more interacting subsystems that are locally coupled to possibly independent reservoirs (Cattaneo et al. 2019), a brute force application of a full secular approximation leads to the so called *global* ME, a GKSL equation obtained under the implicit assumption that the environment will perceive the composite system as a unique body irrespectively from the local structure of their mutual interactions. While formally correct in terms of the positivity and complete positivity requirements and predicting long term behaviours which are thermodynamically consistent, the resulting ME is prone to introduce errors in the short term description of the dynamical process. A suitable alternative is provided by the so called *local* ME approach where, contrarily to the global ME, each subsystem is assumed to independently interact with its *own* environment, keeping track of the local nature of the microscopic interaction. Despite in certain situations it can imply the breaking of the second law of thermodynamics (Levy and Kosloff 2014), as we will explicitly see in Sec. 3.3 it allows for a more precise description of the short term dynamics of the composite system. A

local approach is usually justified when the subsystems interact weakly between each other (Hofer et al. 2017, González et al. 2017, Rivas et al. 2010). As well as the global ME, the local ME can be microscopically derived (Hofer et al. 2017) and is in GKSL form. Notably, such master equation has recently acquired full dignity showing that it exactly describes the dynamics induced by an *engineered* bath schematized by a collisional model (De Chiara et al. 2018). Furthermore, even under a more conventional description of the environment, thermodynamics inconsistencies only occur at the order of approximation where the local approach is not guaranteed to be valid and, eventually, it is possible to completely cure such inconsistencies by implementing a perturbative treatment around the local approximation (Trushechkin and Volovich 2016).

2.1.4 Existent literature

In Sec. 3.3 we shall test the effectiveness of different classes of MEs to describe the system dynamics, particularly focusing on alternative approaches beyond those adopted in deriving the local and global MEs and using as benchmark a model that we are able to solve exactly. Differently from previous studies (Hofer et al. 2017, González et al. 2017), where the focus was on the steady state properties of a bipartite system with each subsystem coupled to a different thermal reservoir, we deal with a bipartite system asymmetrically coupled to a single thermal bath and analyze its whole dynamics including both the transient and asymptotic regime. More specifically, in our case the system of interest will be composed of two interacting harmonic oscillators A and B, with only A microscopically coupled with an external bosonic thermal bath described as a collection of extra harmonic oscillators. About the exact dynamics benchmark, the unitary evolution of the joint system+environment compound has been calculated by restricting ourself to exchange interactions and gaussian states (Serafini 2017). Anticipating some of the conclusions of Sec. 3.3, the completely positive version of the Redfield equation obtained as described in Sec. 3.1 (Farina and Giovannetti 2019) by applying the secular approximation via coarse-grain averaging in a partial and tight way, provides a semigroup description of the system dynamics that outperforms both the local and global ME approaches.

About this, we take here the opportunity to clarify that various strategies for avoiding non-positive behaviors have been developed in literature. First of all, choosing appropriate initial conditions often allows one to preserve positivity, while retaining all the advantageous features of the Redfield equation (Purkayastha et al. 2016). Alternatively, second-order approximation to the full density matrix in interaction picture and subsequent – eventually dynamically adapted – coarse-grain averaging was proposed by Schaller and Brandes (2008) as a consistent method for all coarse-grain time-scales and factorized initial conditions. It was also noted that not performing the Markovian ap-

proximation which enforces semigroup dynamics can lead to completely-positive evolutions (Whitney 2008). These last two approaches completely circumvent the Redfield equation in its handy semigroup form. Recently, some of us have proposed instead a procedure (working for any factorized initial conditions) to tightly cure the non-positive character by performing coarse-grain averaging directly on the "fully Markovian" Redfield equation in interaction picture [see Farina and Giovannetti (2019) and Sec. 3.1]. Responding to the question on which is the most accurate method for this particular task – i.e. both ensuring positivity and providing an effective approximation of the system state, by using Redfield-like approaches – is beyond the scope of the present work (see Hartmann and Strunz (2020) for this issue). Specifically, as already mentioned, in Sec. 3.3 (Farina et al. 2020) we will test the version of the partial secular approximation described in Sec. 3.1 (Farina and Giovannetti 2019). We also anticipate that analogous advantages can be obtained by adopting a phenomenological description of the system dynamics, constructed in terms of an appropriate time-dependent convex mixture of the local and global ME solutions.

Regarding the model selected in Sec. 3.3, despite it has been chosen primarily for its minimal character (Deçordi and Vidiella-Barranco 2017), possible implementations of the set up we deal with can be found in cavity (or in circuit) quantum electrodynamics. An example is the open Dicke model (Dicke 1954) for large enough number of two-level atoms inside the cavity (Emary and Brandes 2003) and assuming that the interaction of the cavity mode with the radiation field is more relevant than the direct coupling of the radiation field with the atoms. Alternatively, our bipartite system may directly describe coupled cavities in an array (Hartmann et al. 2008) in the instance of two cavities. About the kind of dynamics we will present, it may be of interest for ground state storage in quantum computation (Nielsen and Chuang 2010) or, conversely, for thermal charging tasks (Farina, Andolina, Mari, Polini and Giovannetti 2019, Hovhannisyan et al. 2020) as we will see in Chapter 4.

2.2 Quantum batteries

Markovian master equations represent a useful tool for schematizing the energy transfer for open quantum batteries (Farina, Andolina, Mari, Polini and Giovannetti 2019).
A battery is a physical system that is capable to store energy supplied by an external source, making it available to other devices. Its performance is characterized by several figures of merit gauging the amount of energy it can store and/or deliver as a function of its mass/volume and how these quantities vary over time. Motivated by the constant progress of miniaturization of electronic devices and stimulated by the success obtained in other sectors by adopting analogous approaches (Riedel et al. 2017, Acín et al. 2018), increasing interest has been recently devoted to analyze the performances of "quantum batteries", i.e. energy storing systems which, at least in principle, could exploit genuine quantum effects to obtain improved performances with respect to conventional (say classical) schemes (Alicki and Fannes 2013, Hovhannisyan et al. 2013, Binder et al. 2015, Campaioli et al. 2017, Ferraro et al. 2018, Le et al. 2018, Andolina et al. 2018, Campaioli et al. 2018, Andolina et al. 2019).

The core of this idea ultimately relies on the possibility of achieving superior performances in the manipulation of energy by cleverly exploiting quantum resources (Vinjanampathy and Anders 2016, Alicki and Kosloff 2018, Goold et al. 2016, Campisi et al. 2011, Horodecki and Oppenheim 2013, Gelbwaser-Klimovsky et al. 2015, Strasberg et al. 2017). Starting from the seminal, but abstract works by Alicki and Fannes (2013), Hovhannisyan et al. (2013), Binder et al. (2015), Campaioli et al. (2017), concrete implementations of quantum batteries have been proposed in Ferraro et al. (2018), Le et al. (2018). At the same time, more sophisticated modelizations of the charging process have been presented (Andolina et al. 2018, 2019) which put emphasis on the problems that could arise at the interface between a quantum battery B and its external energy supply A, the "quantum charger" (also modelled as a quantum system). In particular, in Ref. Andolina et al. (2019) it was pointed out that quantum correlations between B and A, while possibly playing an important role in speeding up the charging of the battery, could result in a net detrimental effect by reducing the amount of energy that one could transform in useful work once having access to B alone (a reasonable scenario in any relevant practical applications).

2.2.1 Ergotropy

In Chapter 4 we will be interested in characterizing how efficiently energy can be transferred into the battery, the last being characterized by a local Hamiltonian H_{B}. For this purpose, we will study the mean energy contained in B at the end of the charging process and the corresponding ergotropy (Allahverdyan et al. 2004), i.e., respectively, the

quantities

$$E_{\rm B}(\tau) \equiv \mathrm{tr}[H_{\rm B}\rho_{\rm B}(\tau)]\,, \tag{2.39}$$

$$\mathcal{E}_{\rm B}(\tau) \equiv E_{\rm B}(\tau) - \min_{U_{\rm B}} \mathrm{tr}\left[H_{\rm B}U_{\rm B}\rho_{\rm B}(\tau)U_{\rm B}^\dagger\right]\,, \tag{2.40}$$

where $\rho_{\rm B}(\tau) \equiv \mathrm{tr}_{\rm A}[\rho_{\rm AB}(\tau)]$ is the reduced state of the battery at time τ, and where minimization in Eq. (2.40) is performed over all the unitaries $U_{\rm B}$ acting locally on such system. The first of these functions measures the total amount of energy that has been transferred to B thanks to the mediation of the charger A. The second, instead, provides us with the part of $E_{\rm B}(\tau)$ which can be turned into work while having access to the battery alone, a reasonable scenario in many applications where A is not available to a generic end user (Andolina et al. 2019). Indeed, it may happen that part of the mean energy of B will be locked into correlations between such system and the charging device, preventing one from accessing it via local operations on the battery. The term we are subtracting from $E_{\rm B}(\tau)$ in right-hand-side of Eq. (2.40) exactly targets such contributions. It formally corresponds to the expectation value of $H_{\rm B}$ computed on the passive state $\rho_{\rm B}^{(p)}(\tau)$, obtained by properly reordering the spectrum of $\rho_{\rm B}(\tau)$ and replacing the associated eigenvectors with those of the system Hamiltonian, as we will see in Sec. 2.2.1.2.

2.2.1.1 Work extraction

We provide now the physical interpretation of the ergotropy (2.40) following Allahverdyan et al. (2004). Not restricting to the case where the system of interest is the battery B (in principle, we could be interested in the ergotropy of A or of the joint AB system), let $\rho(t)$ be the density matrix of a generic system of interest characterized by a Hamiltonian $H_{\rm S}$. Work extraction is obtained thorough an additional time varying Hamiltonian operator $\mathtt{V}(t)$ which is turned on at time τ and off at time $\tau+\mathtt{T}$, i.e. $\mathtt{V}(\tau) = \mathtt{V}(\tau+\mathtt{T}) = 0$. Furthermore, let us consider the system isolated in the time window $[\tau, \tau+\mathtt{T}]$ in which the work extraction is performed, in such a way that the full average energy variation can be interpreted as work made on the system. Accordingly, the extracted work $\mathcal{W}^{(extr)}$ reads as

$$\mathcal{W}^{(extr)} = \mathrm{tr}\left\{H_{\rm S}\left[\rho(\tau) - \rho(\tau+\mathtt{T})\right]\right\}\,, \tag{2.41}$$

$$\rho(\tau+\mathtt{T}) = U\rho(\tau)U^\dagger\,, \quad U = \overleftarrow{\exp}\left[-i\int_\tau^{\tau+\mathtt{T}} ds\,\{H_{\rm S} + \mathtt{V}(s)\}\right]\,,$$

where "$\overleftarrow{\exp}$" is the time-ordered exponential. As a key result, by properly adapting the *shape* of the operator $\mathtt{V}(t)$ as function of time (still under the constraint $\mathtt{V}(\tau) = \mathtt{V}(\tau+\mathtt{T}) = 0$), the maximum over U of $\mathcal{W}^{(extr)}$ in (2.41) can always be attained. One

then arrives to the definition of the ergotropy

$$\mathcal{E}(\tau) = \max_{U} \mathcal{W}^{(extr)} \,, \tag{2.42}$$

same as (2.40), which was applied explicitly to the battery system B.

2.2.1.2 Construction of the passive state

Let us present the state $\rho(\tau)$ (ρ for brevity) and the Hamiltonian $H_{\rm S}$ in terms of their spectral decompositions:

$$\rho = \sum_n r_n |r_n\rangle\langle r_n| \,, \tag{2.43}$$

$$H_{\rm S} = \sum_n e_n |e_n\rangle\langle e_n| \,. \tag{2.44}$$

Here, $\{|r_n\rangle\}_n$ and $\{|e_n\rangle\}_n$ represent the eigenvectors of ρ and $H_{\rm S}$, respectively, and $r_0 \geq r_1 \geq \cdots$ and $\epsilon_0 \leq \epsilon_1 \leq \cdots$ are the associated eigenvalues, which we have been properly ordered. The passive counterpart of ρ is defined as the following density matrix (Allahverdyan et al. 2004, Pusz and Woronowicz 1978)

$$\rho^{(p)} \equiv \sum_n r_n |e_n\rangle\langle e_n| \,. \tag{2.45}$$

By construction, its mean energy is given by

$$E^{(p)} \equiv {\rm tr}[H_{\rm S}\rho^{(p)}] = \sum_n r_n \epsilon_n \,, \tag{2.46}$$

corresponding to the last term in the right-hand side of Eq. (2.40) and making explicit the form of the unitary $\bar{U}$ giving the maximum extractable work:

$$E^{(p)} = \min_U {\rm tr}\left[H_{\rm S} U \rho U^\dagger\right] = {\rm tr}\left[H_{\rm S}\bar{U}\rho\bar{U}^\dagger\right] \,, \quad \bar{U} = \sum_n |e_n\rangle\langle r_n| \,. \tag{2.47}$$

Accordingly, the ergotropy $\mathcal{E}$ of the state ρ can be conveniently expressed as

$$\mathcal{E} = E - E^{(p)} = {\rm tr}[H_{\rm S}(\rho - \rho^{(p)})] \,, \tag{2.48}$$

which makes it evident that zero values of $\mathcal{E}$ can be obtained only for those density matrices which are passive, i.e. for $\rho = \rho^{(p)}$. From the above construction it is also clear that states differing by a unitary transformation V (e.g. ρ and $\rho' = V\rho V^\dagger$) will have the same passive state. Accordingly, we can write the ergotropy of ρ' as

$$\mathcal{E}' = {\rm tr}[H_{\rm S}(\rho' - \rho^{(p)})] = E' - E + \mathcal{E} \,, \tag{2.49}$$

with $E = \mathrm{tr}[H_\mathrm{S}\rho]$ and $E' = \mathrm{tr}[H_\mathrm{S}\rho']$ the mean energies of ρ and ρ', respectively. Property (2.49) turns out to be particularly useful in interaction picture, as we will see in Chapter 4.

2.2.2 Qubit system

Exploiting the above identities we can produce closed-form expressions for the ergotropy of special cases. Consider the case of a qubit with an Hamiltonian of the form

$$H_\mathrm{S} = \omega_0(\sigma_z + \mathbb{1}_2)/2 \tag{2.50}$$

and density matrix

$$\rho = \frac{1}{2}(\mathbb{1}_2 + \vec{a}\cdot\vec{\sigma}) \,, \tag{2.51}$$

where $\mathbb{1}_2$ is the 2×2 identity and

$$\begin{aligned} &\vec{\sigma} \equiv (\sigma_x, \sigma_y, \sigma_z) \,, \text{ with} \\ &\sigma_x = \begin{pmatrix} 0 & 1 \\ 1 & 0 \end{pmatrix}, \quad \sigma_y = \begin{pmatrix} 0 & -i \\ i & 0 \end{pmatrix}, \quad \sigma_z = \begin{pmatrix} 1 & 0 \\ 0 & -1 \end{pmatrix}, \end{aligned} \tag{2.52}$$

and $\vec{a}$ are the Pauli and Bloch vectors, respectively. Then algebraic manipulations yield

$$\mathcal{E} = \frac{\omega_0}{2}\left(a + a_z\right) \,, \tag{2.53}$$

with $a = |\vec{a}|$, or introducing the ladder operators

$$\sigma_+ = (\sigma_x + i\sigma_y)/2 \qquad \text{and} \qquad \sigma_- = (\sigma_x - i\sigma_y)/2 \,, \tag{2.54}$$

the ergotropy can be alternatively written in terms of average values of operators as

$$\mathcal{E} = \frac{\omega_0}{2}\left(\sqrt{\langle\sigma_z\rangle^2 + 4\,\langle\sigma_+\rangle\,\langle\sigma_-\rangle} + \langle\sigma_z\rangle\right) \,. \tag{2.55}$$

2.2.3 Quantum harmonic oscillator system

Considering the case of a quantum harmonic oscillator, the ergotropy turns out to have a compact expression when the bosonic state of interest is Gaussian (Lörch et al. 2018, Brown et al. 2016). We give below a short introduction to the theory of single-mode Gaussian states, whose content is not only functional to Sec. 4.2 where we analyze a quantum harmonic oscillator battery, but also to Sec. 5.4 in the context of statistical tagging and to Sec. 2.3.2.1 concerning the quantum Chernoff bound in the case of single-mode Gaussian states.

2.2.3.1 Single-mode Gaussian states

The most general single-mode Gaussian state can be expressed as a squeezed-displaced-thermal state of the form

$$\rho_G(\bar{\beta}, \boldsymbol{\xi}, \chi) := D^\dagger(\boldsymbol{\xi}) S^\dagger(\chi) \frac{e^{-\bar{\beta}\omega a^\dagger a}}{\mathrm{tr}\left[e^{-\bar{\beta}\omega a^\dagger a}\right]} S(\chi) D(\boldsymbol{\xi}) \,. \tag{2.56}$$

In the above expression a and $a^\dagger$ are the bosonic ladder operators satisfying

$$\left[a, a^\dagger\right]_- = 1 \,, \tag{2.57}$$

$\bar{\beta} \geq 0$ defines the inverse temperature of the state (ω being some relevant energy scale fixing the temperature units), while the complex parameter χ and the 2-D real vector $\boldsymbol{\xi} = (\xi_1, \xi_2)^T$ define the squeezing and the displacement operators respectively, i.e.

$$S(\chi) = \exp\left[\frac{1}{2}\left(\chi^* a^2 - \chi a^{\dagger 2}\right)\right] \,, \tag{2.58}$$

$$D(\boldsymbol{\xi}) = \exp[-i(\xi_2 x - \xi_1 p)] \,, \tag{2.59}$$

with the operators

$$x = (a + a^\dagger)/\sqrt{2} \quad \text{and} \quad p = (a - a^\dagger)/(\sqrt{2}i) \tag{2.60}$$

being the canonical quadratures of the model, with $\left[x, p\right]_- = i$.

Displacement and squeezing The displacement operator $D(\boldsymbol{\xi})$ of Eq. (2.59) sets the first moments of the state (2.56). Its action on the canonical variables is the following

$$D(\boldsymbol{\xi})\, \boldsymbol{r}\, D^\dagger(\boldsymbol{\xi}) = \boldsymbol{r} + \boldsymbol{\xi} \,, \tag{2.61}$$

with $\boldsymbol{r} := \begin{pmatrix} x \\ p \end{pmatrix}$.
The squeezing operator defined in Eq. (2.58) transforms the ladder operators a and $a^\dagger$ as follows (Olivares 2012, Ferraro et al. 2005):

$$S(\chi)\, \boldsymbol{a}\, S^\dagger(\chi) = \mathbb{S}_A(\chi)\, \boldsymbol{a}\,, \tag{2.62}$$

$$\mathbb{S}_A(\chi) := \begin{pmatrix} \cosh(|\chi|) & e^{i2\phi}\sinh(|\chi|) \\ e^{-i2\phi}\sinh(|\chi|) & \cosh(|\chi|) \end{pmatrix}\,, \tag{2.63}$$

where $\boldsymbol{a} := \begin{pmatrix} a \\ a^\dagger \end{pmatrix}$ and with 2ϕ being the phase of χ, i.e $\chi = |\chi|e^{i2\phi}$. Alternatively this can also be expressed as

$$S(\chi)\, \boldsymbol{r}\, S^\dagger(\chi) = \mathbb{S}(\chi)\, \boldsymbol{r}\,, \tag{2.64}$$

where now

$$\mathbb{S}(\chi) = \begin{pmatrix} \cosh(|\chi|) + \sinh(|\chi|)\cos(2\phi) & \sinh(|\chi|)\sin(2\phi) \\ \sinh(|\chi|)\sin(2\phi) & \cosh(|\chi|) - \sinh(|\chi|)\cos(2\phi) \end{pmatrix}\,, \tag{2.65}$$

the matrices $\mathbb{S}(\chi)$ and $\mathbb{S}_A(\chi)$ being related via the transformation

$$\mathbb{S}(\chi) = U\mathbb{S}_A(\chi)U^\dagger\,, \tag{2.66}$$

with U being the unitary matrix

$$U = 1/\sqrt{2}\begin{pmatrix} 1 & 1 \\ -i & i \end{pmatrix}\,. \tag{2.67}$$

First and second moments of the Gaussian state Define the vector

$$\boldsymbol{A} = \langle \boldsymbol{a} \rangle = \begin{pmatrix} \langle a \rangle \\ \langle a^\dagger \rangle \end{pmatrix}\,, \tag{2.68}$$

and the matrix

$$\sigma_A = \begin{pmatrix} 2\langle a^2\rangle - 2\langle a\rangle^2 & 2\langle a^\dagger a\rangle + 1 - 2|\langle a\rangle|^2 \\ 2\langle a^\dagger a\rangle + 1 - 2|\langle a\rangle|^2 & [2\langle a^2\rangle - 2\langle a\rangle^2]^* \end{pmatrix}\,,$$

where $\langle ... \rangle$ represents the average value computed on the Gaussian state of Eq. (2.56). From these expressions one can then easily retrieve the canonical first moments

$$\boldsymbol{R} = \langle \boldsymbol{r} \rangle = \begin{pmatrix} \langle x \rangle \\ \langle p \rangle \end{pmatrix} , \tag{2.69}$$

and the (real-symmetric) covariance matrix

$$\sigma_{ij} = \langle \Big[r_i - \langle r_i \rangle, r_j - \langle r_j \rangle \Big]_+ \rangle , \tag{2.70}$$

Indeed, one has

$$\boldsymbol{R} = U\boldsymbol{A} , \qquad \sigma = U\sigma_A U^T , \tag{2.71}$$

with U as in Eq. (2.67). From the above analysis it follows that the moments of a Gaussian state (2.56) hold

$$\boldsymbol{R} = \boldsymbol{\xi} , \qquad \sigma = \nu_{\bar{\beta}} \mathbb{S}(\chi) \mathbb{S}^T(\chi) , \tag{2.72}$$

with

$$\nu_{\bar{\beta}} \;\; = \;\; 2\mathcal{N}_b(\bar{\beta}) + 1 = \coth\left(\bar{\beta}\omega/2\right) . \tag{2.73}$$

Equation (2.72) is better understood once it is written as

$$\sigma = \mathbb{S}(\chi) \sigma_{\bar{\beta}} \mathbb{S}^T(\chi) , \qquad \sigma_{\bar{\beta}} = \nu_{\bar{\beta}} \mathbb{1}_2 , \tag{2.74}$$

where $\sigma_{\bar{\beta}}$ is the covariance matrix of the thermal state $e^{-\bar{\beta}\omega a^\dagger a}/\mathrm{tr}\left[e^{-\bar{\beta}\omega a^\dagger a}\right]$. Furthermore, exploiting the fact that

$$\det[\mathbb{S}(\chi)] = \det[\mathbb{S}^T(\chi)] = 1 , \tag{2.75}$$

one can extract the inverse temperature $\bar{\beta}$ of the state ρ_G using the following relation

$$\nu_{\bar{\beta}} = \sqrt{\det[\sigma]} = \sqrt{-\det[\sigma_A]} . \tag{2.76}$$

Another quantity of interest is the mean excitation number of a Gaussian state, whose expression in terms of the parameters $(\bar{\beta},\ \boldsymbol{\xi},\ \chi)$ reads as (Lörch et al. 2018)

$$\langle a^\dagger a \rangle = \frac{1}{2}\{\cosh(2|\chi|)[2\mathcal{N}_b(\bar{\beta}) + 1] + |\boldsymbol{\xi}|^2 - 1\} . \tag{2.77}$$

The passive state connected to ρ_G is the thermal state obtained by undoing displacement and squeezing in (2.56). Given the Hamiltonian of the oscillator

$$H_{\rm S} = \omega_0 a^\dagger a \tag{2.78}$$

and by applying (2.48), one hence gets (Lörch et al. 2018)

$$\mathcal{E} = \omega_0(\langle a^\dagger a\rangle - \langle a^\dagger a\rangle_{\bar\beta}) \,, \tag{2.79}$$

where

$$\langle a^\dagger a\rangle_{\bar\beta} = \frac{1}{2}(\nu_{\bar\beta} - 1) = \mathcal{N}_b(\bar\beta) \,, \tag{2.80}$$

with $\nu_{\bar\beta}$ evaluated as in (2.76) (this result will be next applied in Eq. (4.17), where the harmonic oscillator of interest is the quantum battery of bosonic operators b and $b^\dagger$).

Dynamical Evolution A generator that is quadratic in the bosonic ladder operators induces a Gaussian mapping, meaning that it transforms Gaussian states into other Gaussian states: namely, for single-mode Gaussian states, the time evolution from time 0 to time t simply maps

$$\rho_G(\bar\beta_0, \boldsymbol{\xi}_0, \chi_0) \to \rho_G(\bar\beta(t), \boldsymbol{\xi}(t), \chi(t)).$$

To retrieve the explicit temporal dependence of the quantities $\bar\beta(t)$, $\boldsymbol{\xi}(t)$, $\chi(t)$ from the dynamical expressions for the first and second moments one can follow the same path we have detailed previously to link $\bar\beta, \boldsymbol{\xi}, \chi$ to $\boldsymbol{R}$ and σ. Finally, the same machinery can be used to relate the initial conditions to the parameters $(\bar\beta_0, \boldsymbol{\xi}_0, \chi_0)$ of the input state, giving

$$\begin{aligned}
\langle a(0)\rangle &= A_1(0) \,, &(2.81)\\
\langle a^2(0)\rangle &= \frac{1}{2}\sigma_{A11}(0) + A_1(0)^2 \,, &(2.82)\\
\langle a^\dagger a(0)\rangle &= \frac{1}{2}[\sigma_{A12}(0) - 1] + |A_1(0)|^2 \,, &(2.83)
\end{aligned}$$

with

$$\begin{aligned}
\boldsymbol{A}(0) &= U^\dagger \boldsymbol{\xi}_0 \,, &(2.84)\\
\sigma_A(0) &= \nu_{\bar\beta_0} U^\dagger \mathbb{S}(\chi_0)\mathbb{S}^T(\chi_0) U^* &(2.85)
\end{aligned}$$

and eventually one can monitor the initial mean excitation number by applying Eq. (2.77) to the initial state.

2.3 Elements of quantum metrology

Quantum metrology (Giovannetti et al. 2006, 2011) is the branch of quantum information theory treating the optimization of the estimation of a physical parameter, influencing (naturally or artificially) the dynamics of a quantum system, by measuring the latter. It is based on the idea that quantum effects generally imply some kind of enhancement - in precision, efficiency or simplicity of implementation - for measurements and discrimination procedures (Giovannetti et al. 2011).
In literature, one usually distinguishes between quantum estimation theory (Paris 2009) and quantum state discrimination (Helstrom 1976, Nielsen and Chuang 2010). Whether quantum estimation theory focuses on optimizing the precision in the estimation of a continuous parameter and typically relies on the evaluation of the quantum Fisher information (Braunstein and Caves 1994, Cramér 1999, Giovannetti et al. 2011), quantum state discrimination suitably applies for the tagging of discrete parameters.
For the topic developed in Chapter 5, we naturally focus on the latter, with a parameter that can assume only two discrete values. When facing this kind of problems, one typically works with the most general quantum measurements. Including projective measurements on the system as special cases, they allow to formalize the possibility of performing projective measurements on an ancilla, i.e. a probe, that interacting with the system to be measured delivers information on it, and even more sophisticated setups are contained where non-local projective measurements concern the whole system-ancilla compound. Such measurements are described by a complete set of positive operators, referred as positive-operator-valued measure (POVM, cfr. e.g. Nielsen and Chuang (2010)). Conversely, given a POVM, there always exist an ancilla and a unitary channel such that the measure can be viewed as a projective measurement on the ancilla. These generalized measurements represent hence the ideal tool for optimizing quantum state discrimination.

2.3.1 Helstrom error probability

Let us suppose that the state ρ of the quantum system of interest can assume either the value ρ_0 or the value ρ_1 and we are interested in discriminating the two instances. Accordingly, by performing a single quantum measurement having two outcomes, we would like to associate an outcome, say 0, which allows to argue that the hypothesis ρ_0 is true with the highest possible efficiency, and, conversely, an outcome 1 for the opposite situation. In general, the two outcomes are connected to the elements of a

POVM, a set of operators

$$\{E_0, E_1\}\ , \quad \text{with} \tag{2.86}$$

$$E_0,\ E_1 \geq 0\ , \tag{2.87}$$

$$E_0 + E_1 = \mathbb{1}\ , \tag{2.88}$$

E_0 (E_1) being the element of the POVM related to the outcome 0 (1). As usual, (2.87) means that $E_0,\ E_1$ are positive-semidefinite (positive) operators, property that guarantees the non-negativity of the conditional probabilities

$$p(i|\rho) = \mathrm{tr}(E_i\rho) \tag{2.89}$$

of obtaining a certain outcome $i \in \{0, 1\}$, while (2.88) ensures the normalization condition $\sum_k p(k|\rho) = 1$.
For flat priors (i.e. the two hypotheses are equally probable), the error probability, namely the probability of making the wrong guess, is defined as (Helstrom 1976)

$$p_{\mathrm{err}} = \frac{1}{2}[p(0|\rho_1) + p(1|\rho_0)]\ , \tag{2.90}$$

which, using (2.89) and (2.88), assumes the form

$$p_{\mathrm{err}} = \frac{1}{2}\{1 - \mathrm{tr}[E_0(\rho_0 - \rho_1)]\}\ . \tag{2.91}$$

The goal is to find the best POVM (2.86) which minimizes the right-hand side of the above expression[1]. Let us notice that the operator $\rho_0 - \rho_1$ is traceless and Hermitian. We separate its spectral decomposition

$$\rho_0 - \rho_1 = \sum_{l=1}^{d} \lambda_l \left|l\right\rangle \left\langle l\right| := \Delta\rho_{01} \tag{2.92}$$

(d being the dimension of the Hilbert space of the system) in two parts, containing each non-negative, $\lambda_l^{(+)} \geq 0$, and negative, $\lambda_l^{(-)} < 0$, eigenvalues:

$$\Delta\rho_{01} = \sum_{l=1}^{n_+} \lambda_l^{(+)} \left|l\right\rangle \left\langle l\right|^{(+)} + \sum_{l=1}^{n_-} \lambda_l^{(-)} \left|l\right\rangle \left\langle l\right|^{(-)} := \Delta\rho_{01}^{(+)} - \Delta\rho_{01}^{(-)}\ , \tag{2.93}$$

with $\Delta\rho_{01}^{(+)} = \sum_{l=1}^{n_+} \lambda_l^{(+)} \left|l\right\rangle \left\langle l\right|^{(+)}$, $\Delta\rho_{01}^{(-)} = \sum_{l=1}^{n_-}(-\lambda_l^{(-)}) \left|l\right\rangle \left\langle l\right|^{(-)}$ and $n_+ + n_- = d$. Notice that $\Delta\rho_{01}^{(+)}$ and $\Delta\rho_{01}^{(-)}$ are positive operators with orthogonal support.

[1] Refer, e.g., to Nielsen and Chuang (2010), page 404, or to Calsamiglia et al. (2008).

Exploiting this decomposition, (2.91) becomes

$$p_{\rm err} = \frac{1}{2}\{1 - {\rm tr}[E_0(\Delta\rho_{01}^{(+)} - \Delta\rho_{01}^{(-)})]\} \tag{2.94}$$

which gets minimum when ${\rm tr}[E_0\Delta\rho_{01}^{(+)}] = {\rm tr}[\Delta\rho_{01}^{(+)}]$ and ${\rm tr}[E_0\Delta\rho_{01}^{(-)}] = 0$. The last conditions are satisfied when setting E_0 as the projector on the subspace of positive eigenvalues of $\Delta\rho_{01}$, i.e. choosing

$$E_0 \equiv \bar{E}_0 = \sum_{l=1}^{n_+} |l\rangle \langle l|^{(+)} \ . \tag{2.95}$$

Since $\Delta\rho_{01}$ is traceless, ${\rm tr}[\Delta\rho_{01}^{(+)}] = {\rm tr}[\Delta\rho_{01}^{(-)}] = \frac{1}{2}{\rm tr}[\Delta\rho_{01}^{(+)} + \Delta\rho_{01}^{(-)}]$, and we arrive to the expression of the Helstrom error probability (Helstrom 1976)

$$p_{\rm err}^{(\rm min)} := H(\rho_0, \rho_1) := \frac{1}{2}\big(1 - \frac{1}{2}\|\rho_0 - \rho_1\|_1\big) \ , \tag{2.96}$$

which hence represents the saturable lowest bound for $p_{\rm err}$ in (2.90), with $\|\rho_0 - \rho_1\|_1$ denoting the trace norm of the operator $\rho_0 - \rho_1$, i.e. the sum of the modulus of its eigenvalues:

$$\|\rho_0 - \rho_1\|_1 = \sum_{l=1}^{d} |\lambda_l| \ . \tag{2.97}$$

Furthermore, Eq. (2.96) highlights the fact that two states ρ_0 and ρ_1 are perfectly distinguishable (again, having the freedom of choosing the best single-shot POVM) when they have orthogonal support (i.e. they coincide with $\Delta\rho_{01}^{(+)}$ and $\Delta\rho_{01}^{(-)}$, respectively, and $H(\rho_0, \rho_1) = 0$) and completely indistinguishable when they are equal (in this case $\Delta\rho_{01}^{(+)} = \Delta\rho_{01}^{(-)} = 0$ and $H(\rho_0, \rho_1) = 1/2$).

2.3.2 Quantum Chernoff bound

A natural quantifier of the discrimination capability is given by $1 - p_{\rm err}^{(\rm min)}$, where $p_{\rm err}^{(\rm min)}$ is the Helstrom error probability (2.96). More generally, if we have $N \geq 1$ identical copies at disposal, the discrimination process involves $\rho_0^{\otimes N}$ and $\rho_1^{\otimes N}$, while the minimum probability of error reads as

$$p_{\rm err}^{(\rm min)} = H(\rho_0^{\otimes N}, \rho_1^{\otimes N}) = \frac{1}{2}\left(1 - \frac{1}{2}\|\rho_0^{\otimes N} - \rho_1^{\otimes N}\|_1\right) \leq Q^N/2, \tag{2.98}$$

where Q is the minimum of the Chernoff function Q_r, i.e.

$$Q = \min_{r\in[0,1]} Q_r \ , \qquad Q_r := {\rm tr}\left[\rho_0^r \rho_1^{1-r}\right] \ . \tag{2.99}$$

The result (2.98) is known as Quantum Chernoff Bound (Ogawa and Hayashi 2004, Audenaert et al. 2007) and the related rate exponent is asymptotically attainable (Audenaert et al. 2007, Nussbaum and Szkoła 2009). Furthermore, for large N, the computation of the trace norm in (2.98) is tedious and the use of the Chernoff approach represents a valuable choice.

2.3.2.1 Harmonic oscillator

The Chernoff quantity (2.99) takes a compact expression in the case of the single-mode Gaussian states introduced in Sec. 2.2.3.1. Let us suppose we want to distinguish between two hypotheses, say ρ_b and ρ_f (whose meaning will be clear in Chapter 5), of the single-mode Gaussian state ρ. Following Calsamiglia et al. (2008), we can compute the value of the Chernoff quantity Q_r (2.99) via the expression

$$Q_r = \frac{2\,\mathcal{N}_{\bar{\beta}_b,r}\,\mathcal{N}_{\bar{\beta}_f,1-r}\,e^{-\boldsymbol{\delta}^T\left[\tilde{\sigma}_b(r)+\tilde{\sigma}_f(1-r)\right]^{-1}\boldsymbol{\delta}}}{\sqrt{\det\left[\tilde{\sigma}_b(r)+\tilde{\sigma}_f(1-r)\right]}}\,, \tag{2.100}$$

where $\boldsymbol{\delta} = \boldsymbol{\xi}_b - \boldsymbol{\xi}_f$ is the difference between the first moments of the two states; $\nu_{\bar{\beta}_q} = \coth(\bar{\beta}_q\omega/2) = \sqrt{\det[\sigma_q]}$ [see (2.76)] ; $\mathcal{N}_{\bar{\beta}_q,r} = \frac{(1-e^{-\bar{\beta}_q\omega})^r}{1-e^{-\bar{\beta}_q\omega r}}$; $\tilde{\sigma}_q(r) = \frac{\nu_{r\bar{\beta}_q}}{\nu_{\bar{\beta}_q}}\sigma_q$ and σ_q is the covariance matrix [see (2.70)] of the state ρ_q, for $q \in \{b, f\}$.
To conclude, the quantities defined in Eq. (2.99) - particularly useful in the case of single-mode Gaussian states - and Eq. (2.96) - which will be widely applied to qubits in Chapter 5 - provide operationally well defined figures of merit for the precision in the discrimination between two hypotheses of a quantum state.

CHAPTER 3

Formal aspects of open quantum system dynamics

3.1 Completely-Positive Redfield Equation: general formalism

We now introduce another way of curing the non-positive character of the Redfield equation, which does not rely on the assumption (2.24), i.e. , differs from the indiscriminate implementation of the secular approximation.

3.1.1 Coarse grain averaging

The Redfield equation in interaction picture (2.19) can be alternatively simplified by performing a temporal averaging over coarse grain time intervals Δt which are much smaller than the timescale δt where $\tilde{\rho}_{\rm S}(t)$ varies appreciably, i.e.

$$\Delta t \ll \delta t \ . \tag{3.1}$$

This averaging is along the same line of reasoning with the hypothesis underlying the Markov approximation and, as we shall see in the following, is essential in order to recover the GKSL structure of the generator. In particular using the fact that the coarse graining does not affect $\tilde{\rho}_{\rm S}(t)$, we can replace (2.19) with

$$\dot{\tilde{\rho}}_{\rm S}(t) \simeq \sum_{ij} \Gamma_{ij}^{(\Delta t)}(t) \left(A_j^\dagger \tilde{\rho}_{\rm S}(t) A_i - A_i A_j^\dagger \tilde{\rho}_{\rm S}(t) \right) + h.c. \, , \tag{3.2}$$

where now

$$\Gamma_{ij}^{(\Delta t)}(t) := \frac{1}{\Delta t} \int_{t-\Delta t/2}^{t+\Delta t/2} ds \ \Gamma_{ij}(s) = \Gamma_{ij}(t) \ S_{\omega-\omega'}^{(\Delta t)} \tag{3.3}$$

and we introduced the function

$$S_{\omega-\omega'}^{(\Delta t)} \ := \ \text{sinc}[(\omega-\omega')\Delta t/2] \ , \tag{3.4}$$

with $\text{sinc}[x] := \sin x/x$ being the cardinal sinus.

Then we express the matrix $\Gamma_{ij}^{(\Delta t)}(t)$ in terms of its hermitian and anti-hermitian

components, writing

$$\Gamma_{ij}^{(\Delta t)}(t) = \gamma_{ij}^{(\Delta t)}(t)/2 + i\,\eta_{ij}^{(\Delta t)}(t)\,, \tag{3.5}$$

with

$$\gamma_{ij}^{(\Delta t)}(t) \;:=\; \Gamma_{ij}^{(\Delta t)}(t) + (\Gamma_{ji}^{(\Delta t)}(t))^*\,, \tag{3.6}$$

$$\eta_{ij}^{(\Delta t)}(t) \;:=\; \Big(\Gamma_{ij}^{(\Delta t)}(t) - (\Gamma_{ji}^{(\Delta t)}(t))^*\Big)/(2i)\,. \tag{3.7}$$

With this choice, the terms on the r.h.s. of Eq. (3.2) can be expressed as

$$\begin{aligned}\dot{\tilde{\rho}}_{\rm S}(t) \;\simeq\; & -i\left[\tilde{H}_{\rm LS}^{(\Delta t)}(t), \tilde{\rho}_{\rm S}(t)\right]_- \\ & + \sum_{ij}\gamma_{ij}^{(\Delta t)}(t)\Big(A_j^\dagger\tilde{\rho}_{\rm S}(t)A_i - \frac{1}{2}\Big[A_iA_j^\dagger, \tilde{\rho}_{\rm S}(t)\Big]_+\Big)\,,\end{aligned} \tag{3.8}$$

where $\Big[\cdots,\cdots\Big]_+$ in the second line represents the anti-commutator and $\tilde{H}_{\rm LS}^{(\Delta t)}(t)$ the Lamb shift term

$$\tilde{H}_{\rm LS}^{(\Delta t)}(t) := \sum_{ij}\eta_{ij}^{(\Delta t)}(t)\; A_iA_j^\dagger\,. \tag{3.9}$$

Going back in $\mathrm{Schrödinger}$ picture, we can finally remove the time dependence of the coefficients $\gamma_{ij}^{(\Delta t)}(t)$ and $\eta_{ij}^{(\Delta t)}(t)$ obtaining (as it happened for the secular approximation) a master equation with constant generator terms

$$\begin{aligned}\dot{\rho}_{\rm S}(t) \;\simeq\; & -i\left[H_{\rm S}^{(\Delta t)}, \rho_{\rm S}(t)\right]_- \\ & + \sum_{ij}\gamma_{ij}^{(\Delta t)}\Big(A_j^\dagger\rho_{\rm S}(t)A_i - \frac{1}{2}\Big[A_iA_j^\dagger, \rho_{\rm S}(t)\Big]_+\Big)\,,\end{aligned} \tag{3.10}$$

where now

$$H_{\rm S}^{(\Delta t)} \;:=\; H_{\rm LS}^{(\Delta t)} + H_{\rm S}\,, \tag{3.11}$$

$$H_{\rm LS}^{(\Delta t)} \;:=\; \tilde{H}_{\rm LS}^{(\Delta t)}(0) = \sum_{ij}\eta_{ij}^{(\Delta t)}A_iA_j^\dagger\,. \tag{3.12}$$

Explicitly, the $N\times N$ matrices $\gamma_{ij}^{(\Delta t)}$ and $\eta_{ij}^{(\Delta t)}$ appearing in these expressions can be shown to correspond to

$$\gamma_{ij}^{(\Delta t)} \;:=\; \gamma_{ij}^{(\Delta t)}(0) = \gamma^{(+)}_{\alpha\omega,\beta\omega'}\; S^{(\Delta t)}_{\omega-\omega'}\,, \tag{3.13}$$

$$\eta_{ij}^{(\Delta t)} \;:=\; \eta_{ij}^{(\Delta t)}(0) = \frac{\gamma^{(-)}_{\alpha\omega,\beta\omega'}}{2i}\; S^{(\Delta t)}_{\omega-\omega'}\,, \tag{3.14}$$

with

$$\gamma^{(\pm)}_{\alpha\omega,\beta\omega'} \;:=\; \Omega_{\alpha\beta}(\omega') \pm \Omega^{*}_{\beta\alpha}(\omega)\ . \tag{3.15}$$

The last step needed to put Eq. (3.10) in GKSL form is the diagonalization of $\gamma^{(\Delta t)}_{ij}$. It, however, works if and only if such matrix is positive semi-definite (or equivalently non-negative), the presence of negative eigenvalues being formally incompatible with the complete-positivity requirement (Lindblad 1976, Alicki and Lendi 2007) of the resulting dynamics of $\rho_{\rm S}(t)$.
This is the reason for which one introduces the coarse graining transformation (3.3). Indeed thanks to the fact that

$$\lim_{\Delta t\to\infty} S^{(\Delta t)}_{\omega-\omega'} = \delta_{\omega,\omega'}\ , \tag{3.16}$$

as Δt diverges the $N\times N$ matrix $\gamma^{(\Delta t)}_{ij}$ reduces to a block diagonal form with respect to the frequency labels,

$$\gamma^{(\infty)}_{ij} \;:=\; \lim_{\Delta t\to\infty}\gamma^{(\Delta t)}_{ij} = \gamma^{(+)}_{\alpha\omega,\beta\omega}\delta_{\omega,\omega'}\ , \tag{3.17}$$

where for each ω the coefficients $\gamma^{(+)}_{\alpha\omega,\beta\omega}$ identify $M\times M$ matrices

$$\gamma^{(+)}(\omega,\omega) := \Omega(\omega) + \Omega^{\dagger}(\omega)\ , \tag{3.18}$$

that, coinciding with the matrices we defined in (2.28), are, by construction, non-negative (see Sec. 2.1.2.3 for details). Indeed, the $\Delta t\to\infty$ limit identifies the secular approximation we introduced to obtain (2.25) that is the last step one traditionally enforces in order to recover the GKSL form.
The coarse grained Redfield equation (3.10) provides hence a way of mapping in a continuous way the original *uncorrected* Redfield equation, $\Delta t = 0$ (i.e. no average has been performed), with the secular ME, $\Delta t = \infty$, by moving the parameter Δt. More interestingly, there typically exist a finite threshold for Δt above which complete positivity is guaranteed.

3.1.2 Complete positivity: sufficient conditions for the coarse graining time

We are now interested in determining general conditions which guarantee that a certain finite coarse graining time Δt can be adopted to ensure that the matrix $\gamma^{(\Delta t)}$ of elements $\gamma_{ij}^{(\Delta t)}$ defined in Eq. (3.13) is positive semi-definite, i.e. $\gamma^{(\Delta t)} \geq 0$. Formally speaking this consists in finding the values of Δt such that

$$\vec{u}^{\dagger} \cdot \gamma^{(\Delta t)} \cdot \vec{u} = \sum_{ij} u_i^* \gamma_{ij}^{(\Delta t)} u_j \geq 0 \; , \tag{3.19}$$

for all choices of the column vector $\vec{u} \in \mathbb{C}^N$ or, equivalently, such that the minimum eigenvalue $\Lambda_{\min}(\Delta t)$ of $\gamma^{(\Delta t)}$ is non-negative, i.e.

$$\Lambda_{\min}(\Delta t) \geq 0 \; . \tag{3.20}$$

For small values of N, Eq. (3.20) turns out to be the proper way to go. However, as N increases, determining $\Lambda_{\min}(\Delta t)$ can be problematic. In what follows we hence present an alternative, computationally less demanding approach which allows one to characterize the set of suitable Δt, by only focusing on the properties of the $M \times M$ blocks $\Omega(\omega)$ defined in Eq. (2.23). The main result of this analysis is the identification of a critical threshold Δt_c above which the coarse graining time Δt is guaranteed to yield a positive semi-definite $\gamma^{(\Delta t)}$, i.e.

$$\Delta t \geq \Delta t_c \quad \Longrightarrow \quad \gamma^{(\Delta t)} \geq 0 \; . \tag{3.21}$$

Specifically, indicating with $\|\Omega(\omega)\|_\infty$ the operator norm of $\Omega(\omega)$, i.e.

$$\|\Omega(\omega)\|_\infty := \sup_{\vec{v}(\omega)} \frac{\sqrt{\vec{v}^{\dagger}(\omega) \cdot \Omega^{\dagger}(\omega) \Omega(\omega) \cdot \vec{v}(\omega)}}{|\vec{v}(\omega)|} \; , \tag{3.22}$$

and with $\lambda_{\min}(\omega)$ the minimum eigenvalue of its Hermitian component $\gamma^{(+)}(\omega, \omega)$ defined in Eq. (3.18) (which is non-negative by construction), in Sec. 3.1.3 we shall proof that one can identify Δt_c with the quantity

$$\Delta t_c^{(1)} \;\; := \;\; 2(G-1) \max_{\omega, \omega' : \omega \neq \omega'} \left(\frac{\|\Omega(\omega)\|_\infty + \|\Omega(\omega')\|_\infty}{|\omega - \omega'| \; \lambda_{\min}(\omega)} \right) , \tag{3.23}$$

or with its pejorative, but more compact, version

$$\Delta t_c^{(2)} \;\; := \;\; \frac{4(G-1)\|\Omega\|_{\max}}{\nu_{\min} \; \lambda_{\min}} \; , \tag{3.24}$$

where $\lambda_{\min} := \min_\omega \lambda_{\min}(\omega)$, $\|\Omega\|_{\max} := \max_\omega \|\Omega(\omega)\|_\infty$, and where

$$\nu_{\min} := \min_{\omega,\omega':\omega\neq\omega'} |\omega - \omega'| \tag{3.25}$$

is the minimum among all the gaps differences. As $\Delta t_c^{(2)}$ is always larger than $\Delta t_c^{(1)}$, it provides a worst estimation of the real critical threshold Δt_c. Still Eq. (3.24) is more informative as it makes explicit that Δt_c should scale as the inverse of the minimal difference $\nu_{\min}$. An estimation of the critical time Δt_c that is provably better, but more involved than $\Delta t_c^{(1)}$ is finally given by the quantity

$$\Delta t_c^{(0)} \;:=\; \max_\omega \left(\frac{2}{Q(\omega) K(\omega) \lambda_{\min}(\omega)} \right) , \tag{3.26}$$

obtained by the functions

$$Q(\omega) \;:=\; \sum_{\omega':\omega'\neq\omega} \frac{|\omega-\omega'|}{\|\Omega(\omega)\|_\infty + \|\Omega(\omega')\|_\infty} , \tag{3.27}$$

$$q_{\omega'}^{(\omega)} \;:=\; \frac{|\omega-\omega'|}{\|\Omega(\omega)\|_\infty + \|\Omega(\omega')\|_\infty} \frac{1}{Q(\omega)} \qquad (\forall \omega' \neq \omega) , \tag{3.28}$$

$$K(\omega) \;:=\; \frac{1}{\sum_{\omega':\omega'\neq\omega} \frac{1}{q_{\omega'}^{(\omega)}}} . \tag{3.29}$$

Beyond providing the practical upper bounds

$$\Delta t_c^{(0)} \leq \Delta t_c^{(1)} \leq \Delta t_c^{(2)}$$

for the critical coarse grain time Δt_c in a general formalism, the previous analysis gives a hint of the fact that such time scale is possibly finite in reliable situations. The reader interested in the formal derivations of such bounds can find them in Sec. 3.1.3 or, alternatively, can skip it, passing to concrete examples where the main concepts are applied.

3.1.3 Derivation of the bounds via matrix dilution

Here we explicitly show that both the terms (3.23) and (3.26) are suitable choices for the critical time Δt_c entering Eq. (3.21).

We start by observing that by expanding the indexes i and j, Eq. (3.19) can be conveniently arranged in the following form

$$\begin{aligned} &\sum_\omega \vec{u}^\dagger(\omega) \cdot \gamma^{(+)}(\omega,\omega) \cdot \vec{u}(\omega) \\ &+ \sum_{\omega,\omega':\omega\neq\omega'} S_{\omega-\omega'}^{(\Delta t)}\, \vec{u}^\dagger(\omega) \cdot \gamma^{(+)}(\omega,\omega') \cdot \vec{u}(\omega') \geq 0 , \end{aligned} \tag{3.30}$$

where for given ω and ω',

$$\gamma^{(+)}(\omega,\omega') := \Omega^\dagger(\omega) + \Omega(\omega') \,, \tag{3.31}$$

represents the $M \times M$ matrix with elements provided by the terms $\gamma^{(+)}_{\alpha\omega,\beta\omega'}$ of Eq. (3.15), and where $\vec{u}(\omega)$ is the M-dimensional vector defined by the components of $\vec{u}$ associated with the corresponding block ω. Indeed, making the blocks explicit, the vector $\vec{u}$ reads $\vec{u} = (\vec{u}(\omega_1), ..., \vec{u}(\omega_G))^T$.

It is worth observing that the first contribution of Eq. (3.30) corresponds to the term one would get when enforcing the secular approximation (i.e. , enforcing the $\Delta t \to \infty$ limit): accordingly, for all choices of $\vec{u}$ this term can always be guaranteed to be non negative, i.e.

$$\sum_\omega \vec{u}^\dagger(\omega) \cdot \gamma^{(+)}(\omega,\omega) \cdot \vec{u}(\omega) \geq 0 \,. \tag{3.32}$$

Problems on the contrary can arise from the second contribution which involves the off-diagonal blocks $\gamma^{(+)}(\omega,\omega')$ with $\omega \neq \omega'$. To treat them we adopt the following *dilution* technique dividing the contribution coming from the diagonal block terms $\omega = \omega'$ into fractions which are then added to the terms associated with the off-diagonal blocks $\omega \neq \omega'$. Specifically, for each given ω let us introduce a set of numbers $\{p^{(\omega)}_{\omega'}\}_{\omega'}$ such that

$$p^{(\omega)}_{\omega'} \geq 0 \,,\, \omega' \neq \omega \quad \text{and} \quad \sum_{\omega' \colon \omega' \neq \omega} p^{(\omega)}_{\omega'} = 1 \,. \tag{3.33}$$

They form G sets of probabilities with $G-1$ entries, which we shall employ as free parameters in our analysis and which allow us to rewrite (3.30) in the following symmetrized form

$$\sum_{\omega,\omega' \colon \omega' > \omega} \Big\{ p^{(\omega)}_{\omega'} \; \vec{u}^\dagger(\omega) \cdot \gamma^{(+)}(\omega,\omega) \cdot \vec{u}(\omega) + p^{(\omega')}_{\omega} \; \vec{u}^\dagger(\omega') \cdot \gamma^{(+)}(\omega',\omega') \cdot \vec{u}(\omega') \\ + 2 \; S^{(\Delta t)}_{\omega-\omega'} \, \text{Re} \left[\vec{u}^\dagger(\omega) \cdot \gamma^{(+)}(\omega,\omega') \cdot \vec{u}(\omega') \right] \Big\} \geq 0 \,, \tag{3.34}$$

where we grouped together all the contributions of all the couples ω and $\omega' \neq \omega$, used the fact that $S^{(\Delta t)}_{\omega-\omega'}$ is invariant under exchange of ω and ω', and the identity $\gamma^{(+)}(\omega',\omega) = [\gamma^{(+)}(\omega,\omega')]^\dagger$.

Now a sufficient condition ensuring that Eq. (3.34) holds for all $\vec{u}$, can be obtained by forcing each one of such contributions to verify the same property. More specifically, we can claim that the matrix $\gamma^{(\Delta t)}$ is non-negative at least for those Δt such that there

exists a proper choice of the probabilities $\{p^{(\omega)}_{\omega'}\}_{\omega'}$ for which

$$\mathcal{F}^{(\Delta t)}_{\omega,\omega'}(\vec{u}(\omega),\vec{u}(\omega')) := p^{(\omega)}_{\omega'}\ \vec{u}^{\dagger}(\omega)\cdot\gamma^{(+)}(\omega,\omega)\cdot\vec{u}(\omega) + p^{(\omega')}_{\omega}\ \vec{u}^{\dagger}(\omega')\cdot\gamma^{(+)}(\omega',\omega')\cdot\vec{u}(\omega') \\ +2\ S^{(\Delta t)}_{\omega-\omega'}\ \mathrm{Re}\left[\vec{u}^{\dagger}(\omega)\cdot\gamma^{(+)}(\omega,\omega')\cdot\vec{u}(\omega')\right] \geq 0\ , \tag{3.35}$$

for all possible choices of ω, ω', $\vec{u}(\omega)$ and $\vec{u}(\omega')$, with $\omega \neq \omega'$. Next step is to construct a lower bound for the quantity $\mathcal{F}^{(\Delta t)}_{\omega,\omega'}(\vec{u}(\omega),\vec{u}(\omega'))$. For this purpose we begin observing that, indicating with $\lambda_{\min}(\omega)$ the minimum eigenvalue of the matrix $\gamma^{(+)}(\omega,\omega)$, we have

$$\vec{u}^{\dagger}(\omega)\cdot\gamma^{(+)}(\omega,\omega)\cdot\vec{u}(\omega) \geq |\vec{u}(\omega)|^2\ \lambda_{\min}(\omega)\ , \tag{3.36}$$

with $|\vec{u}(\omega)|$ being the norm of the vector $\vec{u}(\omega)$. Then by using Eq. (3.31), the triangle inequality, the Cauchy-Schwarz inequality, and the fact that, for generic $\vec{u}$, one has $\sqrt{\vec{u}^{\dagger}(\omega)\cdot\Omega^{\dagger}(\omega)\Omega(\omega)\cdot\vec{u}(\omega)} \leq |\vec{u}(\omega)|\ \|\Omega(\omega)\|_{\infty}$, we observe that

$$\begin{aligned}
&\left|\mathrm{Re}\left[\vec{u}^{\dagger}(\omega)\cdot\gamma^{(+)}(\omega,\omega')\cdot\vec{u}(\omega')\right]\right| \\
&\leq |\vec{u}^{\dagger}(\omega)\cdot\gamma^{(+)}(\omega,\omega')\cdot\vec{u}(\omega')| \leq |\vec{u}^{\dagger}(\omega)\cdot\Omega^{\dagger}(\omega)\cdot\vec{u}(\omega')| + |\vec{u}^{\dagger}(\omega)\cdot\Omega(\omega')\cdot\vec{u}(\omega')| \\
&\leq |\vec{u}(\omega')|\ \sqrt{\vec{u}^{\dagger}(\omega)\cdot\Omega^{\dagger}(\omega)\Omega(\omega)\cdot\vec{u}(\omega)} + |\vec{u}(\omega)|\ \sqrt{\vec{u}^{\dagger}(\omega')\cdot\Omega^{\dagger}(\omega')\Omega(\omega')\cdot\vec{u}(\omega')} \\
&\leq |\vec{u}(\omega')||\vec{u}(\omega)|\ (\|\Omega(\omega)\|_{\infty} + \|\Omega(\omega')\|_{\infty})\ ,
\end{aligned} \tag{3.37}$$

which implies

$$\begin{aligned}
&2\ S^{(\Delta t)}_{\omega-\omega'}\ \mathrm{Re}\left[\vec{u}^{\dagger}(\omega)\cdot\gamma^{(+)}(\omega,\omega')\cdot\vec{u}(\omega')\right] \\
&\geq -2\ |S^{(\Delta t)}_{\omega-\omega'}|\ \left|\mathrm{Re}\left[\vec{u}^{\dagger}(\omega)\cdot\gamma^{(+)}(\omega,\omega')\cdot\vec{u}(\omega')\right]\right| \\
&\geq -2|S^{(\Delta t)}_{\omega-\omega'}||\vec{u}(\omega')||\vec{u}(\omega)|\ (\|\Omega(\omega)\|_{\infty} + \|\Omega(\omega')\|_{\infty})\ .
\end{aligned} \tag{3.38}$$

Replacing hence (3.36) and (3.38) into the definition of $\mathcal{F}^{(\Delta t)}_{\omega,\omega'}(\vec{u}(\omega),\vec{u}(\omega'))$ we arrive to establish the following bound

$$\mathcal{F}^{(\Delta t)}_{\omega,\omega'}(\vec{u}(\omega),\vec{u}(\omega')) \geq \bar{\mathcal{F}}^{(\Delta t)}_{\omega,\omega'}(\vec{u}(\omega),\vec{u}(\omega'))\ , \tag{3.39}$$

with $\bar{\mathcal{F}}^{(\Delta t)}_{\omega,\omega'}(\vec{u}(\omega),\vec{u}(\omega'))$ being the function

$$\begin{aligned}
\bar{\mathcal{F}}^{(\Delta t)}_{\omega,\omega'}(\vec{u}(\omega),\vec{u}(\omega')) &:= p^{(\omega)}_{\omega'}\ |\vec{u}(\omega)|^2\ \lambda_{\min}(\omega) + p^{(\omega')}_{\omega}\ |\vec{u}(\omega')|^2\ \lambda_{\min}(\omega') \\
&\quad -2|S^{(\Delta t)}_{\omega-\omega'}||\vec{u}(\omega')||\vec{u}(\omega)|\ (\|\Omega(\omega)\|_{\infty} + \|\Omega(\omega')\|_{\infty}) \\
&= |\vec{u}(\omega)|^2(A_{\omega,\omega'} - B^{(\Delta t)}_{\omega,\omega'}) + |\vec{u}(\omega')|^2(A_{\omega',\omega} - B^{(\Delta t)}_{\omega,\omega'}) + B^{(\Delta t)}_{\omega,\omega'}(|\vec{u}(\omega)| - |\vec{u}(\omega')|)^2\ ,
\end{aligned} \tag{3.40}$$

with

$$A_{\omega,\omega'} := p^{(\omega)}_{\omega'}\lambda_{\min}(\omega)\ , \tag{3.41}$$

$$B^{(\Delta t)}_{\omega,\omega'} := |S^{(\Delta t)}_{\omega-\omega'}|\ (\|\Omega(\omega)\|_\infty + \|\Omega(\omega')\|_\infty)\ , \tag{3.42}$$

From Eq. (3.39) it then follows that a sufficient condition for Eq. (3.35) is the positivity of the function $\bar{\mathcal{F}}^{(\Delta t)}_{\omega,\omega'}(\vec{u}(\omega),\vec{u}(\omega'))$, which by looking at (3.40), can be guaranteed by imposing the function $B^{(\Delta t)}_{\omega,\omega'}$ to be smaller than $A_{\omega,\omega'}$ and $A_{\omega',\omega}$, i.e.

$$B^{(\Delta t)}_{\omega,\omega'} \leq \min\{A_{\omega,\omega'}, A_{\omega',\omega}\}\ , \tag{3.43}$$

which can be cast in the equivalent form

$$|S^{(\Delta t)}_{\omega-\omega'}| \leq \frac{p^{(\omega)}_{\omega'}\lambda_{\min}(\omega)}{\|\Omega(\omega)\|_\infty + \|\Omega(\omega')\|_\infty}\ , \tag{3.44}$$

by exploiting the symmetry $B^{(\Delta t)}_{\omega,\omega'} = B^{(\Delta t)}_{\omega',\omega}$ [1]. Noticing that from Eq. (3.4) we have $|S^{(\Delta t)}_{\omega-\omega'}| \leq 2/(|\omega-\omega'|\Delta t)$, the latter can then be replaced by the (stronger) requirement

$$\Delta t \geq \frac{2}{p^{(\omega)}_{\omega'}}\ \frac{\|\Omega(\omega)\|_\infty + \|\Omega(\omega')\|_\infty}{|\omega-\omega'|\ \lambda_{\min}(\omega)}\ . \tag{3.45}$$

To summarize, any coarse graining time Δt admitting a set of probability functions $\{p^{(\omega)}_{\omega'}\}_{\omega'}$ for which the inequality (3.45) holds for all ω and ω', with $\omega \neq \omega'$, ensures the fulfillment of Eq. (3.34), hence the non-negativity of the matrix $\gamma^{(\Delta t)}$ (notice that if $\lambda_{\min}(\omega) = 0$ for some ω, Eq. (3.45) can still be used: simply it implies that Δt has to be infinite). Alternatively, we can say that, for each assigned choice of the dilution probabilities (3.33), the fulfillment of the inequality (3.34) allows us to identify a coarse graining time Δt that implies the non-negativity of $\gamma^{(\Delta t)}$. Taking for instance $\{p^{(\omega)}_{\omega'}\}_{\omega'}$ to be flat distributions, i.e.

$$p^{(\omega)}_{\omega'} = 1/(G-1)\ , \qquad \forall \omega' \neq \omega \tag{3.46}$$

equation (3.45) becomes

$$\Delta t \geq 2(G-1)\frac{\|\Omega(\omega)\|_\infty + \|\Omega(\omega')\|_\infty}{|\omega-\omega'|\ \lambda_{\min}(\omega)}\ , \tag{3.47}$$

which, maximizing the right-hand side term with respect to all possible choices of ω and $\omega' \neq \omega$, allows us to claim that a sufficient condition for the non-negativity of $\gamma^{(\Delta t)}$ can be obtained by taking Δt larger than the quantity $\Delta t^{(1)}_c$ of Eq. (3.23).

[1] See Eq. (3.121) for an application of the (3.44) in a particular case.

To prove that also Eq. (3.26) yields a legitimate estimation of Δt_c, we look for the optimal choice of the probability functions $\{p^{(\omega)}_{\omega'}\}$ entering Eq. (3.45). To see this let us use the functions (3.27)-(3.29) to rewrite the latter inequality as

$$\frac{2}{\lambda_{\min}(\omega)\Delta t} \leq \frac{p^{(\omega)}_{\omega'}|\omega-\omega'|}{\|\Omega(\omega)\|_\infty + \|\Omega(\omega')\|_\infty} = Q(\omega)p^{(\omega)}_{\omega'}q^{(\omega)}_{\omega'} , \quad \forall\omega \text{ and } \omega' \neq \omega. \tag{3.48}$$

Now observe that for given ω, similarly to the $\{p^{(\omega)}_{\omega'}\}_{\omega'}$, the terms $\{q^{(\omega)}_{\omega'}\}_{\omega'}$ define a proper set of probabilities with $G-1$ entries. As we have the freedom to arbitrarily choose whatever set of $\{p^{(\omega)}_{\omega'}\}_{\omega'}$, in order to get a less stringent condition on Δt, we want to focus on those that maximize the right-hand side of Eq. (3.48). A proof by contradiction[2] shows that this can be achieved by ensuring that, for all given ω, the quantity $p^{(\omega)}_{\omega'}q^{(\omega)}_{\omega'}$ should be constant in ω', for all $\omega' \neq \omega$. By imposing the normalization condition it then follows that such constant must coincide with the function $K(\omega)$ defined in Eq. (3.29), i.e. $p^{(\omega)}_{\omega'}q^{(\omega)}_{\omega'} = K(\omega)$ which inserted into Eq. (3.48) yields

$$\frac{2}{\lambda_{\min}(\omega)\Delta t} \leq Q(\omega)K(\omega) \Longleftrightarrow \Delta t \geq \frac{2}{\lambda_{\min}(\omega)Q(\omega)K(\omega)} \tag{3.49}$$

that, upon maximization over ω, finally leads to Eq. (3.26).

[2] In this regard, notice that, for fixed ω, searching the best distribution $\{p^{\omega}_{\omega'}\}_{\omega'}$ for the right-hand side of Eq. (3.48), means finding the solution of the problem

$$\max_{\{p^{\omega}_{\omega'}\}_{\omega'}} \left\{ \min_{\omega':\omega'\neq\omega} \left[Q(\omega)p^{(\omega)}_{\omega'}q^{(\omega)}_{\omega'} \right] \right\} .$$

Suppose the best distribution $\{\bar{p}^{(\omega)}_{\omega'}\}_{\omega'}$ is such that $\bar{p}^{(\omega)}_{\omega'} \neq K(\omega)/q^{(\omega)}_{\omega'}$, implying that there exist an $\bar{\omega}'$ (as usual $\neq \omega$) such that $\bar{p}^{(\omega)}_{\bar{\omega}'}q^{(\omega)}_{\bar{\omega}'} > K(\omega)$. Consequently, for the normalization condition of $\{\bar{p}^{(\omega)}_{\omega'}\}_{\omega'}$ to be preserved, there must exist (at least) another $\bar{\bar{\omega}}'$, such that $\bar{p}^{(\omega)}_{\bar{\bar{\omega}}'}q^{(\omega)}_{\bar{\bar{\omega}}'} < K(\omega)$, that is, in turn, the one selected by the minimum over ω'. We then arrive to the contradiction we were looking for.

3.1.4 Non-commuting generator components

As previously emphasized, the $\Delta t \to \infty$ limit goes under the name of *secular approximation* and it is the last step one typically enforces in order to recover the GKSL form of the generator (Breuer et al. 2002). This is a rather drastic approximation, which forces structural constraints on the resulting master equation. Specifically, from (3.14) it follows that under the secular approximation also the matrix $\eta_{ij}^{(\Delta t)}$ gets block diagonal with respect to the gap indexes ω and ω',

$$\eta_{ij}^{(\infty)} \;:=\; \lim_{\Delta t\to\infty} \eta_{ij}^{(\Delta t)} = \frac{\gamma^{(-)}_{\alpha\omega,\beta\omega}}{2i}\,\delta_{\omega,\omega'}\;, \tag{3.50}$$

yielding the following properties:

(i) Commutation between the Lamb shift Hamiltonian operator $H_{\rm LS}^{(\infty)}$ and the free Hamiltonian operator $H_{\rm S}$;

(ii) Commutation between the free Hamiltonian, $\mathcal{H}_{\rm S}$, and the dissipative, $\mathcal{D}^{(\infty)}$, super-operator components of the generator;

(iii) In reliable situations, commutation between the full Hamiltonian super-operator $\mathcal{H}_{\rm S}^{(\infty)}$ and $\mathcal{D}^{(\infty)}$.

Property (i) can be easily verified by expanding the indexes i, j appearing in Eq. (3.12) and using the identities

$$H_{\rm S}\pi_\epsilon = \pi_\epsilon H_{\rm S} = \epsilon\pi_\epsilon\;. \tag{3.51}$$

Accordingly, we get

$$\left[H_{\rm S}, H_{\rm LS}^{(\Delta t)}\right]_- = \sum_{\alpha\beta\omega\omega'} (\omega-\omega')\;\eta^{(\Delta t)}_{\alpha\omega,\beta\omega'} \sum_\epsilon \pi_{\epsilon+\omega}A_\alpha\pi_\epsilon A_\beta\pi_{\epsilon+\omega'}\;, \tag{3.52}$$

which in the secular limit, where Eq. (3.50) forces $\eta^{(\Delta t)}_{\alpha\omega,\beta\omega'}$ to be proportional to the Kronecker delta $\delta_{\omega,\omega'}$, gets explicitly null:

$$\lim_{\Delta t\to\infty}\left[H_{\rm S}, H_{\rm LS}^{(\Delta t)}\right]_- = \left[H_{\rm S}, H_{\rm LS}^{(\infty)}\right]_- = 0\;. \tag{3.53}$$

To properly express property (ii), let us rewrite the right-hand side of Eq. (3.10) in the formal compact way

$$\mathcal{L}^{(\Delta t)}[\rho_{\rm S}(t)] := \mathcal{H}^{(\Delta t)}[\rho_{\rm S}(t)] + \mathcal{D}^{(\Delta t)}[\rho_{\rm S}(t)]\;, \tag{3.54}$$

where $\mathcal{H}_{\rm S}^{(\Delta t)} := \mathcal{H}_{\rm S} + \mathcal{H}_{\rm LS}^{(\Delta t)}$ and $\mathcal{D}^{(\Delta t)}$ represent the Hamiltonian and dissipative contributions to the super-operator $\mathcal{L}^{(\Delta t)}$ generating the dynamics, namely:

$$\mathcal{H}_{\rm S}[\cdots] := -i\Big[H_{\rm S}, \cdots\Big]_- , \tag{3.55}$$

$$\mathcal{H}_{\rm LS}^{(\Delta t)}[\cdots] := -i\Big[H_{\rm LS}^{(\Delta t)}, \cdots\Big]_- , \tag{3.56}$$

$$\mathcal{D}^{(\Delta t)}[\cdots] := \sum_{ij} \gamma_{ij}^{(\Delta t)} \Big(A_j^\dagger \cdots A_i - \frac{1}{2}\Big[A_i A_j^\dagger, \cdots\Big]_+ \Big) . \tag{3.57}$$

The commutator between $\mathcal{H}_{\rm S}$ and $\mathcal{D}^{(\infty)}$ is zero, i.e.

$$\big[\mathcal{H}_{\rm S}, \mathcal{D}^{(\infty)}\big]_- := \mathcal{H}_{\rm S} \circ \mathcal{D}^{(\infty)} - \mathcal{D}^{(\infty)} \circ \mathcal{H}_{\rm S} = 0 , \tag{3.58}$$

with "$\circ$" being the composition of super-operators:

$$A \circ B[\cdots] := A[B[\cdots]] . \tag{3.59}$$

Eq. (3.58) can be proven by inspection, exploiting that, by construction, the operators $A_{\alpha\omega}$ are eigen-operators of $\mathcal{H}_{\rm S}$, i.e. (Breuer et al. 2002)

$$i\, \mathcal{H}_{\rm S}[A_{\alpha\omega}] = [H_{\rm S}, A_{\alpha\omega}]_- = \omega A_{\alpha\omega} . \tag{3.60}$$

In reliable situations, commutation between the (full) Hamiltonian and the dissipator is also achieved in the secular limit:

$$\Big[\mathcal{H}_{\rm S}^{(\infty)}, \mathcal{D}^{(\infty)}\Big]_- = 0 . \tag{3.61}$$

Remarkably, as we shall see explicitly in the next Sections, going beyond the secular approximation by working with finite values of the coarse graining time Δt, in general one has

$$\Big[H_{\rm S}, H_{\rm LS}^{(\Delta t)}\Big]_- \neq 0 , \tag{3.62}$$

and

$$\big[\mathcal{H}_{\rm S}, \mathcal{D}^{(\Delta t)}\big]_- \neq 0 . \tag{3.63}$$

Furthermore, when Eq. (3.61) is satisfied, the breaking of commutation rules in Eqs. (3.62) and (3.63) can induce non-commutation also between $\mathcal{H}_{\rm S}^{(\Delta t)}$ and $\mathcal{D}^{(\Delta t)}$, i.e.

$$\Big[\mathcal{H}_{\rm S}^{(\Delta t)}, \mathcal{D}^{(\Delta t)}\Big]_- \neq 0 . \tag{3.64}$$

Having strong implications on the spectral properties of the generator, Eqs. (3.62)-(3.64) can imply dramatic consequences on the steady state of the system, which can show deviations from the Gibbsian state asymptotic limit predicted by conventional secular treatment of the Redfield equation, as well as non-trivial transient dynamics. An example of the breaking of commutation rules described by Eqs. (3.63) and (3.64) will be presented in Sec. 3.2 [cfr. Eq. (3.100)], while deviations from the Gibbsian state in the long time limit and an example for Eq. (3.62) will be shown in Sec. 3.3 in the context of multipartite open quantum systems [cfr. Eq. (3.149) and Fig. 3.9].

3.2 Tightly recovering complete positivity: an example

3.2.1 The model: dipole-like interaction

The methods of the previous sections can be applied in the case of a single qubit coupled to a bosonic thermal bath at temperature $1/\beta$ via dipole-like interaction, describing the well known spin-boson model (Leggett et al. 1987). In this case, when using the Redfield approach, the presence of counter-rotating terms in the interaction Hamiltonian originates non-positive behaviors. The Hamiltonian components of Eq. (2.6) now read as follows

$$H_{\rm S} = \omega_0 \sigma_+ \sigma_- \,, \tag{3.65}$$

$$H_{\rm E} = \sum_k \omega_k c_k^\dagger c_k \,, \tag{3.66}$$

$$H_1 = \sum_k \gamma_k (c_k^\dagger + c_k)(\sigma_- + \sigma_+) \,, \tag{3.67}$$

where we assumed $\omega_0,\ \omega_k,\ \gamma_k \geq 0$.
Equations (3.65) and (3.66) account for the free Hamiltonians of the system and environment, respectively, and Eq. (3.67) is the system-environment interaction which contains both excitation-number-conserving terms, $c_k\sigma_+$, $c_k^\dagger\sigma_-$, and counter-rotating terms, $c_k\sigma_-$, $c_k^\dagger\sigma_+$. The ladder operators of the system $\sigma_- = |0\rangle\langle 1|$ and $\sigma_+ = |1\rangle\langle 0|$ and the ones of the bosonic environment c_k and $c_k^\dagger$ satisfy the following commutation rules:

$$\sigma_-\sigma_+ + \sigma_+\sigma_- = \mathbb{1}_2 \tag{3.68}$$

$$c_k c_{k'}^\dagger - c_{k'}^\dagger c_k = \delta_{k,k'} \tag{3.69}$$

$$c_k c_{k'} - c_{k'} c_k = 0 \,. \tag{3.70}$$

In the framework set by Eqs. (3.65)–(3.70), the Redfield ME in interaction picture of Eq. (2.19) reduces to

$$\dot{\tilde{\rho}}_{\rm S}(t) = \int_0^\infty d\tau\ c(\tau)[\tilde{A}(t-\tau)\tilde{\rho}_{\rm S}(t)\tilde{A}(t) - \tilde{A}(t)\tilde{A}(t-\tau)\tilde{\rho}_{\rm S}(t)] + h.c. \,, \tag{3.71}$$

where, at variance with (2.19), the index α does not appear because the interaction in Eq. (3.67) is a single tensor product ($M = 1$) of two hermitian operators A and B, the first on the system and the second on the bath, that read as

$$A = \sigma_- + \sigma_+, \qquad B = \sum_k \gamma_k (c_k + c_k^\dagger) \,. \tag{3.72}$$

This leads to a single bath correlation function (see Eq. (2.17))

$$c(\tau) := \left\langle \tilde{B}(\tau) B \right\rangle = c_1(\tau) + c_2(\tau)\,, \text{ with} \tag{3.73}$$

$$c_1(\tau) = \sum_k \gamma_k^2 \mathcal{N}_b(\omega_k) e^{i\omega_k \tau}\,, \tag{3.74}$$

$$c_2(\tau) = \sum_k \gamma_k^2 [\mathcal{N}_b(\omega_k) + 1] e^{-i\omega_k \tau}\,, \tag{3.75}$$

with $\mathcal{N}_b(\omega_k) := \langle c_k^\dagger c_k \rangle$ being the occupation number at wave vector k, following the Bose-Einstein distribution

$$\mathcal{N}_b(\omega_k) = \frac{1}{e^{\beta\omega_k} - 1}\,. \tag{3.76}$$

The expression of the system operator A in interaction picture,

$$\tilde{A}(t) = \sigma_- e^{-i\omega_0 t} + \sigma_+ e^{i\omega_0 t}, \tag{3.77}$$

makes explicit its eigenstate representation:

$$A = \sum_{\omega \in \{-\omega_0, \omega_0\}} A_\omega, \text{ with} \tag{3.78}$$

$$A_{-\omega_0} = \sigma_- \text{ and } A_{\omega_0} = \sigma_+ \tag{3.79}$$

and also the value of $G = 2$ in this particular example.
Once performed coarse-grain averaging on the Redfield equation in interaction picture (3.71), we obtain the following master equation in the Shrödinger picture:

$$\dot{\rho}_{\rm S}(t) = -i \left[H_{\rm S} + H_{\rm LS}^{(\Delta t)}\,,\, \rho_{\rm S}(t) \right]_- + \tag{3.80}$$

$$\sum_{\omega\omega'} \gamma_{\omega\omega'}^{(\Delta t)} \left\{ A_{\omega'}^\dagger \rho_{\rm S}(t) A_\omega - \frac{1}{2} \left[A_\omega A_{\omega'}^\dagger\,,\, \rho_{\rm S}(t) \right]_+ \right\}\,,$$

$$H_{\rm LS}^{(\Delta t)} = \sum_{\omega\omega'} \eta_{\omega\omega'}^{(\Delta t)} A_\omega A_{\omega'}^\dagger\,, \tag{3.81}$$

where, indicating for brevity the subscripts $\pm\omega_0$ as $\pm$ and introducing the system decay rate function

$$\kappa(\epsilon) = 2\pi \sum_k \delta(\omega_k - \epsilon) \gamma_k^2\,, \tag{3.82}$$

the secular components of the dissipation and Lamb shift matrices read as

$$\gamma_{--} = \kappa(\omega_0)\mathcal{N}_b(\omega_0)\,, \tag{3.83}$$

$$\gamma_{++} = \kappa(\omega_0)[1+\mathcal{N}_b(\omega_0)]\,, \tag{3.84}$$

$$\eta_{--} = \frac{1}{2\pi}\fint_0^\infty d\epsilon\,\kappa(\epsilon)\left[\frac{\mathcal{N}_b(\epsilon)}{-\omega_0+\epsilon}+\frac{1+\mathcal{N}_b(\epsilon)}{-\omega_0-\epsilon}\right], \tag{3.85}$$

$$\eta_{++} = \frac{1}{2\pi}\fint_0^\infty d\epsilon\,\kappa(\epsilon)\left[\frac{\mathcal{N}_b(\epsilon)}{\omega_0+\epsilon}+\frac{1+\mathcal{N}_b(\epsilon)}{\omega_0-\epsilon}\right], \tag{3.86}$$

which, explicitly, do not depend upon Δt. The non-secular entries are instead

$$\gamma_{-+}^{(\Delta t)} = \gamma_{+-}^{(\Delta t)*} \tag{3.87}$$
$$= \left[\frac{\gamma_{++}+\gamma_{--}}{2}+i(\eta_{++}-\eta_{--})\right]\mathrm{sinc}(\omega_0\Delta t)\,,$$

$$\eta_{-+}^{(\Delta t)} = \eta_{+-}^{(\Delta t)*} \tag{3.88}$$
$$= \left[\frac{\eta_{++}+\eta_{--}}{2}+\frac{1}{4i}(\gamma_{++}-\gamma_{--})\right]\mathrm{sinc}(\omega_0\Delta t)\,,$$

that we conveniently expressed in terms of the secular ones.
Using the relations (3.79) and the fact that $\sigma_\pm^2 = 0$, Eqs. (3.80) and (3.81) can be rewritten as

$$\dot\rho_{\rm S}(t) = -i\left[H_{\rm S}+H_{\rm LS}^{(\Delta t)}\,,\,\rho_{\rm S}(t)\right]_- + \tag{3.89}$$
$$\gamma_{--}\left(\sigma_+\rho_{\rm S}(t)\sigma_- - \frac{1}{2}\left[\sigma_-\sigma_+\,,\,\rho_{\rm S}(t)\right]_+\right)+\gamma_{++}\left(\sigma_-\rho_{\rm S}(t)\sigma_+ - \frac{1}{2}\left[\sigma_+\sigma_-\,,\,\rho_{\rm S}(t)\right]_+\right)$$
$$+\gamma_{-+}^{(\Delta t)}\sigma_-\rho_{\rm S}(t)\sigma_- + \gamma_{+-}^{(\Delta t)}\sigma_+\rho_{\rm S}(t)\sigma_+$$

and

$$H_{\rm S}+H_{\rm LS}^{(\Delta t)} = \bar\omega\,\sigma_+\sigma_-\,,\quad \text{where}\quad \bar\omega := \omega_0+\eta_{++}-\eta_{--}\,. \tag{3.90}$$

In particular, notice that, because $\sigma_\pm^2 = 0$, the Hamiltonian of the system is modified just by a change of the two level spacing that is independent of Δt and the anti-commutator terms in the non-secular part of the dissipator nullify.

3.2.2 Dynamics

To study the pathology of the Redfield ME, the most informative dynamics we can choose concerns the local application of the channel described by Eq. (3.89) on the qubit system $\mathcal{S}$ when it is initially entangled to an additional (ancillary) qubit $\mathcal{A}$. In this case the positivity of the joint state $\rho_{\mathrm{SA}}(t)$ (Choi state) will encode information on the complete positivity of the channel [3]. Furthermore, notice that, by doing so, we re-propose the construction of Eq. (2.4) with a particular choice of the input state.

To begin, let us observe that the right-hand side of Eq. (3.89) concerns the action of a time independent generator $\mathcal{L}^{(\Delta t)}$ (which depends on the coarse grain parameter) on the system state at time t. Hence, let us rewrite Eq. (3.89) as

$$\dot{\rho}_{\mathrm{S}}(t) = \mathcal{L}^{(\Delta t)}\rho_{\mathrm{S}}(t) \,, \tag{3.91}$$

which defines the channel $\Phi_t^{(\Delta t)}$ mapping the state of the system from time 0 to time t :

$$\rho_{\mathrm{S}}(t) = \Phi_t^{(\Delta t)}\rho_{\mathrm{S}}(0) \,, \quad \Phi_t^{(\Delta t)} = e^{t\mathcal{L}^{(\Delta t)}} \,. \tag{3.92}$$

By applying the channel locally on $\mathcal{S}$, we get

$$\rho_{\mathrm{SA}}(t) := (\{\Phi_t^{(\Delta t)}\}_{\mathrm{S}} \otimes I_{\mathrm{A}})\,(\rho_{\mathrm{SA}}(0)) \,, \tag{3.93}$$

where the initial state

$$\rho_{\mathrm{SA}}(0) = |\psi\rangle\langle\psi|_{\mathrm{SA}} \,, \quad |\psi\rangle_{\mathrm{SA}} := \frac{1}{\sqrt{2}}(|00\rangle_{\mathrm{SA}} + |11\rangle_{\mathrm{SA}}) \tag{3.94}$$

is a maximally entangled state. Hence, once represented in the basis ($|11\rangle_{\mathrm{SA}}$, $|01\rangle_{\mathrm{SA}}$, $|10\rangle_{\mathrm{SA}}$, $|00\rangle_{\mathrm{SA}}$), $\rho_{\mathrm{SA}}(t)$ is a 4×4-matrix having the following block form:

$$\rho_{\mathrm{SA}}(t) = \frac{1}{2}\begin{pmatrix} \Phi_t^{(\Delta t)}(|1\rangle\langle 1|) & \Phi_t^{(\Delta t)}(|1\rangle\langle 0|) \\ \Phi_t^{(\Delta t)}(|0\rangle\langle 1|) & \Phi_t^{(\Delta t)}(|0\rangle\langle 0|) \end{pmatrix} \,, \tag{3.95}$$

with $\Phi_t^{(\Delta t)}(|i\rangle\langle j|)$ being the 2×2-matrix calculated as the solution of the ME

$$\frac{d}{dt}\left[\Phi_t^{(\Delta t)}(|i\rangle\langle j|)\right] = \mathcal{L}^{(\Delta t)}\left[\Phi_t^{(\Delta t)}(|i\rangle\langle j|)\right] \,, \tag{3.96}$$

under the initial condition $\Phi_{t=0}^{(\Delta t)}(|i\rangle\langle j|) = |i\rangle\langle j|$. [4]

[3] More deeply, the state $\rho_{\mathrm{SA}}(t)$ is in one-to-one correspondence with the channel $\Phi_t^{(\Delta t)}$, formally introduced in Eq. (3.92): Choi-Jamiołkowski isomorphism (Choi 1972, Jamiołkowski 1972, Holevo 2012).

[4] Notice that these initial conditions, as well as $\Phi_t^{(\Delta t)}(|i\rangle\langle j|)$, have not to be interpreted as states

Finally, the occurrence of negative eigenvalues of $\rho_{\rm SA}(t)$ encodes the non-complete positivity of the map $\Phi_t^{(\Delta t)}$, namely of the coarse-grained Redfield ME (3.89).

3.2.2.1 Commutation properties and asymptotic state

To study the asymptotic state it is convenient to find a representation of the generator $\mathcal{L}^{(\Delta t)} = \mathcal{H}_{\rm S}^{(\Delta t)} + \mathcal{D}^{(\Delta t)}$. We hence vectorize the operator basis

$$|1\rangle\langle 1| \to ||1\rangle\rangle\,,\ \ |0\rangle\langle 0| \to ||2\rangle\rangle\,,\ \ |1\rangle\langle 0| \to ||3\rangle\rangle\,,\ \ |0\rangle\langle 1| \to ||4\rangle\rangle\,, \tag{3.97}$$

finding the following representations for the components of the generator:

$$\mathcal{H}_{\rm S}^{(\Delta t)} \equiv -i\bar{\omega}\begin{pmatrix} 0 & 0 & 0 & 0 \\ 0 & 0 & 0 & 0 \\ 0 & 0 & 1 & 0 \\ 0 & 0 & 0 & -1 \end{pmatrix}\,, \tag{3.98}$$

$$\mathcal{D}^{(\Delta t)} \equiv \begin{pmatrix} -\gamma_{++} & \gamma_{--} & 0 & 0 \\ \gamma_{++} & -\gamma_{--} & 0 & 0 \\ 0 & 0 & -\frac{1}{2}(\gamma_{++}+\gamma_{--}) & \gamma_{+-}^{(\Delta t)} \\ 0 & 0 & \gamma_{-+}^{(\Delta t)} & -\frac{1}{2}(\gamma_{++}+\gamma_{--}) \end{pmatrix}\,. \tag{3.99}$$

We notice that, in general, the two matrices do not commute,

$$\left[\mathcal{D}^{(\Delta t)}, \mathcal{H}_{\rm S}^{(\Delta t)}\right]_- \equiv -2i\bar{\omega}\begin{pmatrix} 0 & 0 & 0 & 0 \\ 0 & 0 & 0 & 0 \\ 0 & 0 & 0 & -\gamma_{+-}^{(\Delta t)} \\ 0 & 0 & \gamma_{-+}^{(\Delta t)} & 0 \end{pmatrix}\,, \tag{3.100}$$

thus providing an example for the general statement (3.64) (commutation is achieved in the secular limit $\Delta t \to \infty$). However, for the selected model, both the matrices (3.98) and (3.99) have $(\gamma_{--}, \gamma_{++}, 0, 0)^T$ as eigenvector with eigenvalue 0. Such eigenvector is proportional to the vectorization of the Gibbsian state of Hamiltonian $H_{\rm S}$ and temperature $1/\beta$, the fixed point of the dynamics induced by the map $\Phi_t^{(\Delta t)}$.

The structure of the generator hence implies the following asymptotic expression for the state (3.95):

$$\rho_{\rm SA}(\infty) = \frac{1}{2}\begin{pmatrix} \rho_\beta & \mathbf{0} \\ \mathbf{0} & \rho_\beta \end{pmatrix} = \left\{\rho_\beta\right\}_{\rm S} \otimes \left\{\frac{\mathbb{1}_2}{2}\right\}_{\rm A}\,, \tag{3.101}$$

($|1\rangle\langle 0|$ and $|0\rangle\langle 1|$ are trace-less and non-hermitian), but, consistently, the construction ensures that $\rho_{\rm SA}(t)$ is a proper joint state.

with ρ_β being the Gibbsian state of the qubit at temperature $1/\beta$:

$$\rho_\beta = \begin{pmatrix} \mathcal{N}_f(\omega_0) & 0 \\ 0 & 1-\mathcal{N}_f(\omega_0) \end{pmatrix} , \tag{3.102}$$

$$\mathcal{N}_f(\omega_0) := \frac{1}{e^{\beta\omega_0}+1} . \tag{3.103}$$

As a consequence, for $t \to \infty$ we expect two eigenvalues to converge to the value $\frac{\mathcal{N}_f(\omega_0)}{2}$ and the remaining two eigenvalues to converge to the value $\frac{1-\mathcal{N}_f(\omega_0)}{2}$. In formulas, calling $\lambda_1^{(\Delta t)}(t)$, $\lambda_2^{(\Delta t)}(t)$, $\lambda_3^{(\Delta t)}(t)$, $\lambda_4^{(\Delta t)}(t)$ the four eigenvalues of $\rho_{\rm SA}(t)$, we have that

$$\lambda_1^{(\Delta t)}(t), \lambda_3^{(\Delta t)}(t) \to \frac{\mathcal{N}_f(\omega_0)}{2} , \tag{3.104}$$

$$\lambda_2^{(\Delta t)}(t), \lambda_4^{(\Delta t)}(t) \to \frac{1-\mathcal{N}_f(\omega_0)}{2} , \quad \text{for } t \to \infty . \tag{3.105}$$

Being the quantities on the right-hand sides of the equations above all non-negative, we infer that problems concerning the loss of complete positivity do not arise in the long time limit, i.e. $\Phi_\infty^{(\Delta t)}$ is completely positive for any Δt.

3.2.2.2 Transient evolution

According to the analysis of Sec. 3.1.2 we can ensure that the master Eq. (3.89) will describe a completely positive map provided that the matrix

$$\gamma^{(\Delta t)} \equiv \begin{pmatrix} \gamma_{--} & \gamma_{-+}^{(\Delta t)} \\ \gamma_{+-}^{(\Delta t)} & \gamma_{++} \end{pmatrix} \tag{3.106}$$

is positive semidefinite, i.e. whenever its two eigenvalues

$$\gamma_\mp^{(\Delta t)} := \frac{1}{2}\left(\gamma_{++}+\gamma_{--} \mp \sqrt{(\gamma_{++}-\gamma_{--})^2 + 4|\gamma_{-+}^{(\Delta t)}|^2}\right) , \tag{3.107}$$

are both non-negative (cfr. Eq. (3.20)) or, equivalently, when

$$\det\left[\gamma^{(\Delta t)}\right] := \gamma_{++}\gamma_{--} - |\gamma_{+-}^{(\Delta t)}|^2 \geq 0 , \tag{3.108}$$

where we used the fact that by construction $\gamma_+^{(\Delta t)} \geq 0$ always. In the secular approximation limit, where $\mathrm{sinc}^2(\omega_0\Delta t)$ approaches zero, $\gamma_\mp^{(\Delta t)}$ reduce to γ_{--} and γ_{++} and the complete positivity is guaranteed (the off-diagonal terms of the matrix $\gamma^{(\Delta t)}$ nullify). More generally, Eq. (3.108) leads to the following necessary and sufficient condition

for the coarse graining time Δt to define a completely positive channel:

$$|\mathrm{sinc}(\omega_0\Delta t)| \leq \sqrt{\frac{4\kappa(\omega_0)^2\mathcal{N}_b(\omega_0)(1+\mathcal{N}_b(\omega_0))}{\kappa(\omega_0)^2[2\mathcal{N}_b(\omega_0)+1]^2+4[\frac{\omega_0}{\pi}\int_0^\infty d\epsilon\,\kappa(\epsilon)\frac{1+2\mathcal{N}_b(\epsilon)}{\epsilon^2-\omega_0^2}]^2}} := |\mathrm{sinc}(\omega_0\Delta t_c)|\,. \tag{3.109}$$

To see this in the dynamics, in Fig. 3.1 we plot the four eigenvalues of $\rho_{\rm SA}(t)$ as function of time, for different values of Δt, and choosing as decay rate function (3.82) the expression

$$\kappa(\epsilon) = \kappa_0\epsilon\exp(-\epsilon/\omega_c)\,, \tag{3.110}$$

which behaves Ohmically for small energies, $\kappa(\epsilon)\propto\epsilon$ for $\epsilon\ll\omega_c$, and decays exponentially for $\epsilon\gg\omega_c$, where $\omega_c\geq\omega_0$ is a cutoff energy [5]. Non-CP manifests at short timescales as soon as the threshold value of Eq. (3.109) is overcome. This can be understood by looking at the analytic expression of the eigenvalue $\lambda_3^{(\Delta t)}(t)$ corresponding to the black full lines in Fig. 3.1:

$$\lambda_3^{(\Delta t)}(t) = \frac{1}{4}\left[1-e^{-st}-\frac{\sqrt{2}}{s\bar\omega_{\Delta t}}e^{-st/2}\sqrt{d^2\bar\omega_{\Delta t}^2\left(\cosh(st)-1\right)-|\gamma_{-+}^{(\Delta t)}|^2s^2\left(\cos(2\bar\omega_{\Delta t}t)-1\right)}\right]\,, \tag{3.111}$$

where, for space reasons, we defined the quantities

$$s := \gamma_{++}+\gamma_{--} = \kappa(\omega_0)(2\mathcal{N}_b(\omega_0)+1)\,,\qquad d := \gamma_{++}-\gamma_{--} = \kappa(\omega_0)\,,$$
$$\bar\omega_{\Delta t} := \sqrt{\bar\omega^2-|\gamma_{-+}^{(\Delta t)}|^2}\,. \tag{3.112}$$

Being

$$\lambda_3^{(\Delta t)}(0) = 0\,, \tag{3.113}$$
$$\dot\lambda_3^{(\Delta t)}(0) = \frac{1}{4}\left(s-\sqrt{d^2+4|\gamma_{-+}^{(\Delta t)}|^2}\right)\,, \tag{3.114}$$

we obtain that the first derivative $\dot\lambda_3^{(\Delta t)}(0)\gtrless 0$ when $|\gamma_{-+}^{(\Delta t)}|^2\lessgtr\gamma_{--}\gamma_{++}$ and hence, at short timescales,

$$\lambda_3^{(\Delta t)}(\delta t)\geq 0 \quad\Leftrightarrow\quad \Delta t\geq\Delta t_c\,. \tag{3.115}$$

It is worth noticing that the result (3.115) is independent of the $\mathcal{S}-\mathcal{E}$ interaction strength.

However, not only complete positivity, but also the less stringent positivity condition can be lost when not accomplishing the constraint (3.109). From the state (3.95) it

[5] We notice however that the particular choice made in (3.110) is not stringent.

is possible to calculate the evolution of any system density matrix $\rho_{\rm S}(0)$ (Choi 1972, Jamiołkowski 1972, Holevo 2012) through the identity

$$\rho_{\rm S}(t) = 2{\rm Tr}_{\rm A}\Big[(\{\mathbb{1}_2\}_{\rm S} \otimes \{\rho^T(0)\}_{\rm A})\rho_{\rm SA}(t)\Big] \,. \tag{3.116}$$

An equivalent strategy is to solve the equations

$$\begin{aligned} \frac{d}{dt}\rho_{\rm S00}(t) &= \gamma_{++}\left[1-\rho_{\rm S00}(t)\right] - \gamma_{--}\rho_{\rm S00}(t), \\ \frac{d}{dt}\rho_{\rm S10}(t) &= -i\bar{\omega}\rho_{\rm S10}(t) - \frac{1}{2}\left(\gamma_{++}+\gamma_{--}\right)\rho_{\rm S10}(t) + \gamma_{+-}^{(\Delta t)}\rho_{\rm S10}(t)^* \end{aligned} \tag{3.117}$$

under the same initial condition $\rho_{\rm S}(0)$. Both the two methods allow to show an example of non-positive semi-definite evolution: by considering as initial state the pure vector $|\psi(0)\rangle_{\rm S} := (|0\rangle + |1\rangle)/\sqrt{2}$, we obtain the following analytic expressions for the components of the density matrix $\rho_{\rm S}(t)$:

$$\begin{aligned} {\rm Re}[\rho_{\rm S10}](t) &= {\rm Re}[\rho_{\rm S01}](t) = \frac{1}{2}e^{-\frac{1}{2}st}\left(\frac{{\rm Re}\left[\gamma_{-+}^{(\Delta t)}\right]\sin(\bar{\omega}_{\Delta t}\,t)}{\bar{\omega}_{\Delta t}} + \cos\left(\bar{\omega}_{\Delta t}\,t\right)\right), & (3.118) \\ {\rm Im}[\rho_{\rm S10}](t) &= -{\rm Im}[\rho_{\rm S01}](t) = -\frac{1}{2}e^{-\frac{1}{2}st}\frac{\left({\rm Im}\left[\gamma_{-+}^{(\Delta t)}\right]+\bar{\omega}\right)\sin\left(\bar{\omega}_{\Delta t}\,t\right)}{\bar{\omega}_{\Delta t}}, & (3.119) \\ \rho_{\rm S00}(t) &= 1-\rho_{\rm S11}(t) = \frac{-de^{-st}+2\gamma_{++}}{2s}, & (3.120) \end{aligned}$$

with s, d and $\bar{\omega}_{\Delta t}$ as in (3.112). We plot the results in Fig. 3.2 for different values of Δt corresponding to the secular approximation (i.e. ${\rm sinc}(\omega_0\Delta t) = 0$); to the CP-Redfield ME (${\rm sinc}(\omega_0\Delta t) = {\rm sinc}(\omega_0\Delta t_c)$); and to the Redfield regime (i.e. ${\rm sinc}(\omega_0\Delta t) = 1$). Panels (a), (b) and (c) of the figure show that Redfield-like approaches, when compared to the secular approximation strategy, imply corrections on the off-diagonal terms of $\rho_{\rm S}(t)$ only, while leaving unchanged the diagonal ones and the steady state of the system (3.102). As evident from the plots, CP-Redfield somehow interpolates between the secular and the (uncorrected) Redfield behaviours. In Panel (d) of Fig. 3.2 it is instead plotted the determinant of $\rho_{\rm S}(t)$. For short timescales, Redfield implies non-positive evolution being ${\rm Det}[\rho_{\rm S}({\rm t})] < 0$, whilst positivity is maintained under secular and CP-Redfield approximations. However, with a sufficiently weak system-environment coupling strength κ_0, the positive semi-definiteness of the state $\rho_{\rm S}(t)$ predicted by the Redfield equation can be recovered, but not complete positivity, which, as we previously proved, is lost as soon as the critical condition of Eq. (3.109) is violated.

We finally observe that the positivity threshold $|{\rm sinc}(\omega_0\Delta t_c)|$ in the right-hand side of (3.109) depends on temperature. In Fig. 3.3 we compare such critical value with the value provided by the estimation (3.44), a sufficient positivity condition we derived in Sections 3.1.2 and 3.1.3 under general assumption on the system dynamics and which,

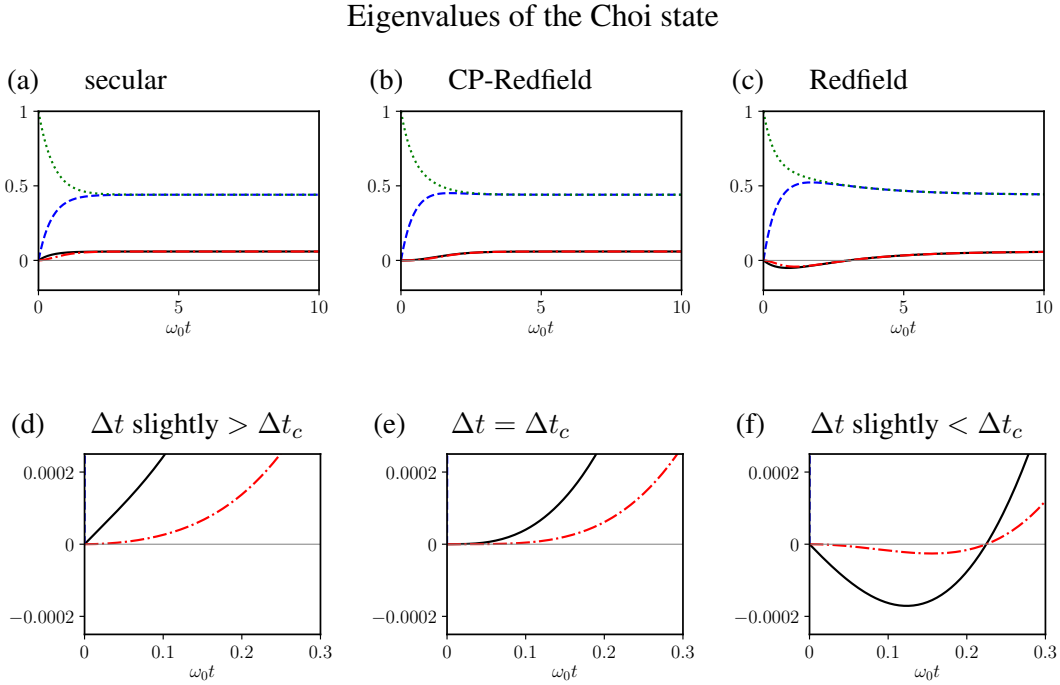

Fig. 3.1 Qubit interacting with a bosonic bath via dipole-like interaction. We plot the four eigenvalues $\lambda_1^{(\Delta t)}(t)$ (red dot-dashed lines), $\lambda_2^{(\Delta t)}(t)$ (blue dashed lines), $\lambda_3^{(\Delta t)}(t)$ (black full lines), $\lambda_4^{(\Delta t)}(t)$ (green dotted lines) of $\rho_{\rm SA}(t)$ defined in Eq. (3.95), as function of time (in units $1/\omega_0$). The Panels differ for the selected values of $\mathrm{sinc}(\omega_0 \Delta t)$. (a) $\mathrm{sinc}(\omega_0 \Delta t) = 0$, secular approximation ($\Delta t \to \infty$); (b) $\mathrm{sinc}(\omega_0 \Delta t) = 0.628$, CP-Redfield ($\Delta t = \Delta t_c$); (c) $\mathrm{sinc}(\omega_0 \Delta t) = 1$, Redfield ($\Delta t = 0$). We also report the results across the critical value to appreciate the crossover between CP and non-CP evolution: (d) $\mathrm{sinc}(\omega_0 \Delta t) = 0.621$, i.e. slightly below the critical value; (e) $\mathrm{sinc}(\omega_0 \Delta t) = 0.628$, i.e. at the critical value; (f) $\mathrm{sinc}(\omega_0 \Delta t) = 0.634$, i.e. slightly above the critical value. Notice the different axes scales in (d)-(f) with respect to (a)-(c). In all Panels, we choose the following values of the master equation parameters: $1/\beta = 0.5\omega_0$, $\kappa_0 = 2$, $\omega_c = 5\omega_0$.

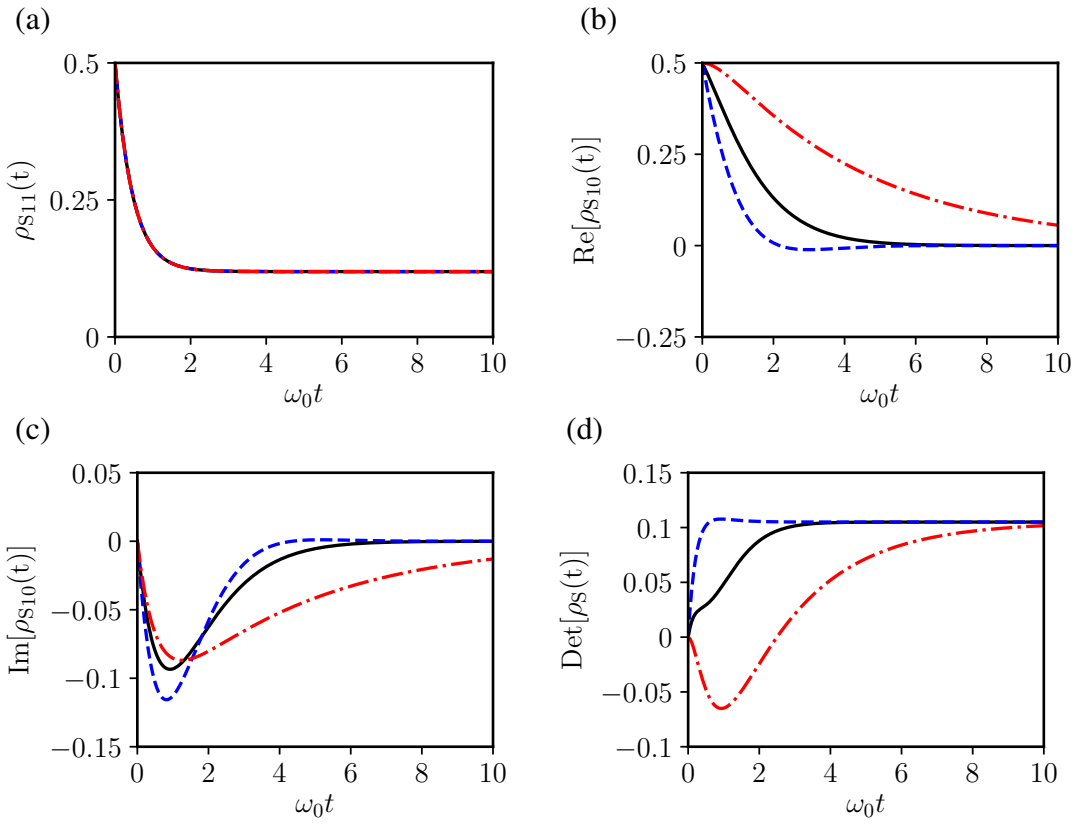

Fig. 3.2 Qubit interacting with a bosonic bath via dipole-like interaction. We plot $\rho_{S11}(t)$ (a), $\mathrm{Re}[\rho_{S10}(t)]$ (b), $\mathrm{Im}[\rho_{S10}(t)]$ (c) and $\mathrm{Det}[\rho_S(t)]$ (d), as function of time (in units $1/\omega_0$) considering as initial state the pure vector $|\psi(0)\rangle_S := (|0\rangle + |1\rangle)/\sqrt{2}$. We choose the following values of the master equation parameters: $1/\beta = 0.5\omega_0$, $\kappa_0 = 2$, $\omega_c = 5\omega_0$, see Eq. (3.110). In all the Panels the black full lines correspond to the results obtained using CP-Redfield ($\mathrm{sinc}(\omega_0\Delta t) = \mathrm{sinc}(\omega_0\Delta t_c) \approx 0.628$), the dash-dotted red lines using Redfield ($\mathrm{sinc}(\omega_0\Delta t) = 1$) and the blue dashed line using the secular approximation ($\mathrm{sinc}(\omega_0\Delta t) = 0$).

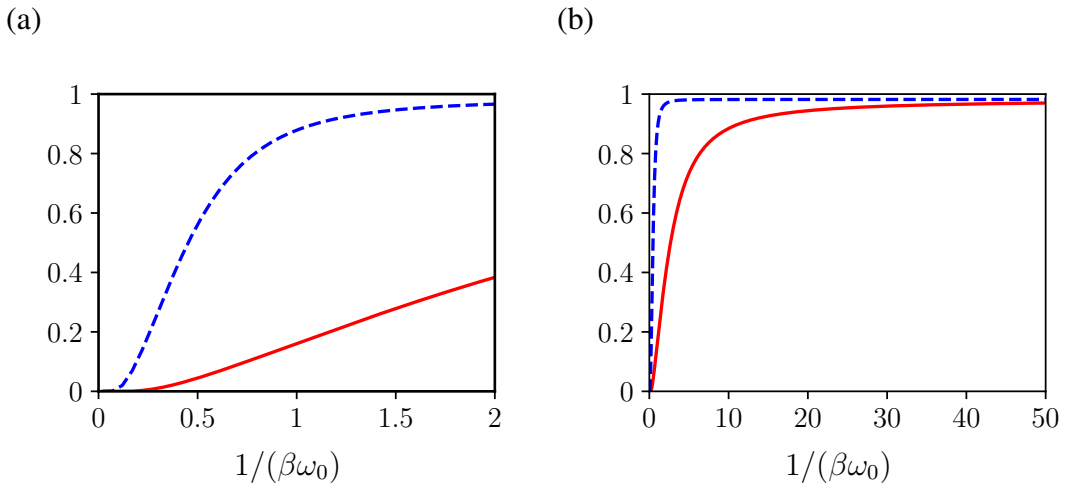

Fig. 3.3 Comparison between $|\mathrm{sinc}(\omega_0 \Delta t_c)|$ (blue dashed line), given by the right-hand side term of Eq. (3.109), and the right-hand side term of Eq. (3.121) (red full line) as function of temperature. (a) and (b) differ for the temperature range. The cutoff energy has been fixed at $\omega_c = 10\omega_0$ for all the curves.

for the example we study here, assumes the form

$$|\mathrm{sinc}(\omega_0 \Delta t)| \leq \frac{\kappa(\omega_0)\mathcal{N}_b(\omega_0)}{\sqrt{[\kappa(\omega_0)\mathcal{N}_b(\omega_0)/2]^2+\eta_{--}^2}+\sqrt{[\kappa(\omega_0)(1+\mathcal{N}_b(\omega_0))/2]^2+\eta_{++}^2}}\,, \tag{3.121}$$

From Fig. 3.3 we infer that the right-hand side of Eq. (3.121) underestimates the critical value $|\mathrm{sinc}(\omega_0 \Delta t_c)|$ at low temperatures and gives better results at high temperatures. More importantly, we deduce that at low temperature the full secular approximation ($\Delta t \to \infty$) is necessary for ensuring positivity, a general behaviour that does not depend upon the special form of the decay rate we choose for the plot. Indeed for $\beta \to \infty$ the right-hand side of Eq. (3.109) always nullifies forcing us to take $\Delta t \to \infty$ in order to satisfy the inequality. For non-zero temperature instead, finite values of Δt are admitted such that the associated master equation is well behaved.

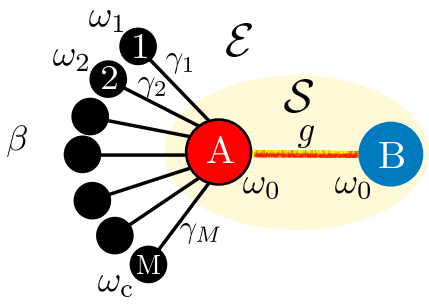

Fig. 3.4 Schematic of the model: the composite system $\mathcal{S}$ is formed of two harmonic oscillators A and B of equal frequency ω_0 which interact via an exchange Hamiltonian coupling characterized by the constant g. The subsystem A is also coupled with the modes $k \in \{1, 2, \dots M\}$ of a thermal environment $\mathcal{E}$ at temperature $1/\beta$ (again the interaction is mediated by an exchange Hamiltonian with constants γ_k).

3.3 Multipartite systems: going beyond local and global approaches

As a further application, the corrected Redfield equation turns out to be useful when the system is made of multiple components. Identifying which master equation is preferable for the description of a multipartite open quantum system is not trivial and has led in the recent years to the *local vs global* debate in the context of Markovian dissipation. In this Section, we treat a paradigmatic scenario in which the system is composed of two interacting harmonic oscillators A and B, with only A interacting with a thermal bath - collection of other harmonic oscillators - and we study the equilibration process of the system initially in the ground state with the bath finite temperature. We show that the completely positive version of the Redfield equation obtained using coarse-grain and an appropriate time-dependent convex mixture of the local and global solutions give rise to the most accurate approximations of the whole exact system dynamics, i.e. both at short and at long timescales, outperforming the local and global approaches.
The results are presented as follows. In Sec. 3.3.1 we introduce the model. The different approximations are described in Sec. 3.3.2. In Sec. 3.3.3 we integrate the dynamical evolution under the various approximations and present a comparison between the various results. In Sec. 3.4 we draw the conclusions and we discuss possible future developments. Details on the approximation methods and on the evaluation of the exact dynamics are finally reported in Sec. 3.3.4.

3.3.1 The model

The model we consider is schematically described in Fig. 3.4. It consists into a bipartite system $\mathcal{S}$ composed of two resonant bosonic modes A and B of frequency ω_0 and described by the ladder operators $a, a^\dagger$ and $b, b^\dagger$, that interact through an excitation preserving coupling characterized by an intensity parameter $g \geq 0$. Accordingly, setting

$\hbar = 1$, the free Hamiltonian of $\mathcal{S}$ reads

$$\begin{aligned} H_{\rm S} &:= H_{\rm S,0} + H_{\rm S,g} \ , \\ H_{\rm S,0} &:= \omega_{\rm A} a^\dagger a + \omega_{\rm B} b^\dagger b \ , \qquad \text{with} \qquad \omega_{\rm A} = \omega_{\rm B} := \omega_0 \ , \\ H_{\rm S,g} &:= g(a^\dagger b + \text{h.c.}) \ , \end{aligned} \tag{3.122}$$

which can also be conveniently expressed as

$$H_{\rm S} \ = \ \omega_+ \gamma_+^\dagger \gamma_+ + \omega_- \gamma_-^\dagger \gamma_- \ , \tag{3.123}$$

with

$$\omega_\pm \ := \ \omega_0 \pm g \ , \qquad \gamma_\pm := \frac{1}{\sqrt{2}}(a \pm b) \ , \tag{3.124}$$

being, respectively, the associated eigenmode frequencies and operators (Emary and Brandes 2003), the last obeying the commutation rules

$$\left[\gamma_-, \gamma_+\right]_- = \left[\gamma_-, \gamma_+^\dagger\right]_- = 0 \ , \ \left[\gamma_\pm, \gamma_\pm^\dagger\right]_- = 1 \ . \tag{3.125}$$

Through the exclusive mediation of subsystem A, we then assume $\mathcal{S}$ to be connected with an external environment $\mathcal{E}$ formed of a collection of a large number M of independent bosonic modes, no direct coupling being instead allowed between B and $\mathcal{E}$. Indicating with $c_k, c_k^\dagger$ the ladder operators of the k-th mode of $\mathcal{E}$, we hence express the full Hamiltonian of the joint system $\mathcal{S} + \mathcal{E}$ as

$$H := H_{\rm S} + H_{\rm E} + H_1 \ , \tag{3.126}$$

with

$$H_{\rm E} := \sum_{k=1}^{M} \omega_k c_k^\dagger c_k \ , \qquad H_1 := \sum_{k=1}^{M} \gamma_k (a^\dagger c_k + \text{h.c.}) \ , \tag{3.127}$$

being respectively the free Hamiltonian of the environment and the exchange coupling between A and $\mathcal{E}$. More in details, in our analysis we shall assume the frequencies ω_k of the environmental modes to be equally spaced with a cut-off value $\omega_c > \omega_0$, i.e.

$$\omega_k := \frac{k}{M}\omega_{\rm c} \ , \qquad\qquad k \in \{1, ..., M\} \ , \tag{3.128}$$

and take the system-environment coupling constants γ_k to have the form

$$\gamma_k := \sqrt{\kappa(\omega_0) \left(\frac{\omega_k}{\omega_0}\right)^\alpha \frac{\omega_c}{2\pi M}} \ , \tag{3.129}$$

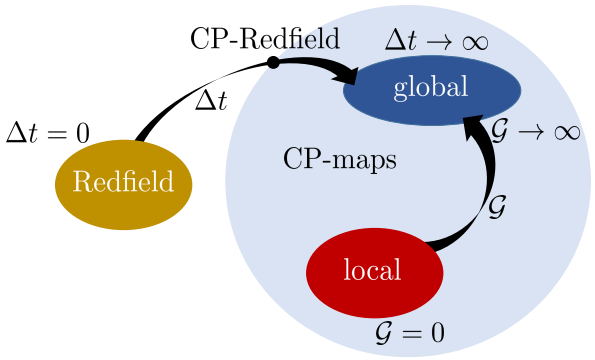

Fig. 3.5 Schematic representation of the continuous transitions from the Redfield ME to the global ME (3.146) passing through the coarse-grained Redfield MEs (3.134), and from the local ME (3.150) to the global ME using the time-dependent convex mixture (3.153). The dot indicates the completely positive map defined by the CP-Redfield ME obtained by saturating the bound in Eq. (3.144).

with $\kappa(\omega_0)$ controlling the effective strength of the interaction between A and $\mathcal{E}$. The parameter $\alpha \geq 0$ appearing in Eq. (3.129) gauges the bath's dispersion relation by imposing the following form for the (rescaled) spectral density of the reservoir modes (Hofer et al. 2017)

$$\kappa(\omega) := 2\pi \sum_{k=1}^{M} \gamma_k^2 \delta(\omega - \omega_k) = \kappa(\omega_0) \left(\frac{\omega}{\omega_0}\right)^{\alpha} \Theta(\omega_{\rm c} - \omega) \,, \tag{3.130}$$

with $\Theta(x)$ being the Heaviside step function ($\alpha = 1$, $\alpha > 1$ and $\alpha < 1$ being associated to the Ohmic, super-Ohmic, and sub-Ohmic scenarios respectively (Leggett et al. 1987)). Finally we shall assume the joint $\mathcal{S}+\mathcal{E}$ system to be initialized into a factorized state

$$\rho_{\rm SE}(0) = \rho_{\rm S}(0) \otimes \rho_{\rm E}(0) \,, \tag{3.131}$$

where the bath is in a thermal state of temperature $1/\beta > 0$:

$$\rho_{\rm E}(0) := \frac{e^{-\beta H_{\rm E}}}{{\rm tr}[e^{-\beta H_{\rm E}}]} = \rho_1(\beta) \otimes \cdots \otimes \rho_M(\beta) \,, \tag{3.132}$$

$$\rho_k(\beta) := \frac{e^{-\beta \omega_k c_k^\dagger c_k}}{{\rm tr}[e^{-\beta \omega_k c_k^\dagger c_k}]} \,. \tag{3.133}$$

3.3.2 Approximated equations for $\mathcal{S}$

In this section we review the different ME approaches one can use to effectively describe the evolution of the system $\mathcal{S}$ by integrating away the degrees of freedom of the

environment $\mathcal{E}$. We shall start our presentation by introducing the coarse-grained regularized version of the Redfield equation [Sec. 3.1 (Farina and Giovannetti 2019)], which includes the global ME as a special case. We then introduce the local ME approach and finally discuss the phenomenological approach which employs convex combinations of local and global ME solutions. Since most of the derivations of the above expressions are discussed in details elsewhere (see e.g. Breuer et al. (2002)) here we just give an overview of the methods involved and refer the interested reader to the Sec. 3.3.4.1 for further details.

3.3.2.1 From CP-Redfield ME to global ME

The starting point of this section is the Redfield equation which one obtains by expressing the dynamical evolution of the joint system in the interaction picture, and enforcing the Born and, then, the Markov approximations (see Sec. 2.1.2). As described in Sec. 2.1.2.1, the Born approximation assumes that the $\mathcal{S}-\mathcal{E}$ coupling is weak in such a way that the state of $\mathcal{E}$ is negligibly influenced by the presence of $\mathcal{S}$, while the Markov approximations assume invariance of the interaction-picture system state over time-scales of order $\tau_{\rm E}$, the last being the time over which $\mathcal{E}$ loses the information coming from $\mathcal{S}$ and can be estimated from the width of the bath correlation functions (see Sec. 3.3.4.4). As emphasized in Sec. 3.2, the Redfield equation does not ensure completely positive evolutions and in certain cases neither positive evolution, hence preventing one from framing the obtained results with the probabilistic interpretation of quantum mechanics. To cure this issue we refer to the version of the partial secular approximation described in Sec. 3.1 (Farina and Giovannetti 2019). Performing a coarse-grain averaging on the Redfield equation in interaction picture over a time interval Δt that is much larger than the typical time scale of the system state in interaction picture, is a way to appropriately smooth the non-secular terms responsible of the non-positive character, even in a tight way. As schematically pictured in Fig. 3.5, by moving the parameter Δt along the interval $[0,\infty[$ the reported technique is also capable to formally connect the original Redfield equation ($\Delta t=0$) and the full secular approximation ($\Delta t=\infty$) in a continuous way. Expressed in Schrödinger picture, the coarse-grained Redfield equation for the evolution of $\rho_{\rm S}$ for fixed coarse-graining time Δt, reads

$$\begin{aligned}\dot\rho_{\rm S}(t) = &-i\Big[H_{\rm S}+H_{\rm LS}^{(\Delta t)},\rho_{\rm S}(t)\Big]_- \\ &+\sum_{\sigma,\sigma'=\pm} S^{(\Delta t)}_{\sigma\sigma'}\Big\{\gamma^{(1)}_{\sigma\sigma'}\Big(\gamma^\dagger_\sigma\rho_{\rm S}(t)\gamma_{\sigma'}-\frac{1}{2}\Big[\gamma_{\sigma'}\gamma^\dagger_\sigma,\rho_{\rm S}(t)\Big]_+\Big) \\ &+\gamma^{(2)}_{\sigma'\sigma}\Big(\gamma_{\sigma'}\rho_{\rm S}(t)\gamma^\dagger_\sigma-\frac{1}{2}\Big[\gamma^\dagger_\sigma\gamma_{\sigma'},\rho_{\rm S}(t)\Big]_+\Big)\Big\},\end{aligned} \tag{3.134}$$

where hereafter we shall use the symbols $\left[\cdots,\cdots\right]_{\mp}$ to represent commutator and anti-commutator relations, $\gamma_{\pm}$ are the eigenmode operators of $H_{\rm S}$ introduced in Eq. (3.124) and

$$H_{\rm LS}^{(\Delta t)} := \sum_{\sigma,\sigma'=\pm} S_{\sigma\sigma'}^{(\Delta t)} (\eta_{\sigma\sigma'}^{(1)} + \eta_{\sigma'\sigma}^{(2)}) \gamma_{\sigma}^{\dagger} \gamma_{\sigma'} \; , \tag{3.135}$$

is the so called Lamb-shift Hamiltonian correction term. As indicated by the notation, the dependence of Eq. (3.134) upon the coarse-graining time interval Δt is carried out by the tensor $S_{\sigma\sigma'}^{(\Delta t)}$ of components

$$\begin{aligned} S_{\sigma\sigma'}^{(\Delta t)} &:= \mathrm{sinc}\left(\tfrac{(\sigma-\sigma')g\Delta t}{2}\right) \\ &= \delta_{\sigma\sigma'} + (1-\delta_{\sigma\sigma'})\,\mathrm{sinc}(g\Delta t) \; , \end{aligned} \tag{3.136}$$

with $\mathrm{sinc}(x) := \sin(x)/x$ being the cardinal sinus. The functional dependence of the right-hand-side of (3.134) upon the bath temperature is instead carried on by the tensors $\gamma_{\sigma\sigma'}^{(i)}$ and $\eta_{\sigma\sigma'}^{(i)}$. Specifically, for $\sigma,\sigma' \in \{+,-\}$ and $i \in \{1,2\}$, these elements fulfill the constraints

$$\gamma_{\sigma\sigma'}^{(i)} := \frac{\gamma_{\sigma\sigma}^{(i)} + \gamma_{\sigma'\sigma'}^{(i)}}{2} + i(\eta_{\sigma\sigma}^{(i)} - \eta_{\sigma'\sigma'}^{(i)}) \; , \tag{3.137}$$

$$\eta_{\sigma\sigma'}^{(i)} := -i\frac{\gamma_{\sigma\sigma}^{(i)} - \gamma_{\sigma'\sigma'}^{(i)}}{4} + \frac{\eta_{\sigma\sigma}^{(i)} + \eta_{\sigma'\sigma'}^{(i)}}{2} \; , \tag{3.138}$$

which allow one to express all of them in terms of their diagonal ($\sigma = \sigma'$) components

$$\gamma_{\sigma\sigma}^{(1)} := \frac{1}{2}\,\kappa(\omega_\sigma)\,\mathcal{N}_b(\omega_\sigma) \; , \tag{3.139}$$

$$\gamma_{\sigma\sigma}^{(2)} := \frac{1}{2}\,\kappa(\omega_\sigma)\,[1+\mathcal{N}_b(\omega_\sigma)] \; , \tag{3.140}$$

$$\eta_{\sigma\sigma}^{(1)} := \frac{1}{2}\fint_0^\infty d\epsilon\,\frac{1}{2\pi}\frac{\kappa(\epsilon)\mathcal{N}_b(\epsilon)}{\epsilon-\omega_\sigma} \; , \tag{3.141}$$

$$\eta_{\sigma\sigma}^{(2)} := -\frac{1}{2}\fint_0^\infty d\epsilon\,\frac{1}{2\pi}\frac{\kappa(\epsilon)[1+\mathcal{N}_b(\epsilon)]}{\epsilon-\omega_\sigma} \; , \tag{3.142}$$

with $\kappa(\omega)$ the spectral density of the reservoir defined in Eq. (3.130), the symbol $\fint$ meaning the principal value of the integral and with

$$\mathcal{N}_b(\omega_k) := \mathrm{Tr}[c_k^\dagger c_k \rho_k(\beta)] = \frac{1}{e^{\beta\omega_k}-1} \tag{3.143}$$

being the Bose-Einstein factor of the mode k of the thermal bath.

For $g\Delta t \to 0$, $S_{\sigma\sigma'}^{(\Delta t)}$ assumes constant value 1 for all σ and σ': this corresponds to the pathological case of the (uncorrected) Redfield equation in which both the diag-

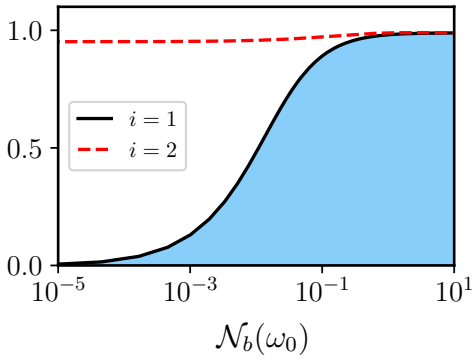

Fig. 3.6 Plot of the quantities in the right hand side of the inequality (3.144) for $i = 1$ (black full line) and $i = 2$ (red dashed line) as function of the bath temperature $1/\beta$ which we parametrize through $\mathcal{N}_b(\omega_0) = 1/(e^{\beta\omega_0} - 1)$. The blue region represents the values of $|S_{+-}^{(\Delta t)}|$ which satisfy the inequality (3.144) ensuring completely positive dynamics of the coarse-grained Redfield equation (3.134). We chose the parameters $g = 0.3\omega_0$, $\omega_c = 3\omega_0$, and $\alpha = 1$ (Ohmic spectral density regime). Notice the logarithmic scale on the abscissa.

onal (secular) and the off-diagonal (non-secular) σ, σ' terms of the right-hand-side of Eq. (3.134) contribute at the same level to the dynamical evolution of $\rho_{\rm S}(t)$ paving the way to unwanted non-positive effects. As $g\Delta t$ increases the off-diagonal component $S_{+-}^{(\Delta t)} = \mathrm{sinc}(g\Delta t)$ acts as the smoothing factor for the non-secular ($\sigma \neq \sigma'$) part of the ME, which gets progressively depressed as the coarse-grain time interval Δt gets comparable or even larger than the inverse of the energy scale g of the system. Following Sec. 3.1 (Farina and Giovannetti 2019), one can then show that the model admits a (finite) threshold value for Δt above which Eq. (3.134) acquires the explicit GKSL form that is necessary and sufficient to ensure complete positivity of the resulting evolution. Specifically, as discussed in details in Sec. 3.3.4.2, such threshold is triggered by the inequality

$$|S_{+-}^{(\Delta t)}| \leq \min_{i\in\{1,2\}} \sqrt{\frac{\gamma_{++}^{(i)}\gamma_{--}^{(i)}}{|\gamma_{+-}^{(i)}|^2}}\,. \tag{3.144}$$

In the following, the equation (3.134) at positivity threshold, i.e. with the choice of $S_{+-}^{(\Delta t)}$ tightly saturating the bound of Eq. (3.144), will be called CP-Redfield.

A numerical study of the condition (3.144) for some selected values of the system parameters is presented in Fig. 3.6. This plot makes it clear that the low temperature regime ($\mathcal{N}_b(\omega_0) \ll 1$) constraints one to take very small values of $|S_{+-}^{(\Delta t)}|$ to guarantee the completely positive character of the evolution (Farina and Giovannetti 2019), while just a tiny correction is needed at high temperatures (similarly to Fig. 3.3). These facts are in full agreement with the observation (Suárez et al. 1992, Cheng and Silbey 2005, Ishizaki and Fleming 2009) that the non-positivity character of the Redfield equation

is enhanced at low temperature as a signature of the deviations from the Born-Markov assumptions underlying it (Hartmann and Strunz 2020). We stress that, in this context, non-positivity is originated by the multipartite nature of $\mathcal{S}$: indeed, as $g \to 0$, the right-hand side of Eq. (3.144) tends to 1 and consequently the non-positivity of the Redfield ME disappears in this limit. Notice finally that irrespectively from the value of g, Eq. (3.144) is trivially fulfilled in the asymptotic $g\Delta t \to \infty$ limit where $|S_{+-}^{(\Delta t)}|$ approaches the value zero leading to

$$S_{\sigma\sigma'}^{(\infty)} = \delta_{\sigma\sigma'} \, . \tag{3.145}$$

This condition identifies the full secular approximation of Eq. (3.134) that transforms such equation into the global ME of the model which, for the sake of completeness, we report here in its explicit form

$$\begin{aligned} \dot{\rho}_{\rm S}(t) = &-i\Big[H_{\rm S} + H_{\rm LS}^{(\rm glob)}, \rho_{\rm S}(t)\Big]_- \\ &+ \sum_{\sigma=\pm} \Big\{ \frac{1}{2}\kappa(\omega_\sigma)\mathcal{N}_b(\omega_\sigma)\Big(\gamma_\sigma^\dagger \rho_{\rm S}(t)\gamma_\sigma - \frac{1}{2}\Big[\gamma_\sigma\gamma_\sigma^\dagger, \rho_{\rm S}(t)\Big]_+\Big) \\ &+ \frac{1}{2}\kappa(\omega_\sigma)[1+\mathcal{N}_b(\omega_\sigma)]\Big(\gamma_\sigma \rho_{\rm S}(t)\gamma_\sigma^\dagger - \frac{1}{2}\Big[\gamma_\sigma^\dagger\gamma_\sigma, \rho_{\rm S}(t)\Big]_+\Big)\Big\} \, , \end{aligned} \tag{3.146}$$

with

$$H_{\rm LS}^{(\rm glob)} := H_{\rm LS}^{(\infty)} = \sum_{\sigma=\pm} \delta\omega_\sigma \gamma_\sigma^\dagger\gamma_\sigma \, , \tag{3.147}$$

$$\delta\omega_\sigma := \eta_{\sigma\sigma}^{(1)} + \eta_{\sigma\sigma}^{(2)} = \frac{1}{4\pi}\int_0^\infty d\epsilon \frac{\kappa(\epsilon)}{\omega_\sigma - \epsilon}, \tag{3.148}$$

being the secular component of the Lamb-shift term (Hofer et al. 2017).
We remark that, while generally for the coarse-grained Redfield ME (3.134) the Lamb shift and the Hamiltonian components do not commute, i.e.

$$\big[H_{\rm S}, H_{\rm LS}^{(\Delta t)}\big]_- = 2g(\eta_{+-}^{(1)} + \eta_{-+}^{(2)})S_{+-}^{(\Delta t)} \, \gamma_-\gamma_+^\dagger - h.c. \, , \tag{3.149}$$

in the global (secular) limit one reaches $\big[H_{\rm S}, H_{\rm LS}^{(\infty)}\big]_- = 0$, hence offering an example for the observation we made in Eqs. (3.52) and (3.53).

3.3.2.2 Local ME

The local ME for $\mathcal{S}$ is a GKSL equation characterized by Lindblad operators which act locally on the mode A. Explicitly it is given by

$$\begin{aligned}\dot{\rho}_{\rm S}(t) = &-i\Big[H_{\rm S} + H_{\rm LS}^{(\rm loc)}, \rho_{\rm S}(t)\Big]_- \\ &+\kappa(\omega_0)\mathcal{N}_b(\omega_0)\Big(a^\dagger\rho_{\rm S}(t)a - \frac{1}{2}\Big[aa^\dagger, \rho_{\rm S}(t)\Big]_+\Big) \\ &+\kappa(\omega_0)(1+\mathcal{N}_b(\omega_0))\Big(a\rho_{\rm S}(t)a^\dagger - \frac{1}{2}\Big[a^\dagger a, \rho_{\rm S}(t)\Big]_+\Big)\,,\end{aligned} \tag{3.150}$$

with $\kappa(\omega_0)$ and $\mathcal{N}_b(\omega_0)$ defined as in the previous section and where now the Lamb-shift term is expressed as a modification of the local Hamiltonian of the A mode only, i.e.

$$H_{\rm LS}^{(\rm loc)} := \delta\omega_{\rm A}\, a^\dagger a\,, \tag{3.151}$$

$$\delta\omega_{\rm A} := \frac{1}{2\pi}\fint_0^\infty d\omega \frac{\kappa(\omega)}{\omega_0 - \omega}. \tag{3.152}$$

Effectively Eq. (3.150) can be obtained starting from a Hamiltonian model for the full compound $\mathcal{S}+\mathcal{E}$ where one initially completely neglects the presence of the B mode, generally enforces the same approximations that lead one to (3.146) (i.e. the Born, Markov, and full secular approximation), and finally introduces B and its coupling with A as an additive Hamiltonian contribution in the resulting expression. More formally as shown e.g. in Ref. Hofer et al. (2017), Eq. (3.150) can be derived in the weak internal coupling limit $g\tau_{\rm E} \ll 1$ ($\tau_{\rm E}$ being the bath memory time scale, see Sec. 3.3.4.4 for details) which allows one to treat the interaction between A and B as a perturbative correction with respect to the direct A-$\mathcal{E}$ coupling – see Sec. 3.3.4.1 for more on this.

3.3.2.3 Convex mixing of local and global solutions

As we shall explicitly see in the next section (see Eq. (3.161)), the main advantage offered by the global ME (3.146) is that it provides an accurate description of the steady state of $\mathcal{S}$ at least in the infinitesimally small $\mathcal{S}+\mathcal{E}$ coupling regime where on pure thermodynamic considerations one expects independent thermalization of the eigenmodes $\gamma_\pm$ of the system. On the contrary the steady state predicted by the local ME (3.150) is wrong (even if increasingly accurate as $g/\omega_0 \to 0$) because it implies the thermalization of the subsystems A and B regardless of the presence of the internal coupling $H_{\rm S,g}$. Conversely, the local ME has the quality to predict Rabi oscillations between A and B at shorter time scales, that are completely neglected when adopting the global ME.

In view of these observations (see, however, Schaller and Brandes (2008) for another strategy for melting different behaviors as function of time), a reasonable way of keeping local effects during the transient still maintaining an accurate steady state

solution is to adopt an appropriate phenomenological *ansatz* describing the evolution of $\mathcal{S}$ in terms of quantum trajectories that interpolate between the solutions $\rho_{\rm S}^{(\rm glob)}(t)$ and $\rho_{\rm S}^{(\rm loc)}(t)$ of the global and local ME, see Fig. 3.5. The simplest of these construction is provided by the following time-dependent mixture:

$$\rho_{\rm S}^{(\rm mix)}(t) := e^{-\mathcal{G}t}\rho_{\rm S}^{(\rm loc)}(t) + \left(1 - e^{-\mathcal{G}t}\right)\rho_{\rm S}^{(\rm glob)}(t)\ . \tag{3.153}$$

In this expression $\mathcal{G} > 0$ is an effective rate, whose inverse fixes the time scale of the problem that determines when global thermalization effects start dominating the system dynamics. Accordingly, Eq. (3.153) allows us to keep local effects for *short* time scales $t \lesssim \mathcal{G}^{-1}$ and the correct thermalization of the eigenmodes of the system at longer time scales $t \gg \mathcal{G}^{-1}$. The above formula can be interpreted as follows: the environment needs a finite amount of time to become aware of the presence of the part B because of its short time correlations (Markovian hypothesis). The specific value of $\mathcal{G}$ is a free variable in this model and works as a fitting parameter: its value can be even estimated quite roughly because of the relatively large time interval at intermediate time scales where the global and local approximations look alike (more on this later). It is finally worth observing that from the complete positivity properties of both the solutions of the global and local ME, it follows that (3.153) also fulfills such requirement (indeed convex combinations of completely positive transformations are also completely positive). On the contrary, at variance with the original expressions (3.146) and (3.150), as well as the CP-Redfield expression of (3.134), Eq. (3.153) will typically exhibit a non Markovian character and will not be possible to present it in the form of a GKSL differential equation. This property is a direct consequence of the fact that the set of Markovian evolutions is not closed under convex combinations (Wolf et al. 2008).

3.3.3 Dynamics

In the study of the approximated equations introduced in the previous section, as well as for their comparison with the exact solution of the $\mathcal{S} + \mathcal{E}$ dynamics, an important simplification arises from the choice we made in fixing the initial condition of $\mathcal{E}$. Indeed thanks to Eqs. (3.132), (3.133) the resulting CP-Redfield, global, and local MEs, happen to be Gaussian processes (Serafini 2017) which admit complete characterization only in terms of the first and second moments of the field operators $\gamma_\pm$ (notice that while the mixture (3.153) does not fit into the set of Gaussian processes – formally speaking it belongs to the convex-hull of such set – we can still resort to the above simplification by exploiting the fact that $\rho_{\rm S}^{(\rm mix)}(t)$ is explicitly given by the sum of the global and local ME solutions). Accordingly in studying the dynamics of our approximated schemes we can just focus on the functions $\langle\gamma_\sigma\rangle(t) := \mathrm{Tr}[\gamma_\sigma\rho_{\rm S}(t)]$, $\langle\gamma_\sigma\gamma_{\sigma'}\rangle(t) := \mathrm{Tr}[\gamma_\sigma\gamma_{\sigma'}\rho_{\rm S}(t)]$, and $\langle\gamma_\sigma^\dagger\gamma_{\sigma'}\rangle(t) := \mathrm{Tr}[\gamma_\sigma^\dagger\gamma_{\sigma'}\rho_{\rm S}(t)]$ whose temporal dependence can be determined by solving

a restricted set of coupled linear differential equations. We also observe that since the full Hamiltonian (3.126) conserves the total number of excitations in the $\mathcal{S}+\mathcal{E}$ model, coupling between excitations conserving and non-conserving moments are prevented (Cattaneo et al. 2020) yielding further simplification in the analysis.

Having clarified these points, in what follows we shall focus on the special case where the input state of $\mathcal{S}$ is fixed assuming that both A and B are initialized in the ground states of their local Hamiltonians, i.e.

$$\rho_{\rm S}(0) \;=\; |0\rangle_{\rm A}\langle 0| \otimes |0\rangle_{\rm B}\langle 0| \;, \tag{3.154}$$

with $|0\rangle$ representing the zero Fock state of the corresponding mode. Under these conditions the input state is Gaussian (Serafini 2017) and, evolved under CP-Redfield, global, local and the exact dynamics, will remain Gaussian at all times. Furthermore all the first order moments and all the non-excitation-conserving second order terms exactly nullify, i.e.

$$\langle\gamma_\sigma\rangle(t) = 0 \;, \qquad \langle\gamma_\sigma\gamma_{\sigma'}\rangle(t) = 0 \;, \tag{3.155}$$

leaving only a restricted set of equations to be explicitly integrated. For the case of the coarse-grained Redfield equation (3.134) we get

$$\begin{aligned}
\frac{d}{dt}\langle\gamma_+^\dagger\gamma_+\rangle(t) \;&=\; -\frac{1}{2}\kappa(\omega_+)[\langle\gamma_+^\dagger\gamma_+\rangle(t) - \mathcal{N}_b(\omega_+)] \\
&\quad + S_{+-}^{(\Delta t)} \times \Big\{ 2\,\mathrm{Im}\left((\eta_{+-}^{(1)} + \eta_{-+}^{(2)})\langle\gamma_-\gamma_+^\dagger\rangle(t)\right) + \\
&\quad \mathrm{Re}\left[(\gamma_{+-}^{(1)} - \gamma_{-+}^{(2)})\langle\gamma_-\gamma_+^\dagger\rangle(t)\right]\Big\} \;, \\
\frac{d}{dt}\langle\gamma_-^\dagger\gamma_-\rangle(t) \;&=\; -\frac{1}{2}\kappa(\omega_-)[\langle\gamma_-^\dagger\gamma_-\rangle(t) - \mathcal{N}_b(\omega_-)] \\
&\quad + S_{+-}^{(\Delta t)} \times \Big\{ -2\,\mathrm{Im}\left((\eta_{+-}^{(1)} + \eta_{-+}^{(2)})\langle\gamma_-\gamma_+^\dagger\rangle(t)\right) + \\
&\quad \mathrm{Re}\left[(\gamma_{+-}^{(1)} - \gamma_{-+}^{(2)})\langle\gamma_-\gamma_+^\dagger\rangle(t)\right]\Big\} \;, \\
\frac{d}{dt}\langle\gamma_-\gamma_+^\dagger\rangle(t) \;&=\; \{i(\omega_+ + \delta\omega_+ - \omega_- - \delta\omega_-) - \frac{1}{4}[\kappa(\omega_+) + \kappa(\omega_-)]\}\langle\gamma_-\gamma_+^\dagger\rangle(t) \\
&\quad + S_{+-}^{(\Delta t)} \times \Big\{ i(\eta_{-+}^{(1)} + \eta_{+-}^{(2)})\left[\langle\gamma_-^\dagger\gamma_-\rangle(t) - \langle\gamma_+^\dagger\gamma_+\rangle(t)\right] + \gamma_{-+}^{(1)} + \\
&\quad \frac{1}{2}(\gamma_{-+}^{(1)} - \gamma_{+-}^{(2)})\left[\langle\gamma_-^\dagger\gamma_-\rangle(t) + \langle\gamma_+^\dagger\gamma_+\rangle(t)\right]\Big\} \;,
\end{aligned} \tag{3.156}$$

with initial values

$$\langle\gamma_+^\dagger\gamma_+\rangle(0) \;=\; \langle\gamma_-^\dagger\gamma_-\rangle(0) = \langle\gamma_-\gamma_+^\dagger\rangle(0) = 0 \tag{3.157}$$

imposed by (3.154). In particular in the case of full secular approximation ($S_{+-}^{(\Delta t)} = 0$) the above set of equations become

$$\begin{aligned}
\frac{d}{dt}\langle\gamma_+^\dagger\gamma_+\rangle(t) &= -\frac{1}{2}\kappa(\omega_+)[\langle\gamma_+^\dagger\gamma_+\rangle(t) - \mathcal{N}_b(\omega_+)] \,, \\
\frac{d}{dt}\langle\gamma_-^\dagger\gamma_-\rangle(t) &= -\frac{1}{2}\kappa(\omega_-)[\langle\gamma_-^\dagger\gamma_-\rangle(t) - \mathcal{N}_b(\omega_-)] \,, \\
\frac{d}{dt}\langle\gamma_-\gamma_+^\dagger\rangle(t) &= \{i(\omega_+ + \delta\omega_+ - \omega_- - \delta\omega_-) - \frac{1}{4}[\kappa(\omega_+) + \kappa(\omega_-)]\}\langle\gamma_-\gamma_+^\dagger\rangle(t) \,,
\end{aligned} \tag{3.158}$$

which yield the evolution of the moments for the global ME (3.146). Similar considerations hold true for the local ME (3.150). In this case following Refs. Hofer et al. (2017), Farina, Andolina, Mari, Polini and Giovannetti (2019) we get

$$\begin{aligned}
\frac{d}{dt}\langle\gamma_+^\dagger\gamma_+\rangle(t) &= -\frac{1}{2}\kappa(\omega_0)[\langle\gamma_+^\dagger\gamma_+\rangle(t) - \mathcal{N}_b(\omega_0) + \mathrm{Re}\langle\gamma_-\gamma_+^\dagger\rangle(t)] + \delta\omega_\mathrm{A}\,\mathrm{Im}\langle\gamma_-\gamma_+^\dagger\rangle(t) \,, \\
\frac{d}{dt}\langle\gamma_-^\dagger\gamma_-\rangle(t) &= -\frac{1}{2}\kappa(\omega_0)[\langle\gamma_-^\dagger\gamma_-\rangle(t) - \mathcal{N}_b(\omega_0) + \mathrm{Re}\langle\gamma_-\gamma_+^\dagger\rangle(t)] - \delta\omega_\mathrm{A}\,\mathrm{Im}\langle\gamma_-\gamma_+^\dagger\rangle(t) \,, \\
\frac{d}{dt}\langle\gamma_-\gamma_+^\dagger\rangle(t) &= [i2g - \frac{1}{2}\kappa(\omega_0)]\langle\gamma_-\gamma_+^\dagger\rangle(t) + \frac{\kappa(\omega_0)}{2}\{\mathcal{N}_b(\omega_0) \\
&\quad -\frac{1}{2}[\langle\gamma_+^\dagger\gamma_+\rangle(t) + \langle\gamma_-^\dagger\gamma_-\rangle(t)]\} + i\,\frac{\delta\omega_\mathrm{A}}{2}[\langle\gamma_-^\dagger\gamma_-\rangle(t) - \langle\gamma_+^\dagger\gamma_+\rangle(t)] \,,
\end{aligned} \tag{3.159}$$

which, for a direct comparison with Eq. (3.158), we express here in terms of the eigenmodes $\gamma_\pm$.

3.3.3.1 Evolution of the second moments

A closer look at Eq. (3.158) reveals that in this case one has that for large enough t we get

$$\langle\gamma_\pm^\dagger\gamma_\pm\rangle\Big|_{(\mathrm{glob})}(\infty) = \mathcal{N}(\omega_\pm) \,, \qquad \langle\gamma_-\gamma_+^\dagger\rangle\Big|_{(\mathrm{glob})}(\infty) = 0 \,. \tag{3.160}$$

This enlightens the fact that, as anticipated at the beginning of Sec. 3.3.2.3, the global ME (3.146) imposes $\mathcal{S}$ to asymptotically converge toward the Gibbs thermal state

$$\rho_\mathrm{S}^{(\mathrm{glob})}(\infty) := \frac{e^{-\beta H_\mathrm{S}}}{\mathrm{tr}[e^{-\beta H_\mathrm{S}}]} \,, \tag{3.161}$$

in agreement with what one would expect from purely thermodynamics considerations under weak-coupling conditions for the system-environment interactions. On the contrary the steady state predicted by the local ME is wrong (even if increasingly accurate as $g/\omega_0 \to 0$) because it implies the thermalization of the subsystems A and B regard-

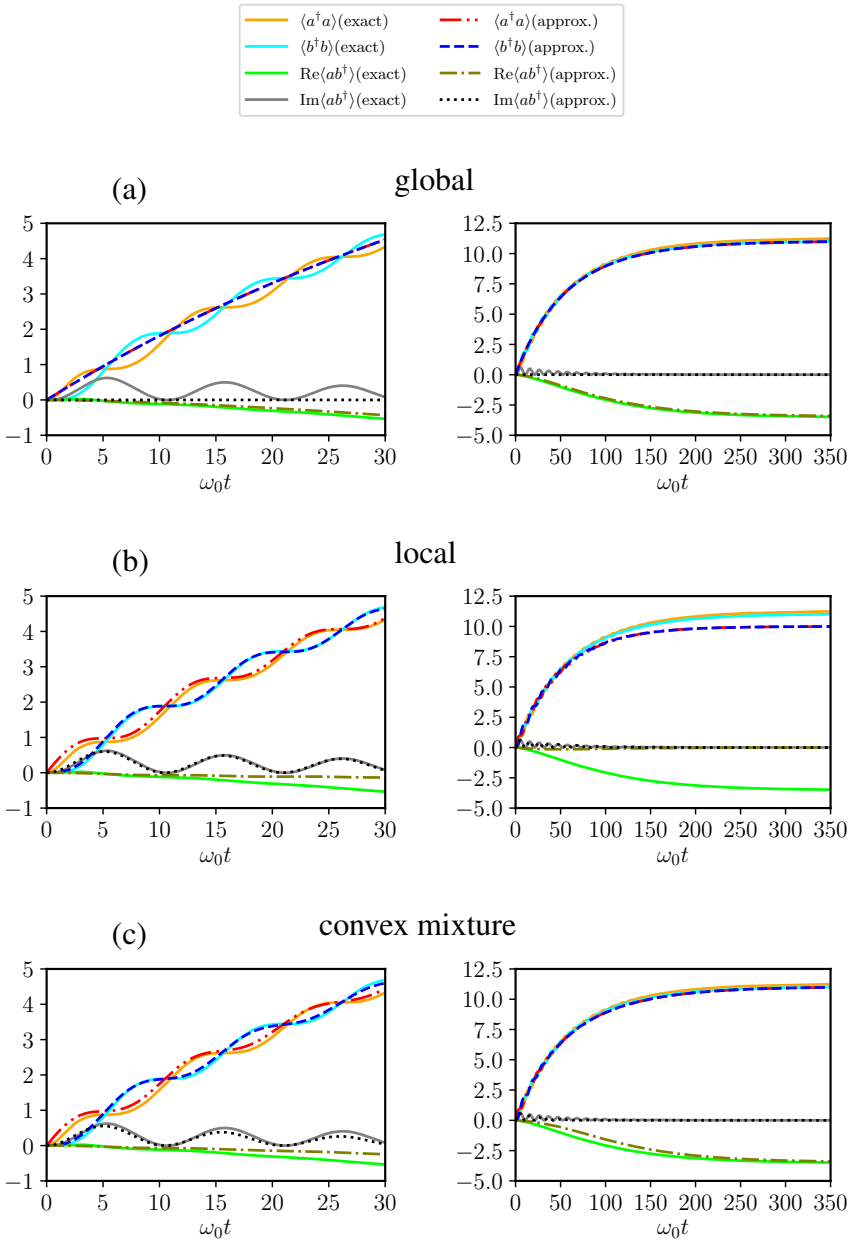

Fig. 3.7 Second order moments evaluated using the global ME (a), the local ME (b), the convex mixture of Eq. (3.153) with $\mathcal{G} = 0.4\kappa(\omega_0)$ (c), compared with the ones predicted by the exact dynamics. As indicated by the legend continuous lines in the plots represent the quantities computed by solving the exact $\mathcal{S} + \mathcal{E}$ Hamiltonian model (3.126); dotted and dashed lines instead refer to the approximated solutions associated with global, local and mixed approaches. Each panel contains two plots corresponding each to shorter (left) and longer (right) time scales. As clear from the right plot of panel (a), the global ME approach provides a pretty good agreement with the exact solutions at large time scales, while fails in the short time domain. Exactly the opposite occurs for the local ME approach presented in panel (b): here a good agreement with the exact solutions is found in the short time domain (left plot), while differences arise in the large time domain (right plot). The convex mixture approach (3.166) finally appears to be able to maintain a good agreement with the exact results at all times. In all the plots we used $\mathcal{N}_b(\omega_0) = 10$ (corresponding to $1/\beta \approx 10.5\omega_0$), $g = 0.3\omega_0$, $\kappa(\omega_0) = 0.04\omega_0$, $\omega_c = 3\omega_0$, $\alpha = 1$.

less of the presence of the internal coupling $H_{\rm S,g}$. Indeed from Eq. (3.159) we get

$$\langle \gamma_{\pm}^{\dagger}\gamma_{\pm}\rangle\Big|_{(\rm loc)}(\infty) = \mathcal{N}_b(\omega_0)\ , \qquad \langle \gamma_{-}\gamma_{+}^{\dagger}\rangle\Big|_{(\rm loc)}(\infty) = 0 \tag{3.162}$$

or equivalently

$$\langle a^{\dagger}a\rangle\Big|_{(\rm loc)}(\infty) = \langle b^{\dagger}b\rangle\Big|_{(\rm loc)}(\infty) = \mathcal{N}_b(\omega_0)\ , \tag{3.163}$$

$$\langle ab^{\dagger}\rangle\Big|_{(\rm loc)}(\infty) = 0\ , \tag{3.164}$$

which identifies

$$\rho_{\rm S}^{(\rm loc)}(\infty) := \frac{e^{-\beta H_{\rm S,0}}}{{\rm tr}[e^{-\beta H_{\rm S,0}}]}\ , \tag{3.165}$$

as the new fixed point for the dynamical evolution (see Walls (1970), Cresser (1992) for pioneering discussions on the topic and Sec. 3.3.4.5 for further details). The discrepancy between the above expressions and Eqs. (3.160), (3.161) is even accentuated in the low temperature regime $\beta\omega_0 \gg 1$, where in particular the ratio $\mathcal{N}_b(\omega_-)/\mathcal{N}_b(\omega_0) \simeq e^{\beta g}$ can explode exponentially.

The situation gets reversed at shorter time scales. Here the local ME correctly presents coherent energy exchanges between A and B which instead the global approach completely neglects. Indeed from Eq. (3.158) it follows that the global ME predicts ${\rm Im}[\langle ab^{\dagger}\rangle(t)] = 0$, the term being responsible of the Rabi oscillations between A and B (see Hofer et al. (2017), Farina, Andolina, Mari, Polini and Giovannetti (2019) and Sec. 3.3.4.5 for details). The local ME on the contrary – when the Lamb-shift correction can be neglected – gives ${\rm Re}[\langle ab^{\dagger}\rangle(t)] = 0$, the latter being proportional to the average internal interaction energy $\langle H_{\rm S,g}\rangle$.

The above observations are confirmed by the numerical study we present in the remaining of the section (see however also the material presented in Sec. 3.3.4.5). In particular, in panels (a) and (b) of Fig. 3.7 the temporal evolution of the second order moments obtained by solving Eq. (3.158) and (3.159) are compared with the exact values of the corresponding quantities obtained by numerical integration of the exact $\mathcal{S}+\mathcal{E}$ Hamiltonian model along the lines detailed in Sec. 3.3.4.4. In panel (c) of such figure we also present the results obtained by using the effective model of Sec. 3.3.2.3, where according to Eq. (3.153) the expectation values of the relevant quantities are computed as

$$\begin{aligned}\langle \gamma_{\sigma}^{\dagger}\gamma_{\sigma'}\rangle\Big|_{(\rm mix)}(t) &= e^{-\mathcal{G}t}\langle \gamma_{\sigma}^{\dagger}\gamma_{\sigma'}\rangle\Big|_{(\rm loc)}(t) \\ &\quad + \big(1-e^{-\mathcal{G}t}\big)\,\langle \gamma_{\sigma}^{\dagger}\gamma_{\sigma'}\rangle\Big|_{(\rm glob)}(t)\ ,\end{aligned} \tag{3.166}$$

with $\langle\gamma_\sigma^\dagger\gamma_{\sigma'}\rangle\Big|_{(\mathrm{loc})}(t)$ and $\langle\gamma_\sigma^\dagger\gamma_{\sigma'}\rangle\Big|_{(\mathrm{glob})}(t)$ representing the solutions of Eq. (3.159) and Eq. (3.158) respectively. In our analysis the system parameters have been set in order to enforce $\mathcal{S}-\mathcal{E}$ weak-coupling conditions ($\omega_0, \omega_\pm \gg \kappa(\omega_0)$) to make sure that the long term prediction (3.161) of the global ME provides a proper description of the system dynamics. By the same token, the temperature of the bath has been fixed to be relatively high, i.e. $1/\beta \approx 10.5\omega_0$, to avoid to enhance correlation effects between the bath and the system which are not included in the Born and Markov approximations needed to derive both the global and the local ME (Hovhannisyan et al. 2020) (a study of the impact of low temperature effects on the $\mathcal{S}-\mathcal{E}$ correlations is presented in Sec. 3.3.4.4). Finally, regarding the value of the phenomenological parameter $\mathcal{G}$ entering in (3.166), we set it equal to $0.4\kappa(\omega_0)$ finding a relatively good agreement with the exact data at all times.

The convex combination (3.153) is not the only way of keeping the best from both the local and the global approximations. Indeed, by making a step back, one can consider the coarse-grained Redfield equations (3.156) once that the pathology related to their non-positivity has been cured. A detailed study of the performances of this approach is presented in Fig. 3.8. Here, for the same values of the parameters used in Fig. 3.7, in panel (a) we exhibit the plots associated with the CP-Redfield equation obtained by fixing $S_{+-}^{(\Delta t)}$ in such a way to saturate the positivity bound (3.144), i.e. $S_{+-}^{(\Delta t)} = 0.989$. As in the case of panel (c) of Fig. 3.7, we notice that CP-Redfield is in a good agreement with the exact data both at long and short time scales. As a check in panel (b) of Fig. 3.8 we also present the (uncorrected) Redfield equation obtained by setting in Eq. (3.156) $\Delta t = 0$, corresponding to have $S_{+-}^{(\Delta t)} = 1$ which for the system parameters we choose gives a clear violation of the positivity bound (3.144). Interestingly enough, despite the fact that the resulting equation does not guarantee complete positivity of the associated evolution, we notice that also in this case one has an apparent good agreement with the exact results for all times (see also Purkayastha et al. (2016) where the effectiveness of the uncorrected Redfield equation is pointed out in other setups). In particular, both CP-Redfield and Redfield equations appear to be able to capture a non-weak coupling correction to the asymptotic value of $2\mathrm{Re}\langle\gamma_-\gamma_+^\dagger\rangle(t) = \langle a^\dagger a\rangle(t) - \langle b^\dagger b\rangle(t)$, an effect that is present in the exact model due to the fact that the subsystem A remains slightly correlated with the bath degrees of freedom, but which is not present when adopting neither global, local, or mixed approximations (see Fig. 3.9). An evidence of this can be obtained by observing that from Eq. (3.156) we have

$$2\mathrm{Re}\langle\gamma_-\gamma_+^\dagger\rangle(\infty) = \frac{S_{+-}^{(\Delta t)}}{\omega_+-\omega_-} \times\int_0^\infty d\epsilon\,\frac{\kappa(\epsilon)}{2\pi}\left(\frac{\mathcal{N}_b(\epsilon)-\mathcal{N}_b(\omega_+)}{\epsilon-\omega_+}-\frac{\mathcal{N}_b(\epsilon)-\mathcal{N}_b(\omega_-)}{\epsilon-\omega_-}\right)+O[\kappa(\omega_0)^2] \tag{3.167}$$

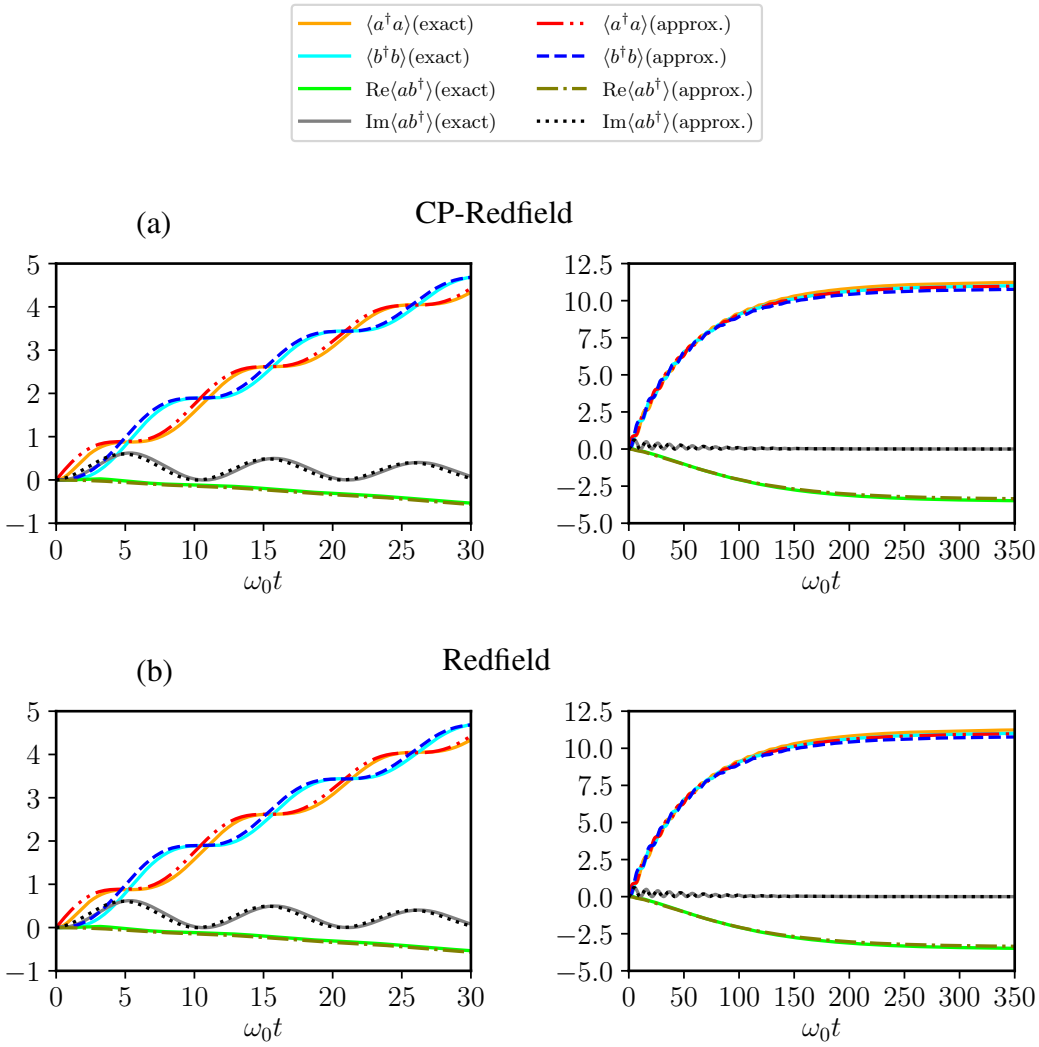

Fig. 3.8 Comparison between second order moments evaluated using the CP-Redfield (a) and Redfield (b) with the ones predicted by the exact dynamics. As in the case of Fig. 3.7 continuous lines represent the quantities computed by solving the exact $\mathcal{S}+\mathcal{E}$ Hamiltonian model (3.126) while dotted and dashed lines instead refer to the approximated solutions. Also each panel contains two plots corresponding each to shorter (left) and longer (right) time scales. In all the plots we used $\mathcal{N}_b(\omega_0)=10$ (corresponding to $1/\beta\approx 10.5\omega_0$), $g=0.3\omega_0$, $\kappa(\omega_0)=0.04\omega_0$, $\omega_c=3\omega_0$, $\alpha=1$ – same as those used in Fig. 3.7. The value of Δt used to define CP-Redfield is such that $S_{+-}^{(\Delta t)}=0.989$, which ensures the saturation of the inequality (3.144).

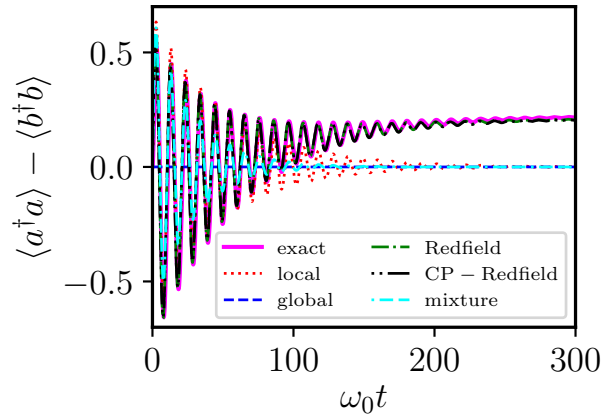

Fig. 3.9 Plot of the local excitation gap $\langle a^\dagger a\rangle(t) - \langle b^\dagger b\rangle(t)$ for the different approximation methods and for the exact dynamics. Global ME (blue dashed line), local ME (red dotted line), and convex mixture approach (cyan dot-dashed-dashed line) predict an asymptotically zero value for this gap. On the contrary, Redfield (green dot-dashed line) and CP-Redfield (black dot-dot-dashed line) give an asymptotic non-zero value for such quantity in agreement with the exact dynamics (magenta full and thicker line). In all the plots we used $\mathcal{N}_b(\omega_0) = 10$ (corresponding to $1/\beta \approx 10.5\omega_0$), $g = 0.3\omega_0$, $\kappa(\omega_0) = 0.04\omega_0$, $\omega_c = 3\omega_0$, $\alpha = 1$ – same as those used in Figs. 3.7, 3.8. The value of Δt used to define CP-Redfield is such that $S_{+-}^{(\Delta t)} = 0.989$, which ensures the saturation of the inequality (3.144).

which is exactly null for the global ME ($S_{+-}^{(\Delta t)} = 0$), but which is different from zero (and in good agreement with the exact result) both for the uncorrected Redfield equation ($S_{+-}^{(\Delta t)} = 1$) and CP-Redfield ($S_{+-}^{(\Delta t)} = 0.989$).

Despite the apparent success of the uncorrected Redfield equation reported above, a clear signature of its non-positivity can still be spotted by looking at a special functional of the second order moments of the model, i.e. the quantity

$$\lambda_c(t) := \frac{1}{2}\min\{\text{ eigenvalues}[\Gamma_{\rm S}(t) + i\Xi_{\rm S}]\ \}\ . \tag{3.168}$$

In the above definition $\Gamma_{\rm S}(t)$ and $\Xi_{\rm S}$ are respectively the covariance matrix and the symplectic form of the two-mode system $\mathcal{S}$. Expressed in terms of the eigenoperators $\gamma_\pm$ their elements are given by

$$[\Gamma_{\rm S}(t)]_{ij} := \left\langle \left[\mathbf{\Gamma}_i - \langle \mathbf{\Gamma}_i\rangle(t), \mathbf{\Gamma}_j^\dagger - \langle \mathbf{\Gamma}_j^\dagger\rangle(t)\right]_+ \right\rangle (t), \tag{3.169}$$

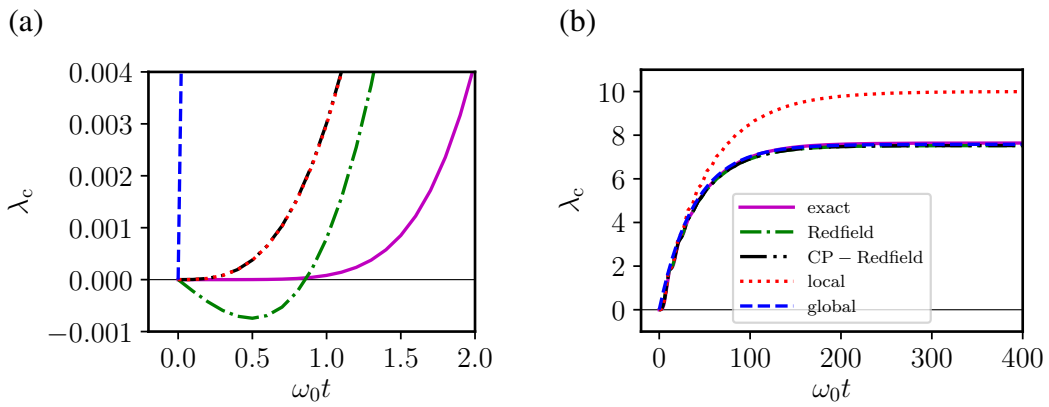

Fig. 3.10 Plots of the quantity $\lambda_c(t)$ of Eq. (3.168) for different approximation methods and using the exact result, at shorter (a) and longer (b) time scales. In all the plots we used $\mathcal{N}_b(\omega_0) = 10$ (corresponding to $1/\beta \approx 10.5\omega_0$), $g = 0.3\omega_0$, $\kappa(\omega_0) = 0.04\omega_0$, $\omega_c = 3\omega_0$, $\alpha = 1$ – same as those used in Figs. 3.7-3.9. The value of Δt used to define CP-Redfield is such that $S_{+-}^{(\Delta t)} = 0.989$, which saturates the inequality (3.144).

and

$$[\Xi_S]_{ij} := -i \left\langle \left[\mathbf{\Gamma}_i, \mathbf{\Gamma}_j^\dagger \right]_- \right\rangle (t) = -i \begin{pmatrix} 1 & 0 & 0 & 0 \\ 0 & -1 & 0 & 0 \\ 0 & 0 & 1 & 0 \\ 0 & 0 & 0 & -1 \end{pmatrix}, \tag{3.170}$$

with $\mathbf{\Gamma}_i$ being the i-th component of the operator vector $\mathbf{\Gamma} := (\gamma_+, \gamma_+^\dagger, \gamma_-, \gamma_-^\dagger)^T$. In particular due to the choice of the input state we made in Eq. (3.154), we get

$$\Gamma_S(t) = \begin{pmatrix} 2\langle \gamma_+^\dagger \gamma_+ \rangle(t) + 1 & 0 & 2\langle \gamma_- \gamma_+^\dagger \rangle(t)^* & 0 \\ 0 & 2\langle \gamma_+^\dagger \gamma_+ \rangle(t) + 1 & 0 & 2\langle \gamma_- \gamma_+^\dagger \rangle(t) \\ 2\langle \gamma_- \gamma_+^\dagger \rangle(t) & 0 & 2\langle \gamma_-^\dagger \gamma_- \rangle(t) + 1 & 0 \\ 0 & 2\langle \gamma_- \gamma_+^\dagger \rangle(t)^* & 0 & 2\langle \gamma_-^\dagger \gamma_- \rangle(t) + 1 \end{pmatrix}, \tag{3.171}$$

and hence

$$\frac{\Gamma_S(t) + i\Xi_S}{2} = \begin{pmatrix} \langle \gamma_+^\dagger \gamma_+ \rangle(t) + 1 & 0 & \langle \gamma_- \gamma_+^\dagger \rangle(t)^* & 0 \\ 0 & \langle \gamma_+^\dagger \gamma_+ \rangle(t) & 0 & \langle \gamma_- \gamma_+^\dagger \rangle(t) \\ \langle \gamma_- \gamma_+^\dagger \rangle(t) & 0 & \langle \gamma_-^\dagger \gamma_- \rangle(t) + 1 & 0 \\ 0 & \langle \gamma_- \gamma_+^\dagger \rangle(t)^* & 0 & \langle \gamma_-^\dagger \gamma_- \rangle(t) \end{pmatrix}, \tag{3.172}$$

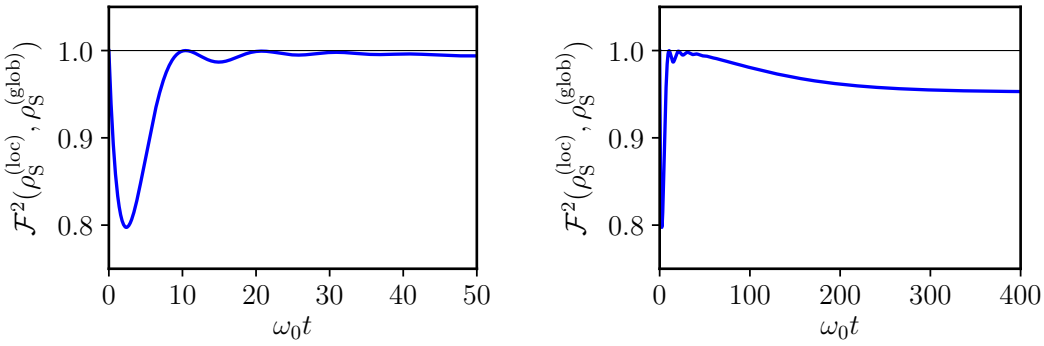

Fig. 3.11 Fidelity between the solutions $\rho_S^{(loc)}(t)$ and $\rho_S^{(glob)}(t)$ of the local and global MEs associated with the initial condition (3.154) at shorter (left) and longer (right) time scales. In the plots we used $\mathcal{N}_b(\omega_0) = 10$ (corresponding to $1/\beta \approx 10.5\omega_0$), $g = 0.3\omega_0$, $\kappa(\omega_0) = 0.04\omega_0$, $\omega_c = 3\omega_0$, $\alpha = 1$ – same as those of Figs. 3.7-3.10.

$$\lambda_c(t) = \frac{1}{2}\{\langle\gamma_+^\dagger\gamma_+\rangle(t) + \langle\gamma_-^\dagger\gamma_-\rangle(t) - \sqrt{[\langle\gamma_+^\dagger\gamma_+\rangle(t) - \langle\gamma_-^\dagger\gamma_-\rangle(t)]^2 + 4|\langle\gamma_-\gamma_+^\dagger\rangle(t)|^2}\} \,. \tag{3.173}$$

When evaluated on a proper state of the system, the Robertson-Schrödinger uncertainty relation (Serafini 2017) forces the spectrum of the matrix (3.172) to be non-negative – see Sec. 3.3.4.3 for details. Accordingly when $\rho_S(t)$ is positive semi-definite (i.e. it is a physical state) one must have $\lambda_c(t) \geq 0$. The temporal evolution of $\lambda_c(t)$ is reported in Fig. 3.10 for the various approximation methods and for the exact dynamics: one notice that while global, local, and CP-Redfield always complies with the positivity requirement, the uncorrected Redfield equation exhibit negative values of $\lambda_c(t)$ at short time scales. Analytically, this can be seen from the short time scale trend of $\lambda_c(t)$, which from Eq. (3.156) can be determined as

$$\lambda_c(\delta t) \simeq \left(\frac{\gamma_{--}^{(1)}+\gamma_{++}^{(1)}}{2}\right)\left[1 - \sqrt{1 + 4\left(S_{+-}^{(\Delta t)^2} - \frac{\gamma_{++}^{(1)}\gamma_{--}^{(1)}}{|\gamma_{+-}^{(1)}|^2}\right)\frac{|\gamma_{+-}^{(1)}|^2}{(\gamma_{--}^{(1)}+\gamma_{++}^{(1)})^2}}\right]\delta t \,, \tag{3.174}$$

which tightly gives $\lambda_c(\delta t) \geq 0$ if and only if the complete positivity constraint (3.144) is fulfilled. Notice also that while none of the approximated methods are able to follow the whole exact behaviour of $\lambda_c(t)$, CP-Redfield and global provide good agreement in the long time limit, while CP-Redfield and local correctly predict $\dot{\lambda}_c(0) = 0$.

3.3.3.2 Fidelity Comparison

In this section we further discuss the difference between the various approximation methods, as well as their relation with the exact solution, evaluating the temporal evolution of the Uhlmann fidelity (Nielsen and Chuang 2010) between the associated density matrices of $\mathcal{S}$. We remind that given $\rho_S^{(1)}$ and $\rho_S^{(2)}$ two quantum states of the system their

fidelity is defined as the positive functional

$$\mathcal{F}(\rho_{\rm S}^{(1)},\rho_{\rm S}^{(2)}) := \left\| \sqrt{\rho_{\rm S}^{(1)}}\sqrt{\rho_{\rm S}^{(2)}} \right\|_1 , \tag{3.175}$$

with $\|\Theta\|_1 := {\rm Tr}[\sqrt{\Theta^\dagger\Theta}]$ being the trace norm of the operator Θ. This quantity provides a *bona-fide* estimation of how close the two density matrices are, getting its maximum value 1 when $\rho_{\rm S}^{(1)} = \rho_{\rm S}^{(2)}$, and achieving zero value instead when the support of $\rho_{\rm S}^{(1)}$ and $\rho_{\rm S}^{(2)}$ are orthogonal, i.e. when they are perfectly distinguishable. In the case of two-mode Gaussian states (Serafini 2017) with null first order moments, a relatively simple closed expression for $\mathcal{F}(\rho_{\rm S}^{(1)},\rho_{\rm S}^{(2)})$ is known in terms of the covariance matrices of the two density matrices (Marian and Marian 2012, González et al. 2017, Hofer et al. 2017). Specifically, in the eigenmode representation, one has

$$\mathcal{F}^2(\rho_{\rm S}^{(1)},\rho_{\rm S}^{(2)}) = \frac{1}{\sqrt{\rm b}+\sqrt{\rm c}-\sqrt{(\sqrt{\rm b}+\sqrt{\rm c})^2-{\rm a}}} , \tag{3.176}$$

with

$$\begin{aligned} {\rm a} &:= 2^{-4}\det[\Gamma_{\rm S}^{(1)}+\Gamma_{\rm S}^{(2)}] , \\ {\rm b} &:= 2^{-4}\det[\Xi_{\rm S}\,\Gamma_{\rm S}^{(1)}\,\Xi_{\rm S}\,\Gamma_{\rm S}^{(2)}-\mathbb{1}_4] , \\ {\rm c} &:= 2^{-4}\det[\Gamma_{\rm S}^{(1)}+i\Xi_{\rm S}]\det[\Gamma_{\rm S}^{(2)}+i\Xi_{\rm S}] , \end{aligned} \tag{3.177}$$

where $\Gamma_{\rm S}^{(1)}$, $\Gamma_{\rm S}^{(2)}$ are the covariance matrices of $\rho_{\rm S}^{(1)}$ and $\rho_{\rm S}^{(2)}$ defined in (3.169), and with $\Xi_{\rm S}$ the symplectic form given in Eq. (3.170) – see final part of Sec. 3.3.4.3 for details. In what follows we shall make extensive use of the identity (3.176) thanks to the fact that for the input state (3.154) we are considering in our analysis, the density matrix of $\mathcal{S}$ remains Gaussian at all times when evolved under global, local, CP-Redfield ME, as well as under the exact integration of the full $\mathcal{S}+\mathcal{E}$ Hamiltonian model. The same property unfortunately does not hold for the convex mixture (3.153) which is explicitly non-Gaussian (indeed it is a convex combination of Gaussian states). In this case hence the result of Marian and Marian (2012) can not be directly applied to compute $\mathcal{F}\left(\rho_{\rm S}^{(\rm mix)}(t),\rho_{\rm S}^{(\rm exact)}(t)\right)$. Still the concavity property (Nielsen and Chuang 2010) of $\mathcal{F}$ can be invoked to compute the following lower bound

$$\begin{aligned} \mathcal{F}\left(\rho_{\rm S}^{(\rm mix)}(t),\rho_{\rm S}^{(\rm exact)}(t)\right) \geq\, & e^{-\mathcal{G}t}\mathcal{F}\left(\rho_{\rm S}^{(\rm loc)}(t),\rho_{\rm S}^{(\rm exact)}(t)\right) \\ & +(1-e^{-\mathcal{G}t})\mathcal{F}\left(\rho_{\rm S}^{(\rm glob)}(t),\rho_{\rm S}^{(\rm exact)}(t)\right) , \end{aligned} \tag{3.178}$$

with the right-hand-side being provided by Gaussian terms. Finally the non-positivity of the (uncorrected) Redfield equation also gives rise to problems in the evaluation of the

associated fidelity (as a matter of fact, in this case the quantity $\mathcal{F}\left(\rho_{\rm S}^{(\rm red)}(t), \rho_{\rm S}^{(\rm exact)}(t)\right)$ is simply ill defined). Aware of this fundamental limitation, but also of the fact that the departure from the positivity condition of the solution $\rho_{\rm S}^{(\rm red)}(t)$ of the Redfield equation is small, in our analysis we decided to present the real part of $\mathcal{F}^2\left(\rho_{\rm S}^{(\rm red)}(t), \rho_{\rm S}^{(\rm exact)}(t)\right)$.

To begin, in Fig. 3.11 we present the value of $\mathcal{F}^2(\rho_{\rm S}^{(\rm loc)}(t), \rho_{\rm S}^{(\rm glob)}(t))$: as clear from the plot, this quantity is sensibly different from 1 at short and at long time scales (confirming the observation of the previous section) while it is ~ 1 at intermediate time scales. In Fig. 3.12 instead we proceed with the comparison of the approximate solutions with the exact one. The reported plots confirm that the convex combination of the local and global solutions (3.153) is an effective ansatz to approximate the system evolution, giving a (lower) bound for the fidelity computed as in Eq. (3.178) that is close to 1 both at short and at long time scales. On the same footing we find the CP-Redfield equation which, still remaining positive, brings all the main qualities of the (full) Redfield ME. For completeness, in Fig. 3.13 we report two situations in which the global ME and the local ME work extremely bad respectively. In Panel (a) we consider weaker internal coupling g such that the local ME gives a satisfying result for the whole dynamics while the inadequacy of the global ME during the transient is accentuated; In Panel (b) we decrease instead the temperature accentuating the inadequacy of the local ME in the steady prediction. In both the Panels we report the curve corresponding to the CP-Redfield approximation. The last follows either the local or the global curve depending on which one performs better in the two instances.

3.3.4 Technical details

3.3.4.1 Derivation of the coarse-grained Redfield and local ME

In this section we provide details about the derivations of the coarse-grained Redfield (3.134) and local (3.150) MEs. For (3.134) we make use of Refs. Hofer et al. (2017), Breuer et al. (2002) and of the method to correct the non-positivity of the Redfield equation given in Sec. 3.1 [Ref. Farina and Giovannetti (2019)], while for (3.150) we follow the approach of Ref. Hofer et al. (2017).

Expressed in interaction picture the evolution of the joint state of $\mathcal{S}+\mathcal{E}$ induced by the Hamiltonian (3.126) is given by the Liouville-von Neumann equation

$$\dot{\tilde{\rho}}_{\rm SE}(t) \;=\; -i\Big[\tilde{H}_1(t), \tilde{\rho}_{\rm SE}(t)\Big]_- \,, \tag{3.179}$$

where given $U_0(t) := e^{i(H_{\rm S}+H_{\rm E})t}$ we have

$$\tilde{H}_1(t) \;:=\; U_0(t) H_1 U_0^\dagger(t) = a^\dagger(t) C(t) + h.c. \tag{3.180}$$

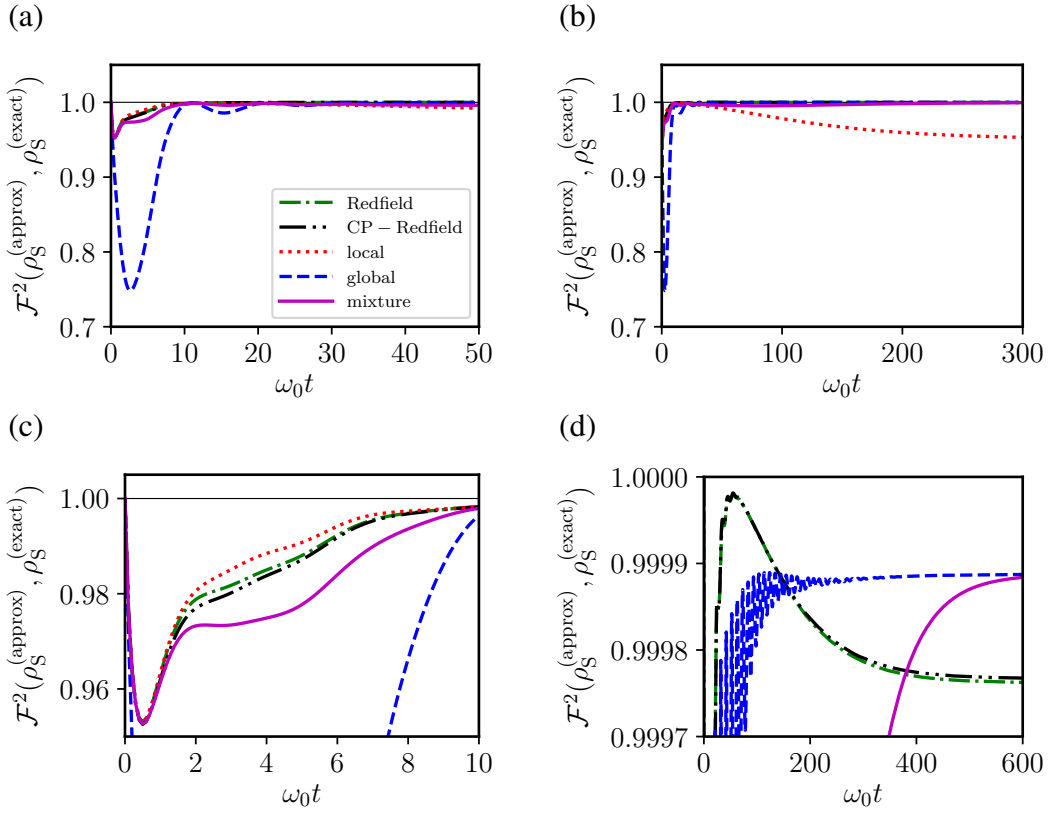

Fig. 3.12 Fidelity between approximated system states and the exact system state. Different curves refer to the kind of approximation (see the legend): Redfield, green dot-dashed line (using $\mathrm{Re}(\mathcal{F}^2)$); CP-Redfield, black dot-dot-dashed line; local, red dotted line; global, blue dashed line; convex mixture of Eq. (3.153) with $\mathcal{G} = 0.4\kappa(\omega_0)$, magenta full line (using the lower bound given in the right-hand-side of Eq. (3.178)). The four panels differ just for the axes scales. In the plots we used $\mathcal{N}_b(\omega_0) = 10$ (corresponding to $1/\beta \approx 10.5\omega_0$), $g = 0.3\omega_0$, $\kappa(\omega_0) = 0.04\omega_0$, $\omega_c = 3\omega_0$, $\alpha = 1$ – same as those of Figs. 3.7-3.11.

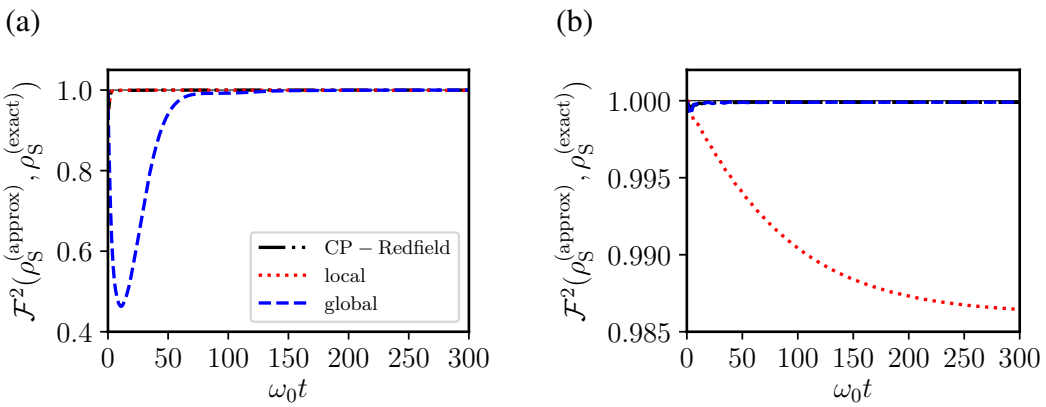

Fig. 3.13 Fidelity between approximated system states and the exact system state for (a) $\mathcal{N}_b(\omega_0) = 10$, $g = 0.04\omega_0$ (weaker internal coupling) and (b) $\mathcal{N}_b(\omega_0) = 0.01$ (low temperature regime), $g = 0.3\omega_0$. As explained in the legend the black dot-dot-dashed lines refer to the CP-Redfield solutions ($S_{+-}^{(\Delta t)} = 0.9998$ in (a) and $S_{+-}^{(\Delta t)} = 0.4813$ in (b)); the red dotted lines to the local ME solutions, and finally the blue dashed lines to the global ME solutions. In all the plots we assumed $\alpha = 1$ (Ohmic spectral density regime) and kept $\kappa(\omega_0) = 0.04\omega_0$, $\omega_c = 3\omega_0$. Notice finally that in (b) the Fidelity is generally higher (see the different ordinate scales in (a) and (b)). This is due to the choice of the ground-state (3.154) as initial state, which implies that at low temperature such initial condition is just weakly modified.

with $a^\dagger(t) := e^{iH_{S,g}t}a^\dagger e^{-iH_{S,g}t}$ and $C(t) := \sum_k \gamma_k c_k e^{-i(\omega_k-\omega_0)t}$. Tracing out the environment degrees of freedom, Eq. (3.179) can be written as

$$\dot{\tilde{\rho}}_S(t) = -i\mathrm{Tr}_E\Big[\tilde{H}_1(t), \tilde{\rho}_{SE}(0)\Big]_- - \int_0^t \mathrm{Tr}_E\Big[\tilde{H}_1(t), \Big[\tilde{H}_1(t'), \tilde{\rho}_{SE}(t')\Big]_-\Big]_- dt' \,. \quad (3.181)$$

We assume now weak system-environment coupling such that the environment stays in its own Gibbs state (3.132) (invariant in interaction picture) for all the system dynamics and the SE state can be approximated by the tensor product

$$\tilde{\rho}_{SE}(t) \simeq \tilde{\rho}_S(t) \otimes \rho_E(0). \quad (3.182)$$

Equation (3.182) means that the environment, being a macroscopic object, can be considered insensitive to the interaction with the system (Born approximation, see Sec. 2.1.2.1 and Breuer et al. (2002)). On the contrary the system state is affected by the coupling with the environment. Being the first moments null over a thermal state, the first commutator in (3.181) is zero and, by inserting the tensor product (3.182), such equation becomes

$$\dot{\tilde{\rho}}_S(t) \simeq \int_0^t dt' c^{(1)}(t-t')\left(a^\dagger(t')\tilde{\rho}_S(t')a(t) - a(t)a^\dagger(t')\tilde{\rho}_S(t')\right) + \quad (3.183)$$
$$c^{(2)}(t-t')\left(a(t')\tilde{\rho}_S(t')a^\dagger(t) - a^\dagger(t)a(t')\tilde{\rho}_S(t')\right) + h.c.\,,$$

where $c^{(1)}(\tau)$ and $c^{(2)}(\tau)$ are bath correlation functions defined as

$$\begin{aligned} c^{(1)}(\tau) &:= \left\langle C^\dagger(\tau)C\right\rangle = \sum_k \gamma_k^2 \mathcal{N}_b(\omega_k) e^{i(\omega_k-\omega_0)\tau} \,, \\ c^{(2)}(\tau) &:= \left\langle C(\tau)C^\dagger\right\rangle = \sum_k \gamma_k^2 [1+\mathcal{N}_b(\omega_k)] e^{-i(\omega_k-\omega_0)\tau} \,. \end{aligned} \tag{3.184}$$

Next step is the Markovian assumption (see Sec. 2.1.2.1) $\tau_{\rm E} \ll \delta t$, where δt is the typical time scale of the state in interaction picture and $\tau_{\rm E}$ is the bath memory time scale, i.e. the characteristic width of the bath correlation functions (3.184). Such time scale separation allows to replace in Eq. (3.183) the upper integration bound with $+\infty$ and to neglect the $\tau := t-t'$ dependence of the state $\tilde{\rho}_{\rm S}$, leading to the Redfield equation (interaction picture):

$$\begin{aligned} \dot{\tilde{\rho}}_{\rm S}(t) \simeq \int_0^\infty d\tau \Big[& c^{(1)}(\tau) \left(a^\dagger(t-\tau)\tilde{\rho}_{\rm S}(t)a(t) - a(t)a^\dagger(t-\tau)\tilde{\rho}_{\rm S}(t) \right) \\ & + c^{(2)}(\tau) \left(a(t-\tau)\tilde{\rho}_{\rm S}(t)a^\dagger(t) - a^\dagger(t)a(t-\tau)\tilde{\rho}_{\rm S}(t) \right) \Big] + h.c. \,. \end{aligned} \tag{3.185}$$

As described in Ref. Hofer et al. (2017), if the bath correlation functions are narrow enough with respect to the internal coupling time scale, i.e. $g\tau_{\rm E} \ll 1$, in Eq. (3.185) one can approximate $a(t-\tau) \approx a(t)$ obtaining the interaction picture version of the local ME (3.150), which is in Lindblad form without the need of any secular approximation. Alternatively, passing to the eigenmode basis of Eq. (3.124), Eq. (3.185) can be equivalently written as

$$\begin{aligned} \dot{\tilde{\rho}}_{\rm S}(t) = \frac{1}{2} \sum_{\sigma,\sigma'} \Big[& \Omega_\sigma^{(1)} e^{i(\sigma-\sigma')gt} \left(\gamma_\sigma^\dagger \tilde{\rho}_{\rm S}(t) \gamma_{\sigma'} - \gamma_{\sigma'} \gamma_\sigma^\dagger \tilde{\rho}_{\rm S}(t) \right) \\ & + \Omega_{\sigma'}^{(2)} e^{i(\sigma-\sigma')gt} \left(\gamma_{\sigma'} \tilde{\rho}_{\rm S}(t) \gamma_\sigma^\dagger - \gamma_\sigma^\dagger \gamma_{\sigma'} \tilde{\rho}_{\rm S}(t) \right) \Big] + h.c. \end{aligned} \tag{3.186}$$

where

$$\Omega_\sigma^{(1)} := \int_0^\infty d\tau c^{(1)}(\tau) e^{-i\sigma g\tau} \,, \tag{3.187}$$

$$\Omega_{\sigma'}^{(2)} := \int_0^\infty d\tau c^{(2)}(\tau) e^{i\sigma' g\tau} \,. \tag{3.188}$$

Last step is to perform a coarse-grain average on Eq. (3.186) over a time interval $\Delta t \ll \delta t$, which amounts in applying the following substitution

$$e^{i(\sigma-\sigma')gt} \longrightarrow \frac{1}{\Delta t} \int_{t-\Delta t/2}^{t+\Delta t/2} ds \, e^{i(\sigma-\sigma')gs} = e^{i(\sigma-\sigma')gt} \mathrm{sinc}\left(\frac{(\sigma-\sigma')g\Delta t}{2} \right), \tag{3.189}$$

without affecting the system state in interaction picture. Equation (3.134) is eventually obtained by passing to the Schrödinger picture. Indeed the Lamb-shift and the dissipator coefficients of Eqs. (3.137) and (3.138) are related to the quantities $\Omega_\sigma^{(i)}$ as

$$\gamma_{\sigma\sigma'}^{(i)} = \frac{1}{2}(\Omega_\sigma^{(i)} + \Omega_{\sigma'}^{(i)*}) \,, \tag{3.190}$$

$$\eta_{\sigma\sigma'}^{(i)} = \frac{1}{4i}(\Omega_\sigma^{(i)} - \Omega_{\sigma'}^{(i)*}) \,. \tag{3.191}$$

3.3.4.2 Completely positive map requirement for the coarse-grained Redfield equation

To discuss the complete positivity condition for the coarse-grained Redfield equation let us observe that its dissipator is given by the last two lines in the right-hand-side of Eq. (3.134). Following Sec. 3.1 [Ref. Farina and Giovannetti (2019)] we write them as

$$\sum_{i,\sigma,i',\sigma'} \gamma_{i'\sigma',i\sigma} \left(\mathcal{A}_{i',\sigma'}^\dagger \rho_{\rm S}(t) \mathcal{A}_{i,\sigma} - \frac{1}{2} \Big[\mathcal{A}_{i,\sigma} \mathcal{A}_{i',\sigma'}^\dagger \,,\, \rho_{\rm S}(t) \Big]_+ \right) ,$$

with $\mathcal{A}_{1,\sigma} = \gamma_\sigma$, $\mathcal{A}_{2,\sigma} = \gamma_\sigma^\dagger$, and $\gamma_{i'\sigma',i\sigma}$ being the elements of the 4×4 hermitian matrix

$$\gamma_{I,J} = \begin{pmatrix} \gamma_{++}^{(1)} & \gamma_{+-}^{(1)} S_{+-}^{(\Delta t)} & 0 & 0 \\ \gamma_{-+}^{(1)} S_{+-}^{(\Delta t)} & \gamma_{--}^{(1)} & 0 & 0 \\ 0 & 0 & \gamma_{++}^{(2)} & \gamma_{+-}^{(2)} S_{+-}^{(\Delta t)} \\ 0 & 0 & \gamma_{-+}^{(2)} S_{+-}^{(\Delta t)} & \gamma_{--}^{(2)} \end{pmatrix} . \tag{3.192}$$

Complete positivity of the evolution described by Eq. (3.134) can now be guaranteed by imposing the positiveness of the spectrum of (3.192), a condition which by explicit diagonalization leads to Eq. (3.144).

3.3.4.3 Covariance matrices

Expressed in terms of the system canonical coordinates

$$\begin{aligned} x_{\rm A} &:= (a + a^\dagger)/\sqrt{2} \,, & p_{\rm A} &:= (a - a^\dagger)/(\sqrt{2}i) \,, \\ x_{\rm B} &:= (b + b^\dagger)/\sqrt{2} \,, & p_{\rm B} &:= (b - b^\dagger)/(\sqrt{2}i) \,, \end{aligned} \tag{3.193}$$

the covariance matrix $\Sigma_{\rm S}$ associated with the quantum state $\rho_{\rm S}$ of the two-mode system $\mathcal{S}$ is defined as the 4×4 real hermitian matrix

$$[\Sigma_{\rm S}]_{\alpha\beta} := \left\langle \Big[\boldsymbol{r}_{{\rm S},\alpha} - \langle \boldsymbol{r}_{{\rm S},\alpha} \rangle , \boldsymbol{r}_{{\rm S},\beta} - \langle \boldsymbol{r}_{{\rm S},\beta} \rangle \Big]_+ \right\rangle \,, \tag{3.194}$$

where as usual we adopt the shorthand notation $\langle \cdots \rangle := \mathrm{Tr}[\cdots \rho_{\mathrm{S}}]$, and where $\boldsymbol{r}_{\mathrm{S},\alpha}$ is the α-th component of the operator vector $\boldsymbol{r}_{\mathrm{S}} := (x_{\mathrm{A}}, p_{\mathrm{A}}, x_{\mathrm{B}}, p_{\mathrm{B}})^T$. In this notation the symplectic form of the system is defined by the matrix Ω_{S} of elements

$$\Omega_{\mathrm{S}} := \begin{pmatrix} 0 & 1 & 0 & 0 \\ -1 & 0 & 0 & 0 \\ 0 & 0 & 0 & 1 \\ 0 & 0 & -1 & 0 \end{pmatrix} , \tag{3.195}$$

which embodies the canonical commutation rules of the model via the identity $\langle [\boldsymbol{r}_{\mathrm{S},\alpha}, \boldsymbol{r}_{\mathrm{S},\beta}]_- \rangle = i[\Omega_{\mathrm{S}}]_{\alpha\beta}$. From the Robertson-Schrödinger uncertainty relation (Serafini 2017), it hence follows that for all choices of ρ_{S} we must have that the matrix $\Sigma_{\mathrm{S}} + i\Omega_{\mathrm{S}}$ is non-negative or equivalently that the following inequality must hold

$$\min\{ \text{ eigenvalues}[\Sigma_{\mathrm{S}} + i\Omega_{\mathrm{S}}] \} \geq 0 . \tag{3.196}$$

Equation (3.196) is at the origin of the study we presented in Fig. 3.10. We notice indeed that introducing the unitary matrix

$$\mathcal{V} := \frac{1}{2} \begin{pmatrix} 1 & 1 & 1 & 1 \\ -i & i & -i & i \\ 1 & 1 & -1 & -1 \\ -i & i & i & -i \end{pmatrix} , \tag{3.197}$$

from Eq. (3.124) the following identity holds,

$$\boldsymbol{r}_{\mathrm{S}} \;\; = \;\; \mathcal{V} \boldsymbol{\Gamma}_{\mathrm{S}} , \tag{3.198}$$

with $\boldsymbol{\Gamma}_{\mathrm{S}}$ the operator vector introduced in Eq. (3.169), which in turn implies

$$\Sigma_{\mathrm{S}} = \mathcal{V} \Gamma_{\mathrm{S}} \mathcal{V}^{\dagger} , \qquad \Omega_{\mathrm{S}} = \mathcal{V} \Xi_{\mathrm{S}} \mathcal{V}^{\dagger} , \tag{3.199}$$

with Ξ_{S} as in Eq. (3.170). Accordingly, we get

$$\Sigma_{\mathrm{S}} + i\Omega_{\mathrm{S}} = \mathcal{V} \left(\Gamma_{\mathrm{S}} + i\Xi_{\mathrm{S}} \right) \mathcal{V}^{\dagger} , \tag{3.200}$$

which finally allows us to translate Eq. (3.196) into the positivity condition for the quantity $\lambda_c(t)$ introduced in Eq (3.168).

Notice finally that the unitary relations (3.199) are also at the origin of Eqs. (3.176) and (3.177) which we derived from Marian and Marian (2012), González et al. (2017),

Hofer et al. (2017) via the identities

$$\begin{aligned} \det[\Gamma_{\rm S}^{(1)} + \Gamma_{\rm S}^{(2)}] &= \det[\Sigma_{\rm S}^{(1)} + \Sigma_{\rm S}^{(2)}] \,, \\ \det[\Xi_{\rm S}\, \Gamma_{\rm S}^{(1)}\, \Xi_{\rm S}\, \Gamma_{\rm S}^{(2)} - \mathbb{1}_4] &= \det[\Omega_{\rm S}\, \Sigma_{\rm S}^{(1)}\, \Omega_{\rm S}\, \Sigma_{\rm S}^{(2)} - \mathbb{1}_4] \,, \\ \det[\Gamma_{\rm S}^{(j)} + i\Xi_{\rm S}] &= \det[\Sigma_{\rm S}^{(j)} + i\Omega_{\rm S}] \,, \end{aligned} \tag{3.201}$$

where, for $j = 1, 2$, $\Gamma_{\rm S}^{(j)}$ and $\Sigma_{\rm S}^{(j)}$ represent the covariance matrices (3.169) and (3.194) of the matrices $\rho_{\rm S}^{(j)}$.

3.3.4.4 The exact model

In this section, following a procedure similar to Rivas et al. (2010), we discuss how to explicitly solve the exact dynamics of the Hamiltonian model for the joint system $\mathcal{S}+\mathcal{E}$.

Passing to the canonical variables of the full model, i.e. introducing the operators $x_{\rm A} = (a + a^\dagger)/\sqrt{2}$, $p_{\rm A} = (a - a^\dagger)/(\sqrt{2}i)$, $x_{\rm B} = (b + b^\dagger)/\sqrt{2}$, $p_{\rm B} = (b - b^\dagger)/(\sqrt{2}i)$ as in Eq. (3.193) and $x_k = (c_k + c_k^\dagger)/\sqrt{2}$, $p_k = (c_k - c_k^\dagger)/(\sqrt{2}i)$, the Hamiltonian (3.126) of $\mathcal{S} + \mathcal{E}$ can be written as

$$H = \frac{1}{2} \boldsymbol{r}^T \mathcal{H} \boldsymbol{r} + \text{const} \,. \tag{3.202}$$

The vector operator $\boldsymbol{r}$ is the generalization of $\boldsymbol{r}_{\rm S}$ introduced in Sec. 3.3.4.3 that now contains the canonical coordinates of all the $\mathcal{S} + \mathcal{E}$ modes, i.e.

$$\boldsymbol{r} \;=\; (x_{\rm A}, p_{\rm A}, x_{\rm B}, p_{\rm B}, x_1, p_1, ..., x_M, p_M)^T \,, \tag{3.203}$$

and $\mathcal{H}$ is a real symmetric $(2M+4) \times (2M+4)$ matrix, having non null elements only on the diagonal and on the first two rows and on the first two columns. This is because only the sub-system A is microscopically attached to the thermal bath:

$$\mathcal{H} = \begin{pmatrix} \omega_{\rm A} & 0 & g & 0 & \gamma_1 & 0 & \dots & \gamma_M & 0 \\ 0 & \omega_{\rm A} & 0 & g & 0 & \gamma_1 & \dots & 0 & \gamma_M \\ g & 0 & \omega_{\rm B} & 0 & 0 & 0 & \dots & 0 & 0 \\ 0 & g & 0 & \omega_{\rm B} & 0 & 0 & \dots & 0 & 0 \\ \gamma_1 & 0 & 0 & 0 & \omega_1 & 0 & \dots & 0 & 0 \\ 0 & \gamma_1 & 0 & 0 & 0 & \omega_1 & \dots & 0 & 0 \\ \vdots & \vdots & \vdots & \vdots & \vdots & \vdots & \ddots & \vdots & \vdots \\ \gamma_M & 0 & 0 & 0 & 0 & 0 & \dots & \omega_M & 0 \\ 0 & \gamma_M & 0 & 0 & 0 & 0 & \dots & 0 & \omega_M \end{pmatrix} . \tag{3.204}$$

Exploiting the above construction the expectation value of $\boldsymbol{r}$ can now be shown to evolve

in time as (Serafini 2017)

$$\langle \boldsymbol{r}(t) \rangle := \mathrm{Tr}[\boldsymbol{r}\rho_{\mathrm{SE}}(t)] = e^{\Omega \mathcal{H} t} \langle \boldsymbol{r}(0) \rangle \ , \tag{3.205}$$

where Ω is the symplectic form of the entire model, i.e. the $(2M+4) \times (2M+4)$ matrix

$$\Omega := \bigoplus_{i=1}^{M+2} \begin{pmatrix} 0 & 1 \\ -1 & 0 \end{pmatrix} \ , \tag{3.206}$$

whose elements embody the canonical commutation rules of the entire $\mathcal{S}+\mathcal{E}$ system via the identity $\langle [\boldsymbol{r}_\alpha, \boldsymbol{r}_\beta]_- \rangle = i\Omega_{\alpha\beta}$. Similarly the covariance matrix of elements

$$\begin{aligned} \Sigma_{\alpha\beta}(t) &:= \mathrm{Tr}\left[\Big[\boldsymbol{r}_\alpha - \langle \boldsymbol{r}_\alpha(t) \rangle, \boldsymbol{r}_\beta - \langle \boldsymbol{r}_\beta(t) \rangle \Big]_+ \rho_{\mathrm{SE}}(t) \right] \\ &= \left\langle \Big[\boldsymbol{r}_\alpha(t) - \langle \boldsymbol{r}_\alpha(t) \rangle, \boldsymbol{r}_\beta(t) - \langle \boldsymbol{r}_\beta(t) \rangle \Big]_+ \right\rangle , \end{aligned} \tag{3.207}$$

can be shown to evolve as

$$\Sigma(t) = e^{\Omega \mathcal{H} t} \Sigma(0) e^{\mathcal{H} \Omega^T t} \ . \tag{3.208}$$

For future reference it is worth stressing that the 4×4 principal minor of the matrix $\Sigma(t)$ (i.e. the sub-matrix obtained from the latter by taking the upper left 4×4 part) corresponds to the covariance matrix $\Sigma_{\mathrm{S}}(t)$ of the $\mathcal{S}$ system alone, whose elements can be formally expressed as in Eq. (3.194).

In the evaluation of Eqs. (3.205), (3.208) one can resort to the exact diagonalization of the Hermitian matrix $\mathcal{M}$ defined as

$$\mathcal{M} := i\Omega\mathcal{H} \ . \tag{3.209}$$

Calling $(g_1, \ldots, g_{2M+4})$ the eigenvalues of $\mathcal{M}$ and

$$V_{\alpha\beta} := [\mathbf{g}^{(\beta)}]_\alpha \tag{3.210}$$

the unitary matrix whose columns are the normalized eigenvectors $\mathbf{g}^{(\alpha)}$ corresponding to the eigenvalues g_α, the diagonal form of the matrix $\mathcal{M}$ is obtained as:

$$\mathrm{diag}(g_1, \ldots, g_{2M+4}) = V^\dagger \mathcal{M} V \ . \tag{3.211}$$

Accordingly, we can now rewrite Eqs. (3.205), (3.208) in the form

$$\begin{aligned} \langle \boldsymbol{r}(t) \rangle &= V E_-(t) V^\dagger \langle \boldsymbol{r}(0) \rangle \\ \Sigma(t) &= V E_-(t) V^\dagger \Sigma(0) V E_+(t) V^\dagger \ , \end{aligned} \tag{3.212}$$

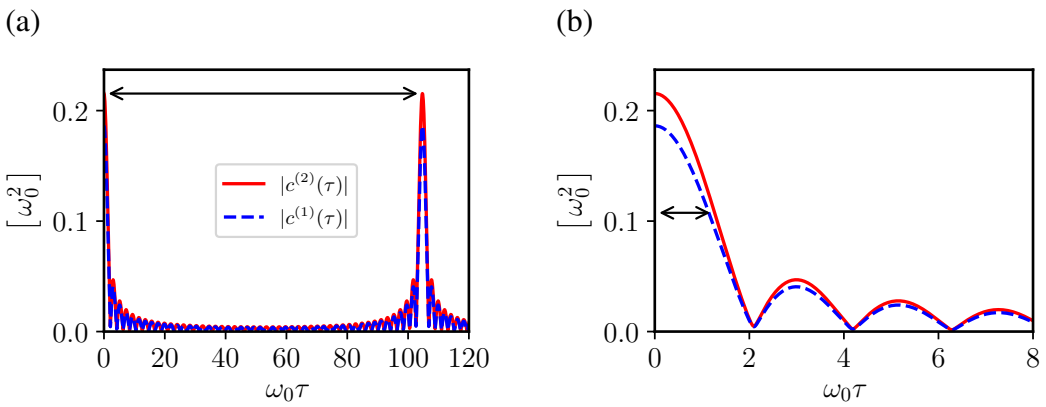

Fig. 3.14 Plot of the modulus of the bath correlation functions $c^{(1)}(\tau)$ and $c^{(2)}(\tau)$ (units ω_0^2) defined in Eq. (3.184) that provide estimations of the recurrence time (a) and of the memory time (b). In Panel (a) we take $M = 50$ oscillators in the thermal bath. We chose the parameters $\mathcal{N}_b(\omega_0) = 10$, $\kappa(\omega_0) = 0.04\omega_0$, $\omega_c = 3\omega_0$ and $\alpha = 1$.

with

$$E_{\mp}(t) = \mathrm{diag}\left(e^{\mp i g_1 t}, \ldots, e^{\mp i g_{2M+4} t}\right) \ . \tag{3.213}$$

In summary, the exact dynamics is obtained thanks to the numerical diagonalization of the matrix $\mathcal{M}$ of Eq. (3.209) and by performing the matrix multiplications in Eq. (3.212). Regarding the initial conditions, we observe that in the case of the input state we have selected in Eqs. (3.131), (3.132) and (3.154), the initial covariance matrix reads as

$$\Sigma(0) = \begin{pmatrix} \mathbb{1}_2 & \mathbf{0} & \mathbf{0} & \ldots & \mathbf{0} \\ \mathbf{0} & \mathbb{1}_2 & \mathbf{0} & \ldots & \mathbf{0} \\ \mathbf{0} & \mathbf{0} & [2\mathcal{N}_b(\omega_1)+1]\mathbb{1}_2 & \ldots & \mathbf{0} \\ \vdots & \vdots & \vdots & \ddots & \vdots \\ \mathbf{0} & \mathbf{0} & \mathbf{0} & \ldots & [2\mathcal{N}_b(\omega_M)+1]\mathbb{1}_2 \end{pmatrix} \tag{3.214}$$

with $\mathbb{1}_2$ being the 2×2 identity matrix and $\mathcal{N}_b(\omega_k)$ being the Bose-Einstein mean occupation numbers introduced in Eq. (3.143). Regarding the first order moments instead, since $\langle \boldsymbol{r}(0) \rangle = 0$ the evolution law of Eq. (3.205) leads to $\langle \boldsymbol{r}(t) \rangle = 0$ for all $t \geq 0$.

Memory and recurrence time scales When resorting to numerical methods in solving the exact Hamiltonian model one should be aware of the fact that since it involves a finite number of parties (i.e. the system modes A and B and the M environmental modes), it will be characterized by a recurrence time scale T_{rec} that, due to the various approximations involved in their derivation, leave no trace in the corresponding ME expressions. An estimation of such quantity can be retrieved directly from the periodicity

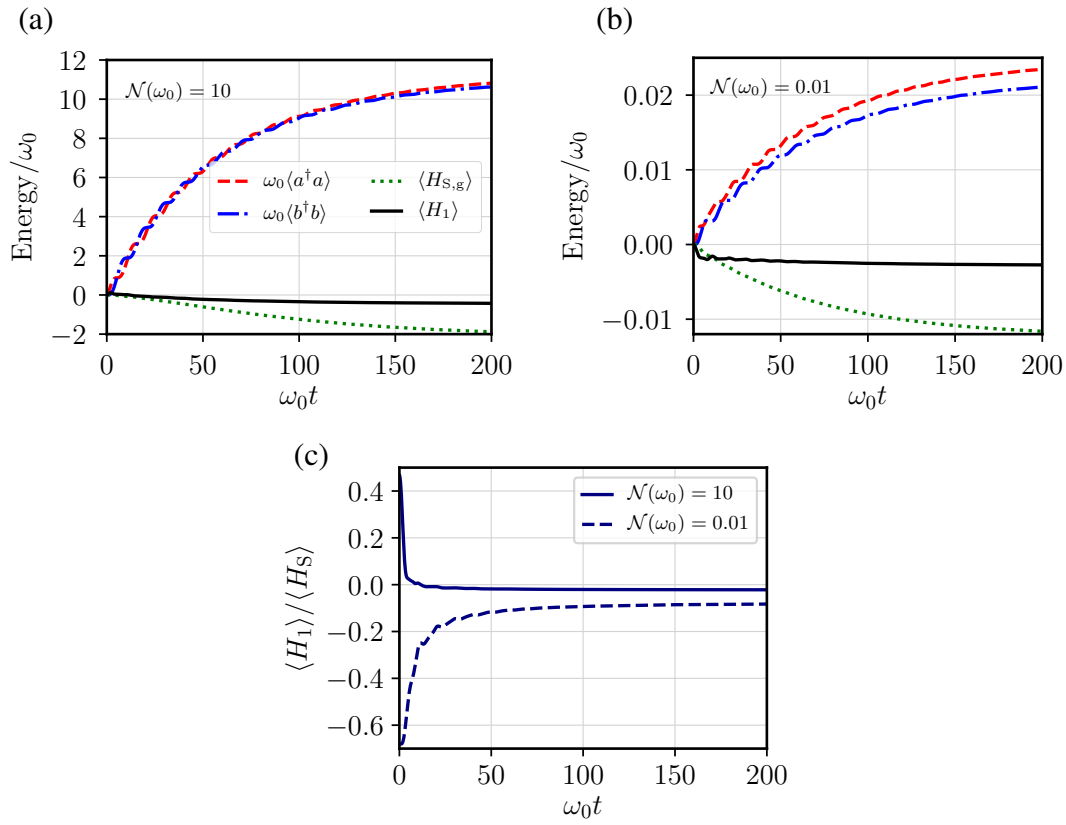

Fig. 3.15 Time evolution of the average components of the Hamiltonian (3.126) obtained by numerically solving the exact dynamics of the full $\mathcal{S}+\mathcal{E}$ model in the high temperature regime $\mathcal{N}_b(\omega_0) = 10$ (a), and in the low temperature regime $\mathcal{N}_b(\omega_0) = 0.01$ (b). As indicated by the legend the red dashed line corresponds to the local energy of mode A; the blue dot-dashed line to the local energy term of mode B; the green dotted line to the Hamiltonian A-B coupling term; and finally the black full line to the Hamiltonian $\mathcal{S}-\mathcal{E}$ coupling term. Notice that as the temperature decreases the incidence of the system-environment coupling gets relatively more consistent: this is explicitly shown in panel (c) where we report the ratio $\langle H_1\rangle/\langle H_{\mathrm{S}}\rangle$ for the two regimes. In all the plots we assumed $g = 0.3\omega_0$, $\kappa(\omega_0) = 0.04\omega_0$, $\omega_c = 3\omega_0$, and $\alpha = 1$.

of the correlation functions of Eq. (3.184) which leads us to (see Panel (a) of Fig. 3.14):

$$T_{\rm rec} = 2\pi M/\omega_c \,. \tag{3.215}$$

The choice of the parameters $\omega_c = 3\omega_0$ and $M \approx 400$ (Hofer et al. 2017) ensures that the discretization does not play any role in the time window we have considered for all the plots.

The width of the correlation functions (3.184) also plays an important role in the model: it yields the time $\tau_{\rm E}$ which takes for the information that emerges from the system to get lost into the environment and never coming back (Breuer et al. 2002). Such time scale can't be resolved by any approximation we have discussed so far, because of the Markovian assumption which is present in all of them. The estimation of this time scale is given by the half width at half maximum (see Panel (b) of Fig. 3.14) of $|c^{(1)}(\tau)|$ and $|c^{(2)}(\tau)|$. For $\mathcal{N}_b(\omega_0) = 10$ we get

$$\tau_{\rm E} \approx 3.8/\omega_c \,. \tag{3.216}$$

Low temperature effects It is well known that in the low temperature regime correlation effects between the bath and the system tent to arise, challenging the Born approximation used in the derivation of the Markovian MEs (Hovhannisyan et al. 2020). An evidence of this fact is presented in Fig. 3.15 where the time evolution of the average components of the Hamiltonian (3.126) are presented for two different choices of the parameter $1/\beta$.

3.3.4.5 On the thermalization of the system eigenmodes

We show here the dual counterparts of the moments reported in Figs. 3.7 and 3.8 in the basis of the eigenmodes (3.124), making clearer when these eigenmodes reach the correct thermalization or not depending on the implemented approximation. The second order moments in the a, b basis and the ones in the γ_+, γ_- basis are related each other as

$$\frac{1}{2}(\langle a^\dagger a\rangle - \langle b^\dagger b\rangle) = {\rm Re}\langle \gamma_-\gamma_+^\dagger\rangle \,, \tag{3.217}$$

$${\rm Im}\langle ab^\dagger\rangle = {\rm Im}\langle \gamma_-\gamma_+^\dagger\rangle \,, \tag{3.218}$$

$${\rm Re}\langle ab^\dagger\rangle = \frac{1}{2}(\langle \gamma_+^\dagger\gamma_+\rangle - \langle \gamma_-^\dagger\gamma_-\rangle) \,, \tag{3.219}$$

$$\langle a^\dagger a\rangle + \langle b^\dagger b\rangle = \langle \gamma_+^\dagger\gamma_+\rangle + \langle \gamma_-^\dagger\gamma_-\rangle \,. \tag{3.220}$$

The steady state (3.161) is what one expects from thermodynamics. It implies $\langle \gamma_\pm^\dagger\gamma_\pm\rangle(\infty) = \mathcal{N}(\omega_\pm)$, $\langle \gamma_-\gamma_+^\dagger\rangle(\infty) = 0$. This result is captured by applying the global approximation

(see Eqs. (3.158)), which under the initial conditions (3.157) gives

$$\langle \gamma_- \gamma_+^\dagger \rangle \Big|_{(\mathrm{glob})}(t) = 0, \tag{3.221}$$

$$\langle \gamma_\pm^\dagger \gamma_\pm \rangle \Big|_{(\mathrm{glob})}(t) = \mathcal{N}_b(\omega_\pm) \left(1 - e^{-\frac{1}{2}\kappa(\omega_\pm)t}\right) . \tag{3.222}$$

On the other hand, the local approximation fails just about the steady state properties. As discussed in Farina, Andolina, Mari, Polini and Giovannetti (2019), under the same initial conditions and when the Lamb-shift correction $\delta\omega_{\mathrm{A}}$ can be neglected, the local ME (see Eqs. (3.159)) leads to

$$\mathrm{Re}\langle \gamma_- \gamma_+^\dagger \rangle \Big|_{(\mathrm{loc})}(t) = \mathcal{N}_b(\omega_0) \frac{e^{-\kappa(\omega_0)t/2}}{\epsilon} \kappa(\omega_0) \sin(\epsilon t/2) ,$$

$$\mathrm{Im}\langle \gamma_- \gamma_+^\dagger \rangle \Big|_{(\mathrm{loc})}(t) = 4\mathcal{N}_b(\omega_0)\kappa(\omega_0) g \frac{e^{-\kappa(\omega_0)t/2}}{\epsilon^2} [1 - \cos(\epsilon t/2)] ,$$

$$\langle \gamma_\pm^\dagger \gamma_\pm \rangle \Big|_{(\mathrm{loc})}(t) = \mathcal{N}_b(\omega_0) \{1 - \frac{e^{-\kappa(\omega_0)t/2}}{\epsilon^2} \left[16g^2 - \kappa(\omega_0)^2 \cos(\epsilon t/2)\right]\} ,$$

with

$$\epsilon := \sqrt{(4g)^2 - \kappa(\omega_0)^2}. \tag{3.223}$$

Using the relations (3.217)-(3.220), the above equations imply in the a, b basis:

$$\langle a^\dagger a \rangle \Big|_{(\mathrm{loc})}(t) = \mathcal{N}_b(\omega_0) \{1 - \frac{e^{-\kappa(\omega_0)t/2}}{\epsilon^2} \left[16g^2 - \kappa(\omega_0)\epsilon \sin(\epsilon t/2) - \kappa(\omega_0)^2 \cos(\epsilon t/2)\right]\} , \tag{3.224}$$

$$\langle b^\dagger b \rangle \Big|_{(\mathrm{loc})}(t) = \mathcal{N}_b(\omega_0) \{1 - \frac{e^{-\kappa(\omega_0)t/2}}{\epsilon^2} \left[16g^2 + \kappa(\omega_0)\epsilon \sin(\epsilon t/2) - \kappa(\omega_0)^2 \cos(\epsilon t/2)\right]\} , \tag{3.225}$$

$$\mathrm{Im}\langle a b^\dagger \rangle \Big|_{(\mathrm{loc})}(t) = 4\mathcal{N}_b(\omega_0)\kappa(\omega_0) g \frac{e^{-\kappa(\omega_0)t/2}}{\epsilon^2} [1 - \cos(\epsilon t/2)] ,$$

$$\mathrm{Re}\langle a b^\dagger \rangle \Big|_{(\mathrm{loc})}(t) = 0 ,$$

i.e.

$$\langle H_{\mathrm{S,g}} \rangle \Big|_{(\mathrm{loc})}(t) = 0 . \tag{3.226}$$

Furthermore, Eqs. (3.159) can be written in the a, b basis as

$$\begin{aligned}
\frac{d}{dt}\langle a^\dagger a\rangle(t) &= -2g\mathrm{Im}\langle ab^\dagger\rangle(t) + \kappa(\omega_0)[\mathcal{N}_b(\omega_0) - \langle a^\dagger a\rangle(t)] \,, \\
\frac{d}{dt}\langle b^\dagger b\rangle(t) &= 2g\mathrm{Im}\langle ab^\dagger\rangle(t) \,, \\
\frac{d}{dt}\langle ab^\dagger\rangle(t) &= ig[\langle a^\dagger a\rangle(t) - \langle b^\dagger b\rangle(t)] - \frac{1}{2}\kappa(\omega_0)\langle ab^\dagger\rangle(t) - i\,\delta\omega_{\mathrm{A}}\,\langle ab^\dagger\rangle(t) \,.
\end{aligned}$$

The last equations are known results (Hofer et al. 2017, Farina, Andolina, Mari, Polini and Giovannetti 2019) that explicitly show how in the local approach having non-null $\mathrm{Im}\langle ab^\dagger\rangle(t)$ (and hence $\mathrm{Im}\langle\gamma_-\gamma_+^\dagger\rangle(t)$ for (3.218)) is required for the description of the dynamical coherent energy exchanges between A and B. Moreover, Eq. (3.217) shows that the real part of $\langle\gamma_-\gamma_+^\dagger\rangle(t)$ controls the difference between $\langle a^\dagger a\rangle(t)$ and $\langle b^\dagger b\rangle(t)$. Both the terms $\mathrm{Im}\langle\gamma_-\gamma_+^\dagger\rangle(t)$ and $\mathrm{Re}\langle\gamma_-\gamma_+^\dagger\rangle(t)$ are well approximated by the local ME and completely neglected by the global ME, see Panels (a) and (b) of Fig. 3.16. The fact that the global ME predicts $\langle\gamma_-\gamma_+^\dagger\rangle(t) = 0$ is a consequence of the cancellation of the oscillating terms in Eq. (3.186) via indiscriminate coarse-grain averaging. This decouples equations (3.156), generating (3.158). In Fig. 3.16 we plot the moments in the eigenmodes basis, comparing the results obtained by the global, local, convex mixture, Redfield, CP-Redfield approximations with the ones predicted by the exact dynamics, by including this time also the Lamb-shift contributions. In the local case for instance the Lambshift implies a tiny splitting between $\langle\gamma_+^\dagger\gamma_+\rangle\Big|_{(\mathrm{loc})}(t)$ and $\langle\gamma_-^\dagger\gamma_-\rangle\Big|_{(\mathrm{loc})}(t)$ at short time scales (connected to a small but non-vanishing $\mathrm{Re}\langle ab^\dagger\rangle\Big|_{(\mathrm{loc})}(t)$, see Eq. (3.219)). Again, the convex mixture of the local and global approximations of Eq. (3.153) and the CP-Redfield equation yield a very good approximation either of the transient than of the steady state properties.

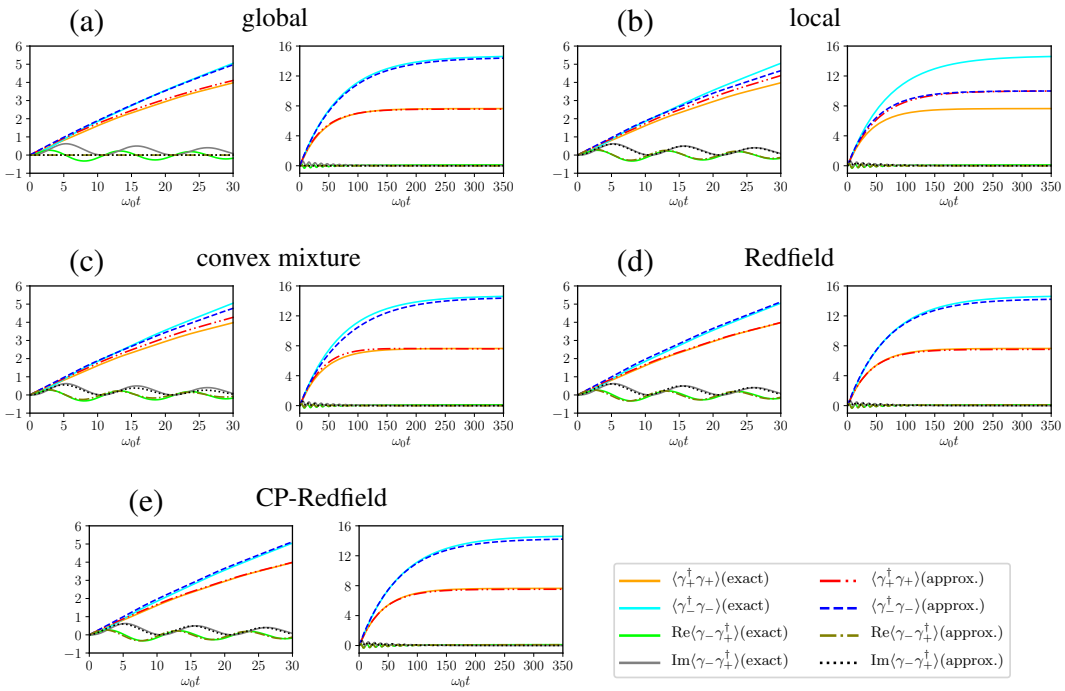

Fig. 3.16 Comparison of second order moments in the eigenmodes basis evaluated using the global (a), local (b), convex mixture (c), Redfield (d), CP-Redfield (e) approximations with the ones predicted by the exact dynamics. As indicated by the legend continuous lines in the plots represent the quantities computed by solving the exact $\mathcal{S}+\mathcal{E}$ Hamiltonian model (3.126); dotted and dashed lines instead refer to the approximated solutions. Each panel contains two plots corresponding each to shorter (left) and longer (right) time scales. We chose the parameters $\mathcal{N}_b(\omega_0) = 10$, $g = 0.3\omega_0$, $\kappa(\omega_0) = 0.04\omega_0$, $\omega_c = 3\omega_0$ and $\alpha = 1$.

3.4 Conclusions

Starting from the Redfield equation the secular approximation is a standard procedure to ensure completely positive dynamics and is equivalent to an infinitely large choice of the coarse grain time scale. On the contrary the partial implementation of the secular approximation keeps such time scale finite. Using a general formalism we found sufficient conditions to guarantee the complete positivity of the Redfield equation, including a tight bound on the coarse-grain time interval. Furthermore we explicitly show that non-secular terms can determine non-commutation between the Hamiltonian and the dissipative parts of the generator. We thus provided an example by specifying the analysis to a qubit interacting with a bosonic thermal environment via dipole-like interaction.

The corrected Redfield equation was also tested in the context of multipartite Markovian open quantum systems, where it is discussed in literature [6] whether the local dissipator or the global one (i.e. the one obtained via the secular approximation) is more suitable to effectively reproduce the system dynamics. In Sec. 3.3 we have treated a case where the system is composed of two interacting harmonic oscillators A and B, with only A interacting with a thermal bath - collection of other harmonic oscillators - and we have analyzed the equilibration process of the system initially in the ground state with the finite bath temperature. We have shown that the "completely positive Redfield" equation - i.e. the cured version of the Redfield equation by means of coarse-grain averaging as illustrated in Sec. 3.1 - and an appropriate time-dependent convex mixture of the local and global solutions - see Eq. (3.153) - give rise to the most accurate approximations of the exact system dynamics, both during the time transient and for the steady state properties, going beyond the pure local and global approximations. The convex mixture of the local and global channels has been introduced phenomenologically for allowing at the same time coherent local energy exchange at short time scales between A and B and the steady state expected from the thermodynamics at long time scales, i.e. the global Gibbsian state. Future developments on this route may concern the search of a microscopic derivation of this (non-Markovian) quantum channel.

[6] See, e.g. , Hofer et al. (2017), Rivas et al. (2010), González et al. (2017), Cattaneo et al. (2019).

CHAPTER 4

Quantum batteries: an open system approach

The local master equation approach described in the previous Chapter will be used to schematize the energy charging of an open quantum battery.
Building up from the observations of Sec. 2.2, we introduce a further generalization of the quantum battery/quantum charger model by explicitly embedding the whole system into an external environment whose action is effectively described in terms of a master equation. Accordingly, and at variance with previous proposals Ferraro et al. (2018), Andolina et al. (2018, 2019) which deal with models which are intrinsically closed, in our approach the energy meant to be transferred to the quantum battery is not assumed to sit initially on the charger A. Instead, it is dynamically injected into the system thanks to the presence of an external source E, either via thermalization or via coherent driving induced by external control, the ancilla A merely playing the role of an effective transducer capable to convert such inherently classical inputs into "quantum signals" for B. In this context, for different implementations of the A and B systems, we explicitly compute the total energy transferred to the battery and the fraction of it that turns out to be useful in terms of extractable work (a topic treated in Sec. 2.2.1). Specifically, we are interested in studying the different ways in which the thermal and coherent driving mechanisms contribute to the process, enlightening possible cross-talking effects between the two. Interestingly enough, while typically the presence of thermal pumping tends to reduce the fraction of stored energy which can be extracted as work, in some implementations which exhibit effective nonlinearities in the coupling between A and B, we find evidences of a positive interplay which, for an assigned intensity of the coherent driving force, tends to increase the performances of the quantum battery, an effect which is reminding us of the noise assisted energy transfer observed in quantum biology (Mohseni et al. 2008, Plenio and Huelga 2008).
This Chapter is organized as follows. In Sec. 4.1 we introduce the general model and the figures of merit we are going to analyze. Sec. 4.2 reports the results we obtained when both the charger A and the battery B are harmonic oscillators, while Sec. 4.3 deals instead with the two-qubit scenario. Finally, results for the hybrid case where A is a harmonic oscillator and B is a qubit are reported in Sec. 4.4. A brief summary and our main conclusions are reported in Sec. 4.5.

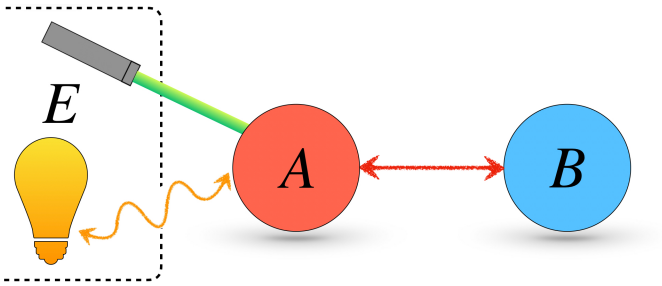

Fig. 4.1 Pictorial representation of the model analyzed in this work. Here, energy from the external world E flows into the ancillary system A, which acts as a classical-to-quantum transducer for B (the quantum battery). The subsystems A and B interact via a time-dependent coupling, which is switched on during the charging interval $[0, \tau]$ only. In our model, the E-A coupling may either occur via the interaction with a thermal source (represented by the yellow lamp), or coherently via the modulation of the local Hamiltonian of A (represented by the green laser), or both.

We stress that all the models we discuss here are experimentally realizable and of current interest. Coupling two qubits is now-day routine in circuit quantum electrodynamics experiments, where superconducting qubits can be put in interaction via lumped circuit elements. In particular the coupling is capacitive in case of charge and phase qubits, and inductive for flux qubits allowing nearest-neighbour interaction between qubits and the intesity of the coupling can be modified via detuning techniques (Majer et al. 2007). The case of two quantum harmonic oscillators can be realized either by coupling an optical cavity with a mechanical resonator via radiation pressure (Verhagen et al. 2012, Mari et al. 2015) or using cavity array schemes implemented via transmission line resonators (Liao et al. 2010, Peropadre et al. 2013, Tomadin and Fazio 2010). Finally the case of a qubit coupled with a quantum harmonic oscillator is an open version of the well known Jaynes-Cummings model (Jaynes and Cummings 1963) which has a plethora of experimental realizations (Haroche 2013, Schoelkopf and Girvin 2008, Chakraborty 1999).

4.1 General Theory

The model we are interested in studying consists in three separate elements: a quantum battery B, an external energy supply E, and an ancillary quantum system A that acts as mediator between the other two elements, see Fig. 4.1. Alternatively, one can interpret A as that part of a structured global bath AE, which is directly interacting with B, E representing instead the nonlocal degrees of freedom of the environment.

4.1.1 Charging protocol

In our treatment we shall represent A and B as actual quantum systems, whose dynamics is determined by a Markovian master equation which effectively accounts for the presence of E. We thus describe the temporal evolution of the density matrix $\rho_{\rm AB}(t)$ of the AB system as:

$$\dot{\rho}_{\rm AB}(t) = -i\left[H_{\rm A} + H_{\rm B}, \rho_{\rm AB}(t)\right]_{-} + \lambda(t)\mathcal{L}_{\rm AB}(t)[\rho_{\rm AB}(t)]\,, \tag{4.1}$$

where $\left[\cdots,\cdots\right]_{-}$ denotes the usual commutator. In the right-hand side of Eq. (4.1), the first term contains the free Hamiltonian of the system composed by the local (time-independent) contributions of A and B which, for sake of convenience, we shall assume to have zero ground-state energy. The second term, instead, is explicitly time dependent and refers to the AB interactions and to the charging terms of the model induced by the coupling between the external energy supply E and A. Here $\lambda(t)$ is a dimensionless function equal to 1 for $t \in [0,\tau[$ and 0 elsewhere, which we use for turning "on/off" such contributions, τ representing the charging time of the protocol. $\mathcal{L}_{\rm AB}(t)$ is instead a GKSL super-operator that contains both coherent and dissipative contributions. Explicitly, we write it as

$$\mathcal{L}_{\rm AB}(t)[\cdots] \equiv -i\left[\Delta H_{\rm A}(t) + H^{(1)}_{\rm AB}, \cdots\right]_{-} + \mathcal{D}_{\rm A}[\cdots]\,, \tag{4.2}$$

where $H^{(1)}_{\rm AB}$ is the interaction Hamiltonian between the charger and the battery, $\Delta H_{\rm A}(t)$ is a local modulation of the energy of A which is externally driven by classical fields that may inject energy into the system, and, finally, $\mathcal{D}_{\rm A}[\cdots]$ implies a purely dissipative contribution that acts locally on A, accounting for the local thermalization of A induced by a bosonic bath at temperature $1/\beta$ (no direct dissipation being assumed for B). In this scenario we assume that for $t < 0$, when A and B do not interact and are isolated from the rest, they are prepared in the ground state of the local terms $H_{\rm A}$ and $H_{\rm B}$, respectively, i.e.

$$\rho_{\rm AB}(t \leq 0) = |0\rangle\langle 0|_{\rm A} \otimes |0\rangle\langle 0|_{\rm B}\ , \tag{4.3}$$

a configuration representing the discharged battery. At time $t = 0$, A is attached to the external supply E by switching on the dissipator $\mathcal{D}_{\rm A}$ and (possibly) the modulation $\Delta H_{\rm A}(t)$, while A and B begin to interact with each other. In the time window $[0, \tau[$ part of the energy coming from the outside, and going only to A at short timescales, flows to B thanks to the non-zero internal coupling term $H^{(1)}_{\rm AB}$, which we assume to commute with the free Hamiltonian $H_{\rm A} + H_{\rm B}$,

$$\Big[H^{(1)}_{\rm AB}, H_{\rm A} + H_{\rm B}\Big]_{-} = 0 \; . \tag{4.4}$$

At the end of the charging process, namely at time τ when $\lambda(t)$ returns to zero, we isolate again the system and turn the interaction between A and B off. The battery is now in a charged state and ready for the energy extraction.

4.1.2 Figures of merit

In what follows, we shall analyze the quantities we defined in Eqs. (2.39) and (2.40) of Sec. 2.2, i.e. the stored energy $E_{\rm B}(\tau)$ and the ergotropy $\mathcal{E}_{\rm B}(\tau)$ of the quantum battery, as well as their ratio

$$R_{\rm B}(\tau) \equiv \mathcal{E}_{\rm B}(\tau)/E_{\rm B}(\tau) \; . \tag{4.5}$$

Furthermore, we will be interested to their associated mean charging powers

$$P_{\rm B}(\tau) \;\equiv\; E_{\rm B}(\tau)/\tau \; , \tag{4.6}$$

$$\mathcal{P}_{\rm B}(\tau) \;\equiv\; \mathcal{E}_{\rm B}(\tau)/\tau \; , \tag{4.7}$$

for different choices of A and B systems and for different energy-injection mechanisms. For all these models we shall enforce resonant conditions of the local energies of A and B, as well as for the driving term $\Delta H_{\rm A}(t)$. This will allow us to simplify the analysis by solving the ME in the time interval $[0, \tau]$ in the interaction picture representation where instead of $\rho_{\rm AB}(t)$ one focuses on its rotated version

$$\tilde{\rho}_{\rm AB}(t) \equiv e^{i(H_{\rm A}+H_{\rm B})t} \rho_{\rm AB}(t) e^{-i(H_{\rm A}+H_{\rm B})t} \; , \tag{4.8}$$

for which Eq. (4.1) for $t \in [0, \tau[$ reduces to

$$\dot{\tilde{\rho}}_{\rm AB}(t) \;=\; \mathcal{L}_{\rm AB}[\tilde{\rho}_{\rm AB}(t)] \; . \tag{4.9}$$

Here, $\mathcal{L}_{\rm AB}$ is as in (4.2) but with $\Delta H_{\rm A}(t)$ replaced by the constant term $\Delta H_{\rm A} \equiv \Delta H_{\rm A}(t = 0)$.

Most importantly, under the above conditions, both the mean energy (2.39) and the

ergotropy (2.40) of B will be then directly computed on the reduced density matrix $\tilde{\rho}_{\rm B}(\tau) = {\rm tr}_{\rm A}[\tilde{\rho}_{\rm AB}(\tau)]$ of $\tilde{\rho}_{\rm AB}(\tau)$. Indeed, the latter differs from $\rho_{\rm B}(\tau)$ by a unitary rotation induced by $H_{\rm B}$, i.e. $\tilde{\rho}_{\rm B}(\tau) = e^{iH_{\rm B}\tau}\rho_{\rm B}(\tau)e^{-iH_{\rm B}\tau}$. Accordingly, we have ${\rm tr}[H_{\rm B}\tilde{\rho}_{\rm B}(\tau)] = {\rm tr}[H_{\rm B}\rho_{\rm B}(\tau)] = E_{\rm B}(\tau)$ while, including $e^{iH_{\rm B}\tau}$ into the minimization over $U_{\rm B}$, we have

$$\min_{U_{\rm B}} {\rm tr}\left[H_{\rm B}U_{\rm B}\tilde{\rho}_{\rm B}(\tau)U_{\rm B}^\dagger\right] = \min_{U_{\rm B}} {\rm tr}\left[H_{\rm B}U_{\rm B}\rho_{\rm B}(\tau)U_{\rm B}^\dagger\right],$$

which, via Eq. (2.40) [or, equivalently, using the result (2.49)], ensures that $\tilde{\rho}_{\rm B}(\tau)$ and $\rho_{\rm B}(\tau)$ possess the same ergotropy value.

4.1.3 Implementations

In the following we study the cases where A is allowed to be either a qubit or a harmonic oscillator, the same holding for B. Hence, having in mind to study different combinations of qubit and harmonic oscillators for the charger-battery compound, we write in a unified form the several contribution in Eq. (4.1) and (4.2) as

$$\begin{aligned} H_{\rm A} = \omega_0\zeta_{\rm A}^\dagger\zeta_{\rm A}\,, \qquad H_{\rm B} = \omega_0\zeta_{\rm B}^\dagger\zeta_{\rm B}\,, \\ \Delta H_{\rm A}(t) = F\left(e^{-i\omega_0 t}\zeta_{\rm A}^\dagger + e^{i\omega_0 t}\zeta_{\rm A}\right)\,, \\ H_{\rm AB}^{(1)} = g\left(\zeta_{\rm A}\zeta_{\rm B}^\dagger + \zeta_{\rm A}^\dagger\zeta_{\rm B}\right)\,. \end{aligned} \tag{4.10}$$

Here, $\zeta_{\rm A}$ and $\zeta_{\rm B}$ ($\zeta_{\rm A}^\dagger$ and $\zeta_{\rm A}^\dagger$) are *generalized* annihilation (creation) operators of the A and B systems, respectively. Accordingly, depending on the implementation, $\zeta_{\rm A} = \sigma_{\rm A}^-$ (qubit annihilation operator, cfr. Eq. (2.54)) when A is a qubit and $\zeta_{\rm A} = a$ (bosonic annihilation operator) when A is a QHO and, analogously, $\zeta_{\rm B} = \sigma_{\rm B}^-$ when B is a qubit and $\zeta_{\rm B} = b$ when B is a QHO (a and b same as in Sec. 3.3).
Furthermore, A and B are assumed to be resonant (again, as in Sec. 3.3), with ω_0 being the fundamental frequency of the local terms. The quantities g and F are coupling constants, gauging, respectively, the AB coupling and the driving field acting on A. Regarding the dissipator we take [cfr. Eq. (3.150)]

$$\begin{aligned} \mathcal{D}_{\rm A}[\cdots] \quad &:= \quad \kappa\,(1+\mathcal{N}_b)\mathcal{D}^{[\zeta_{\rm A}]}[\cdots] + \kappa\,\mathcal{N}_b\mathcal{D}^{[\zeta_{\rm A}^\dagger]}[\cdots]\,, \\ &\text{with} \quad \mathcal{D}^{[\zeta_{\rm A}]}[\cdots] := \zeta_{\rm A}\cdots\zeta_{\rm A}^\dagger - \frac{1}{2}\Big[\zeta_{\rm A}^\dagger\zeta_{\rm A},\cdots\Big]_+\,, \end{aligned} \tag{4.11}$$

where the rate κ fixes the timescale of the dissipation process, $\big[\cdots,\cdots\big]_+$ is the anti-commutator symbol, and $\mathcal{N}_b := 1/[\exp(\beta\omega_0) - 1]$ is the mean number of bath quanta at frequency ω_0 and temperature $1/\beta$. With this choice, the first term on the right-hand side of Eq. (4.11) describes energy flow from the system into the environment with spontaneous and stimulated emission terms, whereas the second one describes energy

flow from the environment into the system.
Finally, under the above conditions and in the interaction picture defined in Eq. (4.8), Eq. (4.1) becomes

$$\dot{\tilde{\rho}}_{\mathrm{AB}}(t) = -i\left[g\left(\zeta_{\mathrm{A}}\zeta_{\mathrm{B}}^{\dagger} + \zeta_{\mathrm{A}}^{\dagger}\zeta_{\mathrm{B}}\right) + F(\zeta_{\mathrm{A}}^{\dagger} + \zeta_{\mathrm{A}})\ ,\ \tilde{\rho}_{\mathrm{AB}}(t)\right]_{-} + \kappa(1+\mathcal{N}_b)\mathcal{D}^{[\zeta_{\mathrm{A}}]}\left[\tilde{\rho}_{\mathrm{AB}}(t)\right] + \kappa\mathcal{N}_b\mathcal{D}^{[\zeta_{\mathrm{A}}^{\dagger}]}\left[\tilde{\rho}_{\mathrm{AB}}(t)\right]\ . \tag{4.12}$$

4.2 Two-harmonic-oscillator model

We begin by considering the case in which both the charger A and the quantum battery B are described by resonant harmonic oscillators. In agreement with the formalism introduced in Sec. 4.1.3, we hence set in Eqs. (4.10)-(4.12), $\zeta_{\rm A} = a$ and $\zeta_{\rm B} = b$, which identify the annihilation operators of the bosonic modes A and B, respectively. The associated interaction-picture-representation ME (4.12) admits explicit integration. In particular, since the generator on the right-hand side of Eq. (4.12) is quadratic in the field modes, the dynamics preserves the Gaussian character (Serafini 2017) of the ground state (4.3), which in this case is the zero Fock state of the A and B modes. Accordingly, a complete characterization of $\tilde{\rho}_{\rm AB}(t)$ can be obtained by simply determining the first and second moments of the field operators. Specifically, using $\langle x\rangle \equiv {\rm tr}[x\tilde{\rho}_{\rm AB}(t)]$ to indicate the average value of a generic operator x on $\tilde{\rho}_{\rm AB}(t)$, for the first moments we have

$$\begin{aligned} \langle \dot{a}\rangle &= -i(g\langle b\rangle + F) - \frac{\kappa}{2}\langle a\rangle \,, \\ \langle \dot{b}\rangle &= -ig\langle a\rangle \,, \end{aligned} \tag{4.13}$$

while, for the second moments,

$$\begin{aligned} \langle \dot{ab^\dagger}\rangle &= i\left[g(\langle a^\dagger a\rangle - \langle b^\dagger b\rangle) - F\langle b\rangle^*\right] - \frac{\kappa}{2}\langle ab^\dagger\rangle \,, \\ \langle \dot{b^\dagger b}\rangle &= 2g\,{\rm Im}\langle ab^\dagger\rangle \,, \\ \langle \dot{a^\dagger a}\rangle &= -2\,{\rm Im}[g\langle ab^\dagger\rangle + F\langle a\rangle] - \kappa\langle a^\dagger a\rangle + \kappa\mathcal{N}_b \,, \end{aligned} \tag{4.14}$$

and

$$\begin{aligned} \langle \dot{a^2}\rangle &= -2i(g\,\langle ab\rangle + F\,\langle a\rangle) - \kappa\,\langle a^2\rangle \,, \\ \langle \dot{ab}\rangle &= -i[g(\langle a^2\rangle + \langle b^2\rangle) + F\,\langle b\rangle] - \frac{\kappa}{2}\,\langle ab\rangle \,, \\ \langle \dot{b^2}\rangle &= -2ig\,\langle ab\rangle \,. \end{aligned} \tag{4.15}$$

The above differential equations, together with the initial conditions associated with (4.3),

$$\begin{aligned} \langle a^\dagger a\rangle\big|_{t=0} &= \langle b^\dagger b\rangle\big|_{t=0} = \langle a^2\rangle\big|_{t=0} = \langle b^2\rangle\big|_{t=0} = 0 \,, \\ \langle a\rangle\big|_{t=0} &= \langle b\rangle\Big|_{t=0} = \langle ab^\dagger\rangle\big|_{t=0} = \langle ab\rangle\big|_{t=0} = 0 \,, \end{aligned} \tag{4.16}$$

are what we need to solve for the determination of the figures of merit introduced in Sec. 4.1.2.

In particular, $E_{\rm B}(\tau)$ simply corresponds to $\omega_0\langle b^\dagger b\rangle|_{t=\tau}$, while for the ergotropy we can use the fact that $\tilde{\rho}_{\rm B}(\tau)$ is Gaussian so that we can apply the results of Sec. 2.2.3 to express it as

$$\mathcal{E}_{\rm B}(\tau) = \omega_0 \left(\langle b^\dagger b\rangle - \frac{\sqrt{D}-1}{2} \right)\Bigg|_{t=\tau} , \tag{4.17}$$
$$D := \left(1 + 2\langle b^\dagger b\rangle - 2\,|\langle b\rangle|^2\right)^2 - 4\left|\langle b^2\rangle - \langle b\rangle^2\right|^2 .$$

4.2.1 Analysis

The model exhibits an effective decoupling between thermal and coherent pumping, which is reflected by the fact that, for assigned values of $\mathcal{N}_b$ and F, each of the functions $\langle x\rangle$ entering in Eqs. (4.13)–(4.15) can be expressed as the sum of two contributions,

$$\langle x\rangle|_{F,\mathcal{N}_b} = \langle x\rangle|_{F=0,\mathcal{N}_b} + \langle x\rangle|_{F,\mathcal{N}_b=0} , \tag{4.18}$$

with $\langle x\rangle|_{F=0,\mathcal{N}_b}$ describing the solution of the differential equations in the absence of the coherent driving terms (i.e. with $F=0$), and with $\langle x\rangle|_{F,\mathcal{N}_b=0}$ describing instead the solution of the same equations with a thermal bath at zero temperature (i.e. $\mathcal{N}_b = 0$). As a consequence of (4.18), for generic values of $\mathcal{N}_b$ and F we have

$$E_{\rm B}(\tau)|_{F,\mathcal{N}_b} = E_{\rm B}(\tau)|_{F=0,\mathcal{N}_b} + E_{\rm B}(\tau)|_{F,\mathcal{N}_b=0} . \tag{4.19}$$

An analogous simplification can also be observed for the ergotropy $\mathcal{E}_{\rm B}(\tau)$. Indeed, notwithstanding the fact that such quantity has a nonlinear dependence on the first and second moments of the field operators [see Eq. (4.17)], only the contribution associated with the coherent driving at zero temperature matters, i.e.

$$\mathcal{E}_{\rm B}(\tau)|_{F,\mathcal{N}_b} = \mathcal{E}_{\rm B}(\tau)|_{F,\mathcal{N}_b=0} = E_{\rm B}(\tau)|_{F,\mathcal{N}_b=0} , \tag{4.20}$$

the ergotropy of the purely thermal charging case being always null, i.e.

$$\mathcal{E}_{\rm B}(\tau)|_{F=0,\mathcal{N}_b} = 0 , \qquad \forall\, \mathcal{N}_b \geq 0 . \tag{4.21}$$

To prove the last two equations starting from the expression (4.17), we observe that, for $\mathcal{N}_b = 0$, Eqs. (4.13)-(4.15) admit solutions for the second-order moments $\langle XY\rangle$, appearing in Eqs. (4.14)-(4.15), that can be written as products of those obtained for the first-order moments, evaluated from (4.13), i.e.

$$\langle XY\rangle|_{F,\mathcal{N}_b=0} \;=\; \langle X\rangle_{F,\mathcal{N}_b=0}\langle Y\rangle_{F,\mathcal{N}_b=0} , \tag{4.22}$$

which, in combination with the decomposition (4.18), leads to (4.20).
Equations (4.19)–(4.21) represent hence an important simplification, which allows us to address the functional dependence upon $\mathcal{N}_b$ and F of $E_{\rm B}(\tau)$ and $\mathcal{E}_{\rm B}(\tau)$ by studying "separately" their effects on the battery model. This is a peculiarity of the two-harmonic-oscillator model, which is not found in different implementations where instead one witnesses a non-trivial interplay between the coherent and thermal driving contributions—see next sections. In the present case, the above identities imply that while non-zero values of $\mathcal{N}_b$ and F both add to $E_{\rm B}(\tau)$, only the F matters in the transferring of energy that is useful for future extractions of work. (A non-zero bath temperature can only decrease the ratio (4.5) but cannot deteriorate the net value of the ergotropy associated with a given choice of F.) Anticipating the analytic solutions we present in the coming subsections, examples of these behaviours can be found in Figs. 4.2 and 4.3—the first displaying the functional dependence of $E_{\rm B}(\tau)$ and $\mathcal{E}_{\rm B}(\tau)$ upon τ for various combinations of $\mathcal{N}_b$ and F, while the second presenting instead the ratio $R_{\rm B}(\tau)$ for two different bath temperatures—and in the asymptotic values attained by $E_{\rm B}(\tau)$, $\mathcal{E}_{\rm B}(\tau)$ in the $\tau \to \infty$ limit, i.e.

$$\begin{aligned} E_{\rm B}(\infty) &= \omega_0 \mathcal{N}_b + \omega_0 (F/g)^2 \,, \\ \mathcal{E}_{\rm B}(\infty) &= \omega_0 (F/g)^2 \,, \end{aligned} \tag{4.23}$$

whose associated ratio (4.5)

$$R_{\rm B}(\infty) = \frac{F^2}{g^2 \mathcal{N}_b + F^2} \,, \tag{4.24}$$

clearly exhibits a monotonic decreasing behaviour with respect to $\mathcal{N}_b$.

4.2.1.1 Thermal energy supply regime ($F = 0$, $\mathcal{N}_b$ generic)

Let us consider first the case where no coherent driving is present (i.e. $F = 0$) while A is in contact with a non-zero temperature bath (i.e. $\mathcal{N}_b > 0$). As anticipated in Eq. (4.21), this regime represents a poor implementation of the charging of a quantum battery as it results in a zero value for the ergotropy $\mathcal{E}_{\rm B}(\tau)$.
For what concerns the mean energies of B and A, their expressions correspond to Eqs. (3.225) and (3.224), respectively, multiplied by ω_0. In the limit of large τ, they show convergency of $E_{\rm A}(\tau)$ and $E_{\rm B}(\tau)$ toward the same value $\omega_0 \mathcal{N}_b$, in agreement with the (local) thermalization of the two subsystems. The transient, however, exhibits two distinct regimes: an oscillating underdamped regime occurring for $\kappa < 4g$, and an overdamped regime for $\kappa \geq 4g$, where, for large enough κ, the stored energy can be conveniently approximated as $E_{\rm B}(\tau) \approx \omega_0 \mathcal{N}_b (1 - e^{-4g^2 \tau/\kappa})$, see panels (a) and (b) of Fig. 4.4. This feature has a profound impact on the timing of the process: a numerical

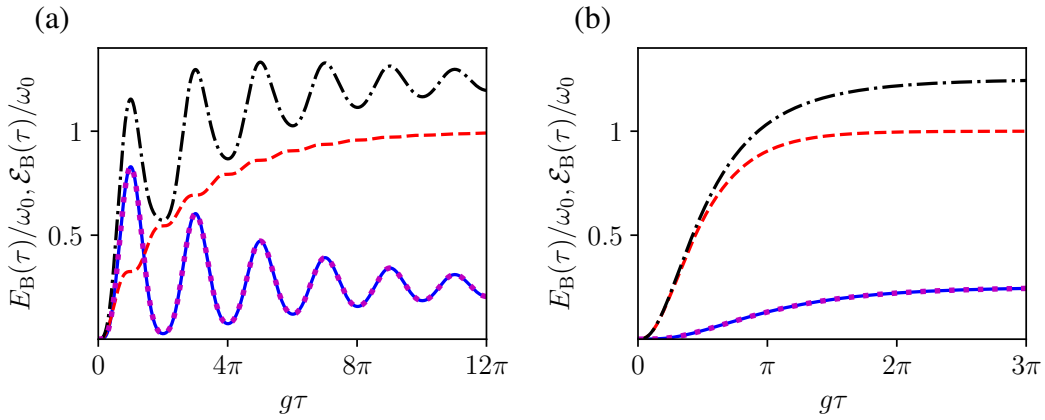

Fig. 4.2 Local energy $E_{\rm B}(\tau)$ and ergotropy $\mathcal{E}_{\rm B}(\tau)$ of the battery B (both in units of ω_0) as functions of $g\tau$, for the two-harmonic oscillator model. (a) The black dash-dotted, red dashed, and magenta dotted curves represent $E_{\rm B}(\tau)$ for $\mathcal{N}_b = 1$ and $F = 0.1\omega_0$, $\mathcal{N}_b = 1$ and $F = 0$ (no coherent driving), and $\mathcal{N}_b = 0$ and $F = 0.1\omega_0$ (zero temperature), respectively. The blue solid curve represents the ergotropy $\mathcal{E}_{\rm B}(\tau)$ for $\mathcal{N}_b = 1$ and $F = 0.1\omega_0$. Note that this curve is superimposed to the magenta dotted curve: this is because, as emphasized in Eq. (4.20), $\mathcal{E}_{\rm B}(\tau)|_{F,\mathcal{N}_b} = E_{\rm B}(\tau)|_{F,\mathcal{N}_b=0}$. All numerical results in (a) have been obtained by setting $g = 0.2\omega_0$ and $\kappa = 0.05\omega_0$ (underdamped regime). (b) Same as in (a) but for $\kappa = \omega_0$ (overdamped regime).

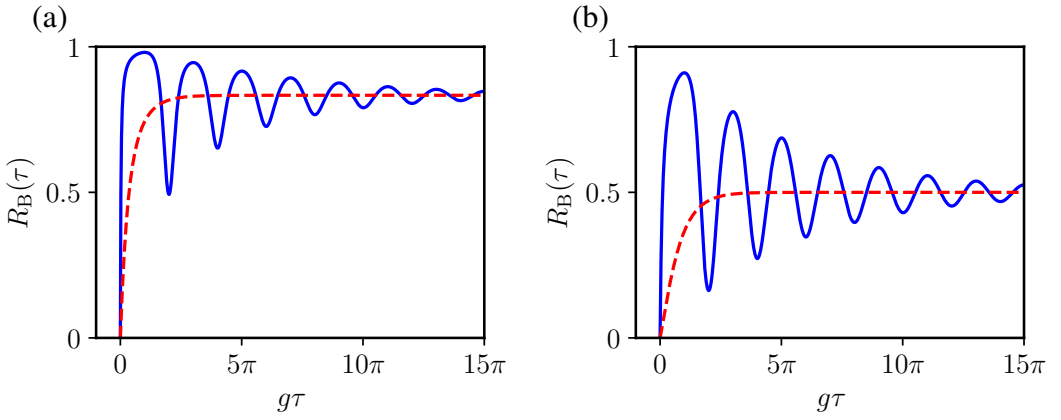

Fig. 4.3 The ratio (4.5), which measures the fraction of energy stored in the battery which can be extracted as work, as a function of $g\tau$ and for the two-harmonic oscillator model. (a) Different curves correspond to different values of the loss parameter κ. $\kappa = 0.05\omega_0$ (underdamped regime): blue solid line; $\kappa = \omega_0$ (overdamped regime): red dashed line. The other parameters are $F = 0.2\omega_0$, $g = 0.2\omega_0$, $\mathcal{N}_b = 0.2$. (b) Same as in (a) but for $\mathcal{N}_b = 1$. In both panels, all curves approach the asymptotic value (4.24) for $\tau \gg 1/g$.

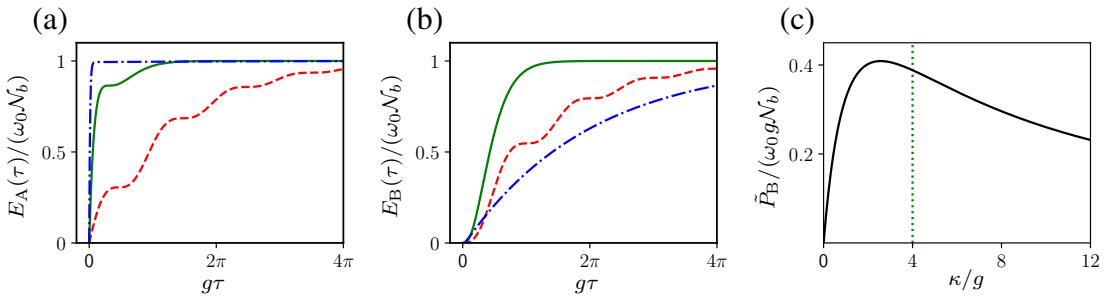

Fig. 4.4 (a) Local energy $E_{\rm A}(\tau)$ of the ancilla A (in units of $\mathcal{N}_b\omega_0$) as a function of $g\tau$ for the two-harmonic oscillator model. Different curves correspond to different values of the ratio κ/g. Red dashed line: $\kappa/g = 1/2$; green solid line: $\kappa/g = 4$; blue dash-dotted line: $\kappa/g = 25$. (b) Same as in (a) but for the energy $E_{\rm B}(\tau)$ stored in the battery B. (c) Maximum average storing power $\tilde{P}_{\rm B}$ (in units of $g\omega_0\mathcal{N}_b$), defined in Eq. (4.25), as a function of κ/g. All results in (a)-(c) have been obtained for the purely thermal energy supply regime (i.e. $F = 0, \mathcal{N}_b > 0$).

analysis reveals that the charging time of the battery (defined, e.g., as the first time at which B reaches a given fraction of its asymptotic value $\omega_0\mathcal{N}_b$), exhibits a non trivial dependence upon the parameters κ and g with optimal performances attained when they are close to the critical point $\kappa = 4g$. A clear evidence of this phenomenon can be found by looking at the maximum of the average storing power (4.6),

$$\tilde{P}_{\rm B} \equiv \max_{\tau} P_{\rm B}(\tau) \, , \tag{4.25}$$

which, as shown in panel (c) of Fig. 4.4, acquires its largest value just below threshold. We anticipate that the same effect will be observed in all the other implementations we discuss in the remaining of this Chapter, at least when the coherent driving is not present (i.e. $F = 0$). A possible explanation of the arising of such fine tuning condition between κ and g in the optimization of the charging process can be found by noticing that while the battery needs a finite loss coefficient to be thermally excited, a too large value of the loss coefficient will tend to freeze the state of A via an environment-mediated quantum Zeno effect (Breuer et al. 2002), preventing the latter to efficiently transfer energy to B.

4.2.1.2 Coherent energy supply regime ($\mathcal{N}_b = 0$, F generic)

Consider next the scenario where $F \neq 0$ and the bath temperature is zero, i.e. $\mathcal{N}_b = 0$. From Eqs. (4.19) and (4.20), it follows that this is the optimal setting in terms of our ability of maximizing the fraction of energy stored in B, which is available for work extraction at later times. Indeed, in this case we have

$$\mathcal{E}_{\rm B}(\tau)|_{F,\mathcal{N}_b=0} = E_{\rm B}(\tau)|_{F,\mathcal{N}_b=0} \, , \tag{4.26}$$

corresponding to the optimal value 1 for the ratio (4.5)—the same identity applying also for the energy that resides on A, i.e. $\mathcal{E}_{\rm A}(\tau)|_{F,\mathcal{N}_b=0} = E_{\rm A}(\tau)|_{F,\mathcal{N}_b=0}$. This result is a consequence of the fact that in the $\mathcal{N}_b = 0$ regime the AB system remains in a factorized, pure coherent state at all times. Specifically, we have

$$\tilde{\rho}_{\rm AB}(\tau) = |\alpha(\tau)\rangle_{\rm A}\langle\alpha(\tau)| \otimes |\beta(\tau)\rangle_{\rm B}\langle\beta(\tau)| \ , \tag{4.27}$$

where, given ϵ as in Eq. (3.223), $\alpha(\tau)$ and $\beta(\tau)$ are the following coherent amplitudes

$$\begin{aligned} \alpha(\tau) &= -i\frac{4F}{\epsilon}e^{-\frac{\kappa\tau}{4}}\sin(\epsilon\tau/4) \ , \\ \beta(\tau) &= -\frac{F}{g}\left\{1 - e^{-\frac{\kappa\tau}{4}}\left[\cos(\epsilon\tau/4) + \frac{\kappa}{\epsilon}\sin(\epsilon\tau/4)\right]\right\} \ . \end{aligned} \tag{4.28}$$

Using the factorization rule (4.22), the associated local mean energies are hence given by

$$E_{\rm A}(\tau)|_{F,\mathcal{N}_b=0} = \omega_0|\alpha(\tau)|^2 = \frac{16\,\omega_0 F^2}{\epsilon^2}e^{-\frac{\kappa\tau}{2}}\sin^2(\epsilon\tau/4) \tag{4.29}$$

and

$$E_{\rm B}(\tau)|_{F,\mathcal{N}_b=0} = \omega_0|\beta(\tau)|^2 \quad = \frac{\omega_0 F^2}{g^2}\left\{1 - e^{-\frac{\kappa\tau}{4}}\left[\cos(\epsilon\tau/4) + \frac{\kappa}{\epsilon}\sin(\epsilon\tau/4)\right]\right\}^2 \ , \tag{4.30}$$

which coincide, respectively, with the ergotropies $\mathcal{E}_{\rm A}(\tau)$ and $\mathcal{E}_{\rm B}(\tau)$ of the two systems. One may observe that, for all non-zero values of the damping parameter κ, in the limit $\tau \to \infty$ the energy of A nullifies testifying that the ancilla asymptotically approaches its local ground-state, while the coherent amplitude of B reaches a finite value $\beta(\infty) = -F/g$. As this result is non-perturbative in g, the energy stored in B in this regime can become very large resulting in

$$E_{\rm B}(\infty)\Big|_{F,\mathcal{N}_b=0} = \omega_0(F/g)^2 \ , \tag{4.31}$$

with the charger A going back to the initial vacuum state after a transient. The way this asymptotic configuration is attained is not influenced by the specific value of F, which in Eqs. (4.28)-(4.30) appears as a multiplicative factor and does not affect the timescales, see Fig. 4.5. As discussed by Andolina et al. (2018), this peculiarity stems from the nature of the spectrum at hand, which is not upper bounded. What instead plays an important role in the transient is once more the ratio between κ and g which, as in the purely thermal energy supply scenario we analyzed before, can again be used to identify underdamped ($\kappa < 4g$) and overdamped ($\kappa \geq 4g$) regimes. Furthermore, as evident from panel (a) of Fig. 4.5, it is clear that losses tend to reduce the value of the

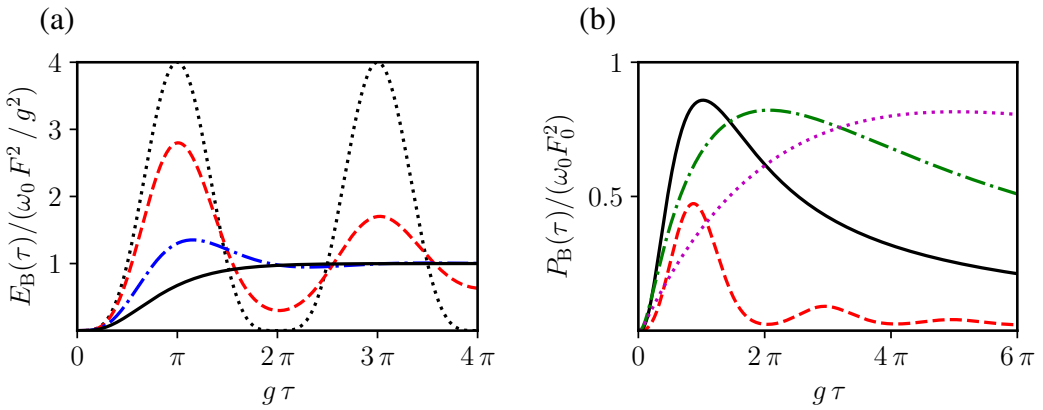

Fig. 4.5 (a) $E_{\rm B}(\tau)$ (in units of $\omega_0 F^2/g^2$) [Eq. (4.30)] as a function of $g\tau$ for the two-harmonic oscillator model and referring to the case of the purely coherent energy supply regime (i.e. $\mathcal{N}_b = 0$), an instance where $E_{\rm B}(\tau)$ and $\mathcal{E}_{\rm B}(\tau)$ coincide. The results of this figure have been obtained by setting $g = 0.2\omega_0$. Different curves correspond to different values of the loss parameter κ. Black dotted line: $\kappa = 0$; red dashed line: $\kappa = 0.1\omega_0$; blue dash-dotted line: $\kappa = 0.4\omega_0$; black solid line: $\kappa = 0.8\omega_0$. (b) Setting $F = F_0\sqrt{\kappa}$ we plot (in units $F_0^2\omega_0$) the average charging power $P_{\rm B}(\tau)$ [Eq. (4.6), coinciding with $\mathcal{P}_{\rm B}(\tau)$ of Eq. (4.7)] as function of $g\tau$. Different curves correspond again to different values of the loss parameter κ. Red dashed line: $\kappa = 0.1\omega_0$; black solid line: $\kappa = 0.8\omega_0$; green dash-dotted line: $\kappa = 2\omega_0$; magenta dotted line: $\kappa = 5\omega_0$. We notice that in this case κ needs to be tuned with g in order to get high power in a short time.

maximum energy. The best configuration is approached for $\kappa \to 0$ where the energy dynamics of B becomes periodic in τ, i.e. $E_{\rm B}(\tau) = 4\omega_0 F^2 \sin^4(g\tau/2)/g^2$, allowing the battery to reach an energy (and ergotropy) level which can be up to four times larger than the asymptotic value $E_{\rm B}(\infty)$, the smallest driving time τ ensuring this result being π/g. Under the same condition, a numerical evaluation shows that the associated storing power (4.6) exhibits a maximum value $\tilde{P}_{\rm B}$ equal to $0.33 \times (4\,\omega_0\,F^2/g)$ for an optimal charging time $\sim 2.78/g$. This is rather different from what we witnessed in the purely thermal setting where, instead, the largest possible value of $\tilde{P}_{\rm B}$ was attained for values of κ close to the threshold point, see panel (c) of Fig. 4.4. A possible reconciliation of this discrepancy can be found by noting that in realistic models the quantities F and κ cannot be treated as independent parameters. For instance considering a standard cavity-QED implementation of the model, from the microscopic derivation of the Lindblad equation (Breuer et al. 2002), it is more correct to assume $F \simeq F_0\sqrt{\kappa}$, indicating that the more the laser is able to pump energy in the system the more the system would be subject to losses, being it more strongly coupled with the external world. In such case, the analogy with the purely thermal setting is restored as it turns out that one must tune κ with g to obtain the highest charging power $P_{\rm B}(\tau)$ in the shortest time—see panel (b) of Fig. 4.5.

4.3 Two-qubit model

In this section we consider the case in which both the charger A and the quantum battery B are (resonant) two-level systems. Accordingly, the operators $\zeta_{\rm X}^\dagger$ in Eqs. (4.10)-(4.12) must be identified with the two-level raising operator $\sigma_{\rm X}^+ = [\sigma_{\rm X}^-]^\dagger = (\sigma_{\rm X}^x + i\sigma_{\rm X}^y)/2$, where, for ${\rm X} = {\rm A}, {\rm B}$, $\sigma_{\rm X}^{x,y,z}$ represent the Pauli matrices acting on the system X (cfr. Eqs. (2.54) and (2.52)).
Using again $\langle x\rangle := {\rm tr}[x\tilde{\rho}_{\rm AB}(t)]$ to indicate the expectation value of a generic operator x on $\tilde{\rho}_{\rm AB}(t)$, we have

$$
\begin{aligned}
&\frac{d}{dt}\langle\sigma_{\rm A}^z\rangle = 2ig\big(\langle\sigma_{\rm A}^-\sigma_{\rm B}^+\rangle - \langle\sigma_{\rm A}^-\sigma_{\rm B}^+\rangle^*\big) + 2iF\big(\langle\sigma_{\rm A}^-\rangle - \langle\sigma_{\rm A}^-\rangle^*\big) - \kappa\big(2\mathcal{N}_b+1\big)\langle\sigma_{\rm A}^z\rangle - \kappa\,,\\
&\frac{d}{dt}\langle\sigma_{\rm B}^z\rangle = 2ig\big(\langle\sigma_{\rm A}^-\sigma_{\rm B}^+\rangle^* - \langle\sigma_{\rm A}^-\sigma_{\rm B}^+\rangle\big)\,,\\
&\frac{d}{dt}\langle\sigma_{\rm A}^-\rangle = ig\langle\sigma_{\rm A}^z\sigma_{\rm B}^+\rangle^* + iF\langle\sigma_{\rm A}^z\rangle - \frac{1}{2}\kappa\big(2\mathcal{N}_b+1\big)\langle\sigma_{\rm A}^-\rangle\,,\\
&\frac{d}{dt}\langle\sigma_{\rm B}^-\rangle = ig\langle\sigma_{\rm A}^+\sigma_{\rm B}^z\rangle^*\,,\\
&\frac{d}{dt}\langle\sigma_{\rm A}^-\sigma_{\rm B}^+\rangle = \frac{1}{2}ig\big(\langle\sigma_{\rm A}^z\rangle - \langle\sigma_{\rm B}^z\rangle\big) + iF\langle\sigma_{\rm A}^z\sigma_{\rm B}^+\rangle - \frac{1}{2}\kappa\big(2\mathcal{N}_b+1\big)\langle\sigma_{\rm A}^-\sigma_{\rm B}^+\rangle\,,\\
&\frac{d}{dt}\langle\sigma_{\rm A}^z\sigma_{\rm B}^+\rangle = -ig\langle\sigma_{\rm A}^-\rangle^* + 2iF\big(\langle\sigma_{\rm A}^-\sigma_{\rm B}^+\rangle - \langle\sigma_{\rm A}^-\sigma_{\rm B}^-\rangle^*\big) - \kappa\big(2\mathcal{N}_b+1\big)\langle\sigma_{\rm A}^z\sigma_{\rm B}^+\rangle - \kappa\langle\sigma_{\rm B}^-\rangle^*\,,\\
&\frac{d}{dt}\langle\sigma_{\rm A}^-\sigma_{\rm B}^-\rangle = iF\langle\sigma_{\rm A}^z\sigma_{\rm B}^+\rangle^* - \frac{1}{2}\kappa\big(2\mathcal{N}_b+1\big)\langle\sigma_{\rm A}^-\sigma_{\rm B}^-\rangle\,,\\
&\frac{d}{dt}\langle\sigma_{\rm A}^+\sigma_{\rm B}^z\rangle = -ig\langle\sigma_{\rm B}^-\rangle^* - iF\langle\sigma_{\rm A}^z\sigma_{\rm B}^z\rangle - \frac{1}{2}\kappa\big(2\mathcal{N}_b+1\big)\langle\sigma_{\rm A}^+\sigma_{\rm B}^z\rangle\,,\\
&\frac{d}{dt}\langle\sigma_{\rm A}^z\sigma_{\rm B}^z\rangle = 2iF\big(\langle\sigma_{\rm A}^+\sigma_{\rm B}^z\rangle^* - \langle\sigma_{\rm A}^+\sigma_{\rm B}^z\rangle\big) - \kappa\big(2\mathcal{N}_b+1\big)\langle\sigma_{\rm A}^z\sigma_{\rm B}^z\rangle - \kappa\langle\sigma_{\rm B}^z\rangle\,,
\end{aligned}
\tag{4.32}
$$

which we solve under the initial condition (4.3), that, for the functions appearing above, is expressed by

$$
\begin{aligned}
&\langle\sigma_{\rm A}^z\rangle(0) = \langle\sigma_{\rm B}^z\rangle(0) = -1\,,\\
&\langle\sigma_{\rm A}^-\rangle(0) = \langle\sigma_{\rm B}^-\rangle(0) = \langle\sigma_{\rm A}^-\sigma_{\rm B}^+\rangle(0) = \langle\sigma_{\rm A}^z\sigma_{\rm B}^+\rangle(0) = \langle\sigma_{\rm A}^-\sigma_{\rm B}^-\rangle(0) = \langle\sigma_{\rm A}^+\sigma_{\rm B}^z\rangle(0) = 0\,,\\
&\langle\sigma_{\rm A}^z\sigma_{\rm B}^z\rangle(0) = 1\,,
\end{aligned}
\tag{4.33}
$$

giving direct access to the stored energy

$$
E_{\rm B} = \frac{\omega_0}{2}\left(\langle\sigma_{\rm B}^z\rangle + 1\right) \tag{4.34}
$$

and ergotropy

$$
\mathcal{E}_{\rm B} = \frac{\omega_0}{2}\left(\sqrt{\langle\sigma_{\rm B}^z\rangle^2 + 4\left\langle\sigma_{\rm B}^+\right\rangle\left\langle\sigma_{\rm B}^-\right\rangle} + \langle\sigma_{\rm B}^z\rangle\right) \tag{4.35}
$$

of the battery B (cfr. Eq. (2.55) and its derivation for more details and Appendix A for an alternative approach).

4.3.1 Analysis

Since at low energy the two-harmonic oscillator model discussed in the previous Section has similar spectral properties to those of the two-qubit setting, we expect the two schemes to exhibit analogous performances in the low supply limit, i.e. for coherent driving constant $F \ll g, \kappa$ and temperature $1/\beta \ll \omega_0$. On the contrary, for not negligible values of F or $1/\beta$, the effective nonlinearities introduced by the finite dimensionality of the two-qubit model we are considering here, result in a more complex interplay between the coherent and incoherent pumping mechanisms than the one we discussed in Sec. 4.2. Specifically, as will shall see, while still one cannot achieve non-zero values of $\mathcal{E}_{\rm B}(\tau)$ in the absence of the external coherent driving (i.e. $F = 0$), decoupling rules similar to the ones reported in Eqs. (4.19)-(4.20) hold no longer for arbitrary values of the system parameters. In particular, it turns out that, at variance with the two-harmonic oscillator model, the presence of a non-zero temperature can strongly interfere with the ergotropy production. Interestingly enough, while typically such interference tends to reduce $\mathcal{E}_{\rm B}(\tau)$, there are special settings of the system parameters for which one observes that a non-zero temperature can indeed result in a larger value of the attainable ergotropy.

4.3.1.1 Steady state

Evidences of such behaviours can be obtained by looking at the values that $E_{\rm B}(\tau)$ and $\mathcal{E}_{\rm B}(\tau)$ attain in the asymptotic $\tau \to \infty$ limit, which can be extrapolated from Eq. (4.32) by enforcing the stationary condition $\dot{\tilde{\rho}}_{\rm AB}(t) = 0$. The resulting expressions for arbitrary values of $1/\beta$ and F in this case are given by

$$\frac{E_{\rm B}(\infty)}{\omega_0} = \frac{1}{2} - \frac{g^2\kappa\kappa_b(2g^2+\kappa_b^2)}{32F^4(2g^2+\kappa^2)+4F^2\kappa^2\left[24\mathcal{N}_b(\mathcal{N}_b+1)g^2+(2g^2+\kappa_b^2)\right]+2g^2\kappa_b^2(2g^2+\kappa_b^2)}\,, \tag{4.36}$$

$$\frac{\mathcal{E}_{\rm B}(\infty)}{\omega_0} = \frac{g\kappa(2g^2+\kappa_b^2)(\sqrt{4\kappa^2F^2+g^2\kappa_b^2}-g\kappa_b)}{32F^4(2g^2+\kappa^2)+4F^2\kappa^2\left[24\mathcal{N}_b(\mathcal{N}_b+1)g^2+(2g^2+\kappa_b^2)\right]+2g^2\kappa_b^2(2g^2+\kappa_b^2)}\,, \tag{4.37}$$

where κ_b is the renomalization of the loss coefficient κ by the Bose occupation number $\mathcal{N}_b$ of the bath, i.e.

$$\kappa_b := \kappa(2\mathcal{N}_b+1)\,. \tag{4.38}$$

In Fig. 4.6 we display the functional dependence of the functions (4.36) and (4.37) and of their ratio $R_{\rm B}(\infty) = \mathcal{E}_{\rm B}(\infty)/E_{\rm B}(\infty)$ in terms of $\mathcal{N}_b$ and F. As evident from panels (a) and (b) of the figure, when F is sufficiently large, $\mathcal{E}_{\rm B}(\infty)$ may indeed take advantage from an increase of the bath temperature. As anticipated, no ergotropy can be generated

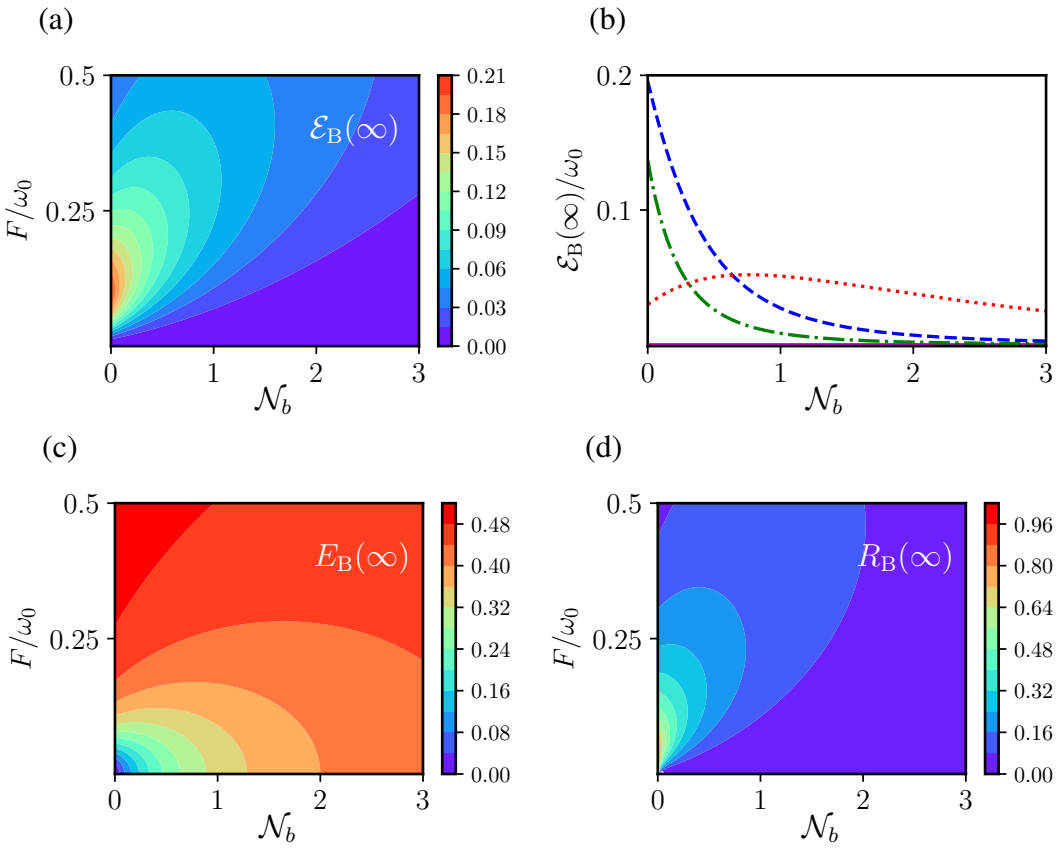

Fig. 4.6 (a) Two-dimensional color plot of $\mathcal{E}_{\rm B}(\infty)$ (in units of ω_0)—Eq. (4.37)—as a function of F (in units of ω_0) and $\mathcal{N}_b$ for the two-qubit model. Notice that $\mathcal{E}_{\rm B}(\infty)$ approximately reaches its maximum value (4.45) for $\mathcal{N}_b = 0$ (zero temperature) and $F \simeq 1.09g$. For large enough F we notice that $\mathcal{E}_{\rm B}(\infty)$ is not monotonically decreasing in $\mathcal{N}_b$. (b) $\mathcal{E}_{\rm B}(\infty)$ (in units of ω_0) as a function of $\mathcal{N}_b$. Different curves correspond to different values of F. Magenta solid line: $F = 0$ (which yields $\mathcal{E}_{\rm B}(\infty) = 0$); green dash-dotted line: $F = 0.05\omega_0$; blue dashed line: $F = 0.1\omega_0$; red dotted line: $F = 0.5\omega_0$. The non-monotonic behaviour as a function of $\mathcal{N}_b$ is clearly evident for $F = 0.5\omega_0$. (c) Same as in (a) but for the asymptotic value $E_{\rm B}(\infty)$ of the energy stored in B—Eq. (4.36). (d) Same as in (a) and (c) but for the ratio $R_{\rm B}(\infty)$—Eq. (4.5) in the $\tau \to \infty$ limit. $R_{\rm B}(\infty)$ reaches its maximum value for $\mathcal{N}_b = 0$ and in the $F \to 0$ limit. All results in this figure have been obtained by setting $g = 0.1\omega_0$ and $\kappa = \omega_0$.

by only having access to a purely thermal source. Indeed, for $F = 0$, Eqs. (4.36) and (4.37) give

$$E_{\rm B}(\infty)\Big|_{F=0,\,\mathcal{N}_b} = \omega_0 \mathcal{N}_f \,, \tag{4.39}$$

$$\mathcal{E}_{\rm B}(\infty)\Big|_{F=0,\,\mathcal{N}_b} = 0 \,, \tag{4.40}$$

where now

$$\mathcal{N}_f := \frac{1}{\exp\left(\beta\omega_0\right)+1} \,, \tag{4.41}$$

is the fermionic occupation number. In the opposite regime, i.e. when the charging is purely coherent and the bath is at zero temperature ($\mathcal{N}_b = 0$), Eqs. (4.36) and (4.37) yield

$$E_{\rm B}(\infty)\Big|_{F,\,\mathcal{N}_b=0} = \omega_0 \frac{(\kappa^2+8F^2)F^2}{16F^4+\kappa^2(2F^2+g^2)} \,, \tag{4.42}$$

$$\mathcal{E}_{\rm B}(\infty)\Big|_{F,\,\mathcal{N}_b=0} = \frac{\omega_0}{2}\frac{g\kappa^2(\sqrt{4F^2+g^2}-g)}{16F^4+\kappa^2(2F^2+g^2)} \,, \tag{4.43}$$

which we plot in Fig. 4.7 together with their ratio (4.5),

$$R_{\rm B}(\infty)\Big|_{F,\,\mathcal{N}_b=0} = \frac{g\kappa^2(\sqrt{4F^2+g^2}-g)}{2(\kappa^2+8F^2)F^2} \,. \tag{4.44}$$

Eq. (4.43) reveals that in the large loss limit $\kappa \gg F$ and when F and g are tuned so that $F = \sqrt{(\sqrt{2}+1)/2}g \simeq 1.09g$, the asymptotic ergotropy reaches its maximum value

$$\overline{\mathcal{E}}_B(\infty)\Big|_{F,\,\mathcal{N}_b=0} \;=\; \frac{\sqrt{2}-1}{2}\omega_0 \sim 0.207\omega_0 \,, \tag{4.45}$$

which, incidentally, corresponds also to the absolute maximum of (4.37) for arbitrary temperature, as evident from panel (a) of Fig. 4.6. On the contrary, a close inspection of Eq. (4.44) reveals that the ratio achieves its absolute maximum value 1 in the small driving constant/low energy supply limit (i.e. for $F \ll g, \kappa$) for which one gets $E_{\rm B}(\infty)|_{F,\,\mathcal{N}_b=0} \simeq \mathcal{E}_{\rm B}(\infty)|_{F,\,\mathcal{N}_b=0} \simeq \omega_0(F/g)^2$. As anticipated at the beginning of this Section, this exactly reproduces the behaviour (4.26) observed for the two-harmonic oscillator model at zero temperature.

4.3.1.2 Transients

We now analyze the perfomances of the model for finite values of τ. Let us first consider the case where no driving is at play ($F = 0$) while the temperature of the bath is finite ($\mathcal{N}_b > 0$), which is the only case for which we can present explicit analytical expressions. As for the case of the two-harmonic oscillator model, it turns out that the

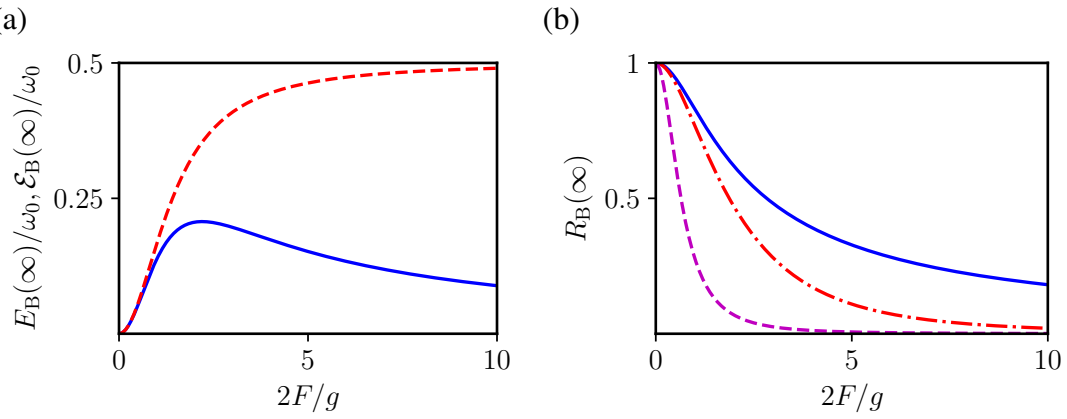

Fig. 4.7 (a) $E_{\rm B}(\infty)/\omega_0$ (red dashed line) [Eq. (4.42)] and $\mathcal{E}_{\rm B}(\infty)/\omega_0$ (blue solid line) [Eq. (4.43)] as functions of $2F/g$, for the two-qubit model. Results in this panel have been obtained by setting $\kappa \gg F, g$. (b) The ratio $R_{\rm B}(\infty)$ [Eq. (4.5) in the $\tau \to \infty$ limit] is plotted as a function of $2F/g$. Different curves correspond to different values of κ. Blue solid line: $\kappa \gg F, g$; red dash-dotted line: $\kappa/g = 5$; magenta dashed: $\kappa/g = 1$. Both panels refer to the purely coherent energy supply regime, i.e. $\mathcal{N}_b = 0$.

ergotropy of the battery is always null at all times, i.e. $\mathcal{E}_{\rm B}(\tau) = 0$, testifying that in the absence of the external driving the density matrix $\tilde{\rho}_{\rm B}(\tau)$ is passive. Regarding the mean energy of B, by direct integration of the equation of motion we find

$$E_{\rm B}(\tau) = \omega_0 \mathcal{N}_f \Big\{ 1 - \frac{e^{-\frac{1}{2}\kappa_b \tau}}{\epsilon_b^2} \left[16g^2 + \kappa_b \epsilon_b \sin(\epsilon_b \tau/2) - {\kappa_b}^2 \cos(\epsilon_b \tau/2) \right] \Big\} , \tag{4.46}$$

with κ_b and $\mathcal{N}_f$ as in Eqs. (4.38) and (4.41), respectively, and where

$$\epsilon_b \equiv \sqrt{(4g)^2 - {\kappa_b}^2} \, . \tag{4.47}$$

For comparison, we also report the value of the local mean energy of A, which in the present case is given by

$$E_{\rm A}(\tau) = \omega_0 \mathcal{N}_f \Big\{ 1 - \frac{e^{-\frac{1}{2}\kappa_b \tau}}{\epsilon_b^2} \left[16g^2 - \kappa_b \epsilon_b \sin(\epsilon_b \tau/2) - {\kappa_b}^2 \cos(\epsilon_b \tau/2) \right] \Big\} . \tag{4.48}$$

One may notice that these expressions for $E_{\rm B}(\tau)$ and $E_{\rm A}(\tau)$ can be formally obtained from Eqs. (3.225) and (3.224), respectively, which apply for the two-harmonic oscillator model in the purely thermal setting (i.e. $F = 0$), by replacing $\mathcal{N}_b \to \mathcal{N}_f$ and $\kappa \to \kappa_b$ and multiplying by ω_0. Accordingly, in this regime the energy charging of the two-qubit model will closely resemble the one observed in Fig. 4.4, with an overdamped and underdamped regime, attained respectively for $\kappa_b \geq 4g$ and $\kappa_b < 4g$, the main difference being that now, because of Eq. (4.38), the critical threshold depends explicitly upon the bath temperature $1/\beta$.

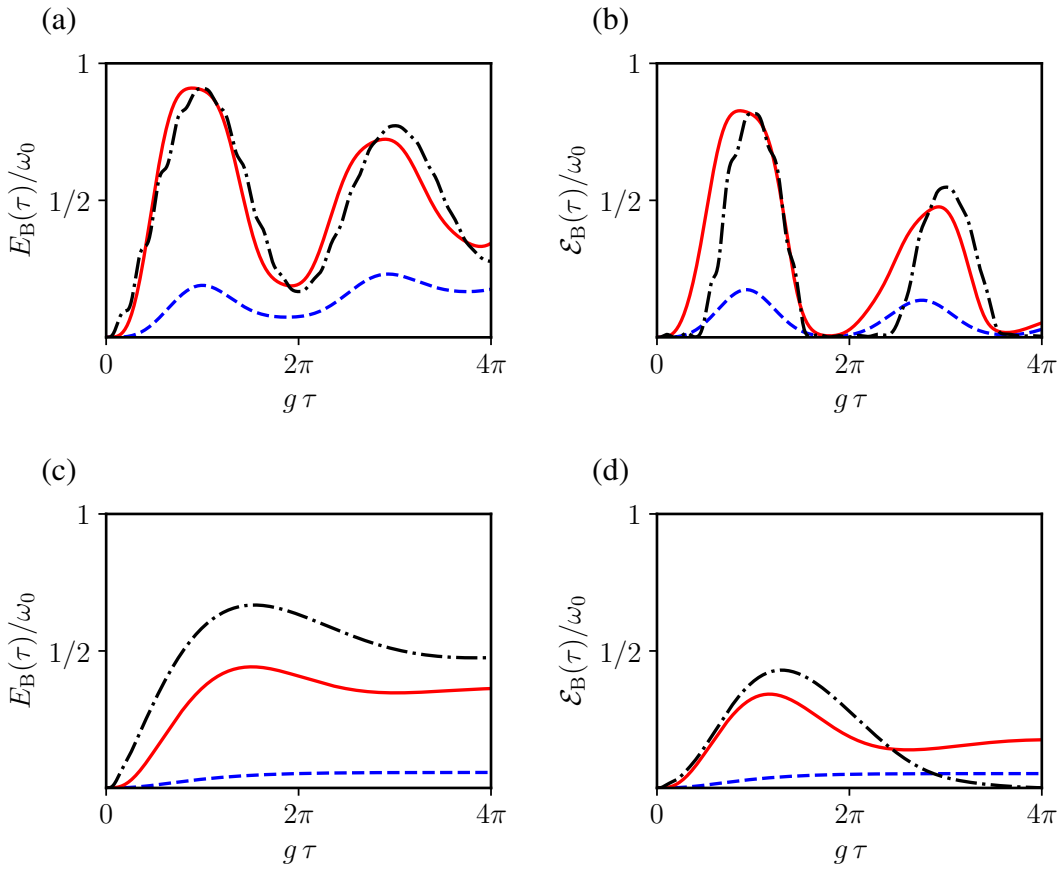

Fig. 4.8 (a) $E_{\rm B}(\tau)$ (in units of ω_0) as a function of $g\tau$, for the two-qubit model. Different curves refer to different values of F (in units of ω_0). Blue dashed line: $F = 0.05\omega_0$; red solid line: $F = 0.2\omega_0$; black dash-dotted: $F = \omega_0$. (b) Same as in (a) but for $\mathcal{E}_{\rm B}(\tau)$. Numerical results in (a) and (b) have been obtained by setting $g = 0.2\omega_0$ and $\kappa = 0.05\omega_0$. (c),(d) Same as in (a) and (b) but for $\kappa = \omega_0$. All results in this figure refer to the purely coherent energy supply regime, i.e., $\mathcal{N}_b = 0$.

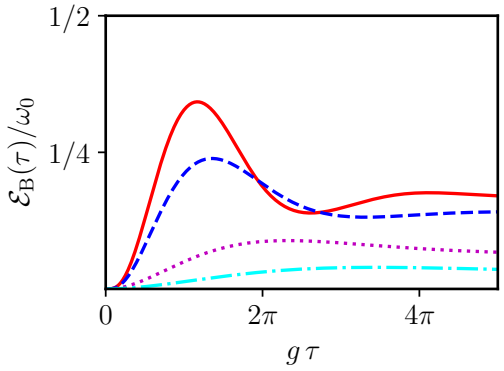

Fig. 4.9 $\mathcal{E}_{\rm B}$ (in units of ω_0) as a function of $g\tau$, for the two-qubit model. Different curves refer to different values of $\mathcal{N}_b$. Red solid line: $\mathcal{N}_b = 0$; blue dashed line: $\mathcal{N}_b = 0.1$; magenta dotted line: $\mathcal{N}_b = 0.5$; cyan dash-dotted line: $\mathcal{N}_b = 1$. Numerical results in this plot have been obtained by setting $g = F = \omega_0/5$ and $\kappa = \omega_0$. Notice that, in a finite range of values of $g\tau$, the result for $\mathcal{N}_b = 0.1$ (blue dashed line) lies above the result for $\mathcal{N}_b = 0$ (red solid line).

To study the finite-time behaviour of $E_{\rm B}(\tau)$ and $\mathcal{E}_{\rm B}(\tau)$ in the case where F is non-zero, we resort to numerical calculations. In particular, in Fig. 4.8 we present plots of these quantities for $\mathcal{N}_b = 0$ (no thermal supply) obtained for different values of F, g, and κ. In Fig. 4.9, instead, a study of $\mathcal{E}_{\rm B}(\tau)$ is presented for fixed F and various values of $\mathcal{N}_b$. Again, oscillatory behaviours can be observed which may lead to an increase of $\mathcal{E}_{\rm B}(\tau)$ as a function of temperature.

We conclude this section by commenting about optimal charging times which, for future reference, we study in the limit of strong coherent driving ($F \gg g$) and for weak dissipation $\kappa \simeq 0$. In this limit, simple analytical solutions can be found, which for the mean energy results in $E_{\rm B}(\tau) = \omega_0 \sin^2(g\tau/2)$, indicating an optimal charging time π/g that is independent of F. This optimal charging time turns out to maximize the ergotropy $\mathcal{E}_{\rm B}(\tau)$ as well.

4.4 Hybrid model

The last model we consider assumes A to be a harmonic oscillator and B a qubit whose energy gap matches the frequency ω_0 of A. Accordingly, the operators $\zeta_{\rm X}^\dagger$ in Eqs. (4.10)-(4.12) are now $\zeta_{\rm B}^\dagger = \sigma_{\rm B}^+$ (as in the previous section) and $\zeta_{\rm A}^\dagger = a^\dagger$ (as in Sec. 4.2).
Being the system hybrid and infinite-dimensional, the integration methods adopted in the previous two cases cannot be applied as they will produce an infinite set of coupled differential equations. Instead, we resort to the characteristic function approach (Walls and Milburn 2007, Lougovski et al. 2007, Bina et al. 2008, Serafini 2017), which allows one to cast Eq. (4.12) into a finite set of linear partial differential equations that can be solved numerically. By choosing this approach, we pass from infinite square matrices (density matrix formalism) to four complex functions for describing the system's state. For this purpose, we decompose $\tilde{\rho}_{\rm AB}(t)$ into the basis of the energy eigenstates $\{|1\rangle_{\rm B}, |0\rangle_{\rm B}\}$ of $H_{\rm B}$, i.e.

$$\tilde{\rho}_{\rm AB}(t) \;=\; \sum_{ij} \tilde{\rho}_{\rm A}^{(ij)}(t) \otimes |i\rangle_{\rm B}\langle j| \;. \tag{4.49}$$

Here, $\tilde{\rho}_{\rm A}^{(ij)}(t) \equiv {}_{\rm B}\langle i|\, \tilde{\rho}_{\rm AB}(t)\, |j\rangle_{\rm B}$ are operators of A which we express as a convolution integral

$$\tilde{\rho}_{\rm A}^{(ij)}(t) = \int \frac{d^2\beta}{\pi} \chi_{ij}(\beta, t) D(-\beta) \tag{4.50}$$

over a complex variable β of the displacement operator $D(\beta) \equiv \exp\left(\beta a^\dagger - \beta^* a\right)$ and

$$\chi_{ij}(\beta, t) \equiv \mathrm{tr}_{\rm A}\left[D(\beta)\tilde{\rho}_{\rm A}^{(ij)}(t)\right] \;, \tag{4.51}$$

where the latter quantity is the associated characteristic χ-function (Serafini 2017). They inherit from $\tilde{\rho}_{\rm AB}(t)$ the following constraints

$$\chi_{00}(0,t) + \chi_{11}(0,t) = 1 \;, \tag{4.52}$$
$$\chi_{ij}(\beta,t) = \chi_{ji}^*(-\beta,t) \;, \tag{4.53}$$

the first deriving from the normalization of $\tilde{\rho}_{\rm AB}(t)$, the second from its self-adjointness. Furthermore, considering that B is a qubit, Eqs. (4.34) and (4.35) can be still exploited, allowing one to express the quantities of interest as

$$\begin{aligned} E_{\rm B}(\tau) &= \omega_0 \chi_{11}(0,\tau) \;, \\ \mathcal{E}_{\rm B}(\tau) &= \frac{\omega_0}{2}\left[\sqrt{(\chi_{11}-\chi_{00})^2 + 4|\chi_{10}|^2} + \chi_{11} - \chi_{00}\right]\Big|_{\beta=0} . \end{aligned} \tag{4.54}$$

Exploiting the algebra of the harmonic oscillator, we can now recast the ME (4.12) into a set of partial differential equations for $\chi_{ij}(\beta,t)$, i.e.

$$\begin{aligned}\dot{\chi}_{ij} &= -ig\mathcal{I}_{ij}\left[\vec{\chi}\right]+2iFx\chi_{ij} \\ &\quad -\kappa\left[\left(\mathcal{N}_b+\frac{1}{2}\right)\left(x^2+y^2\right)+\frac{1}{2}\left(x\partial_x+y\partial_y\right)\right]\chi_{ij}\ ,\end{aligned} \tag{4.55}$$

where x and y are the real and imaginary components of $\beta=x+iy$ and $\mathcal{I}_{ij}\left[\vec{\chi}\right]$ are differential terms describing the energy exchange between the harmonic oscillator and the qubit:

$$\begin{cases}\mathcal{I}_{11}\left[\vec{\chi}\right]=-\frac{1}{2}\left[\left(\partial_x-i\partial_y\right)\chi_{10}+\left(\partial_x+i\partial_y\right)\chi_{01}+\left(x-iy\right)\chi_{10}+\left(x+iy\right)\chi_{01}\right] \\ \mathcal{I}_{10}\left[\vec{\chi}\right]=-\frac{1}{2}\left[\left(\partial_x+i\partial_y\right)\left(\chi_{00}-\chi_{11}\right)+\left(x+iy\right)\left(\chi_{11}+\chi_{00}\right)\right] \\ \mathcal{I}_{01}\left[\vec{\chi}\right]=\frac{1}{2}\left[\left(\partial_x-i\partial_y\right)\left(\chi_{11}-\chi_{00}\right)-\left(x-iy\right)\left(\chi_{11}+\chi_{00}\right)\right] \\ \mathcal{I}_{00}\left[\vec{\chi}\right]=\frac{1}{2}\left[\left(\partial_x-i\partial_y\right)\chi_{10}+\left(\partial_x+i\partial_y\right)\chi_{01}-\left(\left(x-iy\right)\chi_{10}+\left(x+iy\right)\chi_{01}\right)\right]\ .\end{cases}$$

[1] Equations (4.55) have been solved numerically under the usual initial conditions (4.3), which, arranged into the χ-function language, read as

$$\begin{aligned}\chi_{00}(\beta,0) &= e^{-\frac{|\beta|}{2}^2}\ , \\ \chi_{11}(\beta,0) &= \chi_{10}(\beta,0)=\chi_{01}(\beta,0)=0\ .\end{aligned} \tag{4.56}$$

For the case where $F=0$ (no coherent driving) our findings are in agreement with the two previous cases. Specifically, no ergotropy on B is generated, while, regarding $E_{\mathrm{B}}(\tau)$, for small values of κ/g an oscillating behaviour is observed which is then lost for large κ/g, the thermalization value being $E_{\mathrm{B}}(\infty)=\omega_0\mathcal{N}_f$ (data not shown). As we turn on F, non-zero values of $\mathcal{E}_{\mathrm{B}}(\tau)$ are observed with an oscillatory behaviour that reminds us of the results of the previous section, see Fig. 4.10. By numerical analysis we also study the optimal charging times (see Fig. 4.11) noticing that for the hybrid model they appear to have a $1/F^{\alpha}$ scaling, with $\alpha\sim 0.5-1$. This is deeply different with respect to the two-qubit case for which a finite charging time emerges in the same regime, and also with respect to the case of two harmonic oscillators, where the driving amplitude F does not enter in the timescales of the charging process. This peculiarity is a consequence of the structure of the Hilbert space of the hybrid system studied in this Section. Indeed, the quantum harmonic oscillator A can host an arbitrarily large number of excitations coming from the interaction with the coherent source, while the qubit (i.e. the battery B) has an upper bounded spectrum: hence, the more energy is in the mediator the lesser the charging time of the qubit is.

[1] It is worth noticing that the set (4.55) *embodies* both the constraints of Eqs. (4.52) and (4.53).

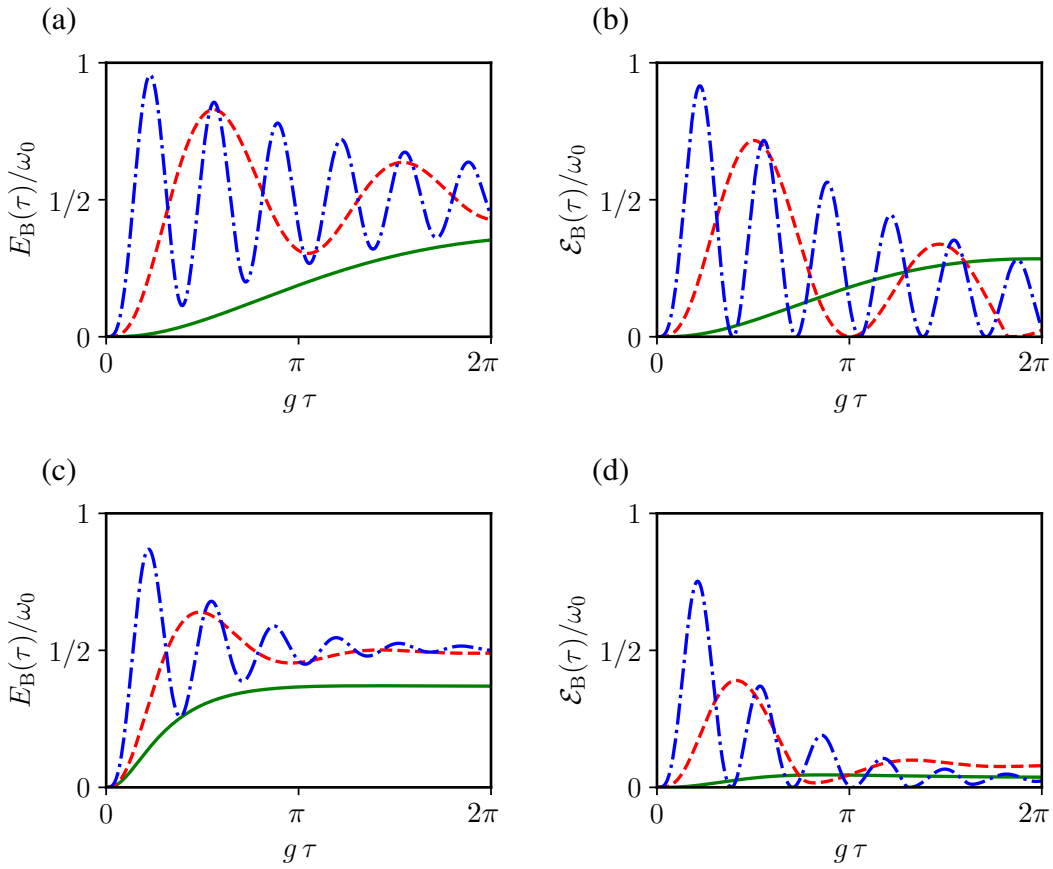

Fig. 4.10 (a) $E_{\rm B}(\tau)$ (in units of ω_0) as a function of $g\tau$, for the hybrid model. Different curves refer to different values of F (in units of ω_0). Green solid line: $F = 0.1\omega_0$; red dashed line: $F = 0.5\omega_0$; blue dash-dotted line: $F = 1.5\omega_0$. (b) Same as in (a) but for $\mathcal{E}_{\rm B}(\tau)$. Numerical results in (a) and (b) have been obtained by setting $g = 0.1\omega_0$, $\kappa = \omega_0$, and $\mathcal{N}_b = 0$. (c), (d) Same as in (a) and (b) but for $\mathcal{N}_b = 1$.

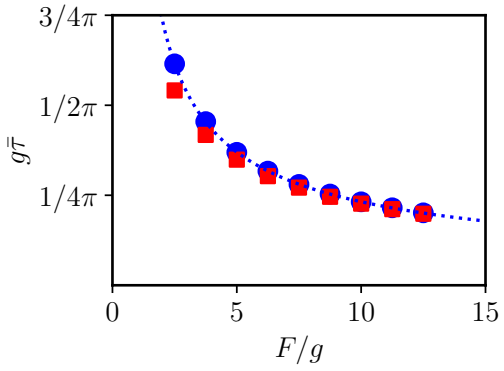

Fig. 4.11 The time scale $\bar{\tau}$ (in units of $1/g$) at which $E_{\rm B}(\tau)$ reaches its maximum value (blue circles) is plotted as a function of F/g. Red squares denote the same quantity but for the case of $\mathcal{E}_{\rm B}(\tau)$. Both results refer to the hybrid model. Numerical results in this figure have been obtained by setting $g = 0.2\omega_0$, $\kappa = \omega_0$, and refer to the purely coherent energy supply regime, i.e. $\mathcal{N}_b = 0$. The blue dotted line denotes a fit of the points $(g\bar{\tau}, F/g)$ for the stored energy, indicating a clear decreasing behavior of $\bar{\tau}$ for increasing values of the driving constant F.

4.5 Conclusions

In this Chapter, we have studied charger-mediated energy transfer for quantum batteries via an open system approach. Specifically, we dealt with three models. One in which both the charger A and the quantum battery B are described by harmonic oscillators (Sec. 4.2), one in which both A and B are qubits (Sec. 4.3), and, finally, one in which A is a harmonic oscillator and B is a qubit (Sec. 4.4). In all cases, the charger A interacts with an external energy supply E, and acts as mediator between E and B. At the beginning of the charging protocol, both A and B are in the ground state with zero energy. Then, energy is dynamically injected into the system thanks to the presence of E, thermally and/or via a resonant driving field of amplitude F. Particular attention has been devoted to the maximum extractable work from B, i.e. the so-called ergotropy of the battery (Allahverdyan et al. 2004).

Our main findings can be summarized as follows.

(i) The case of two harmonic oscillators is profoundly different from the other two cases. Because of the linearity of the system, there is no interplay between the coherent and incoherent energy supplies. In particular, in the coherent protocol ($F > 0$, zero temperature), ergotropy and energy coincide. This happens because A and B remain uncorrelated during the system's evolution.

(ii) In the case of the thermal protocol ($F = 0$, non-zero temperature), the ergotropy is always zero. This holds true for all models.

(iii) In the case of two qubits in the mixed regime ($F > 0$, non-zero temperature) (while typically non-zero temperature tends to reduce the ergotropy) there are special settings for which finite temperature is beneficial for the ergotropy. This is a consequence of the nonlinear character of this model, which leads to a non-trivial interplay among coherent and incoherent channels.

(iv) In the hybrid model, the times at which energy and ergotropy are maximal decrease monotonically with increasing driving field F. This peculiarity stems from the structure of the Hilbert space of the hybrid model and can be compared with the energy dynamics derived in Ref. Andolina et al. (2018), in a closed (i.e. Hamiltonian) setting.

CHAPTER 5

Quantum bath statistics tagging

Going beyond the instance of bosonic bath discussed in the previous Chapters, we treat here the problem of identifying the statistics of a thermal bath - fermionic or bosonic - exploiting the sensitivity of a quantum probe to its surrounding environment. We start by introducing the interest towards statistical tagging in Sec. 5.1. Then we derive in a quite general formalism the master equations of interest in Sec. 5.2, in order to specify the analysis to qubit and harmonic oscillator probes, respectively, in Sections 5.3 and 5.4. The main conclusions will be finally reported in Sec. 5.5.

5.1 Statistical tagging

In equilibrium statistical mechanics, the intrinsic indistinguishability between identical particles gives rise to the Bose-Einstein and Fermi-Dirac equilibrium distributions. These statistics found their earliest evidences in matter physics, describing black body radiation (Bose 1924) and the behavior of electrons in solids (Sommerfeld 1927) while their link with the intrinsic angular momentum of elementary particles stems as a crucial result of quantum field theory (Pauli 1940, Schwabl 2008). A standard tool to discern the statistics of a quantum system is represented by two-body correlations, experimentally accessible through equilibrium response properties to weak external fields (Mahan 2013). For example, typical and exclusive signatures are the Pauli hole in case of fermions (Giuliani and Vignale 2005) and bunching and anti-bunching phenomena in case of bosons (Paul 1982). More in general, statistics tagging turns out to be worth in all modern physics. For instance, in astrophysics, methods to recognize the statistical distributions of particles which are thermally radiated by black holes have been developed (Sannan 1988) or, going beyond *conventional* fermions and bosons, in the context of the fractional quantum hall effect (Laughlin 1983) interferometric measurements (Goldman et al. 2005) confirmed the existence of quasi-particles obeying fractional exclusion statistics (Wilczek 1982, Haldane 1991, Wu 1994). Finally, from a technological point of view, a detailed characterization of the environment surrounding a quantum system is nowadays crucial to implement quantum information protocols and, more generally, for quantum nanotechnology (Palma et al. 1996, Nielsen and Chuang 2010).

Indeed, the interaction with the environment leads to decoherence and dissipation on the system (see previous Chapters), strongly degrading purely quantum resources (Nielsen and Chuang 2010) or even, in other cases, promoting collective quantum phenomena (Scarlatella and Schiró 2016). As described in Sec. 2.3, the characterization of measurement processes and statistical inference methods applied to quantum systems is the core of quantum metrology (Paris 2009, Giovannetti et al. 2006, 2011). The estimation and the discrimination of environmental properties can be achieved both via direct measurements or indirectly, by extracting information from auxiliary systems. For instance, via putting a probe in contact with a thermal environment and performing a measure on such a probe, it is possible to extract information about the temperature (Correa et al. 2015, De Pasquale et al. 2016, Kiilerich et al. 2018, Cavina et al. 2018) and the spectral properties (Benedetti et al. 2018, Salari Sehdaran et al. 2019) of the environment itself. Following this line of reasoning, we present a protocol aimed to discriminate between fermionic and bosonic thermal baths via indirect quantum state discrimination on an auxiliary quantum probe A. More precisely in our construction the tagging of the bath statistics is performed by monitoring the state of A at a convenient finite time evolution $\bar{t}$ during the thermalization process it experiences once put in weak-coupling thermal contact (Breuer et al. 2002) with the environment. The scheme ultimately relies on the fact that, while the final configuration of A is not necessarily influenced by the statistical nature of the bath, the latter leaves residual imprintings on the transient of the thermalization process which can be picked up by proper measurements on the probe. A full characterization of the ultimate discrimination efficiency we can achieve using this technique will be presented by studying a couple of paradigmatic examples where A is assumed to be either a two level system (TLS, or qubit) or a quantum harmonic oscillator (QHO). It is worth stressing that the resulting four scenarios describe situations which are routinely encountered in experiments (Farina and Giovannetti 2019) paving the way for a proof of principle implementations of our findings (at least): indeed a two level system coupled to a bosonic bath $(TLS - bosons)$ is paradigmatic in quantum optics (Walls and Milburn 2007) and quantum computation (Palma et al. 1996); a harmonic oscillator interacting with a bath of other harmonic oscillators $(QHO - bosons)$ can describe an open opto-mechanical resonator (Gröblacher et al. 2015); finally, spin-baths are more rare but also feasible (Pekola et al. 2016) if we deal with a vibrational degree of freedom interacting with two-level defects $(QHO - fermions)$ in quantum-electromechanical systems (Blencowe 2004, Schlosshauer et al. 2008) or with the hyperfine interaction of an electron spin in a quantum dot with the surrounding nuclear spins $(TLS - fermions)$ (Prokof'ev and Stamp 2000, Urbaszek et al. 2013, Fischer et al. 2018, Bortz and Stolze 2007).

5.2 Statistics-dependent master equations

In what follows we shall adopt a compact notation that allows us to treat uniformly the four possible scenarios, *TLS-bosons, TLS-fermions, QHO-bosons*, and *QHO-fermions*. For this purpose, resuming in part the formalism of Sec. 4.1.3, we introduce a system annihilation operator ζ_p where the subscript $p \in \{\text{TLS, QHO}\}$ refers to the two possible species of probes, assuming that $\zeta_{\text{QHO}} = a$ and $\zeta_{\text{TLS}} = \sigma_-$. With this choice we can now describe the coupling between the system and its environment, by assigning the microscopic Hamiltonian $H = H_{\text{S}} + H_{\text{E}} + H_1$ characterized by the following components:

$$
\begin{aligned}
H_{\text{S}} &= \omega_0 \zeta_p^\dagger \zeta_p \,, && (5.1)\\
H_{\text{E}} &= \sum_k \omega_k {c_k^{(q)}}^\dagger c_k^{(q)} \,, && (5.2)\\
H_1 &= \sum_k \gamma_k [{c_k^{(q)}}^\dagger + c_k^{(q)}](\zeta_p + \zeta_p^\dagger) \,, && (5.3)
\end{aligned}
$$

where, at variance with (3.69) and (3.70), the environmental modes $c_k^{(q)}$ and ${c_k^{(q)}}^\dagger(q)$ can be either of bosonic nature $(q = b)$ or of fermionic nature $(q = f)$:

$$
\begin{aligned}
c_k^{(q)}\, {c_{k'}^{(q)}}^\dagger - s_q {c_{k'}^{(q)}}^\dagger\, c_k^{(q)} &= \delta_{k,k'} \,, \\
c_k^{(q)}\, c_{k'}^{(q)} - s_q c_{k'}^{(q)}\, c_k^{(q)} &= 0 \,, \\
\text{with} \quad s_{q=b(q=f)} &:= +(-)1 \,.
\end{aligned} \tag{5.4}
$$

Similarly to what we did earlier in Sec. (3.2) for a qubit coupled to a bosonic bath, following the Born-Markov-Secular microscopic derivation (cfr. Sections 2.1.2.1 and 2.1.2.2) for a thermal environment of inverse temperature β_q one arrives to a Lindblad equation that for the four cases of interest can be written in a unified form as (see also Esposito et al. (2010), Purkayastha et al. (2016), Farina, Cavina and Giovannetti (2019), Farina and Giovannetti (2019))

$$
\begin{aligned}
\dot\rho_q(t) = -i[H_{\text{S}}, \rho_q] &+ \kappa \mathcal{N}_q(\beta_q) \left(\zeta_p^\dagger \rho_q(t) \zeta_p - \tfrac{1}{2}\{\zeta_p \zeta_p^\dagger, \rho_q(t)\}\right) \\
&+ \kappa[1 + s_q \mathcal{N}_q(\beta_q)] \left(\zeta_p \rho_q(t) \zeta_p^\dagger - \tfrac{1}{2}\{\zeta_p^\dagger \zeta_p, \rho_q(t)\}\right) \,,
\end{aligned} \tag{5.5}
$$

with κ being the bare dissipation rate and with

$$
\mathcal{N}_q(\beta_q) := \frac{1}{e^{\beta_q \omega} - s_q} \,, \tag{5.6}
$$

being the Bose-Einstein (Fermi-Dirac) distribution for $q = b$ (f), with $\omega > 0$ being an effective energy parameter (Esposito et al. 2010), that contains a contribution from the

system \ *environment*	fermionic	bosonic
Two-Level System	κ	$n_{\rm th}\kappa$
Quantum Harmonic Oscillator	$\kappa/n_{\rm th}$	κ

Table 5.1 Transition rates governing the dynamics of the system-bath models for the four scenarios: in this expressions κ is a constant that only depends upon the interaction strength of the model, while $n_{\rm th}$ depends on β_q as in Eq. (5.10). Notice that for *homogeneous* settings (TLS-fermions or QHO-bosons) the values of the rates are independent of the bath temperature. Furthermore, since $n_{\rm th} \geq 1$, we observe that for the TLS probe the transition rate associated with the bosonic bath is always larger than the corresponding fermionic value, while exactly the opposite occurs for the QHO probe scenario. We also recognize that in both the TLS and QHO probe configurations, the difference between the transition rates induced by the bosonic and fermionic statistics increases with the temperature. Such gap nullifies instead in the zero-temperature limit ($\beta_q \to \infty$) where $n_{\rm th} = 1$: accordingly, under this conditions the dynamics of the model is expected not to detect any difference in the bath statistics.

bare energy of the system and from the chemical potential of the bath [1].
Notice that the differences between the master equations (5.5) for the two cases $q = b$ and $q = f$ concern the kind of average occupation number that is present and the sign s_q in the second line. Both the features are originated from Eqs. (5.4), i.e. from the different exchange rules of bosons and fermions. Furthermore, Eq. (5.5) implies the following balance equation for the average excitation number of the system:

$$\frac{d}{dt}\langle\zeta_p^\dagger\zeta_p(t)\rangle = -\kappa\left[\mathcal{N}_q(\beta_q)/\mathcal{N}_p(\beta_q)\right]\langle\zeta_p^\dagger\zeta_p(t)\rangle + \kappa\mathcal{N}_q(\beta_q)\,, \tag{5.7}$$

where it is understood that

$$\langle\zeta_p^\dagger\zeta_p(\infty)\rangle \;=\; \mathcal{N}_p(\beta_q)\,, \tag{5.8}$$

with

$$\mathcal{N}_{\rm p=TLS}(\beta_q) = \mathcal{N}_f(\beta_q) \qquad \text{and} \qquad \mathcal{N}_{\rm p=QHO}(\beta_q) = \mathcal{N}_b(\beta_q)\,. \tag{5.9}$$

In Eq. (5.7) we can recognize the characteristic rate $\kappa_{p-q} = \kappa\mathcal{N}_q(\beta_q)/\mathcal{N}_p(\beta_q)$ from which the result of Table 5.1 follows automatically defining the quantity

$$n_{\rm th} := \mathcal{N}_b(\beta_q)/\mathcal{N}_f(\beta_q) = \coth(\beta_q\omega/2)\,. \tag{5.10}$$

[1] We suppose ω to be the same for b and f. When the chemical potential is different between the fermionic and bosonic cases we can opportunely redefine β_f and β_b to preserve the Eq. (5.6).

To comment Table 5.1, let us consider a thermal charging, i.e. a system initially in its ground state gets excited by a finite temperature thermal bath of statistics q, finally reaching the bath temperature $1/\beta_q$ (a process analyzed in the previous Chapters under different perspectives). A TLS interacting with a bosonic environment, realizes a situation in which the great amount of excitation contained in each QHO cannot be hosted by the TLS. This unbalance results in an increase of the charging rate. The opposite is expected to occur when a QHO interacts with a fermionic bath: increasing temperature is expected to decrease the charging rate. Finally, such effect must disappear at low temperature where the difference between the energy spectra is irrelevant, because $\mathcal{N}_b(\beta) \sim \mathcal{N}_f(\beta) \sim e^{-\beta\omega}$ for $\beta \to \infty$.

Other considerations about speed effects arising from coupling a system with a bounded spectrum and a system with an unbounded spectrum can be found in Schlosshauer et al. (2008), Farina, Andolina, Mari, Polini and Giovannetti (2019), Andolina et al. (2018).

5.3 Qubit probe

We treat here the most generic problem that consists in discriminating between two baths with disparate constituents at unequal temperatures. We restrict the analysis to a qubit quantum probe, suitable to the experimental linear-optical simulations by Ilaria Gianani, Marco Barbieri and Valeria Cimini (Gianani et al. 2020). Notably, as a central result of the analysis, there exist temperature regimes in which the presence of coherence in the initial state preparation is beneficial for the discrimination capability. Furthermore, depending on the probe input state of the probe, we found that non-equilibrium measurement conditions turn out to be often (but not always) optimal and detail the cases where it becomes advantageous to wait for complete thermalization of the probe.

5.3.1 The model

The model we studied in Gianani et al. (2020) is the following. At time $t = 0$ a qubit quantum probe A is prepared in some fiduciary initial density operator $\rho(0)$ and let to interact for some time t with a partially unknown environment E that can be of two types: bosonic at temperature $1/\beta_b$, or fermionic at temperature $1/\beta_f$, the values $1/\beta_b$ and $1/\beta_f$ being assigned a priori. We shall attempt to discriminate among the two alternatives by only performing measurements on the reduced final state $\rho(t)$ of A, which hence encodes all the information about the nature of E one can access to. This allows us to describe the whole scheme as a standard hypotheses testing problem (Helstrom 1976), where one has to determine whether $\rho(t)$ corresponds to the density matrix $\rho_b(t)$ of A which one would have obtained by evolving $\rho(0)$ under the influence of the bosonic bath of temperature $1/\beta_b$, or to $\rho_f(t)$, which instead one would have obtained by evolving the same $\rho(0)$ under the influence of the fermionic bath of temperature $1/\beta_f$. To quantify our ability in discriminating between these scenarios we can then use the Helstrom error probability (HEP) functional

$$H(\rho_b(t), \rho_f(t)) \;:=\; \frac{1}{2} - \frac{1}{4}\|\rho_b(t) - \rho_f(t)\|_1 \,, \tag{5.11}$$

with $\|\cdots\|_1$ being the trace norm symbol (see Sec. 2.3.1).
In order to get an analytical expression for (5.11) we assign $\rho_b(t)$ and $\rho_f(t)$ in terms two independent Lindblad master equations for A obtained under standard system-bath weak coupling assumptions (Lindblad 1976, Gorini et al. 1976). Moving into the interaction picture and choosing $\mathrm{p} = \mathrm{TLS}$ such that $\zeta_{\mathrm{TLS}} = \sigma_- = |0\rangle\langle 1|$, Eq. (5.5) becomes

$$\dot{\rho}_q(t) = \kappa[1 + s_q\mathcal{N}_q(\beta_q)]\mathcal{D}_{\sigma_-}[\rho_q(t)] + \kappa\mathcal{N}_q(\beta_q)\mathcal{D}_{\sigma_+}[\rho_q(t)] \,, \tag{5.12}$$

the index $q = f, b$ referring again to the two hypothetical initial configurations of the bath and

$$\mathcal{D}_{\sigma_\pm}[\cdots] := \sigma_\pm[\cdots]\sigma_\pm^\dagger - \frac{\sigma_\pm^\dagger\sigma_\pm[\cdots] + [\cdots]\sigma_\pm^\dagger\sigma_\pm}{2} \tag{5.13}$$

representing the Lindblad dissipators. Introducing the Pauli vector operator $\vec{\sigma} := (\sigma_x, \sigma_y, \sigma_z)$, and writing the density matrix of the system in the Bloch vector formalism $\rho_q(t) = \frac{1+\vec{\sigma}\cdot\vec{a}^{(q)}(t)}{2}$, Eq. (5.12) can then be conveniently cast in the form

$$\begin{aligned} \dot{a}_z^{(q)}(t) &= -\kappa_q a_z^{(q)}(t) - \xi_q, \\ \dot{a}_{x,y}^{(q)}(t) &= -\frac{\kappa_q}{2} a_{x,y}^{(q)}(t), \end{aligned} \tag{5.14}$$

where now

$$\begin{aligned} &\kappa_b := \kappa \coth(\beta_b\omega/2), \qquad && \kappa_f := \kappa\ , \\ &\xi_b := \kappa, && \xi_f := \kappa \tanh(\beta_f\omega/2)\ , \end{aligned} \tag{5.15}$$

showing that in the case of equal temperatures, the evolution occurs at faster scales for the bosonic bath scenario (see the first row of Table 5.1). Explicit integration of (5.14) leads finally to the solution

$$\begin{aligned} a_z^{(q)}(t) &= e^{-\kappa_q t}(a_z(0) - a_z^{(q)}(\infty)) + a_z^{(q)}(\infty)\ , \\ a_{x,y}^{(q)}(t) &= e^{-\kappa_q t/2} a_{x,y}(0), \end{aligned} \tag{5.16}$$

with $a_{x,y,z}(0)$ being the cartesian components of the Bloch vector associated with the input state $\rho(0)$ of A and

$$a_z^{(q)}(\infty) = -\tanh(\beta_q\omega/2) \tag{5.17}$$

defining the equilibrium (thermal) configuration of the system (of course $a_{x,y}^{(q)}(\infty) = 0$).

5.3.2 Discrimination perfomances

Using the fact that the trace norm of the difference between $\rho_b(t)$ and $\rho_f(t)$ is given by the Cartesian distance $|\vec{a}_b(t) - \vec{a}_f(t)|$ of the associated three dimensional Bloch vectors, from (5.16) it follows that Eq. (5.11) can be expressed as

$$\begin{aligned} H(\rho_b(t), \rho_f(t)) = \frac{1}{2} - \frac{1}{4}\Big\{ \Big[&(e^{-\kappa_f t} - e^{-\kappa_b t}) a_z(0) + a_z^{(f)}(\infty)(1 - e^{-\kappa_f t}) \\ &- a_z^{(b)}(\infty)(1 - e^{-\kappa_b t}) \Big]^2 + (e^{-\kappa_f t/2} - e^{-\kappa_b t/2})^2 \big(|\vec{a}(0)|^2 - a_z^2(0)\big) \Big\}^{1/2}\ . \end{aligned} \tag{5.18}$$

A close inspection reveals that all pure input states $\rho(0)$ with the same initial value of $a_z(0)$ achieve the same performance (this simply follows from the symmetry of Eq. (5.14) around the z-axis). Furthermore, and most importantly, for all assigned values of t and $a_z(0)$, one may notice that the associated HEP can be reduced by setting the length of $\vec{a}(0)$ at its maximum 1, i.e. imposing the initial state of the probe to be pure. In other words, mixedness in the input state is always detrimental, implying that, in order to find the best input configuration, it is sufficient to restrict the search to the set of pure states. This leads to

$$H(\rho_b(t),\rho_f(t))\Big|_{\text{pure}} = \frac{1}{2} - \frac{1}{4}\Big\{\Big[(e^{-\kappa_f t} - e^{-\kappa_b t})a_z(0) + a_z^{(f)}(\infty)(1-e^{-\kappa_f t}) \\ -a_z^{(b)}(\infty)(1-e^{-\kappa_b t})\Big]^2 + (e^{-\kappa_f t/2} - e^{-\kappa_b t/2})^2\big(1-a_z^2(0)\big)\Big\}^{1/2} := H(t;a_z(0)) \,, \tag{5.19}$$

which only depends on time and on the z-component $a_z(0) \in [-1,1]$ of the unit vector $\vec{a}(0)$. It is worth recalling that fixing $a_z(0) = 1$ ($a_z(0) = -1$) corresponds to initialize A into the excited state $|1\rangle$ (ground state $|0\rangle$) of its local Hamiltonian. On the contrary, in the more general pure state scenario we are facing in Eq. (5.19), the condition $|a_z(0)| < 1$ identifies input states of the probe which are proper superpositions of the energy eigenstates of the model. Our next goal is to minimize $H(t;a_z(0))$ with respect to all possible choices of $a_z(0)$ and evolution time t, for given values of the temperatures $1/\beta_f$ and $1/\beta_b$. Before doing so, however, we find useful to consider first what happens when $a_z(0) = 1$, a choice that is known to provide the best discriminating strength for statistical tagging under equal bath temperature assumption, i.e. $\beta_f = \beta_b$ (Farina, Cavina and Giovannetti 2019) [as we will see in Fig. 5.3(b)], and for thermometry (Jevtic et al. 2015).

5.3.3 Input excited state

Setting $a_z(0) = 1$, i.e. assuming A to be initialized in the excited state $|1\rangle$ of the model, Eq. (5.19) reduces to

$$H(t;1) = \frac{1}{2} - \frac{1}{4}\Big|e^{-\kappa_f t} - e^{-\kappa_b t} + a_z^{(f)}(\infty)(1-e^{-\kappa_f t}) - a_z^{(b)}(\infty)(1-e^{-\kappa_b t})\Big| \,. \tag{5.20}$$

For $\beta_b = \beta_f \equiv \beta$, we get $H(t;1) = \frac{1}{2} - \frac{1}{4}\frac{n_{\text{th}}+1}{n_{\text{th}}}(e^{-\kappa t} - e^{-\kappa n_{\text{th}} t})$, whose time dependence is reported in Fig. 5.1 for different choices of $1/\beta$. In the limit of large time t the error asymptotically approaches $1/2$ indicating the failure of the tagging procedure. Minimum values for the error are instead obtained for an optimal choice of t given by

$$\bar{t} = \ln(n_{\text{th}})/[2\kappa\mathcal{N}_b(\beta)] = \ln(n_{\text{th}})/[\kappa(n_{\text{th}}-1)] \,, \tag{5.21}$$

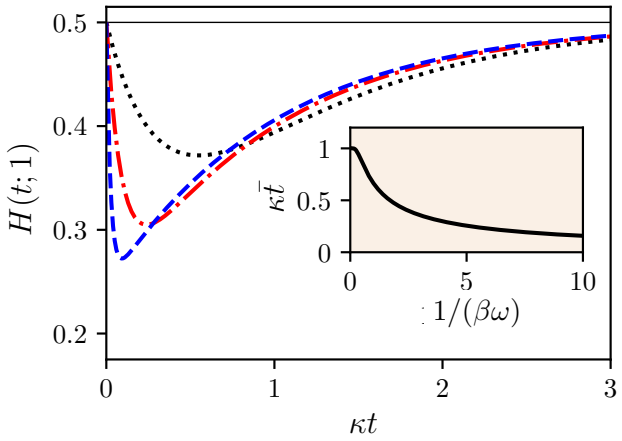

Fig. 5.1 Plots of the Helstrom error probability (5.20) for the TLS probe case, initialized in the excited state and setting $\beta_b = \beta_f \equiv \beta$, as a function of the measurement time t. The three curves represent three different bath temperatures: $1/(\beta\omega) = 1.5$ (black dotted line), $1/(\beta\omega) = 5.5$ (red dot-dashed line) and $1/(\beta\omega) = 20.5$ (blue dashed line). The inset shows $\kappa\bar{t}$ of Eq. (5.21) as function of $1/(\beta\omega)$, with $\bar{t}$ being the time which minimizes the Helstrom error probability.

whose functional dependence upon temperature is reported in the inset of the figure. As anticipated in the caption of Table 5.1 the model exhibit no discrimination strength at zero temperature where $H(t;1)(t) = 1/2$, while better discriminating strength is achieved at high temperatures since in this case $n_{\rm th}$ diverges, and so does the gap between the bosonic and fermionic thermalization rates.

To include the case $\beta_f \neq \beta_b$, we then minimize numerically $H(t;1)$ in (5.20) with respect to t, as a function of β_f and β_b. The optimal times $\bar{t}$ we obtain and the corresponding values of $H(\bar{t};1)$ are reported in Fig. 5.2(a) (left and right plots respectively). For $\beta_b \geq \beta_f$ (fermionic bath hotter than bosonic bath) the best discrimination is still attained at finite time ($\bar{t} < \infty$) where A has not achieved full thermalization and is hence in a non-equilibrium configuration; on the contrary, for $\beta_b < \beta_f$ (fermionic bath cooler than bosonic bath) it can become more advantageous to discriminate the two channels by exploiting the steady state properties of the probe, i.e. $\bar{t} = \infty$. This happens above the critical curve that defines the discontinuity in the left contour plot of Fig. 5.2(a). An analytical treatment of this transition is given in Gianani et al. (2020). We remark that the core of the above observation remains unchanged when we evaluate the discrimination efficiency of the process adopting different figures of merit. For instance we can focus on the quantum Chernoff quantity [see Eq. (2.99)][2]

$$Q(\rho_b(t), \rho_f(t)) := \min_{r\in[0,1]} \mathrm{Tr}[\rho_b^r(t)\rho_f^{1-r}(t)] \; . \tag{5.22}$$

[2]Whose application to the particular case of qubit states can be found in Calsamiglia et al. (2008).

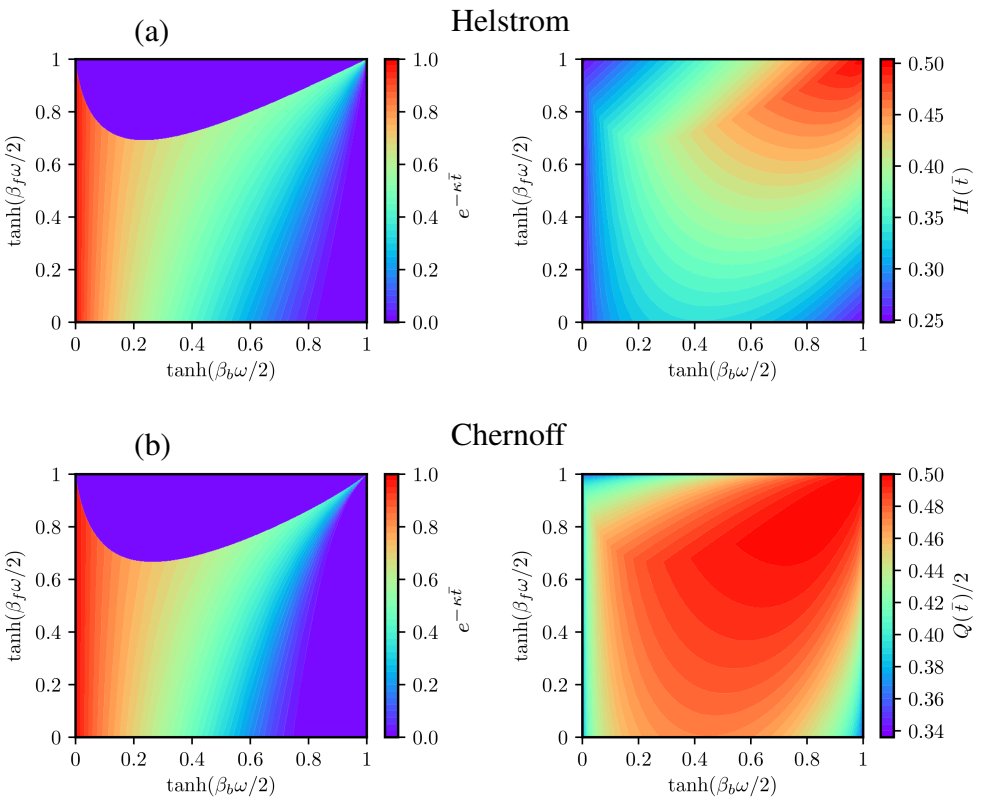

Fig. 5.2 Panel (a). Left: Study of the optimal measurement time $\bar{t}$ minimizing the Helstrom error probability $H(t;1)$ of Eq. (5.20) associated to the excited input state of the probe A (i.e. $a_z(0) = 1$), as a function of the bosonic and fermionic bath inverse temperatures β_b and β_f, using the convenient parametrizations indicated in the plot labels. The discontinuity in the contour plot is the boundary above which the discrimination is optimal only if performed on the steady state of the probe ($\bar{t} = \infty$, i.e. $e^{-\kappa\bar{t}} = 0$), the same holding for the pathological case $\beta_b = \infty$ ($\tanh(\beta_b\omega/2) = 1$). For all the other values of the parameters β_b and β_f the optimal time is finite ($\bar{t} < \infty$, i.e. $e^{-\kappa\bar{t}} > 0$). Right: Corresponding Helstrom probability of error $H(t;1)$ evaluated at $t = \bar{t}$. Panel (b): same calculation as in (a) but using the Chernoff quantity (5.22) instead of the Helstrom error probability.

The optimal values of $\bar{t}$ obtained by numerically minimizing (5.22) when initializing A in the excited state $|1\rangle$, are presented in Fig 5.2(b). Consistently, it exhibits a critical trade-off analogous to the one observed in Fig 5.2(a). We mention that again the same result is obtained via a Bayesian approach to the problem, suitable for immediate experimental checking (Gianani et al. 2020). This general behavior leads to the conclusion that, if we restrict the analysis to the case where A is initially set into the excited state, there are temperature regimes where the optimal discrimination efficiency is attained only letting the system to reach its equilibrium configuration.

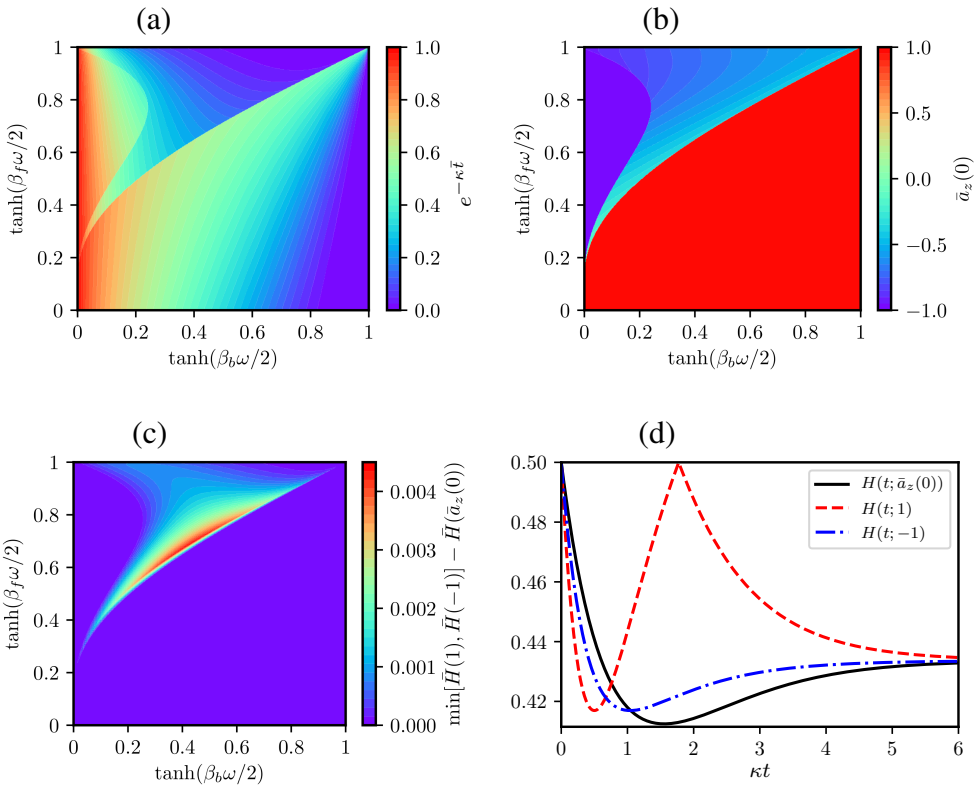

Fig. 5.3 (a)-(c) Optimization of the HEP $H(t; a_z(0))$ of Eq. (5.19) both over time and over the input state of the probe, the latter being a generic pure state with a certain value $a_z(0)$ of the z-component of the Bloch vector. We report the following contour plots with respect to the bath inverse temperatures β_f and β_b . The minimum $\bar{H}(\bar{a}_z(0))$ of the HEP is achieved at a certain time $\bar{t}$ (a) and for an optimal value $\bar{a}_z(0)$ of $a_z(0)$ (b). The advantage coming from allowing coherent superpositions is presented in (c), where we show the gap between the (generally overestimated) quantity obtained by restricting the analysis only to $a_z(0) \in \{1, -1\}$ and the optimal value $\bar{H}(\bar{a}_z(0))$. Notice that for β_f , β_b and $\bar{t}$ we used the convenient parametrizations indicated in the plot labels. (d) Dynamical evolution of $H(t; a_z(0))$ for a case ($\tanh(\beta_f\omega/2) \approx 0.68$, $\tanh(\beta_b\omega/2) \approx 0.41$) in which coherent superpositions ($\bar{a}_z(0) \approx -0.42$) give better performances than the energy eigenstates ($a_z(0) \in \{1, -1\}$) as input of the probe. Notice that at $t \approx 1.8\kappa^{-1}$ the HEP associated with excited state reaches the worst case value $1/2$, indicating zero susceptibility of the probe.

5.3.4 Optimal input states of the probe

Next step is to exploit the full domain of possibilities offered by the model, minimizing the HEP value (5.19) not just with respect to t, but also with respect to the input pure state of the probe. It hence includes the possibility of using input states which are coherent superpositions among the excited and ground states, a situation that is verified taking pure states with $|a_z(0)| < 1$. An indication that such special states could be of some help in improving the performance of the scheme follows by observing that for $|a_z(0)| < 1$ it is not possible to find times $t > 0$ such that $H(t; a_z(0))$ reaches the worst case value of $1/2$, corresponding to an absolute impossibility of distinguishing among the two bath scenarios, a fact that is not generally granted by setting $a_z(0) = \pm 1$ which allows for crossing points between the *trajectories* $\rho_b(t)$ and $\rho_f(t)$. Values of $|a_z(0)| < 1$ can however do much more than this: in some regimes they also give the absolute best performance we can aim to. In Fig. 5.3 we illustrate the optimization of the HEP $H(t; a_z(0))$ over time and input state of the probe, as a function of the bath inverse temperatures β_f and β_b. The first thing to be noticed is that now, at variance with the input excited state case discussed in Sec. 5.3.3, the optimal times $\bar{t}$ are always finite, apart from the asymptotic regimes where the bosonic temperature converges to zero (i.e. $\beta_b \to \infty$) – compare Fig. 5.3 (a) with the left plot of Fig. 5.2 (a). This shows that optimality of non-equilibrium probing times is fully restored once we do not restrict the probe input state to specific conditions. Secondly, denoting by $\bar{a}_z(0)$ the optimal value of $a_z(0)$, Fig. 5.3 (b) reveals that, while using energy eigenstates (either excited or ground states) of the probe as input is often optimal, there is a non trivial regime of temperatures in which a coherent ($|a_z(0)| < 1$) initial preparation is fundamental to reach the best performance. More specifically, there is numerical evidence that whenever the fermionic bath is hotter than the bosonic one ($\beta_b \geq \beta_f$), choosing the excited state of A as input is still the right choice to provide optimal discrimination performances (red region in Fig. 5.3 (b)). The situation changes however if the fermionic bath is cooler than the bosonic one ($\beta_b < \beta_f$): here the optimal input choice depends on the specific values of the temperatures and, in particular, for sufficiently large β_f coherent energy states can dominate (notice also that, for small values of β_b, the optimal input can be the ground state of A - blue region in Fig. 5.3 (b)). The coherent advantage is enlightened in Fig. 5.3 (c) in which we show the gap between the minimum of $H(t; a_z(0))$ obtained by restricting the optimization only to $a_z(0) = 1$ and $a_z(0) = -1$ and the optimal value $\bar{H}(\bar{a}_z(0))$ obtained by allowing also energy coherent preparations. In panel (d) of Fig. 5.3 we finally present as an example the temporal evolution of the HEP for a specific choice of the temperatures that admits as optimal the value $\bar{a}_z(0) \approx -0.42$ that identifies a coherent superposition of energy eigenstates. In such a plot we show $H(t; \bar{a}_z(0))$ aside with the HEP values $H(t; -1)$ and $H(t; 1)$

associated with the ground and the excited input state of A. Notice that while for small t, $H(t;-1)$ and $H(t;1)$ perform better than $H(t;\bar{a}_z(0))$, in the long run the latter gives the lowest HEP values and leads to the identification of the optimal time as $\bar{t} \approx 1.6\kappa^{-1}$ [see Eq. (5.37) for more on this]. Notice also that at $t \approx 1.8\kappa^{-1}$, we have $H(t;1) = 1/2$ indicating that at this special time the probe intialized into the excited state looses all its ability in discriminating between the two alternative hypothesis: on the contrary, as anticipated in the introductory paragraphs of the section, $H(t;\bar{a}_z(0))$ remains strictly below the $1/2$ value for all positive t.

5.3.5 Analytical treatments

We present now an attempt of analytically minimizing the HEP (5.19) both over time and input state of A. We first explicitly show that by considering coherence in the initial preparation allows to avoid crossing points among the *trajectories* $\rho_b(t)$ and $\rho_f(t)$, then we illustrate how to optimize the search of the minimum.

5.3.5.1 Loss of susceptibility under non-coherent inputs

The worst discrimination scenario is attained when HEP reaches its maximum value $1/2$ and we cannot recover information on the nature of the bath from the state of A. From Eq. (5.11) this happens when $\|\rho_b(t) - \rho_f(t)\|_1 = 0$, i.e. when the two trajectories intercept. From Eq. (5.19) we observe that this can only occur when

$$\begin{cases} (e^{-\kappa_f t/2} - e^{-\kappa_b t/2})^2 (1 - a_z^2(0)) = 0 \ , \\ \\ (e^{-\kappa_f t} - e^{-\kappa_b t}) a_z(0) + a_z^{(f)}(\infty)(1 - e^{-\kappa_f t}) - a_z^{(b)}(\infty)(1 - e^{-\kappa_b t}) = 0 \ . \end{cases} \tag{5.23}$$

However, setting $|a_z(0)| < 1$, i.e. allowing the input state of A to be a non trivial superposition of the energy eigenstates, this corresponds to

$$\begin{cases} e^{-\kappa_f t/2} = e^{-\kappa_b t/2} \ , \\ \\ (a_z^{(f)}(\infty) - a_z^{(b)}(\infty))(1 - e^{-\kappa_b t}) = 0 \ , \end{cases} \tag{5.24}$$

which can only be fulfilled for $t = \infty$ and $\beta_f = \beta_b$. On the contrary, setting $a_z(0) = \pm 1$ (i.e forcing the probe to be in one of the two energy eigenstates of the system), the system (5.23) reduces to a single equation

$$\pm(e^{-\kappa_f t} - e^{-\kappa_b t}) + a_z^{(f)}(\infty)(1 - e^{-\kappa_f t}) - a_z^{(b)}(\infty)(1 - e^{-\kappa_b t}) = 0 \ , \tag{5.25}$$

which, depending on the specific values of β_b and β_f may allow for non trivial $t > 0$ solutions, indicating complete loss of susceptibility of the probe.

5.3.5.2 Full optimization

We are interested in determining the minimum value of Eq. (5.19) with respect to all possible inputs (i.e. all possible choices of $a_z(0) \in [-1,1]$) and all possible times $t \geq 0$. According to (5.11) this is formally equivalent to determining the maximum of $\|\rho_b(t) - \rho_f(t)\|_1$ which in this case is given by the function

$$D(t; a_z(0)) := \|\rho_b(t) - \rho_f(t)\|_1 = \Big\{ [(e^{-\kappa_f t} - e^{-\kappa_b t})a_z(0) + a_z^{(f)}(\infty)(1 - e^{-\kappa_f t}) - a_z^{(b)}(\infty)(1 - e^{-\kappa_b t})]^2 + (e^{-\kappa_f t/2} - e^{-\kappa_b t/2})^2(1 - a_z^2(0)) \Big\}^{1/2} . \tag{5.26}$$

The best way to approach the problem seems to first optimize with respect to $a_z(0)$ for fixed t and then maximize with respect to t. Again, we call $(\bar{t}, \bar{a}_z(0))$ the point where the absolute maximum value of $D^2(t; a_z(0))$ is attained. Hence, let us fix t and rewrite $D^2(t; a_z(0))$ as a parabola in $a_z(0)$:

$$D^2(t; a_z(0)) \;=\; f_-^2(f_+^2 - 1)a_z^2(0) + 2Af_-f_+a_z(0) + f_-^2 + A^2 , \tag{5.27}$$

with

$$f_\pm := e^{-\frac{\kappa t}{2}} \pm e^{-\frac{\kappa t}{2y}} , \qquad A := -x(1 - e^{-\kappa t}) + y(1 - e^{-\frac{\kappa t}{y}}) , \tag{5.28}$$

where we used the coordinates

$$x := -a_z^{(f)}(\infty) = \tanh(\beta_f \omega/2) , \qquad y := -a_z^{(b)}(\infty) = \tanh(\beta_b \omega/2) , \tag{5.29}$$

to express the dependence upon β_b and β_f. Since $a_z(0) \in [-1,1]$, $\bar{a}_z(0)$ is either one of the extrema -1 and 1 or the abscissa of the vertex $V = Af_+/[f_-(1 - f_+^2)]$ of the parabola (5.27). The condition for the vertex to be the maximum is that the parabola is concave down and that the abscissa of the vertex strictly falls inside the interval $]-1,1[$:

$$\frac{f_-}{f_+}(1 - f_+^2) > |A| \Leftrightarrow \bar{a}_z(0) = V \in]-1,1[. \tag{5.30}$$

On the other hand, its violation imposes that the maximum is one of the extrema depending on the sign of A:

$$\frac{f_-}{f_+}(1 - f_+^2) \leq |A| \Leftrightarrow \bar{a}_z(0) = \mathrm{sign}[A] . \tag{5.31}$$

The equation above holds for $A \neq 0$, when $A = 0$ the points $a_z(0) = 1$ and $a_z(0) = -1$ are two equivalent maxima (still provided that the function is concave up). In the

end, the choice of the maximum is among $D^2(t_1; V_{t_1})$, $D^2(t_2; 1)$, $D^2(t_2; -1)$ for all t_1 satisfying the inequality in (5.30) and t_2 satisfying the inequality in (5.31). The explicit values of the three quantities above can be computed from Eq. (5.27) and read:

$$D^2(t_1; V_{t_1}) = \frac{f_-^2(t_1)(f_+^2(t_1) - 1) - A^2(t_1)}{f_+^2(t_1) - 1} \,, \tag{5.32}$$

$$D^2(t_2; 1) = (f_+(t_2)f_-(t_2) + A(t_2))^2 \,, \tag{5.33}$$

$$D^2(t_2; -1) = (f_+(t_2)f_-(t_2) - A(t_2))^2 \,. \tag{5.34}$$

Such maximization procedure yields the point $(\bar{t}, \bar{a}_z(0))$ we were searching for fixed x and y. However, notice that in general (for both the cases in which the concavity is up and down) the sign of A determines the sign of $\bar{a}_z(0)$,

$$\text{sign}[\bar{a}_z(0)] = \text{sign}[A] \,, \tag{5.35}$$

implying for instance that when the bosonic bath is not hotter than the fermionic bath, i.e. in the region

$$y \geq x \Rightarrow \bar{a}_z(0) > 0 \,, \tag{5.36}$$

in agreement with Fig. 5.3 (b). Moreover, condition (5.30) cannot be satisfied for t sufficiently close to 0 such that

$$\frac{\kappa t/2}{\ln\left(\frac{1}{1-\exp(-\kappa t/2)}\right)} \leq y \Rightarrow \bar{a}_z(0) = \text{sign}[A] \,. \tag{5.37}$$

This short time condition leads to the conclusion that the coherent advantage can occur only in a "long run", but still out-of-equilibrium, as previously illustrated in Fig. 5.3(d).

5.4 Quantum harmonic oscillator probe

Assume next the probe A to be a quantum harmonic oscillator, formally setting $\zeta_{p=\mathrm{QHO}} = a$ in Eq. (5.5), with a and $a^\dagger$ being the ladder operators of the bosonic mode, see Eq. (2.57). For this kind of probe, in the absence of the input energy limitation, the error probability can be brought to reach arbitrarily small values because of the possibility of injecting arbitrarily large initial energy into the system. Clearly an analogous effect cannot be found when probing the bath with a TLS due to the limited Hilbert space of the latter. To simplify the analysis, we restrict here our attention to the case

$$\beta_f = \beta_b := \beta \, . \tag{5.38}$$

Under these settings, an explicit integration of Eq. (5.5) can be easily obtained in the case of Gaussian input states (Weedbrook et al. 2012, Serafini 2017, Ferraro et al. 2005) discussed in Sec. 2.2.3.1, having vehemently pursued experimental realizations (see e.g. Laurat et al. (2005), Adesso et al. (2014)). As described in Sec. 2.2.3.1, they can be expressed as displaced, squeezed thermal states of the form

$$\rho(0) = D^\dagger(\boldsymbol{\xi}_0) S^\dagger(\chi_0) \frac{e^{-\bar{\beta}_0 \omega a^\dagger a}}{Z(\bar{\beta}_0)} S(\chi_0) D(\boldsymbol{\xi}_0) \, , \tag{5.39}$$

$Z(\bar{\beta}_0) := \mathrm{Tr}[e^{-\bar{\beta}_0 \omega a^\dagger a}]$ being a normalization factor [see Eq. (2.56)]. The dynamics of these inputs is completely determined by the first and second moments of the system annihilation and creation operators which, by direct integration, yield the following expressions

$$\langle a(t) \rangle = \langle a(0) \rangle e^{-\frac{\kappa}{2}/n_{\mathrm{th}}^{(\mathrm{q})} t} e^{-i\omega_0 t} \, , \tag{5.40}$$

$$\langle a^2(t) \rangle = \langle a^2(0) \rangle e^{-\kappa/n_{\mathrm{th}}^{(\mathrm{q})} t} e^{-2i\omega_0 t} \, , \tag{5.41}$$

$$\langle a^\dagger a(t) \rangle = \langle a^\dagger a(0) \rangle e^{-\kappa/n_{\mathrm{th}}^{(\mathrm{q})} t} + \mathcal{N}_b(\beta)(1 - e^{-\kappa/n_{\mathrm{th}}^{(\mathrm{q})} t}) \, , \tag{5.42}$$

with $\langle a^\dagger a(t) \rangle$ exhibiting a transition rate renormalization factor $1/n_{\mathrm{th}}^{(\mathrm{q})}$, holding 1 for $q = b$ and $1/n_{\mathrm{th}}$ for $q = f$, that is the inverse of the one observed for TLS model as anticipated in Table 5.1 [$n_{\mathrm{th}} = \coth(\beta\omega/2)$, see Eq. (5.10)], and with the initial values in Eqs. (5.40)-(5.42) being determined in terms of the parameters of the state (5.39) as previously detailed in Eqs. (2.81)-(2.85).

We immediately notice that, once more, at zero temperature ($n_{\mathrm{th}} = 1$) the probe dynamics is insensitive to the bath statistics. The same occurs for generic β in the asymptotic limit $t \to \infty$ where, independently of the initial state and of the statistics of the bath, the system obtains an average number of photons $\langle a^\dagger a(\infty) \rangle = \mathcal{N}_b(\beta)$ and the coherences disappear: $\langle a(\infty) \rangle = \langle a^2(\infty) \rangle = 0$.

As a measure of distinguishability of the associated $\rho_b(t)$ and $\rho_f(t)$ counterparts of the input (5.39) we utilize the quantum Chernoff quantity (2.99) for which a convenient formula for Gaussian states is known (Calsamiglia et al. 2008, Weedbrook et al. 2012, Pirandola and Lloyd 2008), as reported in Eq. (2.100) of Sec. 2.3.2.1. When the initial state has zero squeezing ($\chi_0 = 0$), Eq. (2.100) assumes the simplified form

$$Q_r(t) = \frac{2\,\mathcal{N}_{\bar{\beta}_b,r}\,\mathcal{N}_{\bar{\beta}_f,1-r}}{\nu_{\bar{\beta}_b r} + \nu_{\bar{\beta}_f(1-r)}}\; e^{-\frac{|\boldsymbol{\delta}|^2}{\nu_{\bar{\beta}_b r}+\nu_{\bar{\beta}_f(1-r)}}}\,, \tag{5.43}$$

with

$$\begin{aligned}
|\boldsymbol{\delta}|^2 &= |\boldsymbol{\xi}_0|^2\left(e^{-\frac{\kappa}{2}t} - e^{-\frac{\kappa}{2}t/n_{\rm th}}\right)^2\,, \\
\nu_{\bar{\beta}_q r} &= 2\frac{1}{\left[1/\mathcal{N}_b(\bar{\beta}_q)+1\right]^r - 1} + 1\,, \\
\mathcal{N}_{\bar{\beta}_q,r} &= \frac{1}{\left[1+\mathcal{N}_b(\bar{\beta}_q)\right]^r - \left[\mathcal{N}_b(\bar{\beta}_q)\right]^r}\,, \\
\mathcal{N}_b(\bar{\beta}_q) &= \mathcal{N}_b(\bar{\beta}_0)e^{-\kappa/n_{\rm th}^{(\rm q)}t} + \mathcal{N}_b(\beta)\left(1 - e^{-\kappa/n_{\rm th}^{(\rm q)}t}\right)\,.
\end{aligned} \tag{5.44}$$

Notice that if we take initial state of the probe to be the ground state, i.e. $\boldsymbol{\xi}_0 = 0$ and $\bar{\beta}_0 \to \infty$, the first moments vanish, i.e. $\boldsymbol{\delta}(t) = 0$, and $\mathcal{N}_b(\bar{\beta}_q) = \mathcal{N}_b(\beta)\left(1 - e^{-\kappa/n_{\rm th}^{(\rm q)}t}\right)$. For $\bar{\beta}_0 = \beta$ and $\boldsymbol{\xi}_0 \neq 0$, instead, the resulting expression for $Q_r(t)$ (5.43) is particularly compact: $Q_r(t) = \exp\left\{-\frac{|\boldsymbol{\delta}(t)|^2}{2}\left[1 + 2\mathcal{N}_b(\beta) - \mathcal{N}_b(\beta)f_r\right]\right\}$, with $f_r := \left(1 + \frac{1}{\mathcal{N}_b(\beta)}\right)^r + \left(1 + \frac{1}{\mathcal{N}_b(\beta)}\right)^{1-r}$ and $\boldsymbol{\delta}(t) := \boldsymbol{\xi}_0\left(e^{-\frac{\kappa}{2}t} - e^{-\frac{\kappa}{2}t/n_{\rm th}}\right)$. In this case the minimum of $Q_r(t)$ can be easily shown to be attained for $r = 1/2$. Hence we get

$$Q(t) = \exp\left\{-\frac{1}{2}\left[\sqrt{\mathcal{N}_b(\beta)+1} - \sqrt{\mathcal{N}_b(\beta)}\right]^2 |\boldsymbol{\delta}(t)|^2\right\}\,, \tag{5.45}$$

which can now be optimized with respect to t leading to the analytical expression

$$\bar{t} = \ln(n_{\rm th})/(\kappa N_f(\beta)) = 2n_{\rm th}\ln(n_{\rm th})/(\kappa(n_{\rm th}-1))\,, \tag{5.46}$$

that *mimics* the one observed in Eq. (5.21) for the TLS analysis. Feeding this into Eq. (5.45) the resulting expression can now be optimized with respect to the bath temperature $1/\beta$, giving $\mathcal{N}_b(\beta_{\rm best}) \approx 1.96$ corresponding to values $\bar{t}_{\beta_{\rm best}} \approx 4/\kappa$ and

$$Q(\bar{t}_{\beta_{\rm best}}) = \exp(-\Gamma\,|\boldsymbol{\xi}_0|^2)\,, \tag{5.47}$$

with $\Gamma \approx 0.0145$.

5.5 Conclusions

Statistical tagging (Farina, Cavina and Giovannetti 2019) and, more generally, bath discrimination, is a simple yet insightful instance of the possibility of indirectly probing an environment. In this setting, information about the bath structure are retrieved via measurements on a quantum probe which has interacted with the bath up to a selected measurement time $\bar{t}$. This approach reveals how different properties of the bath affect the nature of the optimal discrimination procedures. This is clear in the tagging context we presented in this Chapter (Farina, Cavina and Giovannetti 2019, Gianani et al. 2020): a thermal bath has an unknown statistics - fermionic or bosonic - that we want to guess, with the additional information of knowing the respective temperatures - $1/\beta_f$ and $1/\beta_b$ - associated to the two bath instances (Gianani et al. 2020). Here the quantum nature of the problem is manifested both in the statistical properties of the bath and in the coherence of a single-qubit probe. For input energy eigenstates, i.e. when no initial coherence is present, our inspection has revealed a transition between temperature regimes in which either equilibrium - $\bar{t} \to \infty$ - or non-equilibrium states - $\bar{t} < \infty$ - are optimal. States with quantum coherence, instead, do not display such transition - i.e. non-equilibrium conditions are generally optimal - and only their inclusion allows to reach the best discrimination capability.

The analysis has been then extended to the case of a quantum harmonic oscillator probe in the symplified framework $\beta_b = \beta_f$ (Farina, Cavina and Giovannetti 2019). For this kind of probe, in the absence of the input energy limitation and, hence, at variance with the qubit probe, the error probability can be brought to reach arbitrarily small values because of the possibility of injecting arbitrarily large initial energy into the system, possibly in a coherent way (cfr. Eq. (5.45) and related results).

CHAPTER 6

General conclusions

Motivated by the growing interest in the field of open quantum systems, we analyzed the way a generic quantum object is microscopically influenced by the presence of a thermal environment, studying specific implementations and proposing protocols aimed to exploit this kind of sensitivity for quantum technology. After the Literature Review Chapter 2, the thesis was divided into three macro-areas - Chapters 3, 4 and 5 - each containing a summary of the corresponding main conclusions - specifically, Sections 3.4, 4.5 and 5.5. In Chapter 3, we started from the non-positivity issue related to the Redfield equation, curing it of the strict amount that is necessary via coarse-grain averaging (Farina and Giovannetti 2019). We then applied this methodology in the context of dissipative multipartite systems where the *local vs global* debate is of interest in the recent and current literature (see, e.g., Rivas et al. (2010), Hofer et al. (2017), González et al. (2017), Cattaneo et al. (2019)). Beyond finding useful the application of the "CP-Redfield" equation, we also successfully tested a sensible convex-mixture of the local and global solutions based on the timescale separation of the two strategies (Farina et al. 2020). The local approach has been then applied in the context of quantum batteries (Andolina et al. 2018) - Chapter 4 - providing one of the first attempts of schematizing the energy and ergotropy charging in an open setting and paying particular attention to the interplay between coherent and incoherent energy supply mechanisms (Farina, Andolina, Mari, Polini and Giovannetti 2019). The sensitivity of a quantum system to its surroundings has been finally exploited in the context of statistical tagging (Farina, Cavina and Giovannetti 2019, Gianani et al. 2020) - Chapter 5 - where one aims to guess the quantum statistics (fermionic or bosonic) of a thermal bath of interest. Entering hence in the framework of quantum metrology and quantum state discrimination, we treated the cases of qubit and harmonic oscillator probes, observing that, generally, coherences in the input state of the probe are beneficial for the discrimination capability and noticing a bosonic advantage in reducing to zero the error probability.

Future developments may concern the study of the performances of the different master equations in predicting the fluctuations of some quantities of interest, focusing on the *thermodynamic uncertainty relations* in the quantum regime (Timpanaro et al. 2019), and, regarding quantum metrology, novel efforts may be addressed to build up proper

distances between quantum trajectories, hence not restricting to single-shot measurements.

REFERENCES

Acín, A., Bloch, I., Buhrman, H., Calarco, T., Eichler, C., Eisert, J., Esteve, D., Gisin, N., Glaser, S. J., Jelezko, F., Kuhr, S., Lewenstein, M., Riedel, M. F., Schmidt, P. O., Thew, R., Wallraff, A., Walmsley, I. and Wilhelm, F. K. (2018), 'The quantum technologies roadmap: a European community view', *New Journal of Physics* **20**(8), 080201.
URL: https://doi.org/10.1088%2F1367-2630%2Faad1ea

Adesso, G., Ragy, S. and Lee, A. R. (2014), 'Continuous Variable Quantum Information: Gaussian States and Beyond', *Open Systems and Information Dynamics* **21**(01n02), 1440001.
URL: https://doi.org/10.1142/S1230161214400010

Alicki, R. and Fannes, M. (2013), 'Entanglement boost for extractable work from ensembles of quantum batteries', *Phys. Rev. E* **87**, 042123.
URL: https://link.aps.org/doi/10.1103/PhysRevE.87.042123

Alicki, R. and Kosloff, R. (2018), Introduction to quantum thermodynamics: History and prospects, *in* 'Thermodynamics in the Quantum Regime', Springer, pp. 1–33.

Alicki, R. and Lendi, K. (2007), *Quantum dynamical semigroups and applications*, Vol. 717, Springer.

Allahverdyan, A. E., Balian, R. and Nieuwenhuizen, T. M. (2004), 'Maximal work extraction from finite quantum systems', *Europhysics Letters (EPL)* **67**(4), 565–571.
URL: https://doi.org/10.1209%2Fepl%2Fi2004-10101-2

Andolina, G. M., Farina, D., Mari, A., Pellegrini, V., Giovannetti, V. and Polini, M. (2018), 'Charger-mediated energy transfer in exactly solvable models for quantum batteries', *Phys. Rev. B* **98**, 205423.
URL: https://link.aps.org/doi/10.1103/PhysRevB.98.205423

Andolina, G. M., Keck, M., Mari, A., Campisi, M., Giovannetti, V. and Polini, M. (2019), 'Extractable work, the role of correlations, and asymptotic freedom in quantum batteries', *Phys. Rev. Lett.* **122**, 047702.
URL: https://link.aps.org/doi/10.1103/PhysRevLett.122.047702

Argentieri, G., Benatti, F., Floreanini, R. and Pezzutto, M. (2014), 'Violations of the second law of thermodynamics by a non-completely positive dynamics', *EPL (Europhysics Letters)* **107**(5), 50007.
URL: https://doi.org/10.1209%2F0295-5075%2F107%2F50007

Arute, F., Arya, K., Babbush, R. and *et al.* (2019), 'Quantum supremacy using a programmable superconducting processor', *Nature* **574**, 505–510.
URL: https://doi.org/10.1038/s41586-019-1666-5

Audenaert, K. M. R., Calsamiglia, J., Muñoz Tapia, R., Bagan, E., Masanes, L., Acin, A. and Verstraete, F. (2007), 'Discriminating states: The Quantum Chernoff Bound', *Phys. Rev. Lett.* **98**, 160501.
URL: https://link.aps.org/doi/10.1103/PhysRevLett.98.160501

Benatti, F. and Floreanini, R. (2005), 'Open quantum dynamics: Complete positivity and entanglement', *International Journal of Modern Physics B* **19**(19), 3063–3139.
URL: https://doi.org/10.1142/S0217979205032097

Benatti, F., Floreanini, R. and Piani, M. (2003*a*), 'Environment Induced Entanglement in Markovian Dissipative Dynamics', *Phys. Rev. Lett.* **91**, 070402.
URL: https://link.aps.org/doi/10.1103/PhysRevLett.91.070402

Benatti, F., Floreanini, R. and Piani, M. (2003*b*), 'Nonpositive evolutions in open system dynamics', *Phys. Rev. A* **67**, 042110.
URL: https://link.aps.org/doi/10.1103/PhysRevA.67.042110

Benedetti, C., Salari Sehdaran, F., Zandi, M. H. and Paris, M. G. A. (2018), 'Quantum probes for the cutoff frequency of Ohmic environments', *Phys. Rev. A* **97**, 012126.
URL: https://link.aps.org/doi/10.1103/PhysRevA.97.012126

Bina, M., Casagrande, F., Lulli, A. and Solano, E. (2008), 'Monitoring atom-atom entanglement and decoherence in a solvable tripartite open system in cavity QED', *Phys. Rev. A* **77**, 033839.
URL: https://link.aps.org/doi/10.1103/PhysRevA.77.033839

Binder, F. C., Vinjanampathy, S., Modi, K. and Goold, J. (2015), 'Quantacell: powerful charging of quantum batteries', *New Journal of Physics* **17**(7), 075015.
URL: https://doi.org/10.1088%2F1367-2630%2F17%2F7%2F075015

Blencowe, M. (2004), 'Quantum electromechanical systems', *Physics Reports* **395**(3), 159 – 222.

URL: http://www.sciencedirect.com/science/article/pii/S0370157304000080

Bortz, M. and Stolze, J. (2007), 'Exact dynamics in the inhomogeneous central-spin model', *Phys. Rev. B* **76**, 014304.
URL: https://link.aps.org/doi/10.1103/PhysRevB.76.014304

Bose, S. N. (1924), 'Plancks gesetz und lichtquantenhypothese', *Z. Physik* **26**, 178–181.
URL: https://doi.org/10.1007/BF01327326

Braunstein, S. L. and Caves, C. M. (1994), 'Statistical distance and the geometry of quantum states', *Phys. Rev. Lett.* **72**, 3439–3443.
URL: https://link.aps.org/doi/10.1103/PhysRevLett.72.3439

Breuer, H.-P., Petruccione, F. et al. (2002), *The theory of open quantum systems*, Oxford University Press on Demand.

Brown, E. G., Friis, N. and Huber, M. (2016), 'Passivity and practical work extraction using Gaussian operations', *New Journal of Physics* **18**(11), 113028.
URL: https://doi.org/10.1088/1367-2630/18/11/113028

Calsamiglia, J., Muñoz Tapia, R., Masanes, L., Acin, A. and Bagan, E. (2008), 'Quantum Chernoff bound as a measure of distinguishability between density matrices: Application to qubit and Gaussian states', *Phys. Rev. A* **77**, 032311.
URL: https://link.aps.org/doi/10.1103/PhysRevA.77.032311

Campaioli, F., Pollock, F. A., Binder, F. C., Céleri, L., Goold, J., Vinjanampathy, S. and Modi, K. (2017), 'Enhancing the charging power of quantum batteries', *Phys. Rev. Lett.* **118**, 150601.
URL: https://link.aps.org/doi/10.1103/PhysRevLett.118.150601

Campaioli, F., Pollock, F. A. and Vinjanampathy, S. (2018), Quantum batteries, *in* 'Thermodynamics in the Quantum Regime', Springer, pp. 207–225.

Campisi, M., Hänggi, P. and Talkner, P. (2011), 'Colloquium: Quantum fluctuation relations: Foundations and applications', *Rev. Mod. Phys.* **83**, 771–791.
URL: https://link.aps.org/doi/10.1103/RevModPhys.83.771

Cattaneo, M., Giorgi, G. L., Maniscalco, S. and Zambrini, R. (2019), 'Local versus global master equation with common and separate baths: superiority of the global approach in partial secular approximation', *New Journal of Physics* **21**(11), 113045.
URL: https://doi.org/10.1088%2F1367-2630%2Fab54ac

Cattaneo, M., Giorgi, G. L., Maniscalco, S. and Zambrini, R. (2020), 'Symmetry and block structure of the Liouvillian superoperator in partial secular approximation', *Phys. Rev. A* **101**, 042108.
URL: https://link.aps.org/doi/10.1103/PhysRevA.101.042108

Cavina, V., Mancino, L., De Pasquale, A., Gianani, I., Sbroscia, M., Booth, R. I., Roccia, E., Raimondi, R., Giovannetti, V. and Barbieri, M. (2018), 'Bridging thermodynamics and metrology in nonequilibrium quantum thermometry', *Phys. Rev. A* **98**, 050101.
URL: https://link.aps.org/doi/10.1103/PhysRevA.98.050101

Chakraborty, T. (1999), *Quantum Dots: A survey of the properties of artificial atoms*, Elsevier.

Cheng, Y. C. and Silbey, R. J. (2005), 'Markovian approximation in the relaxation of open quantum systems', *The Journal of Physical Chemistry B* **109**(45), 21399–21405. PMID: 16853776.
URL: https://doi.org/10.1021/jp051303o

Choi, M.-D. (1972), 'Positive linear maps on c*-algebras', *Canadian Journal of Mathematics* **24**(3), 520–529.

Correa, L. A., Mehboudi, M., Adesso, G. and Sanpera, A. (2015), 'Individual quantum probes for optimal thermometry', *Phys. Rev. Lett.* **114**, 220405.
URL: https://link.aps.org/doi/10.1103/PhysRevLett.114.220405

Cramér, H. (1999), *Mathematical methods of statistics*, Vol. 43, Princeton University Press.

Cresser, J. (1992), 'Thermal Equilibrium in the Jaynes-Cummings Model', *Journal of Modern Optics* **39**(11), 2187–2192.
URL: https://doi.org/10.1080/09500349214552211

Cresser, J. and Facer, C. (2017), 'Coarse-graining in the derivation of Markovian master equations and its significance in quantum thermodynamics', *arXiv preprint arXiv:1710.09939* .
URL: https://arxiv.org/abs/1710.09939

De Chiara, G., Landi, G., Hewgill, A., Reid, B., Ferraro, A., Roncaglia, A. J. and Antezza, M. (2018), 'Reconciliation of quantum local master equations with thermodynamics', *New Journal of Physics* **20**(11), 113024.
URL: https://doi.org/10.1088%2F1367-2630%2Faaecee

De Pasquale, A., Rossini, D., Fazio, R. and Giovannetti, V. (2016), 'Local quantum thermal susceptibility', *Nature communications* **7**(1), 1–8.
URL: https://doi.org/10.1038/ncomms12782

Deçordi, G. and Vidiella-Barranco, A. (2017), 'Two coupled qubits interacting with a thermal bath: A comparative study of different models', *Optics Communications* **387**, 366 – 376.
URL: http://www.sciencedirect.com/science/article/pii/S003040181630880X

Dicke, R. H. (1954), 'Coherence in spontaneous radiation processes', *Phys. Rev.* **93**, 99–110.
URL: https://link.aps.org/doi/10.1103/PhysRev.93.99

Dowling, J. P. and Milburn, G. J. (2003), 'Quantum technology: the second quantum revolution', *Philosophical Transactions of the Royal Society of London. Series A: Mathematical, Physical and Engineering Sciences* **361**(1809), 1655–1674.
URL: https://royalsocietypublishing.org/doi/abs/10.1098/rsta.2003.1227

Dümcke, R. and Spohn, H. (1979), 'The proper form of the generator in the weak coupling limit', *Z. Phys. B Con. Mat.* **34**, 419–422.
URL: https://doi.org/10.1007/BF01325208

Emary, C. and Brandes, T. (2003), 'Chaos and the quantum phase transition in the Dicke model', *Phys. Rev. E* **67**, 066203.
URL: https://link.aps.org/doi/10.1103/PhysRevE.67.066203

Esposito, M., Kawai, R., Lindenberg, K. and Van den Broeck, C. (2010), 'Quantum-dot Carnot engine at maximum power', *Phys. Rev. E* **81**, 041106.
URL: https://link.aps.org/doi/10.1103/PhysRevE.81.041106

Farina, D., Andolina, G. M., Mari, A., Polini, M. and Giovannetti, V. (2019), 'Charger-mediated energy transfer for quantum batteries: An open-system approach', *Phys. Rev. B* **99**, 035421.
URL: https://link.aps.org/doi/10.1103/PhysRevB.99.035421

Farina, D., Cavina, V. and Giovannetti, V. (2019), 'Quantum bath statistics tagging', *Phys. Rev. A* **100**, 042327.
URL: https://link.aps.org/doi/10.1103/PhysRevA.100.042327

Farina, D., De Filippis, G., Cataudella, V., Polini, M. and Giovannetti, V. (2020), 'Going beyond local and global approaches for localized thermal dissipation', *Phys. Rev. A*

102, 052208.
URL: https://link.aps.org/doi/10.1103/PhysRevA.102.052208

Farina, D. and Giovannetti, V. (2019), 'Open-quantum-system dynamics: Recovering positivity of the redfield equation via the partial secular approximation', *Phys. Rev. A* **100**, 012107.
URL: https://link.aps.org/doi/10.1103/PhysRevA.100.012107

Ferraro, A., Olivares, S. and Paris, M. G. (2005), 'Gaussian states in continuous variable quantum information', *arXiv preprint quant-ph/0503237* .
URL: https://arxiv.org/abs/quant-ph/0503237

Ferraro, D., Campisi, M., Andolina, G. M., Pellegrini, V. and Polini, M. (2018), 'High-power collective charging of a solid-state quantum battery', *Phys. Rev. Lett.* **120**, 117702.
URL: https://link.aps.org/doi/10.1103/PhysRevLett.120.117702

Fischer, A., Evers, E., Varwig, S., Greilich, A., Bayer, M. and Anders, F. B. (2018), 'Signatures of long-range spin-spin interactions in an (in,ga)as quantum dot ensemble', *Phys. Rev. B* **98**, 205308.
URL: https://link.aps.org/doi/10.1103/PhysRevB.98.205308

Gaspard, P. and Nagaoka, M. (1999), 'Slippage of initial conditions for the Redfield master equation', *The Journal of Chemical Physics* **111**(13), 5668–5675.
URL: https://doi.org/10.1063/1.479867

Gelbwaser-Klimovsky, D., Niedenzu, W. and Kurizki, G. (2015), Chapter twelve - thermodynamics of quantum systems under dynamical control, Vol. 64 of *Advances In Atomic, Molecular, and Optical Physics*, Academic Press, pp. 329 – 407.
URL: http://www.sciencedirect.com/science/article/pii/S1049250X15000130

Gianani, I., Farina, D., Barbieri, M., Cimini, V., Cavina, V. and Giovannetti, V. (2020), 'Discrimination of thermal baths by single-qubit probes', *Phys. Rev. Research* **2**, 033497.
URL: https://link.aps.org/doi/10.1103/PhysRevResearch.2.033497

Giovannetti, V., Lloyd, S. and Maccone, L. (2006), 'Quantum metrology', *Phys. Rev. Lett.* **96**, 010401.
URL: https://link.aps.org/doi/10.1103/PhysRevLett.96.010401

Giovannetti, V., Lloyd, S. and Maccone, L. (2011), 'Advances in quantum metrology', *Nature Photonics* **5**(4), 222.
URL: https://doi.org/10.1038/nphoton.2011.35

Gisin, N. and Thew, R. (2007), 'Quantum communication', *Nature photonics* **1**(3), 165–171.
URL: https://doi.org/10.1038/nphoton.2007.22

Giuliani, G. and Vignale, G. (2005), *Quantum theory of the electron liquid*, Cambridge University Press.

Goldman, V. J., Liu, J. and Zaslavsky, A. (2005), 'Fractional statistics of laughlin quasiparticles in quantum antidots', *Phys. Rev. B* **71**, 153303.
URL: https://link.aps.org/doi/10.1103/PhysRevB.71.153303

González, J. O., Correa, L. A., Nocerino, G., Palao, J. P., Alonso, D. and Adesso, G. (2017), 'Testing the validity of the 'local' and 'global' GKLS master equations on an exactly solvable model', *Open Systems and Information Dynamics* **24**(04), 1740010.
URL: https://doi.org/10.1142/S1230161217400108

Goold, J., Huber, M., Riera, A., del Rio, L. and Skrzypczyk, P. (2016), 'The role of quantum information in thermodynamics—a topical review', *Journal of Physics A: Mathematical and Theoretical* **49**(14), 143001.
URL: https://doi.org/10.1088%2F1751-8113%2F49%2F14%2F143001

Gorini, V., Kossakowski, A. and Sudarshan, E. C. G. (1976), 'Completely positive dynamical semigroups of n-level systems', *Journal of Mathematical Physics* **17**(5), 821–825.
URL: https://aip.scitation.org/doi/abs/10.1063/1.522979

Gröblacher, S., Trubarov, A., Prigge, N., Cole, G., Aspelmeyer, M. and Eisert, J. (2015), 'Observation of non-Markovian micromechanical brownian motion', *Nature Communications* **6**, 7606.
URL: https://doi.org/10.1038/ncomms8606

Haldane, F. D. M. (1991), '"Fractional statistics" in arbitrary dimensions: A generalization of the Pauli principle', *Phys. Rev. Lett.* **67**, 937–940.
URL: https://link.aps.org/doi/10.1103/PhysRevLett.67.937

Haroche, S. (2013), 'Nobel lecture: Controlling photons in a box and exploring the quantum to classical boundary', *Rev. Mod. Phys.* **85**, 1083–1102.
URL: https://link.aps.org/doi/10.1103/RevModPhys.85.1083

Hartmann, M., Brandão, F. and Plenio, M. (2008), 'Quantum many-body phenomena in coupled cavity arrays', *Laser and Photonics Reviews* **2**(6), 527–556.
URL: https://onlinelibrary.wiley.com/doi/abs/10.1002/lpor.200810046

Hartmann, R. and Strunz, W. T. (2020), 'Accuracy assessment of perturbative master equations: Embracing nonpositivity', *Phys. Rev. A* **101**, 012103.
URL: https://link.aps.org/doi/10.1103/PhysRevA.101.012103

Helstrom, C. W. (1976), *Quantum Detection and Estimation Theory*, Vol. 123, Academic Press, New York.

Hofer, P. P., Perarnau-Llobet, M., Miranda, L. D. M., Haack, G., Silva, R., Brask, J. B. and Brunner, N. (2017), 'Markovian master equations for quantum thermal machines: local versus global approach', *New Journal of Physics* **19**(12), 123037.
URL: https://doi.org/10.1088%2F1367-2630%2Faa964f

Holevo, A. S. (2012), *Quantum Systems, Channels, Information*, De Gruyter, Berlin, Boston.
URL: https://www.degruyter.com/view/title/122902

Horodecki, M. and Oppenheim, J. (2013), 'Fundamental limitations for quantum and nanoscale thermodynamics', *Nature Communications* **4**(1), 1–6.
URL: https://doi.org/10.1038/ncomms3059

Hovhannisyan, K. V., Barra, F. and Imparato, A. (2020), 'Charging assisted by thermalization', *Phys. Rev. Research* **2**, 033413.
URL: https://link.aps.org/doi/10.1103/PhysRevResearch.2.033413

Hovhannisyan, K. V., Perarnau-Llobet, M., Huber, M. and Acín, A. (2013), 'Entanglement generation is not necessary for optimal work extraction', *Phys. Rev. Lett.* **111**, 240401.
URL: https://link.aps.org/doi/10.1103/PhysRevLett.111.240401

Ishizaki, A. and Fleming, G. R. (2009), 'On the adequacy of the Redfield equation and related approaches to the study of quantum dynamics in electronic energy transfer', *The Journal of Chemical Physics* **130**(23), 234110.
URL: https://doi.org/10.1063/1.3155214

Jamiołkowski, A. (1972), 'Linear transformations which preserve trace and positive semidefiniteness of operators', *Reports on Mathematical Physics* **3**(4), 275 – 278.

URL: http://www.sciencedirect.com/science/article/pii/0034487772900110

Jaynes, E. T. and Cummings, F. W. (1963), 'Comparison of quantum and semiclassical radiation theories with application to the beam maser', *Proceedings of the IEEE* **51**(1), 89–109.
URL: http://doi.org/10.1109/PROC.1963.1664

Jeske, J. and Cole, J. H. (2013), 'Derivation of markovian master equations for spatially correlated decoherence', *Phys. Rev. A* **87**, 052138.
URL: https://link.aps.org/doi/10.1103/PhysRevA.87.052138

Jeske, J., Ing, D. J., Plenio, M. B., Huelga, S. F. and Cole, J. H. (2015), 'Bloch-Redfield equations for modeling light-harvesting complexes', *The Journal of Chemical Physics* **142**(6), 064104.
URL: https://doi.org/10.1063/1.4907370

Jevtic, S., Newman, D., Rudolph, T. and Stace, T. M. (2015), 'Single-qubit thermometry', *Phys. Rev. A* **91**, 012331.
URL: https://link.aps.org/doi/10.1103/PhysRevA.91.012331

Khandelwal, S., Palazzo, N., Brunner, N. and Haack, G. (2020), 'Critical heat current for operating an entanglement engine', *New Journal of Physics* .
URL: http://iopscience.iop.org/10.1088/1367-2630/ab9983

Kiilerich, A. H., De Pasquale, A. and Giovannetti, V. (2018), 'Dynamical approach to ancilla-assisted quantum thermometry', *Phys. Rev. A* **98**, 042124.
URL: https://link.aps.org/doi/10.1103/PhysRevA.98.042124

Laughlin, R. B. (1983), 'Anomalous quantum hall effect: An incompressible quantum fluid with fractionally charged excitations', *Phys. Rev. Lett.* **50**, 1395–1398.
URL: https://link.aps.org/doi/10.1103/PhysRevLett.50.1395

Laurat, J., Keller, G., Oliveira-Huguenin, J. A., Fabre, C., Coudreau, T., Serafini, A., Adesso, G. and Illuminati, F. (2005), 'Entanglement of two-mode Gaussian states: characterization and experimental production and manipulation', *Journal of Optics B: Quantum and Semiclassical Optics* **7**(12), S577–S587.
URL: https://doi.org/10.1088/1464-4266/7/12/021

Le, T. P., Levinsen, J., Modi, K., Parish, M. M. and Pollock, F. A. (2018), 'Spin-chain model of a many-body quantum battery', *Phys. Rev. A* **97**, 022106.
URL: https://link.aps.org/doi/10.1103/PhysRevA.97.022106

Leggett, A. J., Chakravarty, S., Dorsey, A. T., Fisher, M. P. A., Garg, A. and Zwerger, W. (1987), 'Dynamics of the dissipative two-state system', *Rev. Mod. Phys.* **59**, 1–85.
URL: https://link.aps.org/doi/10.1103/RevModPhys.59.1

Levy, A. and Kosloff, R. (2014), 'The local approach to quantum transport may violate the second law of thermodynamics', *EPL (Europhysics Letters)* **107**(2), 20004.
URL: https://doi.org/10.1209%2F0295-5075%2F107%2F20004

Liao, J.-Q., Gong, Z. R., Zhou, L., Liu, Y.-x., Sun, C. P. and Nori, F. (2010), 'Controlling the transport of single photons by tuning the frequency of either one or two cavities in an array of coupled cavities', *Phys. Rev. A* **81**, 042304.
URL: https://link.aps.org/doi/10.1103/PhysRevA.81.042304

Lim, J., Ing, D. J., Rosskopf, J., Jeske, J., Cole, J. H., Huelga, S. F. and Plenio, M. B. (2017), 'Signatures of spatially correlated noise and non-secular effects in two-dimensional electronic spectroscopy', *The Journal of Chemical Physics* **146**(2), 024109.
URL: https://doi.org/10.1063/1.4973975

Lindblad, G. (1976), 'On the generators of quantum dynamical semigroups', *Communications in Mathematical Physics* **48**(2), 119–130.
URL: https://doi.org/10.1007/BF01608499

Lougovski, P., Casagrande, F., Lulli, A. and Solano, E. (2007), 'Strongly driven one-atom laser and decoherence monitoring', *Phys. Rev. A* **76**, 033802.
URL: https://link.aps.org/doi/10.1103/PhysRevA.76.033802

Lörch, N., Bruder, C., Brunner, N. and Hofer, P. P. (2018), 'Optimal work extraction from quantum states by photo-assisted Cooper pair tunneling', *Quantum Science and Technology* **3**(3), 035014.
URL: https://doi.org/10.1088/2058-9565/aacbf3

Mahan, G. D. (2013), *Many-particle physics*, Springer Science and Business Media.

Majer, J., Chow, J., Gambetta, J., Koch, J., Johnson, B., Schreier, J., Frunzio, L., Schuster, D., Houck, A. A., Wallraff, A. et al. (2007), 'Coupling superconducting qubits via a cavity bus', *Nature* **449**(7161), 443–447.
URL: https://doi.org/10.1038/nature06184

Mari, A., Farace, A. and Giovannetti, V. (2015), 'Quantum optomechanical piston engines powered by heat', *Journal of Physics B: Atomic, Molecular and Optical Physics* **48**(17), 175501.
URL: https://doi.org/10.1088%2F0953-4075%2F48%2F17%2F175501

Marian, P. and Marian, T. A. (2012), 'Uhlmann fidelity between two-mode Gaussian states', *Phys. Rev. A* **86**, 022340.
URL: https://link.aps.org/doi/10.1103/PhysRevA.86.022340

Mohseni, M., Rebentrost, P., Lloyd, S. and Aspuru-Guzik, A. (2008), 'Environment-assisted quantum walks in photosynthetic energy transfer', *The Journal of Chemical Physics* **129**(17), 174106.
URL: https://doi.org/10.1063/1.3002335

Nielsen, M. A. and Chuang, I. L. (2010), *Quantum Computation and Quantum Information: 10th Anniversary Edition*, Cambridge University Press.

Nussbaum, M. and Szkoła, A. (2009), 'The Chernoff lower bound for symmetric quantum hypothesis testing', *Ann. Statist.* **37**(2), 1040–1057.
URL: https://doi.org/10.1214/08-AOS593

Ogawa, T. and Hayashi, M. (2004), 'On error exponents in quantum hypothesis testing', *IEEE Transactions on Information Theory* **50**(6), 1368–1372.
URL: https://doi.org/10.1109/TIT.2004.828155

Olivares, S. (2012), 'Quantum optics in the phase space', *The European Physical Journal Special Topics* **203**(1), 3–24.
URL: https://doi.org/10.1140/epjst/e2012-01532-4

Palma, G. M., Suominen, K.-a. and Ekert, A. (1996), 'Quantum computers and dissipation', *Proceedings of the Royal Society of London. Series A: Mathematical, Physical and Engineering Sciences* **452**(1946), 567–584.
URL: https://royalsocietypublishing.org/doi/abs/10.1098/rspa.1996.0029

Paris, M. G. A. (2009), 'Quantum estimation for quantum technology', *International Journal of Quantum Information* **07**(supp01), 125–137.
URL: https://doi.org/10.1142/S0219749909004839

Paul, H. (1982), 'Photon antibunching', *Rev. Mod. Phys.* **54**, 1061–1102.
URL: https://link.aps.org/doi/10.1103/RevModPhys.54.1061

Pauli, W. (1940), 'The connection between spin and statistics', *Phys. Rev.* **58**, 716–722.
URL: https://link.aps.org/doi/10.1103/PhysRev.58.716

Pekola, J. P., Suomela, S. and Galperin, Y. M. (2016), 'Finite-size bath in qubit thermodynamics', *Journal of Low Temperature Physics* **184**(5-6), 1015–1029.
URL: https://doi.org/10.1007/s10909-016-1618-5

Peropadre, B., Zueco, D., Wulschner, F., Deppe, F., Marx, A., Gross, R. and García-Ripoll, J. J. (2013), 'Tunable coupling engineering between superconducting resonators: From sidebands to effective gauge fields', *Phys. Rev. B* **87**, 134504.
URL: https://link.aps.org/doi/10.1103/PhysRevB.87.134504

Pirandola, S. and Lloyd, S. (2008), 'Computable bounds for the discrimination of Gaussian states', *Phys. Rev. A* **78**, 012331.
URL: https://link.aps.org/doi/10.1103/PhysRevA.78.012331

Plenio, M. B. and Huelga, S. F. (2008), 'Dephasing-assisted transport: quantum networks and biomolecules', *New Journal of Physics* **10**(11), 113019.
URL: https://doi.org/10.1088%2F1367-2630%2F10%2F11%2F113019

Prokof'ev, N. V. and Stamp, P. C. E. (2000), 'Theory of the spin bath', *Reports on Progress in Physics* **63**(4), 669–726.
URL: https://doi.org/10.1088%2F0034-4885%2F63%2F4%2F204

Purkayastha, A., Dhar, A. and Kulkarni, M. (2016), 'Out-of-equilibrium open quantum systems: A comparison of approximate quantum master equation approaches with exact results', *Phys. Rev. A* **93**, 062114.
URL: https://link.aps.org/doi/10.1103/PhysRevA.93.062114

Pusz, W. and Woronowicz, S. L. (1978), 'Passive states and KMS states for general quantum systems', *Communications in Mathematical Physics* **58**(3), 273–290.
URL: https://doi.org/10.1007/BF01614224

Redfield, A. G. (1957), 'On the theory of relaxation processes', *IBM Journal of Research and Development* **1**(1), 19–31.
URL: https://ieeexplore.ieee.org/abstract/document/5392713

Riedel, M. F., Binosi, D., Thew, R. and Calarco, T. (2017), 'The european quantum technologies flagship programme', *Quantum Science and Technology* **2**(3), 030501.
URL: https://doi.org/10.1088%2F2058-9565%2Faa6aca

Rivas, A. (2017), 'Refined weak-coupling limit: Coherence, entanglement, and non-markovianity', *Phys. Rev. A* **95**, 042104.
URL: https://link.aps.org/doi/10.1103/PhysRevA.95.042104

Rivas, Á., Plato, A. D. K., Huelga, S. F. and Plenio, M. B. (2010), 'Markovian master equations: a critical study', *New Journal of Physics* **12**(11), 113032.
URL: https://doi.org/10.1088%2F1367-2630%2F12%2F11%2F113032

Salari Sehdaran, F., Bina, M., Benedetti, C. and Paris, M. G. A. (2019), 'Quantum Probes for Ohmic Environments at Thermal Equilibrium', *Entropy* **21**(5), 486.
URL: https://www.mdpi.com/1099-4300/21/5/486

Sannan, S. (1988), 'Heuristic derivation of the probability distributions of particles emitted by a black hole', *General Relativity and Gravitation* **20**(3), 239–246.
URL: https://doi.org/10.1007/BF00759183

Scarlatella, O. and Schiró, M. (2016), 'Dissipation-induced superradiance in a non-Markovian open Dicke model', *arXiv preprint arXiv:1611.09378* .
URL: https://arxiv.org/abs/1611.09378

Schaller, G. and Brandes, T. (2008), 'Preservation of positivity by dynamical coarse graining', *Phys. Rev. A* **78**, 022106.
URL: https://link.aps.org/doi/10.1103/PhysRevA.78.022106

Schlosshauer, M., Hines, A. P. and Milburn, G. J. (2008), 'Decoherence and dissipation of a quantum harmonic oscillator coupled to two-level systems', *Phys. Rev. A* **77**, 022111.
URL: https://link.aps.org/doi/10.1103/PhysRevA.77.022111

Schoelkopf, R. and Girvin, S. (2008), 'Wiring up quantum systems', *Nature* **451**(7179), 664–669.
URL: https://doi.org/10.1038/451664a

Schwabl, F. (2008), *Advanced Quantum Mechanics*, Springer-Verlag Berlin Heidelberg.

Seah, S., Nimmrichter, S. and Scarani, V. (2018), 'Refrigeration beyond weak internal coupling', *Phys. Rev. E* **98**, 012131.
URL: https://link.aps.org/doi/10.1103/PhysRevE.98.012131

Serafini, A. (2017), *Quantum Continuous Variables: A Primer of Theoretical Methods*, CRC Press.

Shor, P. W. (1994), Algorithms for quantum computation: discrete logarithms and factoring, *in* 'Proceedings 35th annual symposium on foundations of computer science', Ieee, pp. 124–134.
URL: https://ieeexplore.ieee.org/abstract/document/365700

Sommerfeld, A. (1927), 'Zur elektronentheorie der metalle', *Naturwissenschaften* **15**(41), 825–832.
URL: https://doi.org/10.1007/BF01505083

Strasberg, P., Schaller, G., Brandes, T. and Esposito, M. (2017), 'Quantum and information thermodynamics: A unifying framework based on repeated interactions', *Phys. Rev. X* **7**, 021003.
URL: https://link.aps.org/doi/10.1103/PhysRevX.7.021003

Suárez, A., Silbey, R. and Oppenheim, I. (1992), 'Memory effects in the relaxation of quantum open systems', *The Journal of Chemical Physics* **97**(7), 5101–5107.
URL: https://doi.org/10.1063/1.463831

Timpanaro, A. M., Guarnieri, G., Goold, J. and Landi, G. T. (2019), 'Thermodynamic uncertainty relations from exchange fluctuation theorems', *Phys. Rev. Lett.* **123**, 090604.
URL: https://link.aps.org/doi/10.1103/PhysRevLett.123.090604

Tomadin, A. and Fazio, R. (2010), 'Many-body phenomena in QED-cavity arrays [Invited]', *J. Opt. Soc. Am. B* **27**(6), A130–A136.
URL: http://josab.osa.org/abstract.cfm?URI=josab-27-6-A130

Trushechkin, A. S. and Volovich, I. V. (2016), 'Perturbative treatment of inter-site couplings in the local description of open quantum networks', *EPL (Europhysics Letters)* **113**(3), 30005.
URL: https://doi.org/10.1209%2F0295-5075%2F113%2F30005

Urbaszek, B., Marie, X., Amand, T., Krebs, O., Voisin, P., Maletinsky, P., Högele, A. and Imamoglu, A. (2013), 'Nuclear spin physics in quantum dots: An optical investigation', *Rev. Mod. Phys.* **85**, 79–133.
URL: https://link.aps.org/doi/10.1103/RevModPhys.85.79

Verhagen, E., Deléglise, S., Weis, S., Schliesser, A. and Kippenberg, T. J. (2012), 'Quantum-coherent coupling of a mechanical oscillator to an optical cavity mode', *Nature* **482**(7383), 63–67.
URL: https://doi.org/10.1038/nature10787

Vinjanampathy, S. and Anders, J. (2016), 'Quantum thermodynamics', *Contemporary Physics* **57**(4), 545–579.
URL: https://doi.org/10.1080/00107514.2016.1201896

Walls, D. (1970), 'Higher order effects in the master equation for coupled systems', *Z. Phys. A Hadron. Nucl.* **234**, 231–241.
URL: https://doi.org/10.1007/BF01396784

Walls, D. F. and Milburn, G. J. (2007), *Quantum optics*, Springer Science and Business Media.

Weedbrook, C., Pirandola, S., García-Patrón, R., Cerf, N. J., Ralph, T. C., Shapiro, J. H. and Lloyd, S. (2012), 'Gaussian quantum information', *Rev. Mod. Phys.* **84**, 621–669.
URL: https://link.aps.org/doi/10.1103/RevModPhys.84.621

Whitney, R. S. (2008), 'Staying positive: going beyond Lindblad with perturbative master equations', *Journal of Physics A: Mathematical and Theoretical* **41**(17), 175304.
URL: https://doi.org/10.1088%2F1751-8113%2F41%2F17%2F175304

Wilczek, F. (1982), 'Quantum mechanics of fractional-spin particles', *Phys. Rev. Lett.* **49**, 957–959.
URL: https://link.aps.org/doi/10.1103/PhysRevLett.49.957

Wilkie, J. (2001), 'Dissipation in media with memory: A master equation in the statistical resonance approximation', *The Journal of Chemical Physics* **114**(18), 7736–7745.
URL: https://doi.org/10.1063/1.1365955

Wolf, M. M., Eisert, J., Cubitt, T. S. and Cirac, J. I. (2008), 'Assessing non-markovian quantum dynamics', *Phys. Rev. Lett.* **101**, 150402.
URL: https://link.aps.org/doi/10.1103/PhysRevLett.101.150402

Wu, Y.-S. (1994), 'Statistical distribution for generalized ideal gas of fractional-statistics particles', *Phys. Rev. Lett.* **73**, 922–925.
URL: https://link.aps.org/doi/10.1103/PhysRevLett.73.922

LIST OF PUBLICATIONS

Publications related to the Ph.D. thesis

1. I. Gianani, D. Farina, M. Barbieri, V. Cimini, V. Cavina, and V. Giovannetti, Phys. Rev. Research **2**, 033497 (2020). *Discrimination of thermal baths by single-qubit probes.*

2. D. Farina, G. De Filippis, V. Cataudella, M. Polini, and V. Giovannetti, Phys. Rev. A **102**, 052208 (2020). *Going beyond local and global approaches for localized thermal dissipation.*

3. D. Farina, V. Cavina, and V. Giovannetti, Phys. Rev. A **100**, 042327 (2019). *Quantum bath statistics tagging.*

4. D. Farina and V. Giovannetti, Phys. Rev. A **100**, 012107 (2019). *Open-quantum-system dynamics: Recovering positivity of the Redfield equation via the partial secular approximation.*

5. D. Farina, G. M. Andolina, A. Mari, M. Polini, and V. Giovannetti, Phys. Rev. B **99**, 035421 (2019). *Charger-mediated energy transfer for quantum batteries: An open-system approach.*

6. G. M. Andolina, D. Farina, A. Mari, V. Pellegrini, V. Giovannetti, and M. Polini, Phys. Rev. B **98**, 205423 (2018). *Charger-mediated energy transfer in exactly solvable models for quantum batteries.*

Extra publications during the Ph.D. studies

7. S. Chibani, D. Farina, P. Massat, M. Cazayous, A. Sacuto, T. Urata, Y. Tanabe, K. Tanigaki, A. E. Böhmer, P. C. Canfield, M. Merz, S. Karlsson, P. Stro-

bel, P. Toulemonde, I. Paul, Y. Gallais, arXiv preprint arXiv:2011.04319 (2020). *Lattice-Shifted Nematic Quantum Critical Point in* $\mathrm{FeSe_{1-x}S_x}$.

8. D. Farina, G. De Filippis, A. S. Mishchenko, N. Nagaosa, J. A. Yang, D. Reznik, Th. Wolf, and V. Cataudella, Phys. Rev. B **98**, 121104(R) (2018). *Electron-phonon coupling in the undoped cuprate* $\mathrm{YBa_2Cu_3O_6}$ *estimated from Raman and optical conductivity spectra.*

Appendices

Appendix A

Solving the master equation for the two-qubit model

With reference to Sec. 4.3, the interaction picture ME for the two-qubit model reads as

$$\dot{\tilde{\rho}}_{\rm AB}(t) = -i\Big[g\left(\sigma_{\rm A}^{-}\sigma_{\rm B}^{+} + \sigma_{\rm A}^{+}\sigma_{\rm B}^{-}\right) + F(\sigma_{\rm A}^{+} + \sigma_{\rm A}^{-})\ ,\ \tilde{\rho}_{\rm AB}(t)\Big]_{-} + \kappa(1+\mathcal{N}_b)\mathcal{D}^{[\sigma_{\rm A}^{-}]}\left[\tilde{\rho}_{\rm AB}(t)\right] + \kappa\mathcal{N}_b\mathcal{D}^{[\sigma_{\rm A}^{+}]}\left[\tilde{\rho}_{\rm AB}(t)\right]\ . \tag{A.1}$$

with $\mathcal{D}^{[x]}$ as in (4.11). In order to solve the above equation we expand all the operators appearing in it by utilizing a global basis set for the two-qubit system $\{||i\rangle\rangle\}_{i\in\{1,\ldots,4\}}$. We choose

$$\begin{aligned} ||1\rangle\rangle &= |1\rangle_{\rm A}|1\rangle_{\rm B}\ , \quad ||2\rangle\rangle = |1\rangle_{\rm A}|0\rangle_{\rm B}\ , \\ ||3\rangle\rangle &= |0\rangle_{\rm A}|1\rangle_{\rm B}\ , \quad ||4\rangle\rangle = |0\rangle_{\rm A}|0\rangle_{\rm B}\ , \end{aligned} \tag{A.2}$$

where $|1\rangle_{\rm A(B)}$ and $|0\rangle_{\rm A(B)}$ are the eigenvectors of the $\sigma^{z}_{\rm A(B)}$ operators with eigenvalues $+1$ and -1, respectively. Accordingly, we write $\tilde{\rho}_{\rm AB}(t) = \sum_{i,j=1}^{4} r_{ij}(t)\,||i\rangle\rangle\,\langle\langle j||$, or, in matrix form,

$$\tilde{\rho}_{\rm AB}(t) \equiv \begin{pmatrix} r_{11}(t) & r_{12}(t) & r_{13}(t) & r_{14}(t) \\ r_{21}(t) & r_{22}(t) & r_{23}(t) & r_{24}(t) \\ r_{31}(t) & r_{32}(t) & r_{33}(t) & r_{34}(t) \\ r_{41}(t) & r_{42}(t) & r_{43}(t) & r_{44}(t) \end{pmatrix}\ , \tag{A.3}$$

$r_{ij}(t)$ being expansion coefficients. In this representation, the ladder operators $\sigma_{\rm A}^{-}, \sigma_{\rm A}^{+}$ of the subsystem A can instead be written as

$$\sigma_{\rm A}^{-} \equiv \left(\begin{array}{c|c} \mathbf{0} & \mathbf{0} \\ \hline \mathbb{1}_2 & \mathbf{0} \end{array}\right) \tag{A.4}$$

$$\sigma_{\rm A}^{+} \equiv \left(\begin{array}{c|c} \mathbf{0} & \mathbb{1}_2 \\ \hline \mathbf{0} & \mathbf{0} \end{array}\right) \tag{A.5}$$

where $\mathbf{0}$ is the 2×2 matrix with all zero entries. Finally, the system Hamiltonian is represented by

$$g\left(\sigma_{\mathrm{A}}^{-}\sigma_{\mathrm{B}}^{+}+\sigma_{\mathrm{A}}^{+}\sigma_{\mathrm{B}}^{-}\right)+F(\sigma_{\mathrm{A}}^{+}+\sigma_{\mathrm{A}}^{-}) \equiv \begin{pmatrix} 0 & 0 & F & 0 \\ 0 & 0 & g & F \\ F & g & 0 & 0 \\ 0 & F & 0 & 0 \end{pmatrix} . \tag{A.6}$$

With these choices, Eq. (A.1) translates into a first-order system of ordinary differential equations in the 16 unknown (generally complex) functions $r_{\mathrm{ij}}(t)$, which has to be solved under the initial conditions (4.3) corresponding to $r_{ij}(0) = 1$ for $i = j = 4$ and zero otherwise.

Explicit expressions for the local energies of A and B can be obtained once the operators $\sigma_z^{(\mathrm{A})}$ and $\sigma_z^{(\mathrm{B})}$ are represented in the basis (A.2). It turns out that they take the following forms

$$E_{\mathrm{A}}(\tau) = \frac{\omega_0}{2}\left[r_{11}(\tau) + r_{22}(\tau) - r_{33}(\tau) - r_{44}(\tau) + 1\right] \tag{A.7}$$

and

$$E_{\mathrm{B}}(\tau) = \frac{\omega_0}{2}\left[r_{11}(\tau) - r_{22}(\tau) + r_{33}(\tau) - r_{44}(\tau) + 1\right] . \tag{A.8}$$

Finally, the ergotropy of B reads as following

$$\mathcal{E}_{\mathrm{B}}(\tau) = \frac{\omega_0}{2}\{\sqrt{4|r_{12}+r_{34}|^2 + [2(r_{11}+r_{33})-1]^2} + 2(r_{11}+r_{33}) - 1\} . \tag{A.9}$$

Finally, we stress that the approach reported here is equivalent to the one presented in Sec. 4.3, cfr. Eqs. (4.32)-(4.35). Indeed, due to the fact that the state $\tilde{\rho}_{\mathrm{AB}}(t)$ is hermitian and that its trace is 1, in equation (A.1) one has, effectively, 15 unknown real functions, same as in (4.32) (considering real and imaginary components of the 9 unknown average values appearing in it and the fact that 3 of them are purely real).